HTL-51, CFD-21
Project 1928
ISU-ERI-Ames-90030

S. G. Gegg R. H. Pletcher J. L. Steger

A Dual Potential Formulation of the Navier-Stokes Equations

Final Report

Funds for the support of this study have been allocated
by the NASA-Ames Research Center, Moffett Field, California
under Interchange No. NCA2-174

Heat Transfer Laboratory
Department of Mechanical Engineering
Computational Fluid Dynamics Center

engineering research institute
iowa state university

TABLE OF CONTENTS

LIST OF TABLES

LIST OF FIGURES

ABSTRACT

A dual potential formulation for numerically solving the Navier-Stokes equations is developed and presented. The velocity field is decomposed using a scalar and vector potential. Vorticity and dilatation are used as the dependent variables in the momentum equations. Test cases in two dimensions verify the capability to solve flows using approximations from potential flow to full Navier-Stokes simulations. A three-dimensional incompressible flow formulation is also described.

An interesting feature of this approach to solving the Navier-Stokes equations is the decomposition of the velocity field into a rotational part (vector potential) and an irrotational part (scalar potential). The Helmholtz decomposition theorem allows this splitting of the velocity field. This approach has had only limited use since it increases the number of dependent variables in the solution. However, it has often been used for incompressible flows where the solution scheme is known to be fast and accurate. This research extends the usage of this method to fully compressible Navier-Stokes simulations by using the dilatation variable along with vorticity.

A time-accurate, iterative algorithm is used for the uncoupled solution of the governing equations. Several levels of flow approximation are available within the framework of this method. Potential flow, Euler and full Navier-Stokes solutions are possible using the dual potential formulation. Solution efficiency can be enhanced

in a straightforward way. For some flows, the vorticity and/or dilatation may be negligible in certain regions (e.g., far from a viscous boundary in an external flow). It is possible to drop the calculation of these variables then and optimize the solution speed. Also, efficient Poisson solvers are available for the potentials.

The relative merits of non-primitive variables versus primitive variables for solution of the Navier-Stokes equations are also discussed.

ACKNOWLEDGMENTS

The authors gratefully acknowledge the support provided for this study by the NASA/Ames Research Center through Interchange No. NCA2-174. We express special thanks to the Allison Gas Turbine Division of General Motors Corporation for supporting the first author on a GM fellowship.

NOMENCLATURE

Roman Symbols

$\vec{A}$	vector potential
A	cross-sectional area
B	dilatation
c	airfoil chord length
C_f	skin-friction coefficient $\left(\frac{\tau_w}{\frac{1}{2}\rho_\infty u_\infty^2}\right)$
C_p	pressure coefficient $\left(\frac{p-p_\infty}{\frac{1}{2}\rho_\infty u_\infty^2}\right)$
c_p	specific heat at constant pressure
c_v	specific heat at constant volume
e	internal energy
E_t	total energy per unit volume
$\vec{F}$	body force
h	enthalpy
h	non-dimensional height of a 2-D grid
I	identity matrix
i, j, k	index in the x, y, z direction respectively
i, j, k	indices in tensor notation
$\hat{i}, \hat{j}, \hat{k}$	unit vector in the x, y, z direction respectively
k	thermal conductivity
L	non-dimensional length of flowfield domain (e.g., channel length)
M	Mach number
n	outward unit normal
Nu	Nusselt number
p	exponent in the viscosity power law variation
p	pressure
Pr	Prandtl number $\left(\frac{\mu c_p}{k}\right)$

Q	volume flow rate
Q	finite-difference approximation to the exact solution
R	gas constant
Re	Reynolds number
T	temperature
u	x component of velocity
$\overline{u}$	average u velocity at an x cross-section
v	y component of velocity
w	z component of velocity
x	streamwise coordinate direction
y	spanwise coordinate direction
$\overline{x}$	streamwise direction in the computational plane
$\overline{y}$	spanwise direction in the computational plane
z	normal coordinate direction
X	conservative body force in the x direction
Y	conservative body force in the y direction
Z	conservative body force in the z direction

Greek Symbols

α	weighting parameter in hybrid differencing scheme
α	parameter in a 2-D stretching transformation
β	parameter in a 2-D stretching transformation
γ	ratio of specific heats
Γ	rate of shear deformation in two dimensions, $u_y + v_x$
δ_{ij}	Kronecker delta function
$\hat{\delta}$	hybrid difference operator for convective terms
$\overline{\delta}$	central difference operator, subscript gives direction to difference e.g., $\overline{\delta}_x u = u_{i+1} - u_{i-1}$
δ^2	central difference operator, subscript gives direction to difference e.g., $\delta_x^2 u = u_{i+1} - 2u_i + u_{i-1}$
δ_2	momentum thickness
κ	parameter in a 2-D stretching transformation
ρ	density
σ	parameter in a 2-D stretching transformation
Θ	temperature parameter
ϕ	scalar potential
$\vec{\omega}$	vector 3-D vorticity

ω	2-D vorticity

Subscripts

hyd	based on the hydraulic diameter
m	mean value
n	normal direction
r	reference
t	time
t	tangential direction
w	wall
x	derivative in x direction
y	derivative in y direction
z	derivative in z direction
∞	freestream value

Superscripts

$*$	non-dimensional quantity
$*$	provisional value
$\hat{}$	unit vector
k	iteration level
n	time level

Other Symbols

$\vec{\nabla}$	gradient operator
∇^2	Laplacian operator
∇	backward difference operator, subscript gives direction to difference e.g., $\nabla_x u = u_i - u_{i-1}$
$\triangle$	forward difference operator, subscript gives direction to difference e.g., $\triangle_x u = u_{i+1} - u_i$
$\triangle$	indicates an increment
[ ]	used to enclose the units of measurement

1. INTRODUCTION

1.1 Background

The topic of this final report is a particular computational approach for solving the Navier-Stokes equations. The Navier-Stokes equations are usually associated with the field of fluid mechanics. Solutions to these equations with the appropriate boundary conditions model fluid motion.

An analysis of fluid motion requires the solution for the physical laws of nature:

1. Conservation of mass

2. Newton's second law of motion

3. Conservation of energy

These laws can be formulated mathematically, with the help of some assumptions, to become the Navier-Stokes equations. Formally, the Navier-Stokes equations refer to the mathematical representation of Newton's second law. It will be more convenient for the purposes here to let the term "Navier-Stokes equations" include the representation of all three physical laws above. Assumptions in the development are that the coefficients of viscosity are related by a factor of $-(2/3)$ according to Stokes' hypothesis and that the fluid is Newtonian (Schlichting 1979). A Newtonian fluid

is one in which the fluid shear stress is linearly proportional to the rate of strain. Additional relationships are included as necessary to describe certain processes or fluids. Examples are the equation of state for a perfect gas, Sutherland's formula for viscosity and Fourier's law of heat conduction.

As one can imagine, the successful solution to the Navier-Stokes equations can help immensely in engineering design and optimization. The numerical solution of the Navier-Stokes equations can be a complement to experimental and theoretical fluid mechanics. Unfortunately, the Navier-Stokes equations are coupled and highly non-linear. Only a few exact analytical solutions are available for simple conditions. In most configurations of practical interest, numerical techniques must be used to obtain a solution.

Much progress has been made in obtaining numerical solutions to the Navier-Stokes equations. Several mathematical formulations for the Navier-Stokes equations have been developed. They can be divided into two classifications:

1. Primitive variable methods

2. Non-primitive variable methods

As the name suggests, primitive variable methods solve the Navier-Stokes equations using the primary variables as the unknowns. The primary variables are velocity, total energy (or a variable related to the energy) and pressure or density. One way to think of the primitive variables is that they are physical quantities which one can measure in the laboratory. Non-primitive variables, on the other hand, are mathematically derived variables. They are derived from the primitive variables. The non-primitive variables used in this report will replace the primary variable of velocity.

The replacements used will be vorticity and dilatation. One can devise techniques to measure vorticity and dilatation experimentally, but the direct measurement of such quantities is uncommon. Both primitive and non-primitive variable methods have been used to obtain solutions to the Navier-Stokes equations by numerical techniques. Primitive variable methods are the most widely used for three-dimensional simulations. Either primitive or non-primitive variables are used for two-dimensional flow solutions although most applications of non-primitive variables have been for incompressible flows. The following sections in this chapter will discuss some primitive and non-primitive variable solution methods. The focus of this study will be on a particular non-primitive variable method that is extended to compressible viscous flow.

1.2 Primitive Variable Methods

Numerical methods of solving the Navier-Stokes equations using the physical variables have attracted much attention. Several popular techniques will be mentioned here. The solution method depends on whether the flow is incompressible or compressible, because the Navier-Stokes equations have a different mathematical classification depending on the compressibility. For an unsteady incompressible flow, the governing equations are elliptic/parabolic in time. For an unsteady compressible flow, the equations are hyperbolic/parabolic in time.

The most common primitive variable solution method for incompressible flow problems involves the use of a Poisson equation for pressure in place of the continuity equation. An algorithm which employs this solution method is the SIMPLE (Semi-

Implicit Method for Pressure-Linked Equations) procedure (Patankar 1975, 1981).

Another primitive variable solution method is the artificial compressibility approach which modifies the continuity equation to include an unsteady term related to pressure (Chorin 1967). The resulting equations are a mixed set of hyperbolic/parabolic equations which can be solved using a time-dependent approach. This approach applies in two and three dimensions and can be modified to compute unsteady flows. An available computer code that uses this method is INS3D (Kwak et al. 1986; Rogers et al. 1987; Rogers and Kwak 1988).

A compressible flow solution is often obtained using a time-dependent or time-dependent-like approach. Most schemes utilize implicit methods, for example, the Beam and Warming (1978), Briley and McDonald (1977), or MacCormack (1981) methods. An available code for these applications is F3D (Steger et al. 1986). Additional discussion and references on primitive variable solution methods can be found in Holst (1987).

1.3 Non-primitive Variable Methods

Methods which in some way replace the velocity with derived variables will be discussed here. At the highest level of approximation, potential flows are typically solved using either the velocity potential or the stream function. Examples of their use are found in most fluid mechanics textbooks (Currie 1974). By definition, a potential flow is irrotational so that the velocity field can be defined by the gradient of a scalar function. This scalar function is called the velocity potential. It is analogous to the electric field potential. For an incompressible potential flow, the

only additional constraint is mass conservation. The equation of mass conservation is a Laplace equation for the velocity potential which is easily solved. The velocity potential is applicable in two and three dimensions. If the stream function is used it is defined to satisfy mass conservation and the Laplacian of the stream function satisfies the irrotationality condition. The stream function as defined here only exists in two dimensions. In both of the above schemes, the momentum equation (vorticity transport equation) is satisfied automatically since the vorticity is zero everywhere for the assumption of irrotational flow.

The vorticity/stream function approach is widely used for solution of the two-dimensional incompressible Navier-Stokes equations. This method is also discussed in most fluid mechanics textbooks and is treated extensively in the book by Roache (1972).

Many would consider this the limit of practicality for non-primitive variable methods. However, there are at least two other noteworthy approaches to solving the Navier-Stokes equations in non-primitive variables. Both are valid for two- and three-dimensional unsteady flows. These methods are known as the

1. Vorticity/velocity approach

2. Vorticity/vector potential approach

These two schemes will be briefly described and then the focus will be placed on the vorticity/vector potential method. The topic of this thesis will cover the vorticity/vector potential method. This method is also referred to by the the aliases scalar/vector potential, vorticity/potential, or dual potential method. Since both

vorticity and dilatation are used in this work to replace the primitive variable momentum equations, it does not seem appropriate to identify the method as the vorticity/vector potential approach. Instead, the term dual potential will be used here following Chaderjian and Steger (1985). This terminology identifies the method as one which uses two potential functions in a velocity decomposition.

1.3.1 Vorticity/velocity approach

In this method for incompressible flow, the momentum equation is replaced by the vorticity transport equation. Derivatives of the vorticity definition then yield Poisson equations for the velocity when the continuity equation is used to make appropriate substitutions. A more general derivation of the Poisson equations is to take the curl of the vorticity and substitute in the vorticity definition from velocity. The identity for the vector triple product then yields Poisson equations for the velocity. The earliest use of this method was by Fasel (1976). He studied the stability of two-dimensional boundary layers using a coupled and iterative algorithm. Dennis et al. (1979) used the vorticity/velocity method in the calculation of the cubical driven box problem. Orlandi (1987) solved high Reynolds number flows over a backward facing step. Other works using the vorticity/velocity formulation are Osswald et al. (1987), Guj and Stella (1988), Gatski et al. (1982), Fasel and Booz (1984) and Farouk and Fusegi (1985). There have been no reported compressible flow applications of this method. However, the dilatation could be used as a dependent variable, as was done in this research, to extend the vorticity/velocity method to compressible flow.

1.3.2 Dual potential approach

Derived variables which can be used to represent the three-dimensional continuity and momentum equations for an incompressible flow are vorticity, a vector potential, and a scalar potential. This is one possible three-dimensional extension of the more familiar two-dimensional vorticity/stream function approach. This approach and others that use the vorticity as a dependent variable are appealing because vorticity is generally located near boundaries in high Reynolds number flows and subsequently diffused and convected away. For a three-dimensional incompressible flow the usual procedure in the dual potential method is to solve the vorticity transport equation, a vector Poisson equation and a scalar Poisson equation. These equations are derived from the continuity and momentum equations where the velocity is defined as the curl of a vector potential plus the gradient of a scalar potential. The existence of these potentials is easily shown for an incompressible flow since the velocity field is divergence free (Aziz and Hellums 1967).

There has been only one reported formulation of the dual potential method for three-dimensional compressible, viscous, unsteady flows (Morino 1985). He derived a set of equations for density, vorticity, entropy and the potentials. There have been no reported calculations using Morino's formulation.

1.3.2.1 Applications of the dual potential method The dual potential method has been applied to inviscid and viscous flow problems. Inviscid flow applications include the work of Rao et al. (1989) and Giannakoglou et al. (1988). Rao et al. (1987) developed a three-dimensional inviscid rotational flow solver based on the dual

potential method. They incorporated a boundary layer interaction scheme for viscous flow problems. Giannakoglou et al. (1988) compute two-dimensional steady rotational transonic flows in arbitrarily shaped ducts and plane cascades. They decomposed the mass flux vector into two potentials.

In the viscous regime, the dual potential method has been applied to problems of three-dimensional natural convection in enclosures (Mallinson and De Vahl Davis 1973) and three-dimensional incompressible flows in ducts (Wong and Reizes 1984). External viscous flows have been computed by Davis et al. (1989). No attempts have been reported on the use of this method to solve three-dimensional unsteady compressible viscous flows.

The dual potential method was first applied to natural convection problems by Aziz and Hellums (1967). They used the dual potential method to transform the Navier-Stokes equations. The transformed equations were solved using an alternating direction implicit (ADI) scheme for the parabolic part of the problem (temperature and vorticity transport equations) and a successive over-relaxation (SOR) method for the elliptic portion (vector potential equations). They tested their technique by applying it to the classical problem of convection in fluid layers bounded by solid walls in both two and three dimensions.

Aziz and Hellums showed the dual potential method to be faster and more accurate than solutions obtained using the primitive variable approach. In fact, though the equations are fewer in number for the primitive variable approach, Aziz and Hellums report that they are much harder to solve than the equations in the dual potential method. The difficulty arises from the highly non-linear nature of the pres-

sure equation and the coupling due to pressure in the momentum equations (as in incompressible flow problems).

The technique developed above was used by Ozoe and co-workers (Ozoe et al. 1976, 1977, 1979, 1985) in solving a variety of natural convection problems. In the 1985 paper, the problem of three-dimensional turbulent natural convection in a cubical enclosure was solved using a two-equation model for turbulence.

Applications of the dual potential method to incompressible duct flow (through-flow) have not been wholly successful due to confusion over the appropriate vector potential boundary conditions. The earliest work in this area was by Aregbesola and Burley (1977). They presented a numerical finite-difference solution for the equations of motion of a steady laminar incompressible flow in two and three dimensions using the dual potential method. Wong and Reizes (1984) presented a dual potential formulation for unsteady incompressible flows in ducts of constant but arbitrary cross section. They showed that the method is capable of handling flows over a wide range of Reynolds numbers and imply that it can deal with flow situations in which other models become inadequate. The dual potential method guarantees a zero divergence of velocity while the usual primitive variable method can at best approximate global continuity. That formulation was limited to simply connected domains. In a later paper Wong and Reizes (1986) showed how to use the dual potential method to solve for the three-dimensional flow in multiply connected regions such as annular geometries. Yang and Camarero (1986) used body fitted coordinates with the dual potential method to simulate incompressible laminar flows in a square elbow and in a twisted square elbow. The dual potential method in this paper is shown to be applicable to

general duct flow situations in simply connected regions. Hafez et al. (1987) used a finite element method to solve the steady two-dimensional Navier-Stokes equations in a dual potential formulation for subsonic and transonic flows. They computed laminar and turbulent flow cases.

Some viscous external flow solutions were obtained by Rao (1987) and Davis et al. (1986) for flow over two- and three-dimensional troughs. Rao (1987) used interacting boundary layer theory to supply the vorticity to a dual potential code for the inviscid rotational part of the flow. Davis et al. (1986, 1989) use a viscous dual potential method for the entire flow field. Matching between the outer inviscid flow and the inner viscous region is automatic in their case.

One possible extension of the dual potential method to three-dimensional compressible viscous flow has been formulated by Morino (1986). There are no reported results in the compressible viscous regime.

Compressible viscous unsteady flows have been solved by a closely related method, however. El-Refaee et al. (1981) used a non-primitive variable method that replaced the momentum equation with vorticity and dilatation transport equations. The velocity field was obtained from the vorticity and dilatation field by an integral representation. They solved compressible unsteady flows and demonstrated that the solution field for vorticity and dilatation can easily be limited in their integral representation. In this report a similar equation set is used, but the velocity is decomposed into two potentials and solved completely by finite differences. The proposed extension of the dual potential method to compressible flow would be directly applicable to the vorticity/velocity method. That is, the dilatation variable would be included to account

for compressibility.

In view of the short list of references on the dual potential method it is evident that this method has not been widely implemented in computations. The main reasons for this have been the need for the solution of several additional variables as compared to the primitive variable approach and the inability to analyze the numerical solution process for convergence. There are no good model problems to guide the way.

Three-dimensional flow solvers are computationally demanding and the introduction of additional variables inevitably increases the computer memory requirement. However, with the increasing memory of today's computers, and since Aziz and Hellums (1967) have shown that the dual potential approach can lead to faster and more stable convergence than for primitive variable formulations (for certain problems), the vector potential will perhaps play an increasing role in the solution of complex three-dimensional fluid dynamics problems (Wong and Reizes 1986). Certainly this kind of formulation deserves continued investigation.

1.3.2.2 Advantages and disadvantages Relative advantages of the primitive variable method and dual potential method are cited in Morino (1985) and Richardson and Cornish (1977). The major advantage of working in primitive variables is the relative simplicity of the equations and the fact that the primitive variables have direct physical meaning.

The advantages of the dual potential method are:

1. The vorticity (and dilatation for compressible flow) need only be resolved in distinct regions.

2. Continuity is automatically satisfied for incompressible flow.

3. The equations are weakly coupled (at least for inviscid flow).

4. Good numerical solution routines exist for Poisson equations.

5. Matching between an inviscid region and viscous region occurs automatically because of the velocity decomposition into rotational and irrotational parts.

Disadvantages of the dual potential method applied to a three-dimensional compressible unsteady flow are:

1. The dual potential method involves ten dependent variables whereas the primitive variable method involves only five to represent conservation of mass, momentum and energy. (In two dimensions the number of dependent variables are six for the dual potential method and four for the primitive variable method.)

2. The equations for the dual potential method are more complex than the equations associated with the primitive variables (or, they are simply unfamiliar).

3. The potentials do not have direct physical significance.

In addition to the natural disadvantages of the dual potential approach listed above, there is a lack of available software as compared to primitive variable solution methods. The extension of this approach to unsteady compressible viscous problems is uncharted territory.

1.4 Scope of the Present Study

It has been the goal of this research to extend the capability of the dual potential method to compute unsteady compressible viscous flows. An algorithm has been developed to provide two-dimensional full Navier-Stokes simulations. A three-dimensional algorithm has been developed for incompressible flow only. Test cases were computed to verify the ability to compute flow fields ranging from full potential flow to flow fields requiring the full Navier-Stokes equations. It has been demonstrated in this work that the calculation region can be limited for vorticity and dilatation, thus providing a speed advantage for certain flows.

Several two-dimensional test cases will be presented to test various aspects of the dual potential method. Both incompressible and compressible flows will be computed.

Incompressible flows will be studied for steady, irrotational, inviscid conditions and for steady, rotational, viscous conditions. The steady, irrotational, inviscid test case is that of flow over a biconvex airfoil (or a bump on a wall). Steady, rotational, viscous conditions are simulated for a channel inlet and laminar boundary-layer case. Heat transfer calculations will be made for the channel cases with constant wall temperature and constant wall heat flux boundary conditions.

For compressible flow, steady and unsteady, irrotational, inviscid flows will be computed and also steady, rotational, viscous flows. The irrotational, inviscid flows are biconvex airfoil cases. The steady, rotational, viscous flows are channel inlet and boundary-layer cases. The channel inlet flows are computed with constant wall temperature and constant wall heat flux boundary conditions at a Mach number of 0.1. Calculations of the flow over a flat plate are made for a subsonic and supersonic

freestream.

In three dimensions only steady, viscous, incompressible channel inlet solutions were obtained. A summary of the test cases to be presented is given below.

I. Two-Dimensional Cases

- A. Incompressible flow
  - 1. Steady irrotational inviscid flow
    - a) bump cases
  - 2. Steady viscous flow
    - a) channel inlet with and without heat transfer
    - b) boundary layer
- B. Compressible flow
  - 1. Steady irrotational inviscid flow
    - a) bump cases
  - 2. Unsteady irrotational inviscid flow
    - a) bump cases
  - 3. Steady viscous flow
    - a) variable property channel flows
    - b) boundary layer

II. Three-Dimensional Cases

- A. Incompressible flow
  - 1. Steady viscous flow
    - a) channel inlet
- B. Compressible flow

Progress in this research area has not been easy. There is very little guidance in the literature on how to proceed with a full Navier-Stokes implementation of a non-primitive variable method. The governing equations in non-primitive variable form are unfamiliar. Non-linear terms were simply lumped into the source term and

the system was solved uncoupled in an iterative manner. As a result, it was necessary to employ rather simple test cases to check various aspects of the formulation.

The work completed here is primarily in the development and evaluation of the dual potential method as a flexible approach to solving the Navier-Stokes equations. Several features of the method have been highlighted. For example, the solution domain for vorticity and/or dilatation may be limited to certain regions. Also demonstrated is the flexibility of the method to accommodate several approximations of the full Navier-Stokes equations. This effort has advanced the understanding of the dual potential method in the viscous compressible regime. It represents the first application of this method to compute throughflow problems with heat transfer. Several basic problems are solved to check out aspects of the algorithm and computer code. Only Cartesian grids are used for the test problems. Further evaluation and optimization of the method reported herein are left for future work.

1.5 Organization

The main body of this report consists of six chapters and two appendices. The presentation follows the logical development of the method from equation derivation to boundary condition determination, grid generation, numerical algorithm selection and, finally, flow simulations. In Chapter 2, the dual potential equations are derived from the velocity decomposition and non-primitive variable dependent variables are selected to represent the usual primitive variable (or pressure-velocity) form of the Navier-Stokes equations. In Chapter 3, the numerical representations of the boundary conditions are derived and the numerical algorithms are presented. The Cartesian

grid stretching is presented also. A comparison is made of the Poisson equation solvers since the Poisson equation solution for the potentials can dominate the computation time. In Chapter 4, the solution strategy is outlined and then numerical results are reported for two- and three-dimensional test cases. The two-dimensional results represent cases from potential flow to situations requiring the full Navier-Stokes equations. The three-dimensional results are for incompressible cases only, but are representative of the speed of this approach for incompressible problems. Chapter 5 includes the overall assessment of this method. Chapter 6 gives some incentives for future work on the dual potential method.

The appendices contain equations for the full three-dimensional Navier-Stokes implementation of this method. Also, alternative non-primitive variables are introduced which could be useful for some problems.

2. DUAL POTENTIAL FORMULATION

2.1 Introduction

In this chapter the mathematical equations which model fluid flow are presented. These equations are the Navier-Stokes equations. They state the conservation of mass, momentum and energy for a Newtonian, Stokesian fluid. The usual form of these equations has the primitive variables $(\rho, \vec{V}, E_t)$ as the primary unknowns. Using the Helmholtz decomposition theorem, the velocity field can be split into a rotational part and an irrotational part. Each part is represented by a potential function. This decomposition yields a non-primitive variable formulation for the Navier-Stokes equations.

2.2 Governing Fluid Dynamics Equations

The following equations apply to a continuum fluid.

The conservation of mass is stated

$$\frac{\mathrm{D}\rho}{\mathrm{D}t} + \rho \vec{\nabla} \cdot \vec{V} = 0 \tag{2.1}$$

The conservation of momentum (Newton's second law), with the assumptions

that Stokes' hypothesis holds and that the fluid is Newtonian, is written

$$\rho\frac{\mathrm{D}\vec{V}}{\mathrm{D}t} = \vec{F} - \vec{\nabla}p + \frac{\partial}{\partial x_j}\left[\mu\left(\frac{\partial u_i}{\partial x_j} + \frac{\partial u_j}{\partial x_i}\right) - \frac{2}{3}\delta_{ij}\frac{\partial u_k}{\partial x_k}\right] \tag{2.2}$$

Where $\vec{F} = X\hat{\imath} + Y\hat{\jmath} + Z\hat{k}$ is the body force and δ_{ij} is the Kronecker delta function:

$$\delta_{ij} = \begin{cases} 1 & \text{if } i = j \\ 0 & \text{if } i \neq j \end{cases}$$

In the energy equation only internal and kinetic energy will be considered important. The conservation of energy is then written

$$\rho\frac{\mathrm{D}e}{\mathrm{D}t} + p\vec{\nabla}\cdot\vec{V} = \frac{\partial Q}{\partial t} - \vec{\nabla}\cdot\vec{q} + \Phi \tag{2.3}$$

where $\frac{\partial Q}{\partial t}$ represents heat energy production by external agencies, $\vec{q}$ is the heat conduction and Φ is dissipation. Fourier's law of heat conduction will be assumed so

$$\vec{q} = -k\,\vec{\nabla}T$$

The dissipation function for a Newtonian fluid in a Cartesian coordinate system becomes

$$\begin{aligned}\Phi \;=\; & \mu\Big[\,2\left(u_x^2 + v_y^2 + w_z^2\right) + \left(v_x + u_y\right)^2 + \left(w_y + v_z\right)^2 + \left(u_z + w_x\right)^2 \\ & - \frac{2}{3}\left(u_x + v_y + w_z\right)^2\Big]\end{aligned} \tag{2.4}$$

The ideal gas equation of state and a viscosity law are used to close the system for laminar flow. Constant specific heats are assumed throughout. Reference conditions are selected to non-dimensionalize the equations. Reference quantities will be denoted by the subscript r. Fluid properties for air will be used in the calculations.

For an ideal (or perfect) gas the following relationships exist:

$$p = \rho RT \tag{2.5}$$

$$e = c_v T \quad h = c_p T \quad \gamma = \frac{c_p}{c_v} \quad R = c_p - c_v \tag{2.6}$$

Sutherland's law of viscosity is used in the form

$$\mu = C_1 \frac{T^{3/2}}{T + C_2} \tag{2.7}$$

where C_1 and C_2 are constants for a particular gas. For air at moderate temperatures (approximately 200K–1000K), $C_1 = 1.458 \times 10^{-6}$ $\left[\text{kg}/(\text{m s}\sqrt{\text{K}})\right]$ and $C_2 = 110.4\text{K}$. Power law variations for μ were also available in the computer code:

$$\frac{\mu}{\mu_r} = \left(\frac{T}{T_r}\right)^{\text{p}} \qquad 0.5 \leq \text{p} \leq 1.0 \tag{2.8}$$

A constant Prandtl number is assumed and thermal conductivity is obtained from the definition, $\text{Pr} = \frac{\mu c_p}{k}$. Typical values of the fixed quantities chosen for air are:

$$\gamma = 1.4 \tag{2.9}$$

$$R = 287 \left[\frac{\text{J}}{\text{kg} \cdot \text{K}}\right] \tag{2.10}$$

$$\text{Pr} = \frac{\mu_r c_{p_r}}{k_r} = 0.7 \tag{2.11}$$

A reference length will be designated by L_r [m] and a reference velocity by U_r $\left[\frac{\text{m}}{\text{s}}\right]$. The reference length is taken to be a characteristic length of the problem such as the hydraulic diameter for internal flow or chord length for external flow. The reference velocity is taken to be the magnitude of either the inlet velocity for internal flows or the freestream velocity for external flows.

The following reference conditions were set for incompressible flow calculations with the Reynolds number and reference length specified:

$$
\begin{aligned}
T_r &= 288.15\text{K } (59^\circ\text{F}) \\
\mu_r &= C_1 \frac{T_r^{3/2}}{T_r + C_2} \left[\frac{\text{kg}}{\text{m} \cdot \text{s}}\right] \\
k_r &= \frac{\mu_r c_p}{\text{Pr}} \left[\frac{\text{W}}{\text{m} \cdot {}^\circ\text{C}}\right] \\
\rho_r &= 1.22 \left[\frac{\text{kg}}{\text{m}^3}\right] \\
U_r &= \frac{\text{Re}\mu_r}{\rho_r L_r} \left[\frac{\text{m}}{\text{s}}\right] \\
\text{M}_r &= \frac{U_r}{\sqrt{\gamma R T_r}} \\
p_r &= \rho_r R T_r \left[\frac{\text{N}}{\text{m}^2}\right]
\end{aligned}
$$

Reference conditions for compressible flow calculations with the Reynolds number, Mach number and reference length specified are as follows:

$$
\begin{aligned}
T_r &= 288.15\text{K } (59^\circ\text{F}) \\
\mu_r &= C_1 \frac{T_r^{3/2}}{T_r + C_2} \left[\frac{\text{kg}}{\text{m} \cdot \text{s}}\right] \\
k_r &= \frac{\mu_r c_p}{\text{Pr}} \left[\frac{\text{W}}{\text{m} \cdot {}^\circ\text{C}}\right] \\
U_r &= \text{M}_r \sqrt{\gamma R T_r} \left[\frac{\text{m}}{\text{s}}\right] \\
\rho_r &= \frac{\text{Re}\mu_r}{U_r L_r} \left[\frac{\text{kg}}{\text{m}^3}\right] \\
p_r &= \rho_r R T_r \left[\frac{\text{N}}{\text{m}^2}\right]
\end{aligned}
$$

The following non-dimensional variables are then obtained:

$$x^* = \frac{x}{L_r} \qquad y^* = \frac{y}{L_r} \qquad z^* = \frac{z}{L_r} \qquad t^* = \frac{t}{(L_r/U_r)}$$

$$u^* = \frac{u}{U_r} \qquad v^* = \frac{v}{U_r} \qquad w^* = \frac{w}{U_r} \qquad \mu^* = \frac{\mu}{\mu_r}$$

$$\rho^* = \frac{\rho}{\rho_r} \qquad p^* = \frac{p}{\rho_r U_r^2} \qquad T^* = \frac{T}{T_r} \qquad e^* = \frac{e}{U_r^2}$$

$$R^* = \frac{R}{(U_r^2/T_r)} \quad c_v^* = \frac{c_v}{(U_r^2/T_r)} \quad c_p^* = \frac{c_p}{(U_r^2/T_r)} \qquad k^* = \frac{k}{k_r}$$

where the variables distinguished by an asterisk are non-dimensional. The non-dimensional variables will be used throughout, so the asterisk will be dropped in the following. The non-dimensional gas constant above is equivalent to

$$R = \frac{1}{\gamma \mathrm{M}_r^2}$$

so that

$$p = \rho R T$$

in dimensional or non-dimensional variables.

2.3 Derivations

2.3.1 Velocity decomposition

The basis of the dual potential method is a splitting of the velocity field into rotational and irrotational parts. In this section, the impetus for splitting the velocity

field in this way is presented. The Helmholtz decomposition theorem formally permits the splitting.

A useful classification of vector fields is possible using the divergence and curl operators (Ames 1977). For $\vec{\nabla} \cdot \vec{E} = 0$ at every point of a region R, the vector field $\vec{E}$ is said to be solenoidal or divergence free. Physically this means that there are no sources or sinks in R. If $\vec{\nabla} \times \vec{E} = 0$ at every point in R, the field is said to be irrotational. The following classification of vector fields can then be made:

Class I Solenoidal and irrotational:
$$\vec{\nabla} \times \vec{E} = 0 \qquad \vec{\nabla} \cdot \vec{E} = 0$$

Class II Irrotational but not solenoidal:
$$\vec{\nabla} \times \vec{E} = 0 \qquad \vec{\nabla} \cdot \vec{E} \neq 0$$

Class III Solenoidal but not irrotational:
$$\vec{\nabla} \times \vec{E} \neq 0 \qquad \vec{\nabla} \cdot \vec{E} = 0$$

Class IV Neither solenoidal nor irrotational:
$$\vec{\nabla} \times \vec{E} \neq 0 \qquad \vec{\nabla} \cdot \vec{E} \neq 0$$

An important theorem in vector field theory is called the Helmholtz decomposition theorem. It states that any vector field can be split into a curl free and divergence free part. Using the above classifications, it can be observed that the velocity field of an incompressible fluid is in *Class III* and the velocity field of a rotational compressible flow is in *Class IV*. Applying the Helmholtz decomposition theorem to the velocity vector one obtains:

$$\vec{V} = \vec{\nabla}\phi + \vec{\nabla} \times \vec{A} \tag{2.12}$$

It is obvious that the curl free part of the velocity is $\vec{\nabla}\phi$. The divergence free part (recall from the above that another word for divergence free is solenoidal) is the

vector field $\vec{A}$. The vector $\vec{A}$ has been assumed to be solenoidal by design. This is an arbitrary but appropriate choice to fit the Helmholtz decomposition theorem and to remove the redundancy of describing a three component vector ($\vec{V}$) using another three component vector ($\vec{A}$) plus the gradient of a scalar (ϕ).

For the classification of the velocity field then, one can compute the divergence and curl of Equation 2.12 to obtain:

$$\vec{\nabla} \cdot \vec{V} = \nabla^2 \phi = B \tag{2.13}$$

$$\vec{\nabla} \times \vec{V} = \vec{\omega} = \vec{\nabla} (\vec{\nabla} \cdot \vec{A}) - \nabla^2 \vec{A} \tag{2.14}$$

where ϕ is the scalar potential, B is the dilatation or rate of volumetric strain, $\vec{\omega}$ is the vorticity and $\vec{A}$ is the vector potential. The vector potential, $\vec{A}$, is chosen to be divergence free. The Laplacian operator in Equation 2.14 is the vector Laplacian. Throughout this report only rectangular coordinates are used so each component of the vector Laplacian is similar to a scalar Laplacian.

The vector potential and vorticity will be represented in three dimensions as follows:

$$\vec{A} = A_1 \hat{\imath} + A_2 \hat{\jmath} + A_3 \hat{k} \tag{2.15}$$

$$\vec{\omega} = \omega_1 \hat{\imath} + \omega_2 \hat{\jmath} + \omega_3 \hat{k} \tag{2.16}$$

The components of the vorticity are obtained from:

$$\vec{\omega} = \vec{\nabla} \times \vec{V}$$

$$\omega_1 = w_y - v_z, \qquad \omega_2 = -w_x + u_z, \qquad \omega_3 = v_x - u_y$$

The velocity components are then:

$$\vec{V} = \begin{pmatrix} u \\ v \\ w \end{pmatrix} = \begin{pmatrix} \phi_x + A_{3y} - A_{2z} \\ \phi_y + A_{1z} - A_{3x} \\ \phi_z + A_{2x} - A_{1y} \end{pmatrix} \tag{2.17}$$

In two dimensions only one component of $\vec{A}$ and $\vec{\omega}$ exist. For the standard two-dimensional geometry shown in Figure 3.3 the single components are A_3 and ω_3. To simplify things in two dimensions, the subscripts will be dropped on the vector potential and vorticity so that A and ω refer to the two-dimensional case. The velocity components in two dimensions are then:

$$\vec{V} = \begin{pmatrix} u \\ v \end{pmatrix} = \begin{pmatrix} \phi_x + A_y \\ \phi_y - A_x \end{pmatrix} \tag{2.18}$$

2.3.2 New dependent variables

In the well known incompressible application of the above decomposition, the momentum equations become the vorticity transport equation. Continuity is satisfied by the solution of a Laplace equation for ϕ, since $\vec{\nabla} \cdot \vec{V} = 0$ in Equation 2.13. Finally, the potentials are used to compute the velocity field. Any other governing equations remain unchanged (energy equation, equation of state, etc.).

For a compressible flow, however, $\vec{\nabla} \cdot \vec{V} \neq 0$. In this case, $\vec{\nabla} \cdot \vec{V} = \nabla^2\phi = B \neq 0$ in Equation 2.13. An additional equation is required to give the dilatation, B, for the solution of the scalar potential. By counting the number of equations and unknowns, one can see that the three-dimensional momentum equations represent three equations with three unknowns (or two equations and two unknowns in two

dimensions). The vorticity transport equations formed by taking the curl of the three-dimensional momentum equations yield just two independent vorticity component equations (see Appendix A). In two dimensions, the vorticity is a single scalar quantity so again there is one remaining usage of the momentum equations permitted. This means that an equation (hopefully for the dilatation, B) can be derived by some operation on the momentum equations in either two or three dimensions. Looking at possible operations on the momentum equations, one choice is to take the divergence of the momentum equation.

The divergence of the momentum equation yields for possible dependent variables either the pressure (as in the pressure Poisson equation) or the divergence of the velocity, $\vec{\nabla} \cdot \vec{V}$. The divergence of velocity will be represented by the scalar variable, B, known as the dilatation or rate of volumetric strain.

Another possible combination of the momentum equations gives a scalar variable which is the rate of shear deformation (or shear strain rate). Let the shear strain rate be represented by the symbol, Γ. In two dimensions, $\Gamma = u_y + v_x$. This dependent variable is formed by taking $\frac{\partial}{\partial x}$ of the y momentum equation + $\frac{\partial}{\partial y}$ of the x momentum equation. The wall shear stress is simply $\mu\Gamma$. The variable set of Γ and $\vec{\omega}$ can form the basis for an interesting computational procedure in two dimensions. Unfortunately, one usually hopes to compute the skin friction, not give it as a boundary condition. However, this could be a useful inverse type calculation procedure (see Appendix B).

2.4 Derivation of Non-Primitive Variable Equations

The dual potential equations will be derived starting from the governing equations written in primitive variable form. For purposes of comparison, the number of unknowns required in a flow simulation using either primitive variables or the dual potentials will be given. The number of unknowns is computed by considering the continuity, momentum and energy equations only.

2.4.1 Two dimensions

The derivation of the dual potential method in two dimensions will contain the fewest simplifying assumptions except, of course, that it only considers two space dimensions. The solution capability will be for flows that require the full Navier-Stokes equations (i.e., unsteady compressible viscous flow).

In the primitive variables, the continuity, momentum and energy equations represent four equations for four unknowns. These four unknowns may be ρ, u, v and T. These variables are solved using:

- continuity:

$$\rho_t + (\rho u)_x + (\rho v)_y = 0 \tag{2.19}$$

- x momentum:

$$\rho \frac{\mathrm{D}u}{\mathrm{D}t} = X - \frac{\partial p}{\partial x} + \frac{1}{\mathrm{Re}} \frac{\partial}{\partial x} \left[\mu \left(2 \frac{\partial u}{\partial x} - \frac{2}{3} \vec{\nabla} \cdot \vec{V} \right) \right] + \frac{1}{\mathrm{Re}} \frac{\partial}{\partial y} \left[\mu \left(\frac{\partial u}{\partial y} + \frac{\partial v}{\partial x} \right) \right] \tag{2.20}$$

- y momentum:

$$\rho \frac{\mathrm{D}v}{\mathrm{D}t} = Y - \frac{\partial p}{\partial y} + \frac{1}{\mathrm{Re}} \frac{\partial}{\partial y} \left[\mu \left(2 \frac{\partial v}{\partial y} - \frac{2}{3} \vec{\nabla} \cdot \vec{V} \right) \right] + \frac{1}{\mathrm{Re}} \frac{\partial}{\partial x} \left[\mu \left(\frac{\partial u}{\partial y} + \frac{\partial v}{\partial x} \right) \right] \tag{2.21}$$

- energy:

$$\frac{\mathrm{D}T}{\mathrm{D}t} = -(\gamma - 1)(\vec{\nabla} \cdot \vec{V})T + \frac{\gamma}{\rho \mathrm{Re}\,\mathrm{Pr}} \vec{\nabla} \cdot \vec{\nabla}\, T + \frac{\mu}{\rho \mathrm{Re}\, c_v}\Phi \qquad (2.22)$$

The pressure may be obtained from the ideal gas law, $p = \rho RT$. Any additional variables ($\mu, k, \gamma, \mathrm{Pr}$, etc.) must be accompanied by their own equation of state or constitutive equation.

For the non-primitive variables of the dual potential method, the same two-dimensional flow requires the solution for ϕ, A, ω, B, T and ρ. The potentials give the velocity field. The potentials themselves are determined by the solution of Poisson equations derived from the divergence and curl of the velocity (*cf.* Equations 2.13 and 2.14).

To see what is needed for the dual potential formulation, consider the primitive variable equations above. They are the governing equations for fluid flow, but now it is desired to solve not for velocities directly but rather for the potentials. The velocities are subsequently determined from the potentials by solving Equation 2.18. The momentum equations must be recast to generate a solution to be used by the potentials. Equations 2.13 and 2.14 for the velocity field splitting suggest that the divergence and curl of velocity be sought as dependent variables. These are obtainable from the x and y momentum equations above by taking the divergence and curl of the primitive variable momentum equation.

The curl of the velocity (vorticity) is obtained as a dependent variable by taking the curl of the momentum equation. The group, $v_x - u_y = \omega$, is retained as the dependent variable. The divergence of the velocity is obtained as a dependent variable by taking $\frac{\partial}{\partial x}$ of the x momentum equation and $\frac{\partial}{\partial y}$ of the y momentum equation and

summing. The grouping, $u_x + v_y = B$, can be retained as the dependent variable. The remaining governing equations can be left unchanged from the primitive variable equation set.

The continuity equation can be used to compute the density. The energy equation can be used to solve for T or enthalpy, or any other variable that is related to energy. The ideal gas equation of state can then be used to compute the pressure if it is needed.

To summarize: The six variables of the dual potential method corresponding to the solution of the continuity, momentum and energy equations are determined as described below:

1. The continuity equation is used to compute the density, ρ.

2. The curl of the momentum equations gives the vorticity transport equation for ω. Conservative body forces are eliminated by this operation. Also, for incompressible flow, the pressure is eliminated. For compressible flow, however, the pressure derivatives remain but can be expressed in terms of other variables by using the equation of state.

3. The divergence of the momentum equations gives the dilatation transport equation to be solved for B.

4. The energy equation is solved for T, or enthalpy, or a related variable.

5. A Poisson equation is solved for ϕ with B as the source term.

6. A Poisson equation is solved for A with $-\omega$ as the source term.

The equations for a two-dimensional dual potential formulation will be presented below and subsequently solved in non-conservative form. Body forces will be neglected.

In two dimensions the dual potential representation of the compressible Navier-Stokes equations for constant specific heats are:

$$\rho_t + u\rho_x + v\rho_y + \rho B = 0 \tag{2.23}$$

$$\omega_t + u\omega_x + v\omega_y - \left(\frac{\mu}{\rho \mathrm{Re}}\right)\nabla^2\omega = S_1(\rho, B, \omega, T) \tag{2.24}$$

$$B_t + uB_x + vB_y - \left(\frac{4}{3}\frac{\mu}{\rho \mathrm{Re}}\right)\nabla^2 B = S_2(\rho, B, \omega, T) \tag{2.25}$$

$$T_t + uT_x + vT_y - \left(\frac{\gamma k}{\rho \mathrm{Re}\,\mathrm{Pr}}\right)\nabla^2 T = S_3(\rho, B, \omega, T) \tag{2.26}$$

$$\nabla^2\phi = B \tag{2.27}$$

$$\nabla^2 A = -\omega \tag{2.28}$$

The source terms for the ω, B and T transport equations are given below. For the vorticity transport equation, S_1 contains the compressibility and c_1 contains the variable viscosity terms.

$$\begin{aligned} S_1 = & -B\omega + \frac{\mu}{\rho^2 \mathrm{Re}}\left[\rho_y(-\omega_y + \frac{4}{3}B_x) - \rho_x(\omega_x + \frac{4}{3}B_y)\right] \\ & + \frac{R}{\rho}(\rho_x T_y - \rho_y T_x) + \frac{c_1}{\mathrm{Re}} \end{aligned} \tag{2.29}$$

$$
\begin{aligned}
c_1 &= \frac{1}{\rho}(u_y + v_x)(\mu_{xx} - \mu_{yy}) + \frac{2}{\rho}(v_y - u_x)\mu_{xy} \\
&\quad + \mu_x \left[\frac{2}{\rho}(\omega_x + B_y) - \frac{1}{\rho^2}(\rho_x u_y + \rho_x v_x - 2\rho_y u_x + \frac{2}{3}\rho_y B)\right] \\
&\quad + \mu_y \left[-\frac{2}{\rho}(-\omega_y + B_x) - \frac{1}{\rho^2}(2\rho_x v_y - \rho_y u_y - \rho_y v_x - \frac{2}{3}\rho_x B)\right] \qquad (2.30)
\end{aligned}
$$

For the dilatation transport equation, S_2 contains the "compressibility" and c_2 contains the variable viscosity terms.

$$
\begin{aligned}
S_2 &= -(u_x^2 + v_y^2 + 2u_y v_x) - \frac{\mu}{\rho^2 \mathrm{Re}}\left[\rho_x(-\omega_y + \frac{4}{3}B_x) + \rho_y(\omega_x + \frac{4}{3}B_y)\right] \\
&\quad - R\nabla^2 T - \frac{RT}{\rho}\nabla^2\rho - \frac{R}{\rho}(T_x\rho_x + T_y\rho_y) + \frac{RT}{\rho^2}(\rho_x^2 + \rho_y^2) + \frac{c_2}{\mathrm{Re}} \qquad (2.31)
\end{aligned}
$$

$$
\begin{aligned}
c_2 &= \frac{2}{\rho}\left[\mu_{xy}(u_y + v_x) + \mu_{xx}u_x + \mu_{yy}v_y\right] - \frac{2}{3}\frac{B}{\rho}\nabla^2\mu \\
&\quad + \frac{\mu_x}{\rho}\left[-2\omega_y + \frac{8}{3}B_x + \frac{2}{3}\frac{\rho_x}{\rho}B - 2\frac{\rho_x}{\rho}u_x - \frac{\rho_y}{\rho}(u_y + v_x)\right] \\
&\quad + \frac{\mu_y}{\rho}\left[2\omega_x + \frac{8}{3}B_y + \frac{2}{3}\frac{\rho_y}{\rho}B - 2\frac{\rho_y}{\rho}v_y - \frac{\rho_x}{\rho}(u_y + v_x)\right] \qquad (2.32)
\end{aligned}
$$

The energy equation source term, S_3, contains the compressibility and variable thermal conductivity.

$$
\begin{aligned}
S_3 &= -(\gamma - 1)BT + \frac{\mu}{\rho \mathrm{Re} c_v}\left[\frac{4}{3}B^2 + \omega^2 + 4(v_x u_y - v_y u_x)\right] \\
&\quad + \frac{\gamma}{\rho \mathrm{Re}\,\mathrm{Pr}}[k_x T_x + k_y T_y] \qquad (2.33)
\end{aligned}
$$

The solution strategy for this system of equations is outlined in Section 4.2. Briefly, the equations are grouped into an "incompressible" and compressible part. An incompressible solution is obtained by computing among the equations in the

"incompressible" set of equations given below. A compressible solution requires a pass through both the "incompressible" and compressible sets of equations. In that case the "incompressible" equations actually contain terms representing compressible effects. This grouping is used to allow an incompressible solution to be the starting solution for a compressible problem.

$$\text{Incompressible} \begin{cases} \text{vorticity transport equation} \\ \nabla^2\phi = 0 \\ \nabla^2 A = -\omega \end{cases}$$

$$\text{Compressible} \begin{cases} \text{dilatation transport equation} \\ \text{energy equation} \\ \text{continuity equation} \\ \nabla^2\phi = B \\ \text{ideal gas law}, p = \rho RT \\ \text{property updates} : \mu, k \end{cases}$$

The transport equations above are solved using an ADI scheme. Source terms of the dependent variable (undifferentiated) are treated implicitly. Derivatives of the dependent variable in the source term are treated explicitly so as not to weight the off-diagonals. This did provide a slightly faster solution than treating all dependent variable source terms implicitly.

One will immediately notice the many derivatives introduced in the governing equations by this method. Even though most of the test cases to be presented are for subsonic flows, it was necessary to handle some terms conservatively. In particular, the pressure related terms in the dilatation transport equation and the conduction

terms in the energy equation are best handled conservatively for the heat transfer test cases computed. By treating these terms conservatively it is easier to obtain an accurate representation than by expanding out in the chain rule form and differencing.

2.4.2 Three dimensions

Only the incompressible equations will be derived here. The three-dimensional compressible set is given in Appendix A.

2.4.2.1 Incompressible flow The governing equations for viscous incompressible flow in non-dimensional vector form are:

- continuity:

$$\vec{\nabla} \cdot \vec{V} = 0 \tag{2.34}$$

- momentum:

$$\frac{\partial \vec{V}}{\partial t} + (\vec{V} \cdot \vec{\nabla})\ \vec{V} = -\ \vec{\nabla}\ P + \frac{1}{\mathrm{Re}} \nabla^2 \vec{V} + \vec{F} \tag{2.35}$$

There are four unknowns to be determined for the primitive variable solution of a three-dimensional incompressible flow. Usually these unknowns are u, v, w and p. It will be seen that the dual potential method requires the solution for seven variables to satisfy the continuity and momentum equations.

By taking the curl of the momentum equation the pressure is eliminated yielding the vorticity transport equation:

$$\frac{\partial \vec{\omega}}{\partial t} + (\vec{V} \cdot \vec{\nabla})\ \vec{\omega} - (\vec{\omega} \cdot \vec{\nabla})\ \vec{V} \ = \ \frac{1}{\mathrm{Re}} \nabla^2 \vec{\omega} + \vec{\nabla} \times \vec{F} \tag{2.36}$$

If $\vec{F}$ is a conservative body force (such as gravity) then it too is eliminated by the curl.

Decomposing the velocity vector according to the Helmholtz decomposition theorem as in Equation 2.12 one obtains:

$$\vec{V} = \vec{\nabla}\phi + \vec{\nabla} \times \vec{A} \tag{2.37}$$

Since $\vec{\nabla} \cdot (\vec{\nabla} \times \vec{A}) = 0$, the substitution of Equation 2.37 into Equation 2.34 leads to:

$$\nabla^2 \phi = 0$$

The relation between the vector potential, $\vec{A}$, and vorticity is obtained by taking the curl of Equation 2.37. This becomes:

$$\nabla^2 \vec{A} - \vec{\nabla}(\vec{\nabla} \cdot \vec{A}) = -\vec{\omega}$$

The vector potential is chosen to be solenoidal so that the above reduces to:

$$\nabla^2 \vec{A} = -\vec{\omega}$$

Therefore, for viscous incompressible flow, the momentum and mass conservation equations and the vorticity definition can be solved using:

$$\frac{\partial \vec{\omega}}{\partial t} + (\vec{V} \cdot \vec{\nabla})\,\vec{\omega} - (\vec{\omega} \cdot \vec{\nabla})\,\vec{V} = \frac{1}{\mathrm{Re}} \nabla^2 \vec{\omega} + \vec{\nabla} \times \vec{F} \tag{2.38}$$

$$\nabla^2 \phi = 0 \tag{2.39}$$

$$\nabla^2 \vec{A} = -\vec{\omega} \tag{2.40}$$

Then, the velocity is decoded from the potentials according to the Helmholtz decomposition:

$$\vec{V} = \vec{\nabla}\phi + \vec{\nabla} \times \vec{A}$$

If the pressure field is needed it can be obtained by solving for pressure from one of the primitive variable momentum equations or by solving the pressure Poisson equation. It is also possible to solve for the pressure by computing a force balance on an appropriate fluid element since the velocity field and hence the shear stress field is already determined by the solution strategy above.

3. PRELIMINARY ANALYSIS

3.1 Introduction

In this chapter the essential parts for assembling a dual potential code are gathered together. First the boundary conditions for the dependent variables are presented. Next, the Cartesian stretched grids are described and, finally, the necessary solvers are explained.

3.2 Boundary Conditions

A general presentation of the boundary conditions will be given here. The boundary conditions are applicable for two- or three-dimensional problems. Boundaries have been classified as one of the following:

1. Solid — impermeable boundary (slip or no slip)

2. Throughflow boundary — boundary crossed by the streamwise velocity

3. Far-field boundary — a freestream boundary which may be modeled as an impermeable boundary, a porous boundary or some other freestream condition according to the problem.

The boundary conditions are, of course, also identified with a partial differential equation. For ease of presentation, only the boundary types as listed above are discussed here. To determine what conditions are imposed in a particular problem it is necessary to know the classification of the governing partial differential equation (hyperbolic, parabolic or elliptic) and the number and type of derivatives of the dependent variable. Specific boundary conditions for each model problem will be given in figures in the discussion of the results. The solid boundary and throughflow boundary conditions for the potentials are thoroughly derived in Wong and Reizes (1984) and Hirasaki and Hellums (1970). For the transport variables ($\vec{\omega}, B, \rho, T$), a fully-developed exit condition is specified by dropping second order streamwise derivatives (except for density) and upwinding other streamwise derivatives at the exit. Example boundary conditions for a two-dimensional channel throughflow case are illustrated in Figure 3.3 for reference.

3.2.1 Scalar potential boundary conditions

The scalar potential is obtained from the solution of the Poisson equation, $\nabla^2\phi = B$. This is an elliptic equation so a condition on ϕ or its derivative must be given on all boundaries.

Since the velocity is decomposed into two potentials, it is useful to ascribe certain of the velocity boundary conditions to each potential. It has already been demonstrated by Hirasaki and Hellums (1970) that if the scalar potential were used to deal with possible throughflow velocities, then simple boundary conditions on the vector

potential are possible. Following Hirasaki and Hellums,

$$\frac{\partial \phi}{\partial n} = \hat{n} \cdot \vec{V}$$

on the boundaries. Thus, the scalar potential has Neumann conditions all around. The normal derivative of the scalar potential is the normal outflow velocity at the boundary. For a pure Neumann problem such as this, existence and uniqueness of the solution are concerns. Existence is ensured if the compatibility condition given by Green's theorem is satisfied. Uniqueness is ensured by prescribing the scalar potential at some point. For the test cases to be discussed later, it was possible to make one boundary a Dirichlet boundary and still satisfy the Neumann boundary condition by virtue of Green's theorem. The positive n direction in the following is the outward normal.

3.2.1.1 Solid boundaries For no flow through the boundary, the condition on the scalar potential is

$$\frac{\partial \phi}{\partial n} = 0$$

3.2.1.2 Throughflow boundaries An inlet or exit is the best example of a throughflow boundary. The condition on ϕ is then

$$\frac{\partial \phi}{\partial n} = \text{streamwise velocity, say } u_i$$

where,

$$u_i = \frac{1}{\mathrm{A}_i} \iint \vec{V} \cdot \hat{n} \, ds$$

and A_i is the cross-sectional area of the throughflow boundary.

3.2.1.3 Far-field boundaries A derivative condition on the scalar potential is also used at a far-field boundary as follows:

$\frac{\partial \phi}{\partial n}$ = normal component of velocity through the far-field boundary, usually 0.

3.2.2 Vector potential boundary conditions

The vector potential is obtained from the solution of the Poisson equation, $\nabla^2 \vec{A} = -\vec{\omega}$. This is an elliptic equation so a condition on the components of $\vec{A}$ or its derivatives must be given on all boundaries.

With the above choice of scalar potential boundary conditions, the boundary conditions on $\vec{A}$ for a simply connected region may be shown to be

$$A_t = \frac{\partial A_n}{\partial n} = 0 \tag{3.1}$$

where the subscripts t and n denote the tangential and normal components of $\vec{A}$ respectively. An example of the potential boundary conditions for a solid surface in the x–z plane are shown in Figure 3.1.

3.2.3 Vorticity boundary conditions

Vorticity is only needed for rotational flow computations. It is generated, for example, at no-slip boundaries and diffused and convected away. Vorticity may also be specified as part of the inlet or initial conditions. Vorticity can also be generated by shocks, but such flows will not be considered here. The transport equation for vorticity states the conservation of vorticity. Therefore, the boundary conditions are extremely important in defining the flow field.

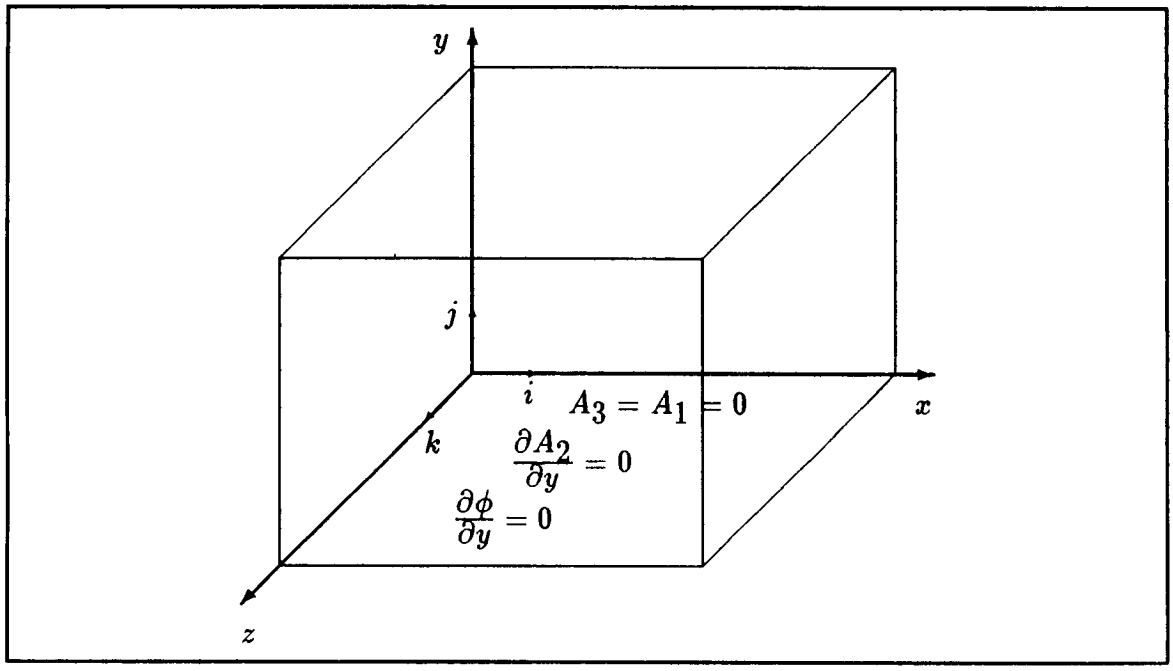

Figure 3.1: 3-D Cartesian coordinate system with example boundary conditions for the potentials on a solid impermeable surface in the x–z plane

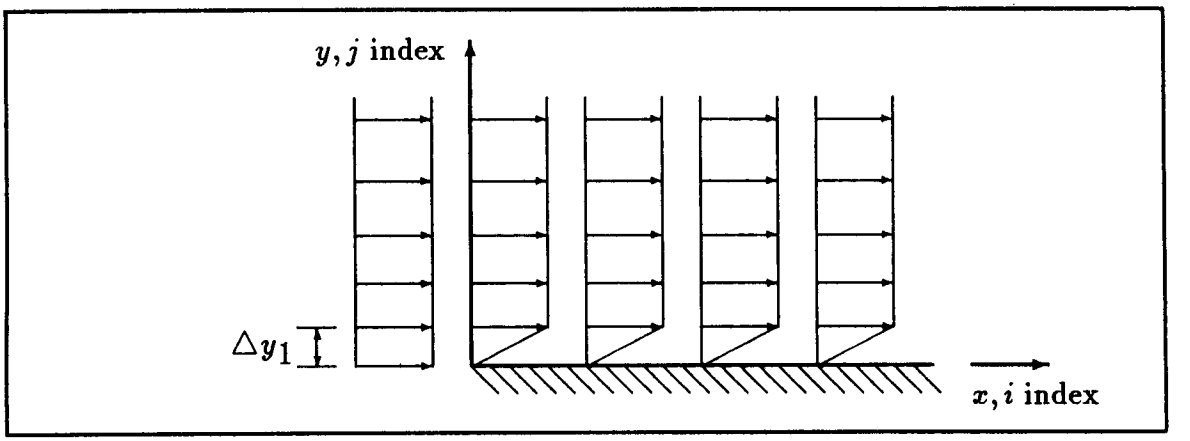

Figure 3.2: An initial uniform velocity profile along a viscous boundary for an impulsive start

3.2.3.1 **Solid boundaries** The vorticity at a solid boundary is obtained from the no-slip conditions. Several different formulations are possible. The wall vorticity can be computed from the velocity derivatives or from a Taylor series expansion of the vector potential. Consider a wall in the (x, z) plane. Using the vorticity definition from velocities, the wall vorticity (at $y = 0$) is

$$\omega_1 = w_y \tag{3.2}$$

$$\omega_2 = 0 \tag{3.3}$$

$$\omega_3 = -u_y \tag{3.4}$$

This method was used by Aziz and Hellums (1967). It was only used in this work to compute an initial wall vorticity based on an impulsive start. For example, the initial wall vorticity for a two-dimensional impulsive start is given by $\omega = -u_y$ (see Figure 3.2. The finite-difference initial wall vorticity is then:

$$\omega(i,1) = -\frac{u(i,2)}{y(i,2) - y(i,1)}$$

For subsequent global loops, a better approach (Roache 1972) was used to obtain the wall vorticity. This better approach uses the vector potential. Consider a vorticity producing surface at $y = 0$ $(j = 1)$ in a two-dimensional flow. The grid may be stretched, so let the transverse spacing to the first node point be $\triangle y_1$ as in Figure 3.2. For the i index in the x direction and j index in the y direction, write the Taylor series expansion for the vector potential at $(i,2)$ about the wall values as follows:

$$\begin{aligned} A(i,2) &= A(i,1) + \left.\frac{\partial A}{\partial y}\right|_{i,1} \triangle y_1 + \frac{1}{2}\left.\frac{\partial^2 A}{\partial y^2}\right|_{i,1} (\triangle y_1)^2 + \frac{1}{6}\left.\frac{\partial^3 A}{\partial y^3}\right|_{i,1} (\triangle y_1)^3 \\ &\quad + \mathcal{O}(\triangle y_1)^4 \end{aligned} \tag{3.5}$$

From the velocity decomposition in two dimensions (Equation 2.18), $u = \phi_x + A_y$. At the wall this is

$$u(i,1) = \left.\frac{\partial \phi}{\partial x}\right|_{i,1} + \left.\frac{\partial A}{\partial y}\right|_{i,1}$$

but, $u(i,1)$ is zero for a no-slip boundary. Therefore, $\left.\frac{\partial A}{\partial y}\right|_{i,1}$ in the Taylor series above can be replaced by the scalar potential derivative along the boundary.

$$\left.\frac{\partial A}{\partial y}\right|_{i,1} = -\left.\frac{\partial \phi}{\partial x}\right|_{i,1} \tag{3.6}$$

Again using the velocity decomposition in two dimensions, $u = \phi_x + A_y$, the y derivative of this equation gives: $u_y = \phi_{xy} + A_{yy}$. At the solid impermeable wall this is:

$$\left.\frac{\partial u}{\partial y}\right|_{i,1} = \left.\frac{\partial^2 \phi}{\partial x \partial y}\right|_{i,1} + \left.\frac{\partial^2 A}{\partial y^2}\right|_{i,1}$$

From the scalar potential boundary condition at a solid boundary, $\left.\frac{\partial \phi}{\partial y}\right|_{i,1} = 0$. Hence, the second order y derivative of A at the wall is simply:

$$\left.\frac{\partial^2 A}{\partial y^2}\right|_{i,1} = \left.\frac{\partial u}{\partial y}\right|_{i,1}$$

The wall vorticity in two dimensions is the component $\omega_3 = \omega = v_x - u_y$. Along the wall $v = 0$, so that $\omega(i,1) = -\left.\frac{\partial u}{\partial y}\right|_{i,1}$. Therefore, the wall vorticity is introduced into the Taylor series for the A_{yy} term as:

$$\left.\frac{\partial^2 A}{\partial y^2}\right|_{i,1} = \left.\frac{\partial u}{\partial y}\right|_{i,1} = -\omega(i,1) \tag{3.7}$$

Equation 3.7 is also obtainable from the Poisson equation for the vector potential, $\nabla^2 A = -\omega$. At the wall, $A = 0$, so $A_{xx} = 0$ and $A_{yy} = -\omega$. Substituting for A_y and A_{yy} in the Taylor series of Equation 3.5 one obtains:

$$A(i,2) = A(i,1) - \left.\frac{\partial \phi}{\partial x}\right|_{i,1} \triangle y_1 + \frac{1}{2}(-\omega(i,1))(\triangle y_1)^2 + \frac{1}{6}\left.\frac{\partial^3 A}{\partial y^3}\right|_{i,1} (\triangle y_1)^3 + \mathcal{O}(\triangle y_1)^4 \tag{3.8}$$

Solving for $\omega(i,1)$ yields the following first order approximation for the wall vorticity

$$\omega(i,1) = \frac{2}{(\triangle y_1)^2}\left[A(i,1) - A(i,2) - \left.\phi_x\right|_{i,1} \triangle y_1\right] + \mathcal{O}(\triangle y_1) \tag{3.9}$$

The vector potential in two dimensions is zero at a solid impermeable wall, so $A(i,1) = 0$ in the above. Using a second order central difference for ϕ_x with possible stretching in the x direction (Section 3.3), the finite-difference formula for the wall vorticity becomes:

$$\omega(i,1) = \frac{2}{(\triangle y_1)^2}\left[A(i,1) - A(i,2) - \frac{\partial \overline{x}}{\partial x}(i,1)\frac{\phi(i+1,1) - \phi(i-1,1)}{2} \triangle y_1\right] \tag{3.10}$$

In a similar fashion the Taylor series and above substitutions could be carried out in the computational plane $(\overline{x}, \overline{y})$. The unequal grid spacing is accounted for by the metrics to yield the following formula:

$$\omega(i,1) = 2\left(\frac{\partial \overline{y}}{\partial y}\right)^2(i,1)\Bigg[A(i,1) - A(i,2) + \frac{\frac{\partial \overline{x}}{\partial x}(i,1)}{\frac{\partial \overline{y}}{\partial y}(i,1)}\left(\frac{\phi(i+1,1)-\phi(i-1,1)}{2}\right)\left(\frac{1}{2}\frac{\left(\frac{\partial^2 \overline{y}}{\partial y^2}\right)(i,1)}{\left(\frac{\partial \overline{y}}{\partial y}\right)^2(i,1)} - 1\right)\Bigg] \quad (3.11)$$

The above first order form was used most frequently in the results to be reported here. A second order formulation also based on the Taylor series is obtainable from Equation 3.5 by retaining the $(\triangle y_1)^3$ term. The second order boundary conditions will be derived here for a three-dimensional case. Consider the x–z plane again. The boundary condition on the ω_1 component will be derived first by starting with the Taylor series expansion of the vector potential component A_1. The Taylor series expansion for A_1 at a mesh point adjacent to the boundary, ($y = \triangle y_1$ at $j = 2$), is given by

$$A_1(i,2,k) = A_1(i,1,k) + \left.\frac{\partial A_1}{\partial y}\right|_{i,1,k}\triangle y_1 + \frac{1}{2}\left.\frac{\partial^2 A_1}{\partial y^2}\right|_{i,1,k}(\triangle y_1)^2 + \frac{1}{6}\left.\frac{\partial^3 A_1}{\partial y^3}\right|_{i,1,k}(\triangle y_1)^3 + \mathcal{O}(\triangle y_1)^4 \quad (3.12)$$

where the indices i, j, k denote the x, y, z positions, respectively.

The first term of the expansion is zero since the tangential components of $\vec{A}$ vanish on an impermeable boundary. Hence

$$A_1(i,1,k) = 0 \quad (3.13)$$

To evaluate the second term, use the velocity component which contains A_{1_y} in its decomposition. From Equation 2.17 note that

$$w = \phi_z + A_{2_x} - A_{1_y}$$

Since $w = 0$ on the boundary, the derivative in the second term of the expansion can be written

$$\left.\frac{\partial A_1}{\partial y}\right|_{i,1,k} = \left.\frac{\partial \phi}{\partial z}\right|_{i,1,k} + \left.\frac{\partial A_2}{\partial x}\right|_{i,1,k} \tag{3.14}$$

From Equations 2.14 and 3.1, the second order derivative in the third term may easily be identified as

$$\left.\frac{\partial^2 A_1}{\partial y^2}\right|_{i,1,k} = -\omega_1(i,1,k) \tag{3.15}$$

Here is where the second order method departs from the first order approach given earlier. To obtain an expression for the third order derivative of A_1, a linear distribution of vorticity and $A_{1_{yy}}$ over the first mesh interval is assumed (Wong and Reizes 1984), so that

$$\omega_1 = \omega_1(i,1,k) + \frac{y}{\triangle y_1}[\omega_1(i,2,k) - \omega_1(i,1,k)] \tag{3.16}$$

$$\frac{\partial^2 A_1}{\partial y^2} = \frac{\partial^2 A_1}{\partial y^2}(i,1,k) + \frac{y}{\triangle y_1}\left[\frac{\partial^2 A_1}{\partial y^2}(i,2,k) - \frac{\partial^2 A_1}{\partial y^2}(i,1,k)\right] \tag{3.17}$$

Combining the above linear distributions in order to write ω_1 as a function of $A_{1_{yy}}$ yields

$$\omega_1 = -\frac{\partial^2 A_1}{\partial y^2} + \frac{y}{\triangle y_1}\left[\omega_1(i,2,k) + \frac{\partial^2 A_1}{\partial y^2}(i,2,k)\right] \tag{3.18}$$

Differentiating Equation 3.18 with respect to y yields

$$\frac{\partial \omega_1}{\partial y} = -\frac{\partial^3 A_1}{\partial y^3} + \frac{1}{\triangle y_1}\left[\omega_1(i,2,k) + \frac{\partial^2 A_1}{\partial y^2}(i,2,k)\right] \tag{3.19}$$

Solving Equation 3.19 for A_{1yyy} at $y = 0$ gives

$$\frac{\partial^3 A_1}{\partial y^3}(i,1,k) = \frac{\omega_1(i,1,k) - \omega_1(i,2,k)}{\triangle y_1} + \frac{1}{\triangle y_1}\left[\omega_1(i,2,k) + \frac{\partial^2 A_1}{\partial y^2}(i,2,k)\right] \quad (3.20)$$

Finally, substituting Equations 3.13, 3.14, 3.15 and 3.20 into Equation 3.12 gives a second order relationship between the boundary vorticity and the potentials, that is,

$$\begin{aligned} \omega_1(i,1,k) &= -\frac{3A_1(i,2,k)}{(\triangle y_1)^2} + \frac{3}{\triangle y_1}\left[\phi_z(i,1,k) + A_{2x}(i,1,k)\right] \\ &\quad + \frac{1}{2}A_{1yy}(i,2,k) + \mathcal{O}(\triangle y_1)^2 \end{aligned} \quad (3.21)$$

Similarly, the z component of vorticity at this boundary is found to be:

$$\omega_3(i,1,k) = -\frac{3A_3(i,2,k)}{(\triangle y_1)^2} + \frac{3}{\triangle y_1}A_{2z}(i,1,k) + \frac{1}{2}A_{3yy}(i,2,k) + \mathcal{O}(\triangle y_1)^2 \quad (3.22)$$

The third and final vorticity component at this boundary is computed from the no-slip condition and the definition of vorticity to be

$$\omega_2(i,1,k) = 0 \quad (3.23)$$

as already stated at the beginning of this discussion. In actual use, the second order vorticity boundary condition increased the CPU time with no noticeable improvement in accuracy. Roache (1972) also reports that second order vorticity boundary conditions can be less stable and less capable than the first order boundary conditions.

3.2.3.2 Throughflow boundaries The only throughflow boundaries used here are the inlet plane and exit plane for two- and three-dimensional problems. The inlet flow field may be specified as either rotational or irrotational. This is controlled

by the inlet plane transverse velocity. For two-dimensional flow, the inlet v velocity is controlled to provide rotational or irrotational flow as follows:

$$\text{inlet condition} \begin{cases} \text{rotational} & ; \text{set } v = 0 \\ \text{irrotational} & ; \text{compute } v \text{ from the decomposition} \end{cases} \tag{3.24}$$

The inlet plane vorticity is then computed from the definition, $\vec{\omega} = \vec{\nabla} \times \vec{V}$.

For a two-dimensional rotational inlet condition, the inlet transverse velocity is set to zero and used throughout the code. The irrotational inlet condition is achieved by computing the inlet plane transverse velocity from the decomposition and using that non-zero inlet transverse velocity throughout the code. The streamwise velocity component is unchanged since it fixes the inlet mass flux.

At the exit the second order streamwise derivative is dropped and other streamwise derivatives are upwinded.

3.2.3.3 Far-field boundaries The far-field vorticity must be specified or determined from the specified upstream flow conditions. It is not safe to extrapolate the vorticity to a far-field boundary, or any boundary since that does not account for the physics of vorticity production, convection and diffusion. Far enough away from a surface generating vorticity, the vorticity should be zero. If the velocity is known at the far-field, vorticity may be obtained from the definition.

3.2.4 Dilatation boundary conditions

The dilatation, B, is only needed for a compressible flow. Boundary conditions are developed from the expected velocity boundary conditions and the definition of

the dilatation,

$$B = \vec{\nabla} \cdot \vec{V} = u_x + v_y + w_z$$

or by applying the continuity equation,

$$\rho_t + u\rho_x + v\rho_y + w\rho_z + \rho B = 0$$

The treatment of this variable is the most uncertain. There is little guidance in the literature. El-Refaee (1981) used the dilatation in his non-primitive variable formulation. He extrapolated to obtain the dilatation at the boundary. The boundary values of dilatation were relaxed and set to zero as the solution approached steady state. El-Refaee solved external flow problems only.

3.2.4.1 **Solid boundaries** For a viscous flow along an impermeable wall, all velocities are zero. This reduces the continuity equation to

$$\rho_t + \rho B = 0$$

For steady boundary conditions on density, or at steady state it is clear that

$$B = 0$$

Otherwise, the density time derivative or the velocity derivatives must be evaluated to compute

$$B = -\frac{\rho_t}{\rho}\bigg|_{\text{wall}} \text{, from continuity} \tag{3.25}$$

or,

$$B = u_x + v_y + w_z \text{ , from the definition of } B. \tag{3.26}$$

In any case, $B = 0$ at the boundary at steady state.

3.2.4.2 Throughflow boundaries The only throughflow boundaries used here are the inlet plane and exit plane for two-dimensional compressible flow problems. The inlet flow may be specified as either rotational or irrotational as stated in the section on vorticity boundary conditions. From the definition of dilatation, $B = u_x + v_y$, an inlet Dirichlet condition can be computed. For the rotational flow inlet condition (which corresponds to a uniform parallel inlet flow), $v = 0$ at the inlet. This gives $B = u_x$ for the inlet boundary condition. For the irrotational flow inlet condition, $v \neq 0$ and in general $v_y \neq 0$. This gives $B = u_x + v_y$ for the inlet boundary condition. It has been found that an inlet boundary condition of $B = 0$ may be used for either inlet condition. By setting $B = 0$ at the inlet one avoids the ambiguity of specifying the dilatation inlet condition using velocities which in turn depend on B. At the exit, the second order streamwise derivative is dropped and other streamwise derivatives are upwinded.

3.2.4.3 Far-field boundaries Generally, the velocity field is unchanging at the far field, so B is given by the unchanging velocity derivatives. A typical far-field condition is uniform parallel flow so that $B = 0$.

3.2.5 Density boundary conditions

The density boundary conditions are set using one of the following approaches, depending on the problem:

1. By applying the boundary-layer assumption for viscous compressible flow at a solid boundary and the ideal gas law,

$$p_y = 0$$

so,

$$\rho(i,1) = \frac{\rho(i,2)\,T(i,2)}{T(i,1)}$$

2. By using the Bernoulli equation for inviscid irrotational compressible flows,

$$\rho = \left[1 + \frac{\gamma - 1}{2} \mathrm{M}_\infty^2 \left(1 - u^2 - v^2 - w^2\right)\right]^{\frac{1}{\gamma - 1}}$$

3. By application of the continuity equation written along the boundary,

$$\rho_t + u\rho_x + v\rho_y + \rho B = 0$$

3.2.6 Temperature boundary conditions

The temperature boundary conditions are either set as Dirichlet conditions or derivative conditions based on a prescribed wall heat flux. First through fourth order polynomial derivative conditions are included in the computer code as options. The inlet temperature field is user specified. At the exit plane, second order streamwise derivatives are dropped and other streamwise derivatives are upwinded.

3.2.7 Velocity boundary conditions

The velocity is not a primary variable in this method. Velocity boundary conditions are dictated by the flow physics and are used to develop boundary conditions on

the derived variables, such as the dilatation boundary conditions above. The conditions to use are straightforward—e.g., no-slip at solid boundaries for a viscous fluid. It is important to point out that the velocity boundary conditions are used, but not necessarily enforced by the dual potential formulation. For example, a no-slip condition is used to develop boundary conditions for the vorticity at a solid viscous wall. However, there is a small slip velocity computed by the velocity decomposition. The slip velocity goes to zero as the grid is refined. To see how the slip velocity arises, consider the velocity decomposition for a two-dimensional flow over a flat plate oriented as in Figure 3.2. The velocity decomposition for this case is given by Equation 2.18, repeated here for convenience.

$$\vec{V} = \begin{pmatrix} u \\ v \end{pmatrix} = \begin{pmatrix} \phi_x + A_y \\ \phi_y - A_x \end{pmatrix} \tag{3.27}$$

At the flat plate surface, the boundary conditions on the potentials are:

$$\begin{aligned} \phi_y &= 0 \\ A &= 0 \end{aligned}$$

It is obvious that the v component of velocity will be zero both analytically and numerically (provided the same difference formula is used to compute v as was used to enforce the boundary condition on ϕ). However, the u component will only be zero if $\phi_x = -A_y$. This is not exactly satisfied numerically.

3.3 Cartesian Grid Clustering

Simple independent variable transformations are used to allow for stretching of the two-dimensional Cartesian grids (Anderson et al. 1984). The stretching trans-

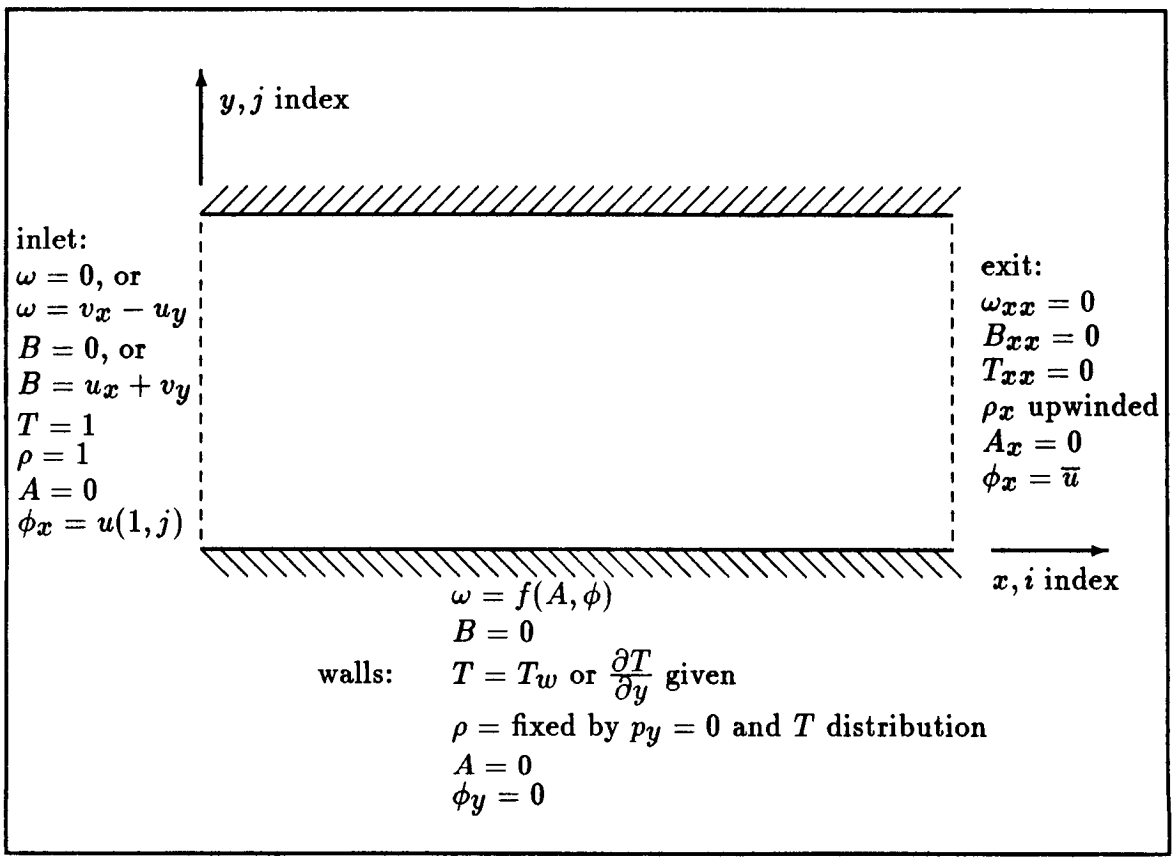

Figure 3.3: 2-D channel boundary conditions

formations may be readily applied to a third coordinate direction for use in a three-dimensional Cartesian grid. The transformations used here are from the family of general stretching transformations proposed by Roberts (1971).

The coordinate transformation maps the physical plane (x, y) into the computational plane $(\overline{x}, \overline{y})$:

$$(x, y) \rightarrow (\overline{x}, \overline{y})$$

where, $\overline{x} = f(x)$ only and $\overline{y} = f(y)$ only. Also, the transformations are scaled so that $\triangle\overline{x} = \triangle\overline{y} = 1$. The computational grid coordinate values then correspond to the grid indices like $(\overline{x}, \overline{y}) = (i-1, j-1)$. This simplifies the coding and avoids divisions in the numerical algorithm for a slight speedup advantage. In the following, NI is the largest x index and NJ is the largest y index in the domain. NI and NJ correspond to the maximum dimensions of the physical grid L, h (see Figure 3.4).

Applying these transformations to the governing fluid dynamic equations requires the following partial derivatives: (These have been simplified since $\overline{x}$ and $\overline{y}$ are only functions of the respective coordinate directions.)

$$\frac{\partial}{\partial x} = \frac{\partial \overline{x}}{\partial x}\frac{\partial}{\partial \overline{x}}$$

$$\frac{\partial}{\partial y} = \frac{\partial \overline{y}}{\partial y}\frac{\partial}{\partial \overline{y}}$$

$$\frac{\partial^2}{\partial x^2} = \left(\frac{\partial \overline{x}}{\partial x}\right)^2 \frac{\partial^2}{\partial \overline{x}^2} + \left(\frac{\partial^2 \overline{x}}{\partial x^2}\right)\frac{\partial}{\partial \overline{x}}$$

$$\frac{\partial^2}{\partial y^2} = \left(\frac{\partial \overline{y}}{\partial y}\right)^2 \frac{\partial^2}{\partial \overline{y}^2} + \left(\frac{\partial^2 \overline{y}}{\partial y^2}\right)\frac{\partial}{\partial \overline{y}}$$

$$\frac{\partial^2}{\partial x \partial y} = \frac{\partial \overline{x}}{\partial x}\frac{\partial \overline{y}}{\partial y}\frac{\partial^2}{\partial \overline{x}\partial \overline{y}}$$

The above metric terms are computed numerically using second order accurate differences for the unequal mesh spacing. Analytical calculation of the metrics are possible for the stretchings to be presented. It was found, however, that the numerical calculation provided better flow results.

3.3.1 Clustering near boundaries

Take the x direction to be streamwise. The transverse direction is then y with "walls" at $y = 0$ and $y = h$. The following transformation allows packing near the inlet and near one or both walls.

$$\overline{x} = \mathrm{NI}\left(1 - \frac{\ln\left\{\left[\sigma + 1 - (x/L)\right]/\left[\sigma - 1 + (x/L)\right]\right\}}{\ln\left[(\sigma+1)/(\sigma-1)\right]}\right) \qquad 1 < \sigma < \infty \tag{3.28}$$

$$\overline{y} = \alpha + (1-\alpha)\frac{\ln\left(\left\{\beta + \left[y\left(2\alpha+1\right)/h\right] - 2\alpha\right\}/\left\{\beta - \left[y\left(2\alpha+1\right)/h\right] + 2\alpha\right\}\right)}{\ln\left[(\beta+1)/(\beta-1)\right]} \tag{3.29}$$

This is designed so that $0 \le \overline{x} \le (\mathrm{NI}-1)$ and $0 \le \overline{y} \le (\mathrm{NJ}-1)$ for $0 \le x \le L$, $0 \le y \le h$ with $\triangle\overline{x} = \triangle\overline{y} = 1$. Equation 3.29 for $\overline{y}$ packs near $y = h$ for $\alpha = 0$ and near both walls equally for $\alpha = 0.5$. The inverse of equations 3.28 and 3.29 are needed to construct the physical grid (x, y). The inverse for the above transformation is readily found as:

$$x = L\frac{(\sigma+1) - (\sigma-1)\left[\frac{\sigma+1}{\sigma-1}\right]^{\left(1-\frac{\overline{x}}{\mathrm{NI}-1}\right)}}{\left[\frac{\sigma+1}{\sigma-1}\right]^{\left(1-\frac{\overline{x}}{\mathrm{NI}-1}\right)}+1} \tag{3.30}$$

$$y = h\left(-\kappa + \mathrm{sgn}(\kappa)\frac{(\beta+2\alpha)\left[\frac{\beta+1}{\beta-1}\right]^{\frac{\bar{y}}{NJ-1}-\alpha} - \beta + 2\alpha}{(2\alpha+1)\left(1+\left[\frac{\beta+1}{\beta-1}\right]^{\frac{\bar{y}}{NJ-1}-\alpha}\right)}\right) \qquad (3.31)$$

where,

$$\mathrm{sgn}(\kappa) = \begin{cases} 1 & \text{for } \kappa \geq 0 \\ -1 & \text{for } \kappa < 0 \end{cases}$$

The inverse for y has been modified using κ to direct the y clustering to either wall as described below. The stretching parameters in the above transformation have the following affects:

x direction clustering

$1 < \sigma < \infty$ — The stretching parameter σ clusters more points near $x = 0$ as σ approaches 1. The grid becomes more uniform as $x \to \infty$. An essentially uniform x grid is generated for $\sigma = 10$.

y direction clustering

$1 < \beta < \infty$ — The stretching parameter β controls the y direction clustering (spacing ratio). Maximum clustering is achieved as β approaches 1. An essentially uniform y grid is generated for $\beta = 10$.

The stretching parameter α is either 0 or 0.5.

$\alpha = 0$ $\begin{cases} \kappa \geq 0 & \text{clusters near } y = h \text{ only.} \\ \kappa < 0 & \text{clusters near } y = 0 \text{ only.} \end{cases}$

$\alpha = 0.5$ Cluster points near $y = 0$ and $y = h$ equally. κ makes no difference when $\alpha = 0.5$.

An example of the above clustering is shown in Figure 3.4.

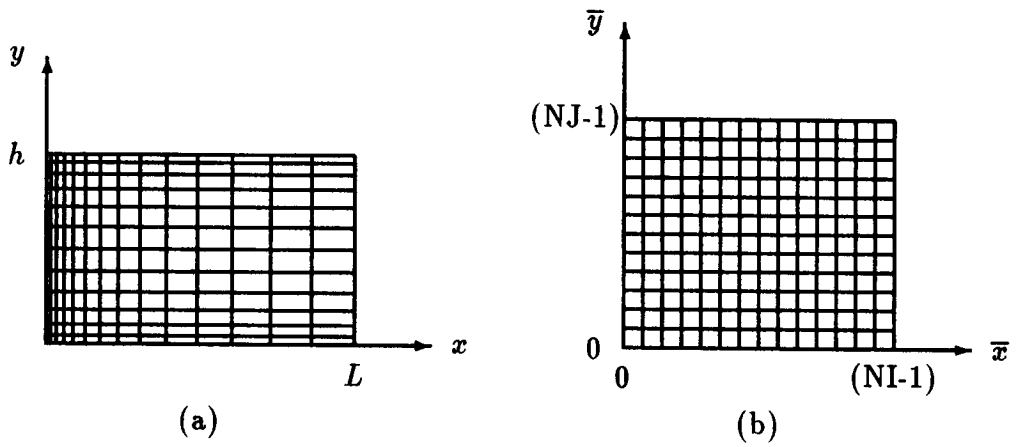

Figure 3.4: Typical 2-D channel grid. (a) Physical plane using $\sigma = 1.05, \alpha = 0.5, \beta = 1.2$; (b) Computational plane

3.3.2 Clustering near an interior point

This clustering technique was used for the bump problem (isolated airfoil). It can also be used to cluster points about an obstacle located within the grid. The equations given will work in either the x or y directions and are designed to cluster near a single point or to symmetrically cluster about an object by reflecting the generated grid about the line of symmetry.

The x coordinate scheme for the bump problem will be given here. This requires an odd number of i points and assumes that the bump or airfoil is always placed in the center of the x grid. (The bump in the test cases is simulated by the blowing condition rather than occupying x, y space.)

As stated previously, $\overline{x}$ is simply given by the grid point index, $i - 1$, so that

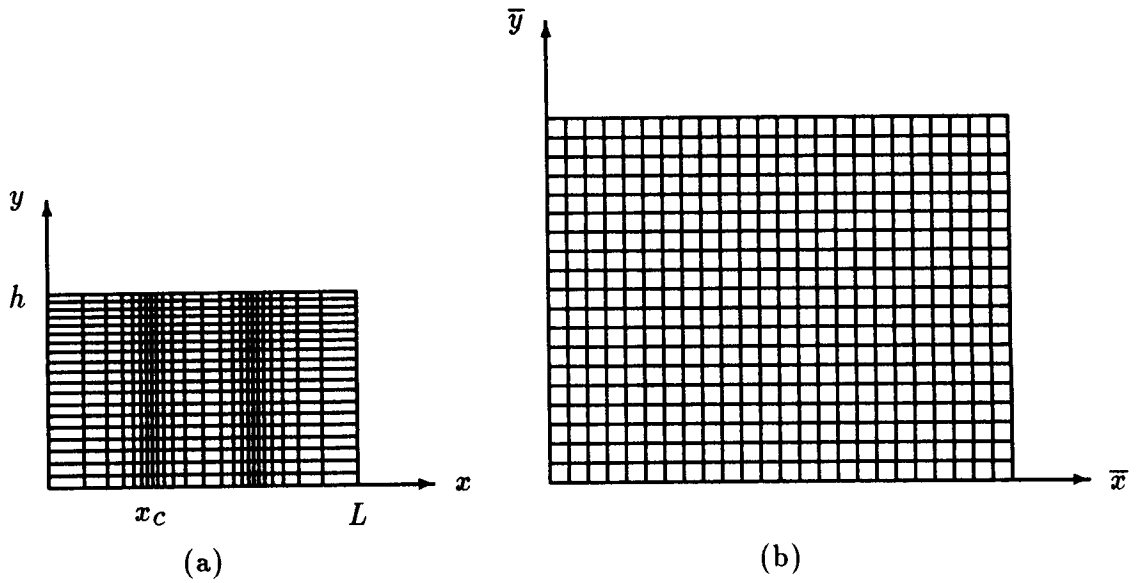

Figure 3.5: Typical 2-D grid for an isolated airfoil at $y = h$. (a) Physical plane using $\tau = 5.0, \alpha = 0, \kappa = 0, \beta = 1.5$; (b) Computational plane

$\triangle\overline{x} = 1$. The inverse transformation is:

$$x = x_C \left\{ 1 + \frac{\sinh\left[\tau\left(\frac{\overline{x}}{\mathrm{NI}/2} - W\right)\right]}{\sinh(\tau W)} \right\} \tag{3.32}$$

where

$$W = \frac{1}{2\tau} \ln\left[\frac{1 + (e^{\tau} - 1)\left(\frac{x_C}{L/2}\right)}{1 + \left(e^{-\tau} - 1\right)\left(\frac{x_C}{L/2}\right)} \right] \qquad 0 < \tau < \infty \tag{3.33}$$

The stretching parameter, τ varies from zero (no stretching) to large values which produce the most refinement near $x = x_C$. An example of this stretching is shown in Figure 3.5 where the grid has been refined near the line x_C and reflected about the line of symmetry at $x = L/2$.

3.3.3 Arbitrary user defined clustering

The dual potential computer program will accept any user defined clustering so long as $\overline{x} = f(x)$ only and $\overline{y} = f(y)$ only. These may be input as arbitrary x, y points or as equations relating x, y to $\overline{x}, \overline{y}$ as in the above examples. The code automatically scales the metrics to form a two-dimensional computational space with $\triangle\overline{x} = \triangle\overline{y} = 1$.

3.4 Poisson Equation Solvers

Three different methods have been used to solve the Poisson equations for the potentials. One method is the vectorized point Gauss-Seidel scheme with successive over-relaxation (SOR). The other two are alternating direction implicit (ADI) type schemes (Mitchell and Griffiths 1980). The two ADI type schemes will be distinguished as follows:

1. A scheme formed by factoring and then splitting into a two step formula similar to the D'Yakonov (1963) approach. This will be referred to as the approximately factored (AF) scheme in this discussion.

2. A Peaceman-Rachford type scheme with a half-time step level (Peaceman and Rachford 1955). This scheme will be referred to hereafter as the ADI scheme.

In summary, the three schemes to be used to solve the Poisson equations are:

1. Vectorized point Gauss-Seidel with SOR

2. AF scheme

3. ADI scheme

The model equation $\nabla^2\Phi = S$ will be used to demonstrate the above algorithms. For the AF and ADI schemes, the Poisson equation is written with a fictitious time derivative: $\Phi_t + \nabla^2\Phi = S$. The iterations represent "time" levels with time step h. The time step may also be thought of as a relaxation parameter. At convergence the time derivative term is negligible.

For a Cartesian grid with possible stretching according to the coordinate transformations in Section 3.3, the equation to discretize is:

$$\Phi_t + \left(\frac{\partial\overline{x}}{\partial x}\right)^2 \Phi_{\overline{x}\overline{x}} + \left(\frac{\partial^2\overline{x}}{\partial x^2}\right) \Phi_{\overline{x}} + \left(\frac{\partial\overline{y}}{\partial y}\right)^2 \Phi_{\overline{y}\overline{y}} + \left(\frac{\partial^2\overline{y}}{\partial y^2}\right) \Phi_{\overline{y}} = S$$

The computational plane grid spacing is unity so $\triangle\overline{x}$ and $\triangle\overline{y}$ do not appear in the algorithms below.

3.4.1 Vectorized point Gauss-Seidel with SOR

The finite-difference form of the equation to solve is:

$$\left[\left(\frac{\partial\overline{x}}{\partial x}\right)^2 \delta^2_{\overline{x}} + \left(\frac{\partial^2\overline{x}}{\partial x^2}\right) \frac{\overline{\delta}_{\overline{x}}}{2} + \left(\frac{\partial\overline{y}}{\partial y}\right)^2 \delta^2_{\overline{y}} + \left(\frac{\partial^2\overline{y}}{\partial y^2}\right) \frac{\overline{\delta}_{\overline{y}}}{2}\right] \Phi^{\text{most recent}} = S$$

Since Gauss-Seidel is a point iterative method, the exact application of the above algorithm will depend on the mesh point ordering. The Gauss-Seidel method is based on immediate use of the most recent values. Therefore, the $\Phi^{\text{most recent}}$ used in the above equation is either Φ^{k+1} or Φ^k. Solving the above equation iteratively by points will not vectorize due to data dependency. This can be illustrated by a simple example. Consider the five-point formula finite-difference scheme for the two-dimensional Laplace equation, $\nabla^2 U = 0$, on a uniform Cartesian grid with Dirichlet

boundary conditions:

$$\frac{U_{i+1,j} - 2U_{i,j} + U_{i-1,j}}{(\triangle x)^2} + \frac{U_{i,j+1} - 2U_{i,j} + U_{i,j-1}}{(\triangle y)^2} = 0$$

As a further simplification take $\triangle x = \triangle y = 1$ so that solving this by points one would code the following:

```
      DO 40 J=2,NJ-1
      DO 40 I=2,NI-1
      U(I,J) = 0.25 * (U(I-1,J) + U(I+1,J) + U(I,J-1) + U(I,J+1))
40    CONTINUE
```

The dependency of `U(I,J)` on `U(I-1,J)` inhibits vectorization. Notice, however, that for a fixed `J`, the even `I` indexed values of `U` on the left hand side depend only on the odd `I` indexed ones on the right hand side. A vectorization strategy is now apparent. The data dependency is removed from the computation by "coloring" the grid as a checkerboard and updating the `U` in two sweeps. At a starting `J`, the odd `I` index points may be thought of as black squares on a checkerboard and the even `I` index points may be thought of as red squares. At the next `J`, the odd `I` points are then red squares and the even `I` points are black squares. This red-black coloring continues in `J` until the grid is patterned like a checkerboard. In one sweep the black points are updated using only red points and in another sweep the red points are updated using only black points. This is easily implemented by incrementing the `I` loop by 2. Some initial work is required to determine the starting and ending `I` indices for each `J`. Therefore, in two sweeps the solution is iteratively updated and the code will vectorize. The compiler, however, will not recognize that the data dependency has been removed. The programmer must direct the compiler to vectorize the loops. This strategy is coded below. Note that the starting and stopping `I` indices are a

function of J. It is a simple alternating function, such as 2,3,2,3,...for IBSTRT(J) and then 3,2,3,2,...for IRSTRT(J).

```
C...BLACK POINTS
      DO 40 J=2,NJ-1
C...COMPILER DIRECTIVE: IGNORE VECTOR DEPENDENCIES IN THE I LOOP
      DO 40 I=IBSTRT(J),IBEND(J),2
      U(I,J) = 0.25 * (U(I-1,J) + U(I+1,J) + U(I,J-1) + U(I,J+1))
40    CONTINUE

C...RED POINTS
      DO 41 J=2,NJ-1
C...COMPILER DIRECTIVE: IGNORE VECTOR DEPENDENCIES IN THE I LOOP
      DO 41 I=IRSTRT(J),IREND(J),2
      U(I,J) = 0.25 * (U(I-1,J) + U(I+1,J) + U(I,J-1) + U(I,J+1))
41    CONTINUE
```

This may be combined with SOR for a further speed advantage. The extension of this vectorization concept to three dimensions is straightforward. The three-dimensional problem may be solved as a stack of two-dimensional checkerboards, as a four-color point method, or by extending the idea of colored points to colored lines and solving by lines rather than points. The red-black strategy and other vectorizable structures are discussed in Gentzsch and Neves (1987).

3.4.2 AF scheme

Using first order temporal differencing and second order spatial differencing on the model Poisson equation one obtains:

$$\frac{\Phi^{k+1} - \Phi^k}{h} + \left[\left(\frac{\partial \overline{x}}{\partial x} \right)^2 \delta_{\overline{x}}^2 + \left(\frac{\partial^2 \overline{x}}{\partial x^2} \right) \frac{\overline{\delta}_{\overline{x}}}{2} + \left(\frac{\partial \overline{y}}{\partial y} \right)^2 \delta_{\overline{y}}^2 + \left(\frac{\partial^2 \overline{y}}{\partial y^2} \right) \frac{\overline{\delta}_{\overline{y}}}{2} \right] \Phi^{k+1} = S \tag{3.34}$$

It is convenient to use the "delta" form of the dependent variable so define

$$\triangle^k \Phi = \Phi^{k+1} - \Phi^k$$

To form a "delta" in the difference equation above subtract the spatial derivatives of Φ^k from each side. Multiplying through by the time step (or relaxation parameter), h, gives

$$\left(I + h\left[\left(\frac{\partial \overline{x}}{\partial x}\right)^2 \delta_{\overline{x}}^2 + \left(\frac{\partial^2 \overline{x}}{\partial x^2}\right)\frac{\overline{\delta}_{\overline{x}}}{2} + \left(\frac{\partial \overline{y}}{\partial y}\right)^2 \delta_{\overline{y}}^2 + \left(\frac{\partial^2 \overline{y}}{\partial y^2}\right)\frac{\overline{\delta}_{\overline{y}}}{2}\right]\right) \triangle^k \Phi =$$
$$hS - h\left[\left(\frac{\partial \overline{x}}{\partial x}\right)^2 \delta_{\overline{x}}^2 + \left(\frac{\partial^2 \overline{x}}{\partial x^2}\right)\frac{\overline{\delta}_{\overline{x}}}{2} + \left(\frac{\partial \overline{y}}{\partial y}\right)^2 \delta_{\overline{y}}^2 + \left(\frac{\partial^2 \overline{y}}{\partial y^2}\right)\frac{\overline{\delta}_{\overline{y}}}{2}\right] \Phi^k$$

The "delta" form allows easy implicit handling of the boundary conditions. Steady Dirichlet conditions are automatically satisfied by the fact that $\triangle^k \Phi = 0$ on the boundary. Steady Neumann conditions are easily handled by reflecting the $\triangle^k \Phi$ at the boundary. The derivative function cancels so there is nothing to be added to the right hand side. The actual Dirichlet values or derivatives are input by the source term spatial derivatives of Φ^k.

An approximately factored form of the equation above is:

$$\left(I + h\left(\frac{\partial \overline{x}}{\partial x}\right)^2 \delta_{\overline{x}}^2 + h\left(\frac{\partial^2 \overline{x}}{\partial x^2}\right)\frac{\overline{\delta}_{\overline{x}}}{2}\right)\left(I + h\left(\frac{\partial \overline{y}}{\partial y}\right)^2 \delta_{\overline{y}}^2 + h\left(\frac{\partial^2 \overline{y}}{\partial y^2}\right)\frac{\overline{\delta}_{\overline{y}}}{2}\right) \triangle^k \Phi =$$
$$hS - h\left[\left(\frac{\partial \overline{x}}{\partial x}\right)^2 \delta_{\overline{x}}^2 + \left(\frac{\partial^2 \overline{x}}{\partial x^2}\right)\frac{\overline{\delta}_{\overline{x}}}{2} + \left(\frac{\partial \overline{y}}{\partial y}\right)^2 \delta_{\overline{y}}^2 + \left(\frac{\partial^2 \overline{y}}{\partial y^2}\right)\frac{\overline{\delta}_{\overline{y}}}{2}\right] \Phi^k$$

where the factors can be denoted as L_1 and L_2 so that the AF representation is $L_1 L_2 \triangle^k \Phi = \text{RHS}$.

As it is written, the algorithm is implemented by sweeping implicitly in the x direction then in the y direction. The solution ($\triangle^k \Phi$) is attained in the two steps:

Step 1: L_1 TEMP = RHS

Step 2: $L_2 \triangle^k \Phi$ = TEMP

3.4.3 ADI scheme

The starting form of the difference equation is the same as for the AF scheme (Equation 3.34). The ADI scheme splits the calculation for Φ into two steps. In the first step, the x derivatives are treated implicitly at the iteration level $k + \frac{1}{2}$, while the y derivative terms are lagged. The provisional solution is denoted as $\Phi^{k+\frac{1}{2}}$. The second step obtains the solution, Φ^{k+1} by discretizing the y derivative terms implicitly at the iteration level $k + 1$ and using the x derivative terms at the $k + \frac{1}{2}$ level.

$$\left[I + \frac{h}{2}\left(\frac{\partial \overline{x}}{\partial x}\right)^2 \delta_{\overline{x}}^2 + \frac{h}{2}\left(\frac{\partial^2 \overline{x}}{\partial x^2}\right)\frac{\overline{\delta}_{\overline{x}}}{2}\right]\Phi_{i,j}^{k+\frac{1}{2}} = \frac{h}{2}S_{i,j}^k + \left[I - \frac{h}{2}\left(\frac{\partial \overline{y}}{\partial y}\right)^2 \delta_{\overline{y}}^2 - \frac{h}{2}\left(\frac{\partial^2 \overline{y}}{\partial y^2}\right)\frac{\overline{\delta}_{\overline{y}}}{2}\right]\Phi_{i,j}^k$$

$$\left[I + \frac{h}{2}\left(\frac{\partial \overline{y}}{\partial y}\right)^2 \delta_{\overline{y}}^2 + \frac{h}{2}\left(\frac{\partial^2 \overline{y}}{\partial y^2}\right)\frac{\overline{\delta}_{\overline{y}}}{2}\right]\Phi_{i,j}^{k+1} = \frac{h}{2}S_{i,j}^k + \left[I - \frac{h}{2}\left(\frac{\partial \overline{x}}{\partial x}\right)^2 \delta_{\overline{x}}^2 - \frac{h}{2}\left(\frac{\partial^2 \overline{x}}{\partial x^2}\right)\frac{\overline{\delta}_{\overline{x}}}{2}\right]\Phi_{i,j}^{k+\frac{1}{2}}$$

3.5 Poisson Solver Comparisons

An assessment of the two-dimensional Poisson solvers was made on test problems for the scalar and vector potentials. The test problems are from incompressible channel throughflow cases. The three solvers were tested on stretched and uniform grids with various aspect ratios. The L_2 norm of the error is used to compare the

convergence history for each method:

$$L_2 = \sqrt{\frac{\sum(\Phi^{k+1} - \Phi^k)^2}{\text{number of points}}}$$

However, the requirement used for a converged solution is

$$\frac{|\Phi^{k+1} - \Phi^k|}{\Phi_{\max}^{k+1}} \leq \epsilon \tag{3.35}$$

where Φ represents either potential and k is the iteration level. The tolerance used for the comparisons below is $\epsilon = 10^{-6}$. This rather strict tolerance can yield a decrease in the L_2 error by as much as 6 orders of magnitude. It was found that the scalar potential had to be obtained to this accuracy for reliable flow solutions.

All of the Poisson solvers were coded with the boundary conditions incorporated in the solution algorithm. The relaxation parameter used for the vectorized SOR method will be designated by ω. The range for ω is $0 < \omega < 2$. The relaxation parameter used for the AF and ADI schemes will be designated by h, the fictitious time step. The time derivative term which was added to the Poisson equation simulates a parabolic problem, $\Phi_t + \nabla^2\Phi = S$. The way this is written, marching is only permitted in the negative "time" direction. Therefore, a negative h was used to march the AF and ADI solvers. The need for a negative h is also evident in the numerical representation of these schemes since a negative h will add to the diagonal term of the coefficient matrix. The AF and ADI schemes were solved using a vectorized tridiagonal solver.

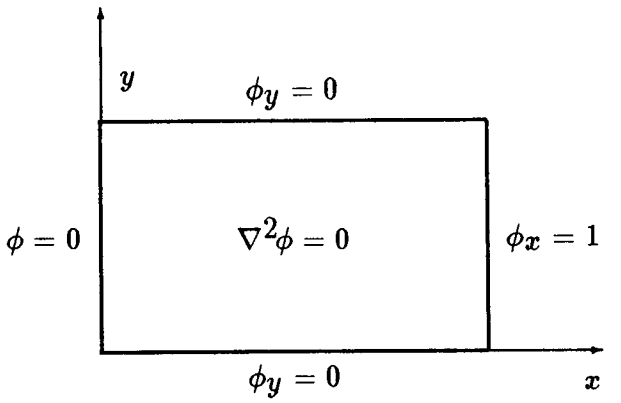

Figure 3.6: Scalar potential test problem

3.5.1 Scalar potential test problem

The scalar potential is given by the Poisson equation, $\nabla^2\phi = B$. For an incompressible flow the dilatation, B, is zero. The test problem for incompressible flow through a channel is then, $\nabla^2\phi = 0$, with boundary conditions as shown in Figure 3.6. The exact solution for this case is $\phi = x$ (notice that the problem is actually one-dimensional). This is a difficult problem to solve numerically due to the many Neumann boundary conditions. For incompressible problems, whether steady or unsteady, the equation for the scalar potential can be solved once and for all. An efficient solver may not seem important for the incompressible case. For a compressible flow, however, the dilatation field will be computed by a time marching method so the scalar potential will have to be solved as often as every global iteration. The cases to be studied in this report are mostly subsonic and the dilatation may be expected to be small. Therefore, the incompressible solution may be used as a starting solution for a compressible problem. Also, in some cases the dilatation may be so

small as to be treated as a perturbation of the solution to the incompressible problem. For these reasons and the fact that the exact solution is easily obtained for the incompressible case, the incompressible problem will be used to assess the solvers for the scalar potential.

The first comparison on the scalar potential test problem is with uniform grids. The aspect ratio, defined as $\alpha = \frac{\triangle y}{\triangle x}$, is varied for each case. The results for a 21×21 grid are shown in Table 3.1 and for a 41×41 grid in Table 3.2. The SOR method has trouble with this problem and requires an unusually high optimum relaxation parameter, ω. It can be seen from these results that the SOR method cannot compete with ADI or AF when the grid aspect ratio is far from 1. Stretched grids will be necessary in the solution of viscous problems so this immediately excludes the SOR method for use in solving for the scalar potential, especially when B is non-zero. Notice that the AF and ADI schemes solve the problem in the same number of iterations regardless of the cell aspect ratio. Also, the optimum relaxation parameter for AF and ADI can be reasonably predicted from the results shown in Tables 3.1 and 3.2 for $0 < \alpha \leq 1$. This is the most likely range of α for channel type viscous flow geometries. The optimum h for the AF scheme behaves like

$$h_\alpha = h_{\alpha_1}(1 + 64 \log \frac{1}{\alpha})$$

The optimum h for the ADI scheme behaves like

$$h_\alpha = h_{\alpha_1} \left(\frac{1}{\alpha}\right)^2$$

where h_{α_1} denotes the optimum h for a uniform grid with $\alpha = 1$. This can be used to get a reasonable estimate for the optimum relaxation parameter to use for a stretched grid.

Table 3.1: Poisson solver comparison on a 21 × 21 uniform grid

Uniform 21 × 21 grid							
	iterations to convergence			CPU time (s)			
method	α =1.0	0.1	0.01	1.0	0.1	0.01	MFLOP
SOR	109	611	7253	0.0634	0.349	4.11	39.7
AF	3	3	3	0.001645	0.001626	0.001667	54.1
ADI	138	138	138	0.1234	0.1265	0.1236	64.6

Optimum relaxation parameters (ω or h)			
method	α =1.0	0.1	0.01
SOR	1.898	1.9854	1.9991
AF	-160	-10240	-1310720
ADI	-0.0089	-0.89	-89

Testing these solvers for the scalar potential on a realistic grid with stretching gives the convergence behavior shown in Figure 3.7. The grid is stretched as shown in Figure 3.4. The cell aspect ratios for this stretched grid range from α = 0.4044–0.01265. Notice that the AF scheme converges over a very wide range of the relaxation parameter, h. In contrast, the SOR method has a very limited range of relaxation parameter which gives convergence in the thousands of iterations at the very fastest. The extremely good performance of the AF scheme on this test problem is incidental. It is explained by the fact that the exact solution for this test case is $\phi = x$, and the factorization error introduced in the AF scheme contains cross derivative terms. The cross derivatives and hence the factorization error therefore go to zero quickly. The optimum conditions for the solvers on this problem are shown in Table 3.3. The convergence history at the optimum conditions for the solvers is shown in Figure 3.8.

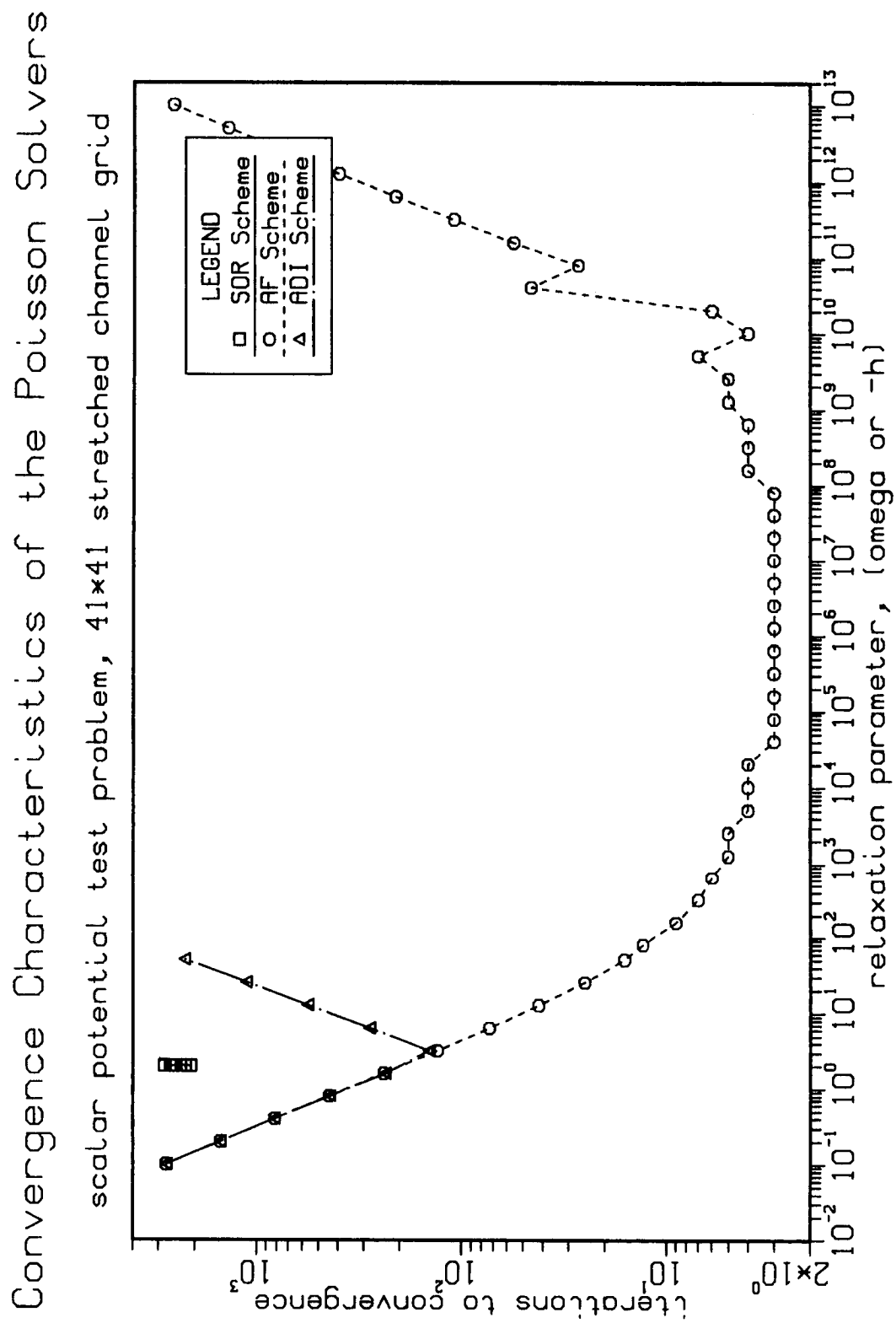

Figure 3.7: Convergence behavior of the Poisson solvers on the scalar potential test problem

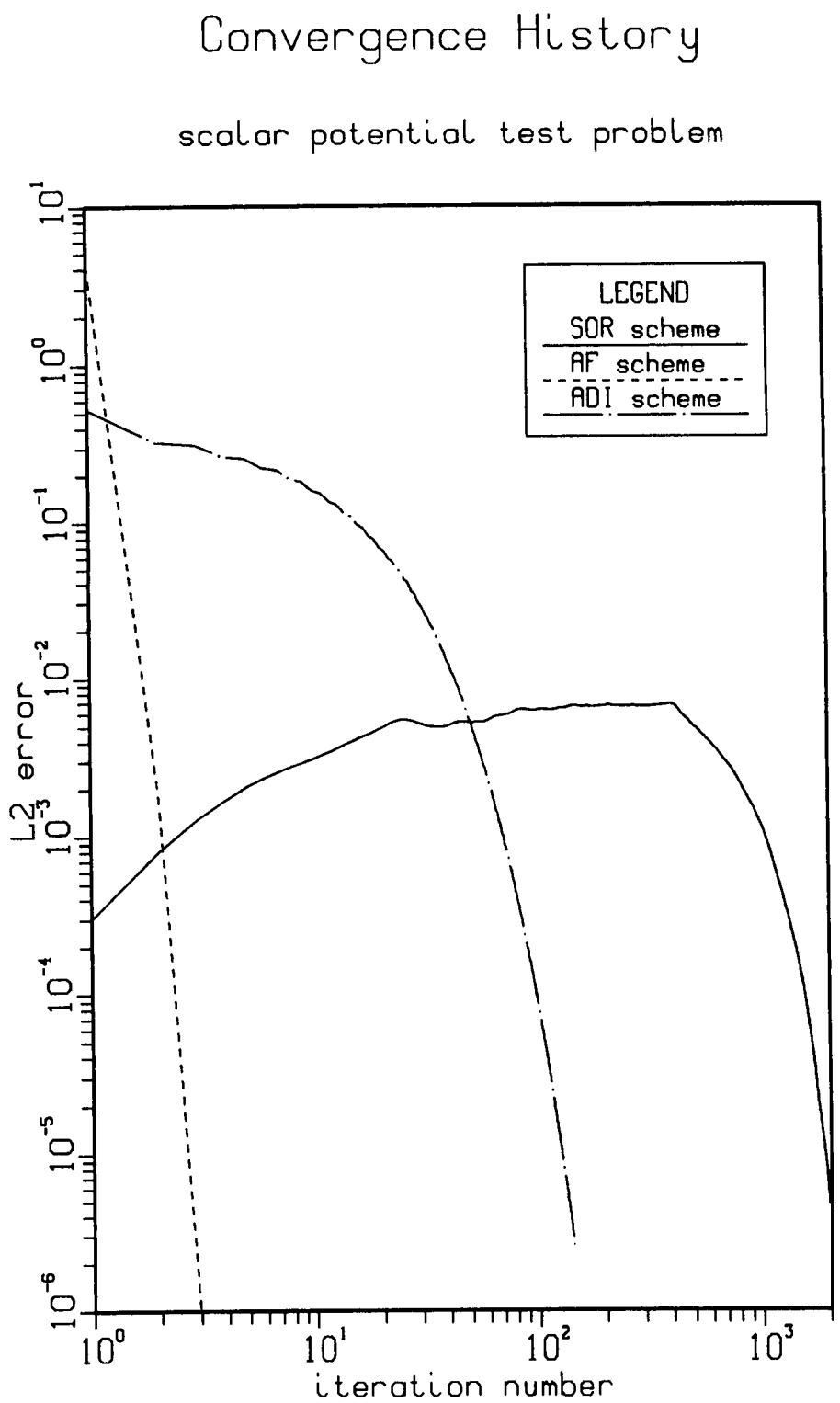

Figure 3.8: Convergence history for the scalar potential test problem

Table 3.2: Poisson solver comparison on a 41 × 41 uniform grid

Uniform 41 × 41 grid							
	iterations to convergence			CPU time (s)			
method	α =1.0	0.1	0.01	1.0	0.1	0.01	MFLOP
SOR	195	1260	8105	0.306	2.01	12.7	55.3
AF	3	3	3	0.00468	0.00475	0.00483	72.8
ADI	258	258	258	0.719	0.713	0.701	82.1

Optimum relaxation parameters (ω or h)			
method	α =1.0	0.1	0.01
SOR	1.9482	1.9925	1.99932
AF	-160	-10240	-1310720
ADI	-0.0045	-0.45	-45

With stretching, AF and ADI outperform the vectorized Gauss-Seidel easily on this problem. With non-zero dilatation and more complicated geometry the AF scheme is not expected to display such a tremendous advantage over ADI as in the example here. Also note the high relaxation parameter required for the fastest convergence by the SOR method.

Table 3.3: Poisson solver comparison on the scalar potential test problem

41 × 41 stretched channel grid				
method:	optimum relaxation param.	iterations to convergence	CPU time (s)	MFLOP
SOR	1.99644	1954	3.33	53.7
AF	-80000	3	0.00509	70.9
ADI	-3.0	142	0.4059	80.8

Table 3.4: Poisson solver comparison on the vector potential test problem

41×41 stretched channel grid				
method:	optimum relaxation param.	iterations to convergence	CPU time (s)	MFLOP
SOR	1.721	39	0.0629	54.1
AF	-0.003	35	0.0531	70.1
ADI	-0.00071	105	0.2143	82.2

3.5.2 Vector potential test problem

The vector potential test problem has been taken from an incompressible channel throughflow case. The equation and boundary conditions are shown in Figure 3.9. For these conditions, the SOR method did not exhibit extreme sensitivity to the grid aspect ratio and compared favorably with the AF and ADI methods. The Poisson equation for the vector potential, with three of the four boundaries having Dirichlet conditions, is easily handled by SOR using optimum relaxation parameters in the approximate range $1.2 < \omega < 1.8$. This equation must be solved as often as every global iteration for a rotational flow.

The vector potential equation was solved here on a 41×41 grid stretched as shown in Figure 3.4. A converged incompressible channel flow at $\mathrm{Re} = 300$ provided the vorticity source term. The behavior of the solvers over a range of relaxation parameters is given in Figure 3.10. The optimum conditions are given in Table 3.4 and the L_2 error for the optimum convergence of each solver is shown in Figure 3.11. In this case the AF and SOR schemes compare favorably in CPU time. In an actual flow solution, however, the ADI scheme has achieved convergence faster than AF or SOR when the vector potential solver is called at each global iteration.

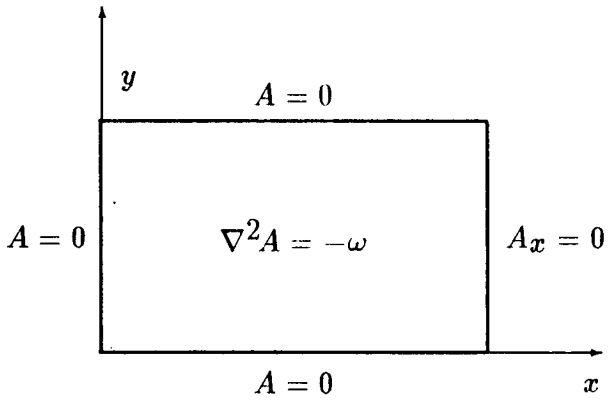

Figure 3.9: Vector potential test problem

3.5.3 Summary of Poisson solver experience

This was not meant to be an exhaustive study of methods for solving Poisson's equation numerically. Two very specific Poisson equation problems were studied to assess the numerical solvers. The results for the scalar potential test problem are particularly perplexing. The point SOR method performs poorly while the AF scheme is unbelievably fast. This is at least partly due to the one-dimensional nature of the scalar potential test problem. Point SOR cannot take advantage of the one-dimensional nature of the solution because it solves the domain pointwise. In the first iteration, point SOR creates a two-dimensional distribution. This happens because the solver cannot sense the information from opposite boundaries simultaneously. This is unlike the AF and ADI schemes which can immediately detect the influence of opposing boundaries in the implicit direction. The AF and ADI performance on the scalar potential test problem could be dependent on the sweep order, especially since the solution is one-dimensional. This was not tested, however. The biggest advantage

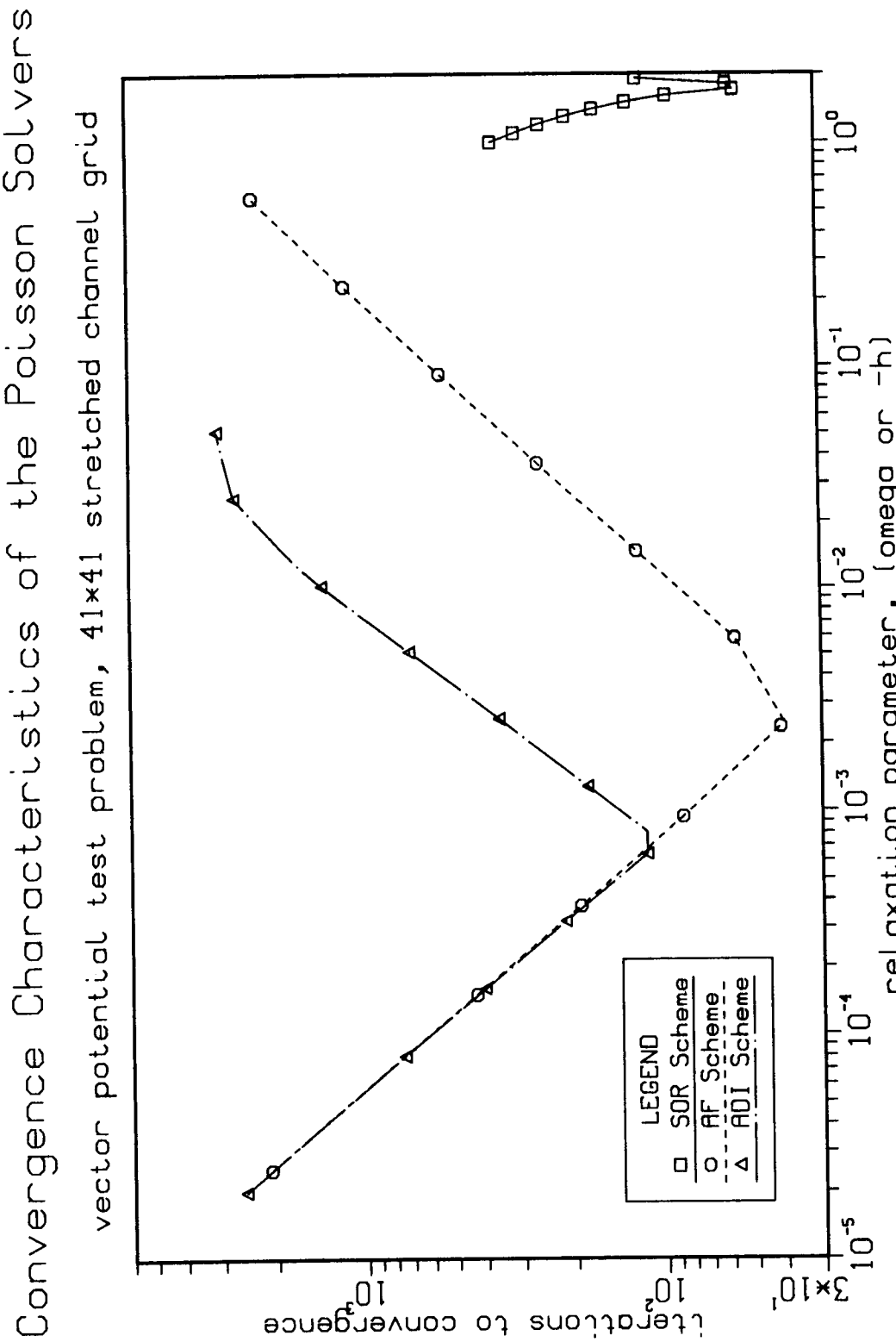

Figure 3.10: Convergence behavior of the Poisson solvers on the vector potential test problem

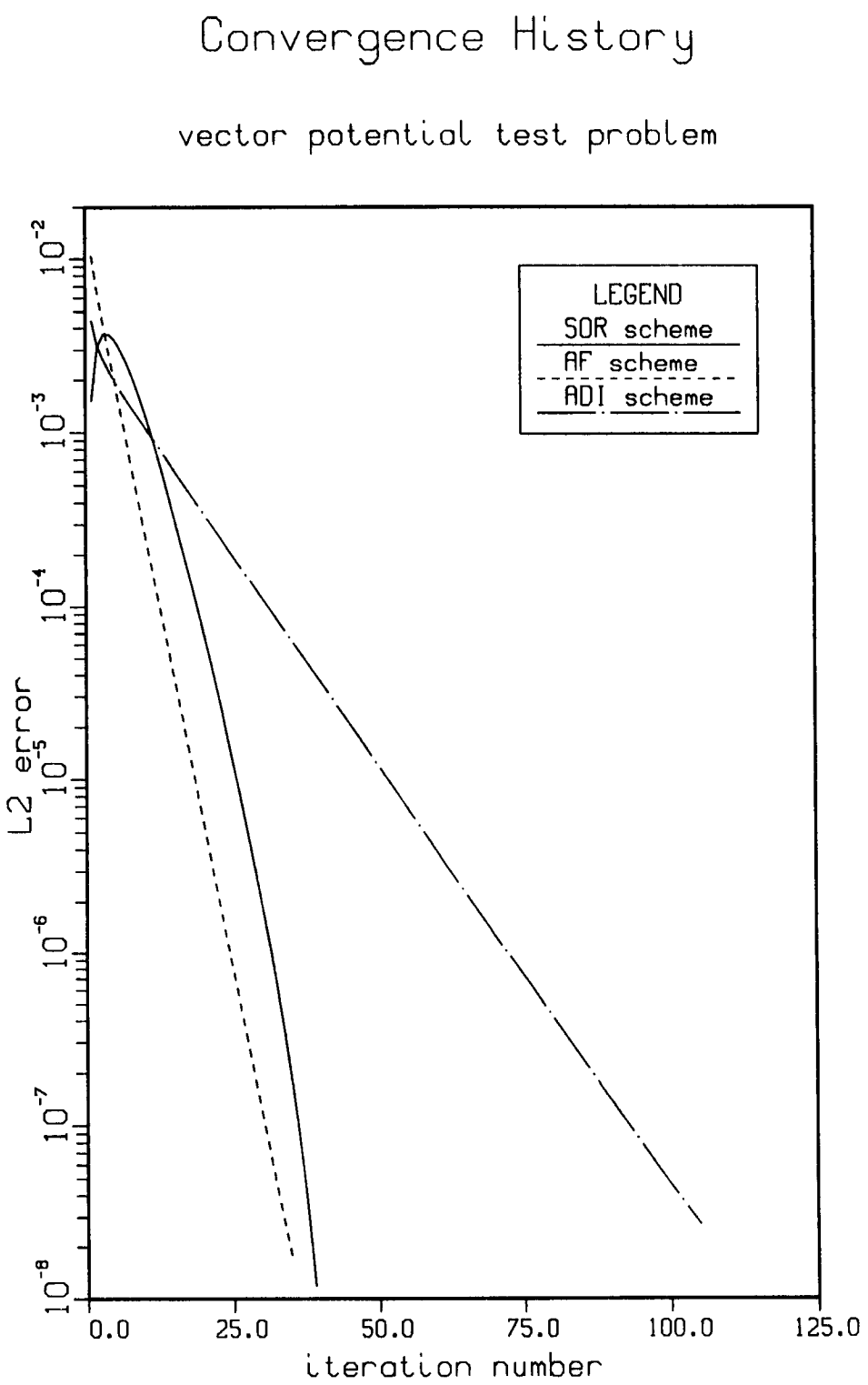

Figure 3.11: Convergence history for the vector potential test problem

for the AF scheme is that the factorization error is fortuitously zero because of the one-dimensional solution to the scalar potential test problem.

The vector potential problem doesn't offer the anomalies that the scalar potential problem does. Point SOR and the AF scheme are very competitive. The poorer performance of the ADI scheme is perhaps due to the fact that it is not written in delta form.

The apparent overall best solver for the Poisson equations in the dual potential method is the AF scheme. At the optimum convergence condition it converges in the fewest iterations and in the least CPU time. The AF scheme converges rapidly over a large range of relaxation parameter. This is important in getting started with a solution for a new problem. Almost any reasonable relaxation parameter, h, will work whereas some effort is required to get a fast solution by the SOR method. The ADI scheme is a consistent performer for the very different problems tested, but its optimum is not as fast as AF at its optimum for the conditions tested above. However, in actual flow calculations where the solver may be called at each global iteration the ADI scheme is always competitive. SOR is competitive when the boundary conditions are Dirichlet. It has a narrow band of relaxation parameter giving fast convergence as compared to either AF or ADI. This narrow band and steep slope (see Figures 3.7 and 3.10) is undesirable for predicting a good relaxation parameter to use on a new problem. One rule of thumb, however, is that the optimum relaxation parameter for SOR increases as the number of grid points increase on the same problem.

The above results and discussion suggest that the scalar potential Poisson equation is best handled by AF or ADI. The vector potential problem is best handled

by AF or SOR, though the ADI scheme was found to be competitive on actual flow problems. In actual use, the AF scheme was the easiest to code, followed by the ADI scheme and then the vectorized point SOR. All three schemes were fastest when the boundary condition information was incorporated into the algorithm. Not indicated in the simple test cases above is the fact that SOR loses any advantage on large grids. The computational effort for SOR is greater than for the AF or ADI schemes. Beyond some grid size then, the SOR scheme should be dropped in favor of the more efficient AF or ADI schemes. Pointwise iterative schemes tend to bias the solution depending on the sweep direction. The effect of sweep direction was not studied for the SOR scheme above.

For the three-dimensional (incompressible) problems the vector potential equation was solved using point SOR. The exact solution of the scalar potential was used so that the Poisson equation was not solved numerically.

3.6 Time Marching ADI Solver for the Transport Equations

The ADI scheme presented here is based on the one proposed by Douglas (1962). The transport equations for $\vec{\omega}, B, \rho$ and T in three dimensions may be written as

$$\frac{\partial S}{\partial t} = \left(\frac{s}{\mathrm{Re}}\frac{\partial^2 S}{\partial x^2} - u\frac{\partial S}{\partial x}\right) + \left(\frac{s}{\mathrm{Re}}\frac{\partial^2 S}{\partial y^2} - v\frac{\partial S}{\partial y}\right) + \left(\frac{s}{\mathrm{Re}}\frac{\partial^2 S}{\partial z^2} - w\frac{\partial S}{\partial z}\right) + cS - \theta$$

where S represents any of the dependent variables $\vec{\omega}, B, \rho$ or T and $\frac{s}{\mathrm{Re}}$ represents the coefficient of the diffusion terms. The term θ includes all remaining terms. The source term cS may be lumped into θ, but here it will be treated implicitly.

The above is written in a uniform Cartesian grid. A stretching transformation can easily be introduced, but would only clutter the development here. The stretching

transformations were used in Section 3.4 on the Poisson equations to provide an example of their use. Here, the complete three-dimensional algorithm on a uniform grid will be sufficiently complicated without metric terms included.

In the development of the ADI scheme for the transport equations, the following definitions will be used

$$x_i = i\,\triangle x, \quad y_j = j\,\triangle y, \quad z_k = k\,\triangle z \tag{3.36}$$

$$t^n = n\,\triangle t \tag{3.37}$$

$$\hat{\delta}_x = \alpha u \frac{\overline{\delta}_x}{2\,\triangle x} + (1-\alpha)\left[\frac{u+|u|}{2}\frac{\nabla_x}{\triangle x} + \frac{u-|u|}{2}\frac{\triangle_x}{\triangle x}\right] \tag{3.38}$$

$$\hat{\delta}_y = \alpha v \frac{\overline{\delta}_y}{2\,\triangle y} + (1-\alpha)\left[\frac{v+|v|}{2}\frac{\nabla_y}{\triangle y} + \frac{v-|v|}{2}\frac{\triangle_y}{\triangle y}\right] \tag{3.39}$$

$$\hat{\delta}_z = \alpha w \frac{\overline{\delta}_z}{2\,\triangle z} + (1-\alpha)\left[\frac{w+|w|}{2}\frac{\nabla_z}{\triangle z} + \frac{w-|w|}{2}\frac{\triangle_z}{\triangle z}\right] \tag{3.40}$$

where $\hat{\delta}_x, \hat{\delta}_y$ and $\hat{\delta}_z$ are hybrid finite-difference expressions for the convective terms $u\frac{\partial}{\partial x}, v\frac{\partial}{\partial y}$ and $w\frac{\partial}{\partial z}$, respectively. The weighting parameter, α, is in the range $0 \leq \alpha \leq 1$. A central difference formula is obtained for $\alpha = 1$ and an upwind formula for $\alpha = 0$. A different weighting parameter may be used for each direction. Note that this formula is written for the physical grid with uniform spacing. If there is stretching, the metrics are required.

The notation in Equations 3.38–3.40 could be confusing. It is important to note that the ∇ and $\triangle$ in the numerator are operators and the $\triangle$ in the denominator represents increments.

Let Q denote the finite-difference approximation to S and define:

$$Q^n = Q^n(i,j,k) = Q(x_i, y_j, z_k, t^n) \tag{3.41}$$

$$\delta_x Q^n = \left(\frac{s}{\mathrm{Re}} \frac{\delta_x^2}{(\triangle x)^2} - \hat{\delta}_x \right) Q^n \tag{3.42}$$

$$\delta_y Q^n = \left(\frac{s}{\mathrm{Re}} \frac{\delta_y^2}{(\triangle y)^2} - \hat{\delta}_y \right) Q^n \tag{3.43}$$

$$\delta_z Q^n = \left(\frac{s}{\mathrm{Re}} \frac{\delta_z^2}{(\triangle z)^2} - \hat{\delta}_z \right) Q^n \tag{3.44}$$

An alternating direction method for the solution of S may now be developed. From a known solution at time level n, a first estimate of the solution for time level $n+1$ may be obtained by evaluating half of the differences with respect to x at a provisional time level denoted by $n+1^*$ (Aziz and Hellums, 1967). The source term cS will also be evaluated at the implicit time level, so that

$$\begin{aligned} \frac{1}{2}\delta_x \left(Q^{n+1^*} + Q^n \right) + cQ^{n+1^*} &+ \delta_y Q^n + \delta_z Q^n \\ &= \left[\left(Q^{n+1^*} - Q^n \right) / \triangle t \right] + \theta \end{aligned} \tag{3.45}$$

where θ can be evaluated at $n, n+\frac{1}{2}$ or $n+1$. In the algorithm described here, θ was evaluated at the n time level only. In the following, one asterisk denotes the first approximation with more asterisks for successive estimates. Each successive estimate is made by evaluating half of the differences in one direction implicitly.

$$\begin{aligned} \frac{1}{2}\delta_x \left(Q^{n+1^*} + Q^n \right) &+ \frac{1}{2}\delta_y \left(Q^{n+1^{**}} + Q^n \right) + cQ^{n+1^{**}} + \delta_z Q^n \\ &= \left[\left(Q^{n+1^{**}} - Q^n \right) / \triangle t \right] + \theta \end{aligned} \tag{3.46}$$

$$\begin{aligned} \frac{1}{2}\delta_x \left(Q^{n+1^*} + Q^n \right) &+ \frac{1}{2}\delta_y \left(Q^{n+1^{**}} + Q^n \right) + \frac{1}{2}\delta_z \left(Q^{n+1} + Q^n \right) + cQ^{n+1} \\ &= \left[\left(Q^{n+1} - Q^n \right) / \triangle t \right] + \theta \end{aligned} \tag{3.47}$$

The equations 3.46 and 3.47 may be simplified by subtracting Equation 3.45 from 3.46 and Equation 3.46 from 3.47, respectively. The resulting algorithm, which

is second order accurate in time and up to second order accurate in space, is:

$$(\delta_x + 2c - 2/\triangle t)\, Q^{n+1^*} = -\left(\delta_x + 2\delta_y + 2\delta_z + 2/\triangle t\right) Q^n + 2\theta \quad (3.48)$$

$$\left(\delta_y + 2c - 2/\triangle t\right) Q^{n+1^{**}} = \delta_y Q^n + (2c - 2/\triangle t)\, Q^{n+1^*} \quad (3.49)$$

$$(\delta_z + 2c - 2/\triangle t)\, Q^{n+1} = \delta_z Q^n + (2c - 2/\triangle t)\, Q^{n+1^{**}} \quad (3.50)$$

This is the algorithm used for the three-dimensional solution. A tridiagonal system of linear algebraic equations for Q is solved three times to obtain Q^{n+1}. The first pass treats the x direction implicitly, the second treats y implicitly and the final pass treats z implicitly. The alternating direction implicit method used here reduces to the one proposed by Douglas if δ_x, δ_y and δ_z are replaced by δ_x^2, δ_y^2 and δ_z^2. Also, the non-linearities in the method of Douglas are included as part of θ only.

In two dimensions the provisional time level is $n + \frac{1}{2}$. The time increment is $\frac{\triangle t}{2}$ and the entire differences in one direction are taken at the implicit time level. In the (x, y) plane, the algorithm to solve the transport equations can be written

$$\frac{Q^{n+\frac{1}{2}} - Q^n}{\triangle t/2} = \delta_x Q^{n+\frac{1}{2}} + \delta_y Q^n + c Q^{n+\frac{1}{2}} - \theta \quad (3.51)$$

$$\frac{Q^{n+1} - Q^{n+\frac{1}{2}}}{\triangle t/2} = \delta_x Q^{n+\frac{1}{2}} + \delta_y Q^{n+1} + c Q^{n+1} - \theta \quad (3.52)$$

In a form ready to code, the two-dimensional algorithm becomes:

$$(2/\triangle t - \delta_x - c)\, Q^{n+\frac{1}{2}} = \left(\delta_y + 2/\triangle t\right) Q^n - \theta \quad (3.53)$$

$$\left(2/\triangle t - \delta_y - c\right) Q^{n+1} = (\delta_x + 2/\triangle t)\, Q^{n+\frac{1}{2}} - \theta \quad (3.54)$$

C-2

4. NUMERICAL RESULTS

4.1 Introduction

In this chapter the test cases will be discussed. It will be seen that the dual potential method can be used to solve the full potential equation, the Euler equations and the Navier-Stokes equations. The results generated from the dual potential code will be designated as DP in the comparisons.

4.2 Solution Strategy

The solution strategy has been broken down into three parts: an incompressible segment, a compressible segment and an iterative update. Certain steps are common to both the incompressible and compressible procedure. The incompressible segment and iterative update are always needed. The transport equations are solved uncoupled and iterated only once at each time level. The ADI scheme for the transport variables $(\vec{\omega}, B, T, \rho)$ provides up to second order accuracy in time and space. The Poisson equations may be iterated to convergence at each time level for a time accurate result. It is possible to limit the iterations on the Poisson equations to speed up the solution for a steady state case. The iterations may also be limited for a time accurate solution, but numerical experimentation is required.

The step by step calculation procedure is:

"Incompressible" segment:

1. Using known values (or assumed initial values at startup) for $\rho, \vec{\omega}, B, T, \vec{V}$ at all points at a given time level, n, solve the vorticity transport equation by an ADI method to give $\vec{\omega}^{n+1}$.

2. Solve the vector potential equation using the $n+1$ level vorticity. If the calculation is for a constant property, incompressible flow without heat transfer, go to step 7. Otherwise, continue with step number 3.

Compressible segment:

3. Solve the dilatation transport equation for B^{n+1} using n level source terms.

4. Solve the energy equation for T^{n+1} using n level source terms.

5. Solve the continuity equation for ρ^{n+1} using n level source terms.

6. Update the properties μ, k and p using $n+1$ level quantities.

Iterative update:

7. Compute the scalar potential, ϕ.

8. Update the velocity to time level $n+1$.

9. Solve for the vorticity boundary conditions at time level $n+1$.

10. Check for steady state convergence and stop if the solution has converged. Otherwise, transfer the just computed $n+1$ level results to the n level and repeat

the sequence from step 1 until steady state convergence or to some point of interest.

Though the segments above may be somewhat misnamed (since the equations listed under the "incompressible" segment must be solved for a compressible solution), the idea is to suggest possible solution strategies. One strategy which may be used to obtain a compressible flow solution is to start with a converged incompressible solution. The governing equations of the dual potential method are neatly segregated by incompressible/compressible or constant property/variable property criteria.

The convergence requirement is (usually) applied to all dependent variables. For example, a compressible case requires that $\vec{\omega}, B, T, \rho, \vec{A}$ and ϕ all satisfy the convergence requirement. The requirement is

$$\frac{|\Phi^{n+1} - \Phi^{n}|}{\Phi^{n+1}_{\max}} \leq \epsilon \tag{4.1}$$

applied at each point, where Φ represents any dependent variable and n is the iteration level or time level according to the nature of the variable. The tolerance is usually $\epsilon = 10^{-5}$. This type of convergence requirement is more stringent than an L_2 norm and more helpful for a self-interrogating scheme to determine where to concentrate computational effort and where to avoid computation. In particular, for the variables used in this method, the vorticity and dilatation can be negligibly small. For example, in external boundary-layer flows the vorticity and dilatation can be expected to approach zero at some distance away from a disturbance. This point by point error checking, normalized on a representative maximum field value, can indicate that the largest errors are near the disturbance and initiate a check to see if function values, such as B or $\vec{\omega}$, are small at some distance away. If this is the case, the code can

automatically reduce the computational field for that variable. The more common L_2 measure of error that other investigators use has been found to be somewhat deceiving. Convergence in the L_2 sense may not satisfy convergence in the absolute sense above. Since the L_2 measurement averages out the error contribution of each point, it doesn't identify particular locations of large error. That is, the L_2 measurement may satisfy its convergence criterion and yet there may be isolated areas of large and unacceptable error. Hence L_2 convergence may have little to do with the accuracy attained by the solution.

Regarding the actual tolerance used in calculations, it has been observed that the vector potential error tolerance may be loosened to speed the solution with no negative effects. The scalar potential, on the other hand, requires a tight tolerance in all cases. The potentials, given by solutions of the Poisson equations, can be very time consuming to calculate.

4.3 Two-dimensional Cases

The dual potential formulation is rather thoroughly tested in two dimensions. Example problems will be computed for incompressible and compressible flows. A potential flow solution will be computed for the flow about a thin biconvex airfoil (or bump on an inviscid wall). An unsteady calculation for the compressible flow about a thickening airfoil will also be discussed. Steady viscous flows will be computed for the channel inlet case and flat plate boundary layer. The results with discussion follow.

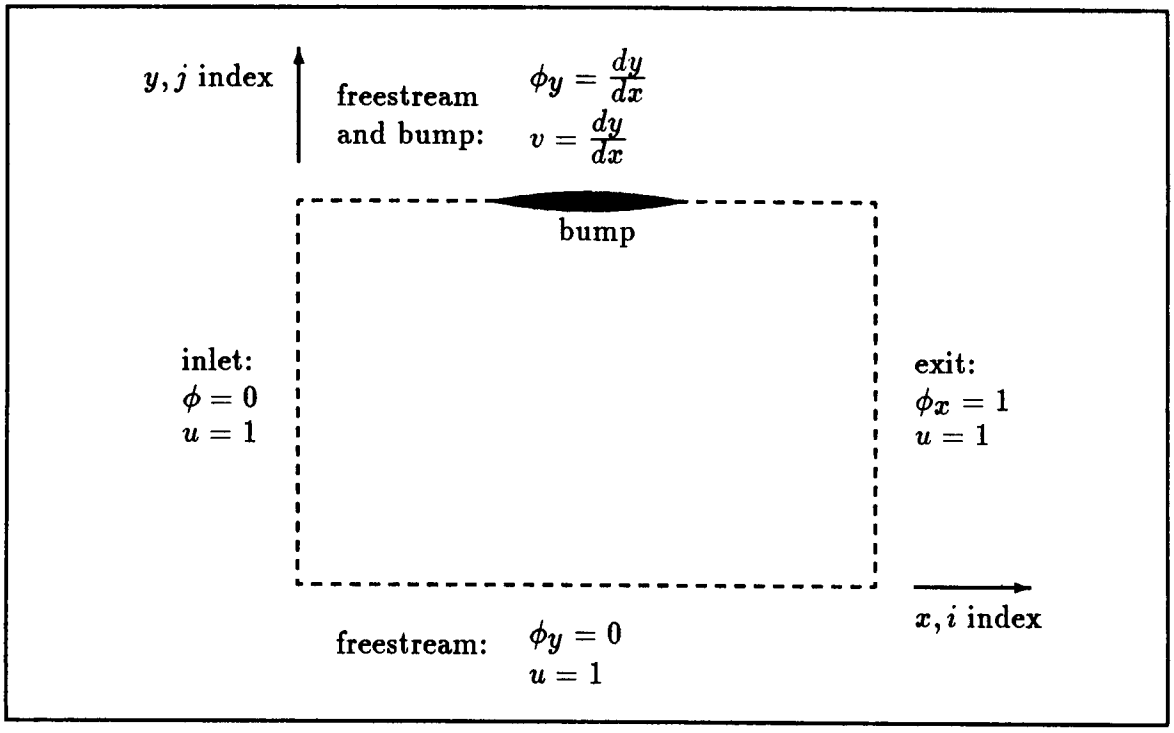

Figure 4.1: Boundary conditions for laminar incompressible irrotational flow over a bump

4.3.1 Incompressible flow

4.3.1.1 Steady irrotational inviscid flow

Bump cases This test case and the corresponding compressible test cases for the flow over thin biconvex airfoils were included to demonstrate the calculation of simple irrotational inviscid flows. By considering only very thin airfoils, the small disturbance theory boundary conditions may be used. The geometry is therefore simple so that the dual potential formulation can be tested with fewer complications. Also, velocity potential and stream function solutions are readily obtainable for com-

parison. The biconvex airfoil may also be considered to be a thin bump on an inviscid wall. Airfoil and bump will be used interchangeably in referring to the bump test cases.

Problems of this type were solved extensively in the 1970s as models for the flow over helicopter blades (Ballhaus and Steger 1975; Beam and Ballhaus 1975). The bump is generated by blowing according to the small disturbance theory (Ashley and Landahl 1965). The airfoil in this case is very thin so that the freestream is only slightly perturbed by the presence of the body. Tangency is then imposed by requiring the resultant flow velocity at the body to be tangent to the thin body. Since the body is assumed to be very thin, the tangency condition can be applied at the airfoil chord line. This permits solutions to this problem to be made on a simple Cartesian grid. The assumptions for this case are steady, irrotational, inviscid, isentropic flow.

A sketch of the problem is shown in Figure 4.1. This problem may be solved in many ways using potential methods. Only one of the potentials in the dual potential method is required to solve this flow. Either one of the potentials can be used with little modification to the code. Small perturbation approximations will be used in this problem. The velocity components will be represented by

$$u = U_\infty + \tilde{u} \tag{4.2}$$

$$v = \tilde{v} \tag{4.3}$$

where $\tilde{u}$ and $\tilde{v}$ are perturbation quantities. These are all non-dimensional quantities normalized on the freestream velocity so that $U_\infty = 1.0$ and the perturbation quantities are assumed to be much less than 1.

The scalar potential, ϕ, may be used without modification for a potential flow

solution to this problem. The definition of the scalar potential is designed to satisfy the irrotationality condition automatically:

$$\phi = ux + vy \tag{4.4}$$

Conservation of mass is then satisfied by the solution of

$$\nabla^2\phi = 0 \tag{4.5}$$

The boundary conditions for a solution of this case using the scalar potential are shown in Figure 4.1.

If the vector potential, A, is used it is actually treated as the stream function for irrotational incompressible flow. This is a redefinition of the vector potential that is used elsewhere in this development. The similarity of the stream function with the vector potential is evident in the Poisson type of equation and Dirichlet boundary conditions. This permits the single two-dimensional dual potential code to solve this problem using either potential. Let A be the stream function in the following development. The stream function is designed to satisfy continuity automatically:

$$A_x = u \tag{4.6}$$

$$A_y = -v \tag{4.7}$$

The irrotationality condition is then written

$$\nabla^2 A = 0 \tag{4.8}$$

The boundary conditions on the stream function are all Dirichlet with $A = y$. For a compressible flow solution the vector potential requires a boundary condition modification to emulate the stream function.

The scalar potential is perhaps the most natural potential function to use for this case since there is no need to change its definition. It simply assumes the role of the traditional velocity potential.

Two different bump geometries were computed by the dual potential code. Solutions have been computed for the parabolic arc and the sine wave arc bumps. The parabolic arc has stagnation points at the leading and trailing edges. The sine wave bump was included to avoid stagnation points in the early development of the compressible code. The bumps are described using the small disturbance theory boundary conditions. That is, the bumps are generated by blowing through the boundary. The parabolic and sine wave arcs are described by;

parabolic arc:

$$y = 2\tau x(1-x) \tag{4.9}$$

sine wave arc:

$$y = \frac{\mathrm{PP}}{2}[1-\cos(2\pi x)] \tag{4.10}$$

for $0 \leq x \leq 1$. $\tau/2$ is the height of the parabolic arc and PP (for peak-to-peak) is the height of the sine wave arc. The sine wave amplitude is $\frac{\mathrm{PP}}{2}$, but the sine wave arc is used so that the bump meets the boundary with zero slope. The bump geometries are indicated in Figure 4.2. The computational domain was chosen to be three chord lengths in the streamwise direction and two chord lengths away from the airfoil to the far field. The airfoil is centered in the streamwise direction. A uniform Cartesian grid was used for the results presented here with 61 streamwise and 41 transverse points.

The airfoil surface will be defined by the flow tangency condition imposed along the mean surface of the body. Flow tangency at the airfoil surface can be represented

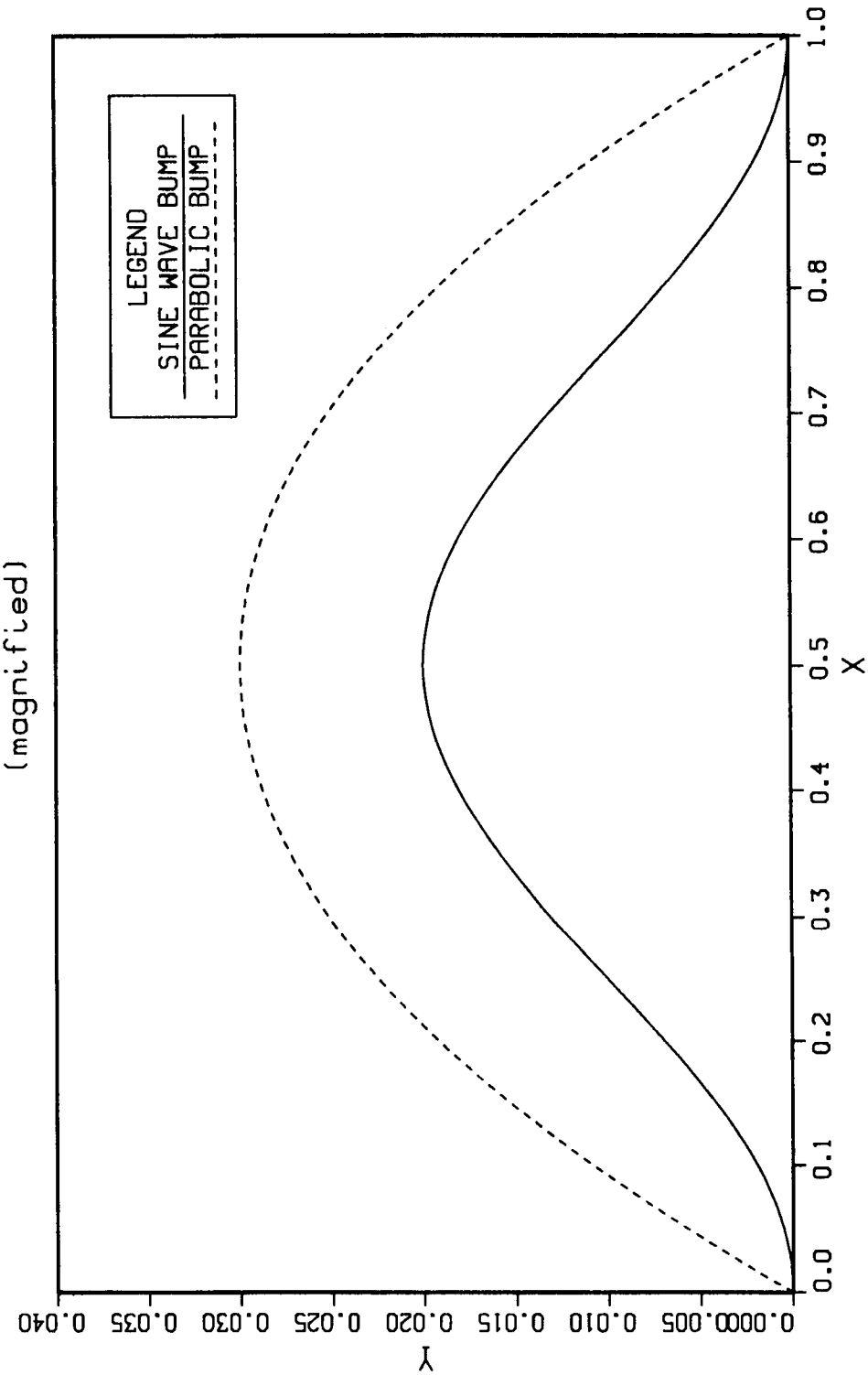

Figure 4.2: Parabolic arc and sine wave bumps

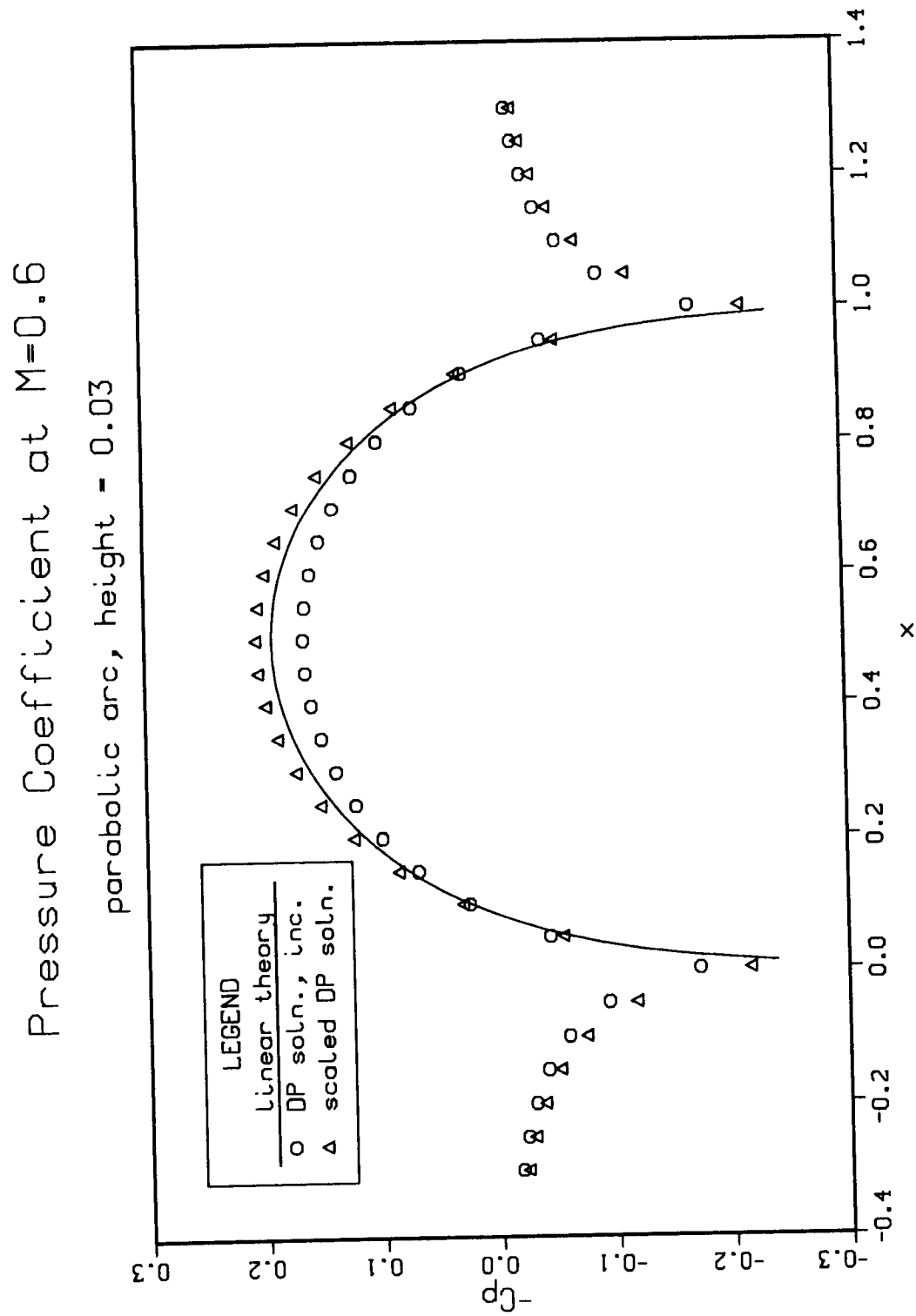

Figure 4.3: Pressure coefficient for $M_\infty = 0.6$ flow over a parabolic arc airfoil

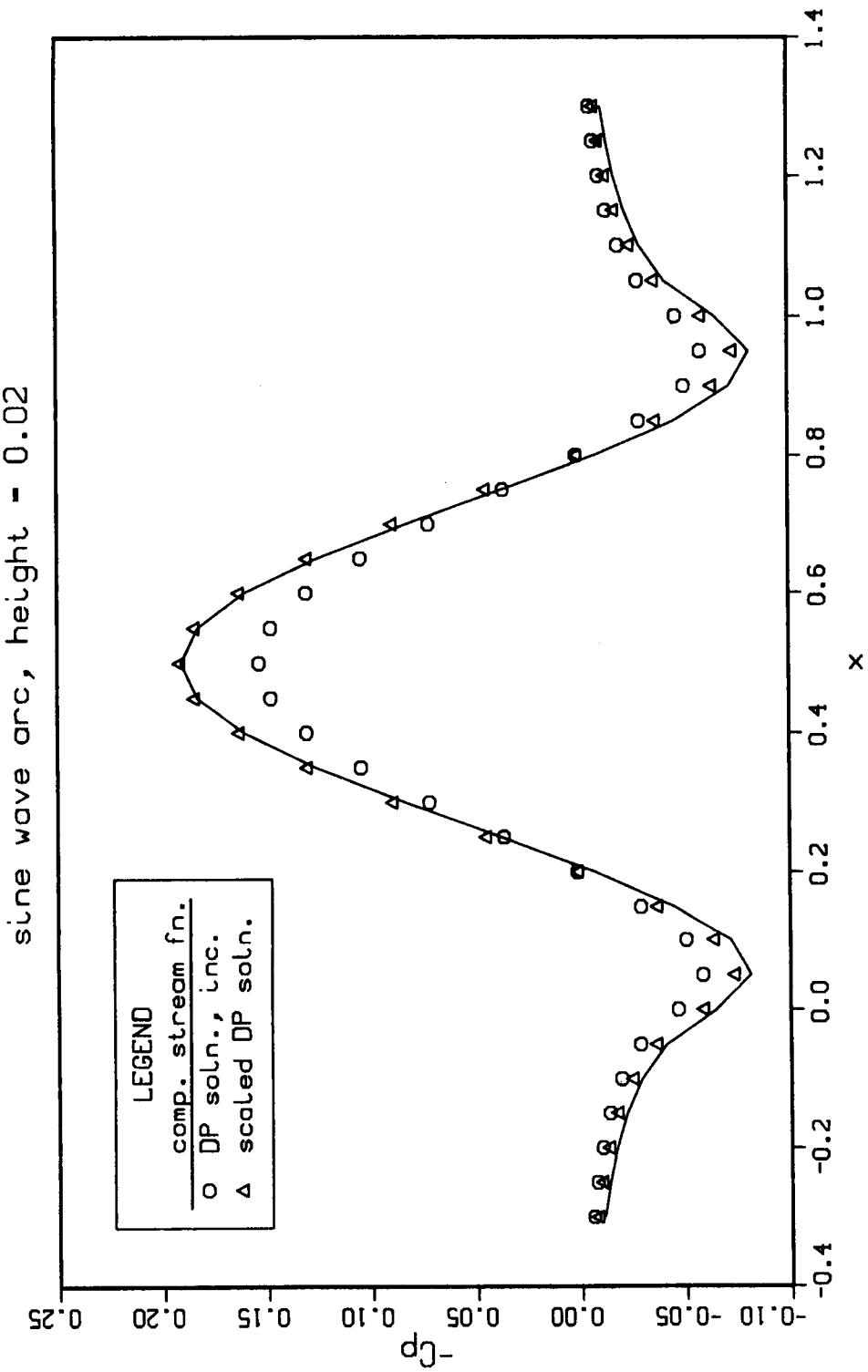

Figure 4.4: Pressure coefficient for $M_\infty = 0.6$ flow over a sine wave arc airfoil

by

$$\left.\frac{dy}{dx}\right|_{\text{surface}} = \frac{\tilde{v}}{U_\infty + \tilde{u}} = \frac{\tilde{v}}{U_\infty\left(1 + \frac{\tilde{u}}{U_\infty}\right)} \approx \frac{\tilde{v}}{U_\infty}\left(1 - \frac{\tilde{u}}{U_\infty}\right) \tag{4.11}$$

In the above equation, $\frac{\tilde{u}}{U_\infty}$ is small compared to 1 so it may be dropped leaving the following approximation for the tangency boundary condition:

$$\left.\frac{dy}{dx}\right|_{\text{surface}} \approx \left.\frac{\tilde{v}}{U_\infty}\right|_{\text{surface}} = \left.\phi_y\right|_{\text{surface}} \quad \text{for } U_\infty = 1. \tag{4.12}$$

Finally, the tangency condition is applied at the mean surface of the airfoil so that

$$\left.\frac{dy}{dx}\right|_{\text{surface}} \approx \left.\frac{\tilde{v}}{U_\infty}\right|_{\text{surface}} = \left.\phi_y\right|_{\text{grid boundary}} \quad \text{for } U_\infty = 1. \tag{4.13}$$

This small perturbation type of boundary condition does not require the use of a body-oriented grid and is therefore very easy to implement. The above development has been for the scalar potential. As used in the test problem, the boundary condition on the scalar potential is

$$\phi_y = \begin{cases} \left.\frac{dy}{dx}\right|_{\text{surface}} & 0 \le x \le 1 \\ 0 & \text{otherwise} \end{cases} \tag{4.14}$$

where the solution domain is $-1 \le x \le 2$.

A similar development for the stream function gives the following small perturbation boundary condition

$$A = \begin{cases} y + \text{local airfoil height} & 0 \le x \le 1 \\ y & \text{otherwise} \end{cases} \tag{4.15}$$

The airfoil height referred to here is the half thickness of the airfoil at a particular x position.

The pressure coefficient is defined as

$$C_p = \frac{p - p_\infty}{\frac{1}{2}\rho_\infty V_\infty^2} \tag{4.16}$$

where $V_\infty^2 = u_\infty^2 + v_\infty^2$. The pressure coefficient for the bump cases is computed by an approximation to the definition

$$C_p = \frac{p - p_\infty}{\frac{1}{2}\rho_\infty V_\infty^2} \approx \frac{-2\tilde{u}}{U_\infty} \tag{4.17}$$

This approximation is obtained by dropping squares of the perturbation velocity components. In terms of the scalar potential or stream function, the pressure coefficient is approximated by

$$C_p \approx 2\left(1 - \phi_x\right) = 2\left(1 - A_y\right) \tag{4.18}$$

where $U_\infty = 1$.

The pressure coefficient for an inviscid and incompressible calculation of M = 0.6 flow over a 6% thick ($\tau = 0.06$) parabolic arc airfoil is shown in Figure 4.3. This result was computed solely to check the DP code in an incompressible calculation. The linear theory result plotted in Figure 4.3 is obtained for the parabolic arc airfoil by a method given in Ashley and Landahl (1965). That method gives the pressure coefficient for thin airfoils in incompressible flow. It can be shown that the pressure coefficient for a subsonic compressible flow is related to the pressure coefficient for incompressible flow by the factor $\beta = \sqrt{1 - \mathrm{M}_\infty^2}$:

$$\mathrm{C}_p = \frac{1}{\beta}\left(\mathrm{C}_p\right)_{\text{incompressible}} \tag{4.19}$$

Hence, the DP incompressible flow result in Figure 4.3 is scaled to a compressible result using Equation 4.19 just as the linear theory result is scaled from Ashley and

Landahl's incompressible calculation. A compressible stream function solution on the same 61 × 41 grid lies right on the scaled incompressible solution for the parabolic arc airfoil case. A similar result is shown for a 4% thick (PP = 0.02) sine wave arc airfoil in Figure 4.4. The incompressible solution using the dual potential code scales to the compressible result of a stream function solution. The computed incompressible solutions here have been scaled to the compressible result for comparison with calculations obtained from available compressible stream function codes.

4.3.1.2 Steady viscous flow

Channel inlet The two-dimensional channel inlet flow has been computed by many researchers (Wang and Longwell 1964; McDonald et al. 1972; Tenpas and Pletcher 1987). This case provides the first test of the vorticity transport equation and the vector potential solver. Also, stretched grids must be used in this problem for the first time to adequately resolve the inlet features. This problem will be a stepping stone to the heat transfer cases presented subsequently. It will be seen that the dual potential formulation can solve this flow problem for either a rotational or irrotational inlet condition.

The developing flow in a two-dimensional inlet has been computed for Re = 10 to 7500. The Reynolds number is based on the hydraulic diameter,

$$D_{\text{hyd}} = \frac{4 \times \text{cross-sectional area}}{\text{wetted perimeter}}$$

For a two-dimensional passage the hydraulic diameter is twice the wall spacing, h. The physical distances, x and y, for the two-dimensional channel cases are non-dimensionalized by the hydraulic diameter. The non-dimensional wall separation

distance is then $y_{max} = \frac{1}{2}$. Note that y for a two-dimensional channel problem will then be in the range $0 \leq y \leq \frac{1}{2}$ for the results plotted here from wall to wall. The geometry and boundary conditions are given in Figure 3.3. A uniform inlet velocity profile was prescribed. The inlet conditions can be made to correspond to a rotational or irrotational inlet flow. The irrotational inlet may be more realistic for experimental models with a rounded entrance (Van Dyke 1970).

The centerline velocity development is shown in Figure 4.5 for Re = 300. Good agreement is obtained for both the irrotational and rotational inlet conditions. Note that the x used in the axis label, $x/(\text{Re}*\text{Dhyd})*16$, in Figure 4.5 is dimensional. This was done to form the dimensionless group used by other researchers. The multiplier of 16 is used to give the same x axis range as others who have used the channel half height instead of the hydraulic diameter in the Reynolds number and dimensionless axial length.

For the results shown in Figure 4.5, all convective terms have been central differenced. Refining the grid for the irrotational inlet case shows that the numerical algorithm is clearly better than first order accurate but is not second order accurate on a stretched grid. The truncation error is estimated to be approximately $\mathcal{O}(\triangle x)^{1.6}$ where $\triangle x$ represents the x and y grid spacing here. (The solution for the 41×41 grid is approximately one-third of the way vertically between the 21×21 grid solution and the 81×81 grid solution). The need to upwind difference the convective terms becomes necessary as the Reynolds number increases in order to maintain stability.

The skin-friction development is shown in Figure 4.6 for the rotational and irrotational inlet conditions. Both computational results asymptote to the expected

fully-developed $C_f \mathrm{Re} = 24.0$ for the two-dimensional channel.

The complete Navier-Stokes equations for incompressible flow were used for these calculations. It is permissible to drop the streamwise second derivatives for high Reynolds number flows. Dropping the ω_{xx} terms causes the flow to develop slightly faster (i.e., in a shorter x distance).

Constant property heat transfer Heat transfer cases have been computed for constant properties. The results are in good agreement with published computational results (Schade and McEligot 1971; Hwang and Fan 1964). Both references above obtained solutions for this problem utilizing boundary-layer approximations.

The heat transfer cases can be classified as in Figure 4.7. As shown in the figure, there are three basic types of problems for specified wall temperature and/or wall heat flux for the parallel plates geometry. Test cases will be computed for wall conditions that are constant with x. The most detailed presentation will be for the constant wall temperature case.

Any combination of the wall boundary conditions in Figure 4.7 can be solved by the dual potential code. The boundary conditions may be functions of x.

The notation used in this heat transfer section is the same as used by Shah and London (1978) and Kays and Crawford (1980). The x distance in the following heat transfer results is referred to the Peclet number as in Shah and London (1978). Therefore,

$$x^* = \frac{x}{\mathrm{Pe}}, \quad \mathrm{Pe} = \mathrm{RePr}$$

A quadratic fit to the computed temperature profile was used to compute the local

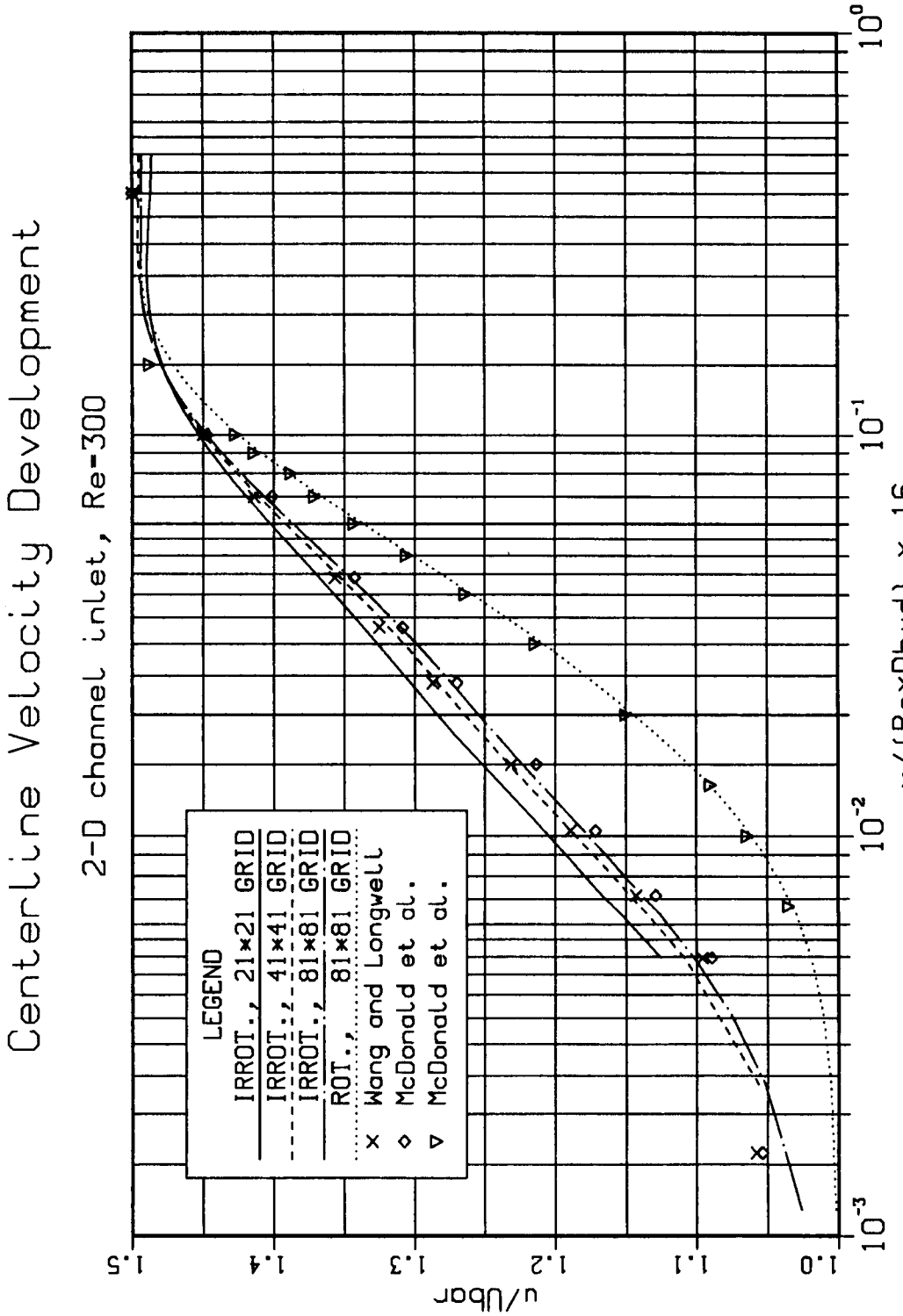

Figure 4.5: Centerline velocity development for a 2-D channel inlet

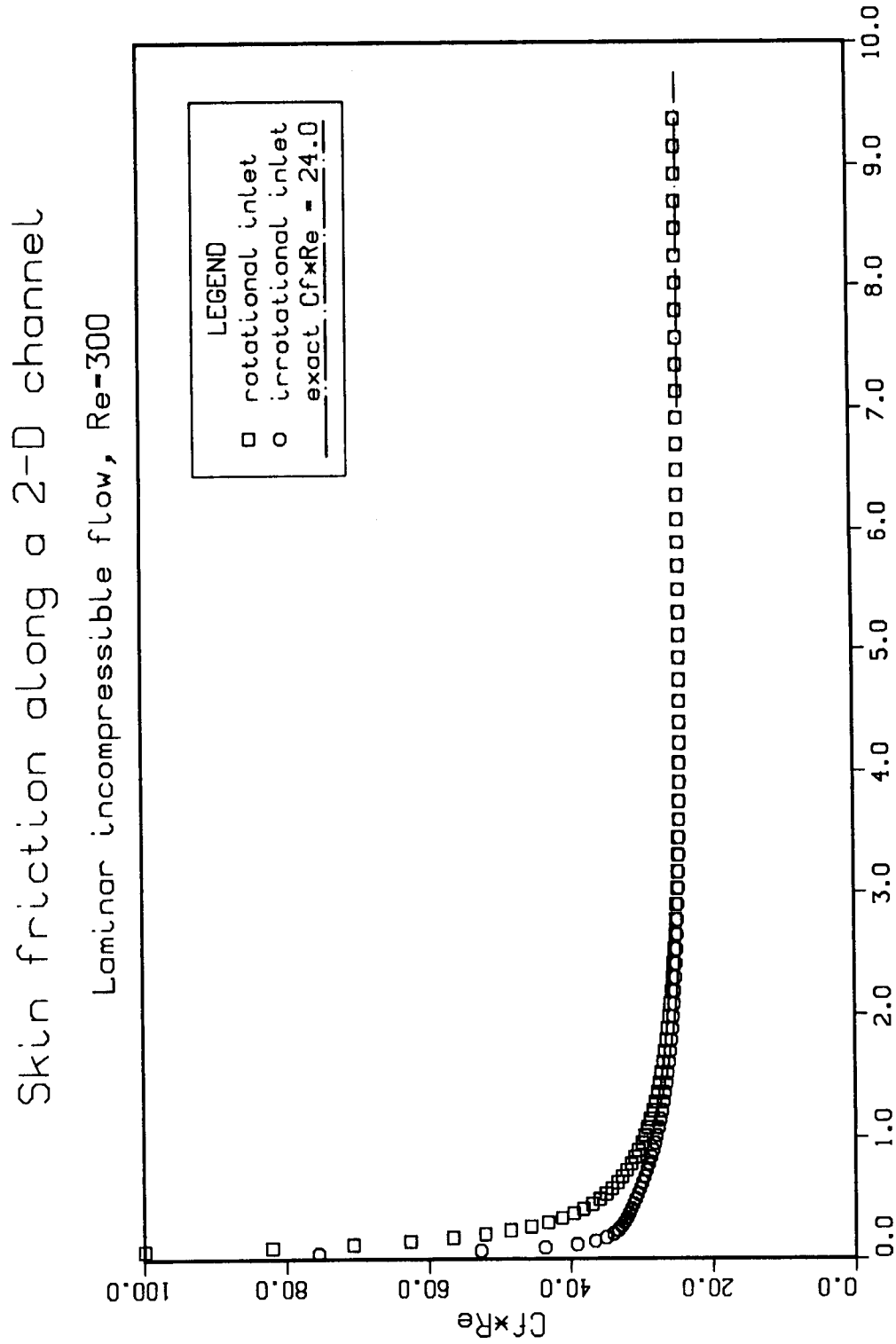

Figure 4.6: Skin-friction development along a 2-D channel

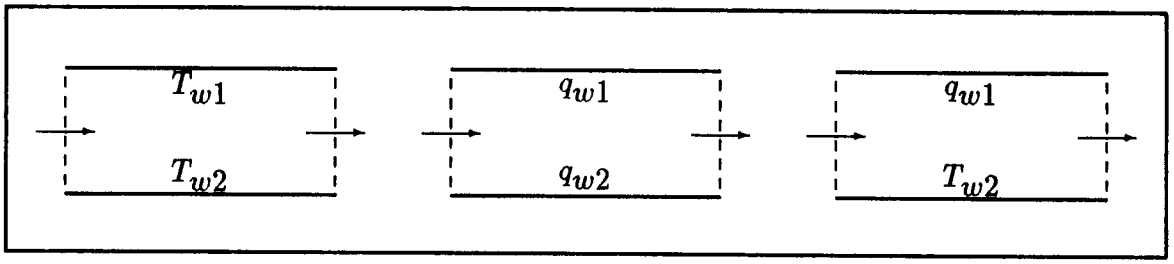

Figure 4.7: Basic wall heat transfer boundary conditions

Nusselt number, where

$$\mathrm{Nu} = \frac{hD_{\mathrm{hyd}}}{k} \tag{4.20}$$

The Nusselt number was computed from the temperature solution. The notation of Kays and Crawford (1980) will be used in the following derivation. Specifically, an overdot indicates a time derivative, the subscript o will mean at the wall and a double prime ($''$) will indicate per unit area. The wall heat flux can then be written as

$$\dot{q}_o'' = h(T_{\mathrm{wall}} - T_{\mathrm{mean}}) \tag{4.21}$$

$$\dot{q}_o'' = -k\frac{\partial T}{\partial y}\bigg|_{\mathrm{wall}} \tag{4.22}$$

The wall heat flux is given by either the convection heat transfer equation or the wall conduction equation as written above. These two must be equal, so

$$h(T_{\mathrm{wall}} - T_{\mathrm{mean}}) = -k\frac{\partial T}{\partial y}\bigg|_{\mathrm{wall}} \tag{4.23}$$

The definition of Nusselt number from Equation 4.20 can then easily be written in terms of the computed temperatures by rearranging Equation 4.23. The result is

$$\mathrm{Nu} = \frac{hD_{\mathrm{hyd}}}{k} = \frac{-\frac{\partial T}{\partial y}\Big|_{\mathrm{wall}} D_{\mathrm{hyd}}}{(T_{\mathrm{wall}} - T_{\mathrm{mean}})} \tag{4.24}$$

where T_{mean} is the local mixed mean fluid temperature. It is also sometimes referred to as the bulk fluid temperature or the mixing cup temperature. T_{mean} is computed as the single (mean) temperature for the axial convection that equals the integrated axial convected thermal energy rate. That is,

$$\dot{m} c_p T_{\text{mean}} = (\rho A_C V)\, c_p T_{\text{mean}} \tag{4.25}$$

$$= \int_{A_C} \rho u c_p T \, dA_C \tag{4.26}$$

where $\dot{m}$ is the mass flow rate, A_C is the cross-sectional area at the x position for which T_{mean} is being computed and V is the mean velocity. Therefore,

$$T_{\text{mean}} = \frac{\int_{A_C} uT \, dA_C}{\int_{A_C} u \, dA_C} \tag{4.27}$$

The constant property cases to be presented have fully-developed temperature solutions which are self-similar. The self-similar temperature function is

$$\Theta = \frac{T_{\text{wall}} - T(i,j)}{T_{\text{wall}} - T_{\text{mean}}} \tag{4.28}$$

The variable, Θ, will be referred to as the temperature parameter in the following results. It is defined and used in the dual potential code to indicate when the temperature solution has become fully developed. This is in addition to an error tolerance on the temperature at each point.

It is important to pack many points close to the channel inlet, so the grid was stretched until grid independent solutions were obtained for a 41×41 grid. Those stretching parameters were then used for further grid refinement by adding points. The length of channel was also chosen so as not to interfere with the natural flow development. The fully-developed skin friction for these two-dimensional cases is

$C_f \mathrm{Re} = 24.0$ as computed analytically and by the dual potential code. It is interesting to note that all of the results for the heat transfer cases were computed for the rotational inlet condition. This is the inlet condition used by others reporting computational results. Van Dyke (1970) reports that the irrotational inlet condition may be more realistic for comparison with experimental models having a rounded entrance. The dual potential code can easily handle either a rotational or irrotational inlet condition.

Constant wall temperature Some comparisons of constant property heat transfer results for constant and equal wall temperatures are shown in Figures 4.8 and 4.9. The published results of Schade and McEligot (1971) are represented in each figure as a solid line. The present results using the dual potential code are indicated by symbols. The grid size for the dual potential results is indicated in the figure legend. The Reynolds number based on the hydraulic diameter is 150 for the present results in Figure 4.8 and 300 for the present results in Figure 4.9. Schade and McEligot use the boundary-layer assumptions and drop their numerical results for approximately the first 20 points in x. The dual potential results for the 161×81 grid have only the first 4 points dropped. There is nothing wrong with those 4 points, they are just well ahead of the data presented in the literature. The dual potential incompressible code makes no assumptions other than constant properties. This accounts for the Nusselt number discrepancy between the two solutions near the inlet. The dual potential code predicts a higher heat transfer rate near the inlet than the results of Schade and McEligot. Figures 4.8 and 4.9 show that there is a Peclet number dependence for the Nusselt number. For the range of results presented, a

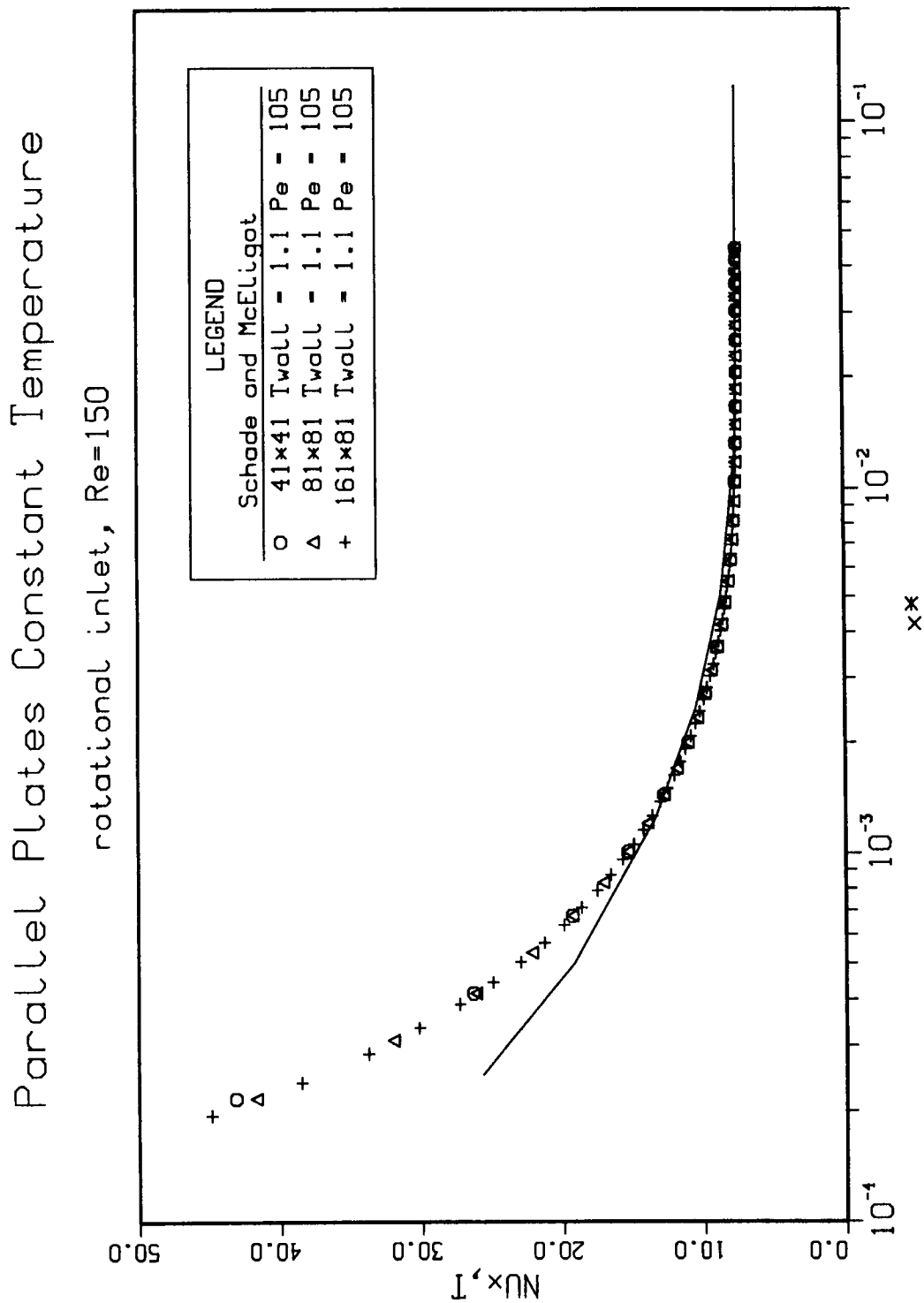

Figure 4.8: Local Nusselt number for flow between parallel plates at constant temperature. Pe=105. Asymptotic Nu=7.541

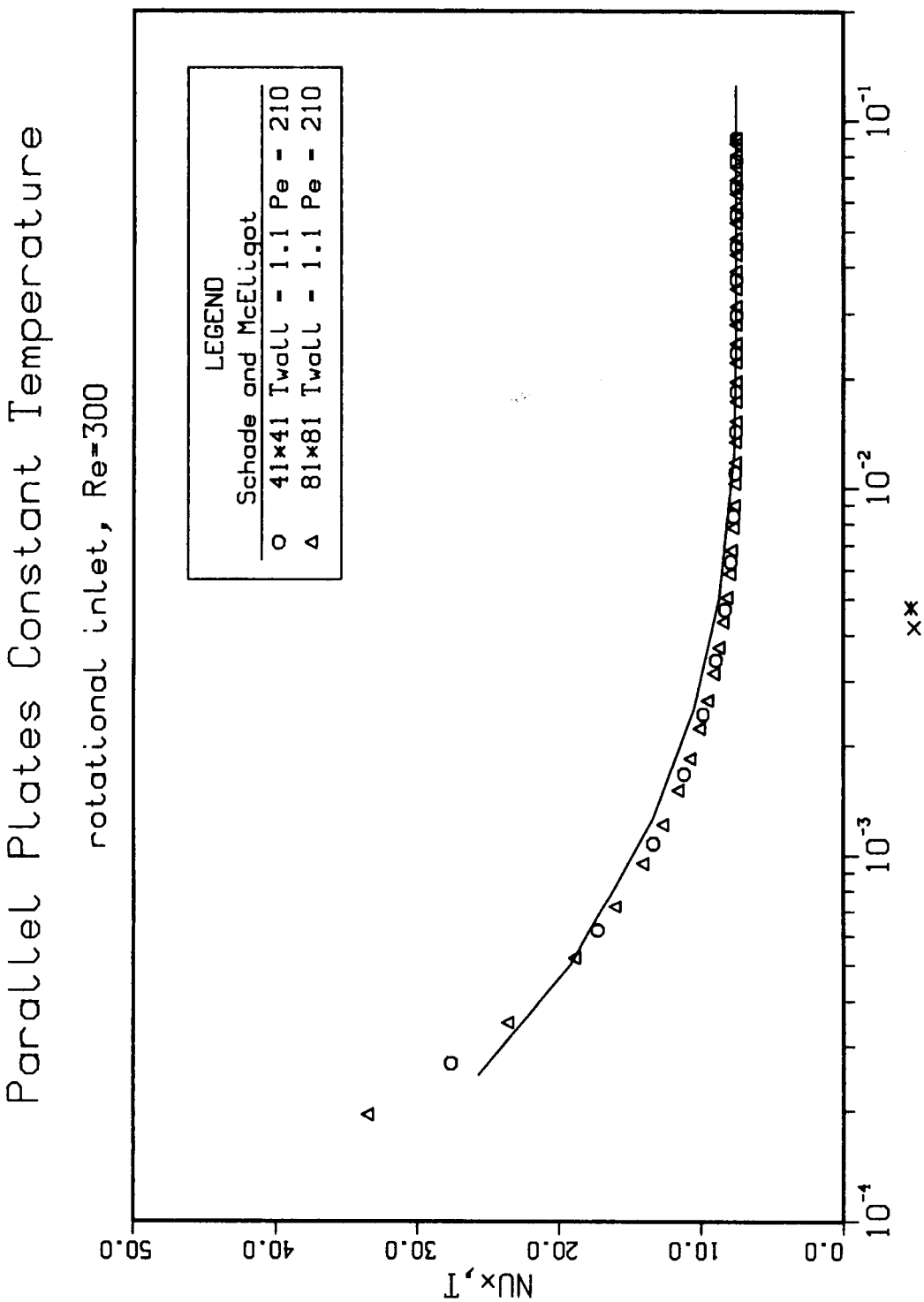

Figure 4.9: Local Nusselt number for flow between parallel plates at constant temperature. Pe=210. Asymptotic Nu=7.541

Peclet number of about 210 is required to give good agreement with the boundary-layer assumptions. Lower Peclet numbers give a higher heat transfer rate near the inlet. Profiles of the temperature parameter, θ, are plotted in Figure 4.11 for several streamwise positions. The fully-developed profile is parabolic.

To match the boundary-layer assumptions used by Schade and McEligot, the streamwise second derivatives must be dropped. The affect is similar to assuming a high Reynolds number flow. Schade and McEligot report that Pe > 100 is sufficient for the boundary-layer assumptions to be valid. Also, Schade and McEligot neglect viscous dissipation. For incompressible flow, the only streamwise second derivatives in the dual potential method are ω_{xx}, A_{xx} and T_{xx}. When these derivatives and the viscous dissipation are dropped, the results approach those of Schade and McEligot, as can be seen in Figure 4.10. It is clear that the boundary-layer assumptions cannot be used to get accurate results near the inlet at lower Reynolds numbers or Peclet numbers. The boundary-layer assumptions neglect the important elliptic effects at the inlet and underpredict the heat transfer.

The computation rate for the dual potential code is 80–100 MFLOPS overall using a single processor on a Cray X-MP. The computation rate can be stated in a more useful manner as $\sim \frac{5.5\,\mu s}{\text{global iteration} \times \text{grid point}}$ on a single processor of the Cray X-MP. The number of global iterations is on the order of the number of grid points. A conservative estimate of Cray X-MP cpu time is:

$$\text{cpu time (s)} = 5.5 \times 10^{-6} \times (\text{number of grid points})^2$$

The two-dimensional dual potential code is a compressible code. The compressible terms are computed for this calculation even though they are zero. If the code was

designed purely for incompressible solutions the code would be much faster—at least twice as fast based on a rough operation count. The error tolerance used for these calculations was $\epsilon \leq 10^{-6}$.

The solution to the constant property case is independent of wall temperature. This was checked using $T_{\text{wall}} = 2.0, 1.1, 1.01, 1.001, 1.0001$ with the same constant property results obtained for each case. Shah and London (1978) also present data for the constant wall temperature case. For the present results, the grid was stretched using $\sigma = 1.05, \alpha = 0.5$ and $\beta = 1.2$.

Constant heat flux The constant temperature case has revealed that Pe = 210 gives good agreement with the boundary-layer approximations used by Schade and McEligot. Just one case will be presented here in Figure 4.12. The results compare well to solutions obtained using the boundary-layer approximations, but are more accurate near the inlet. A second order polynomial curve fit to the temperature distribution was used to obtain the wall temperature. The temperature parameter profiles for this case are presented in Figure 4.13.

Mixed wall boundary conditions Solutions were computed for two cases with one wall insulated and the other wall at either constant heat flux or constant temperature. Shah and London (1978) refer to these boundary conditions as the *fundamental boundary conditions of the second kind* and *third kind* respectively. The asymptotic Nusselt number for the case of one wall insulated and the other at constant heat flux is computed analytically to be Nu = 5.385. This case will be designated by H2 in the results. The asymptotic Nusselt number for the case

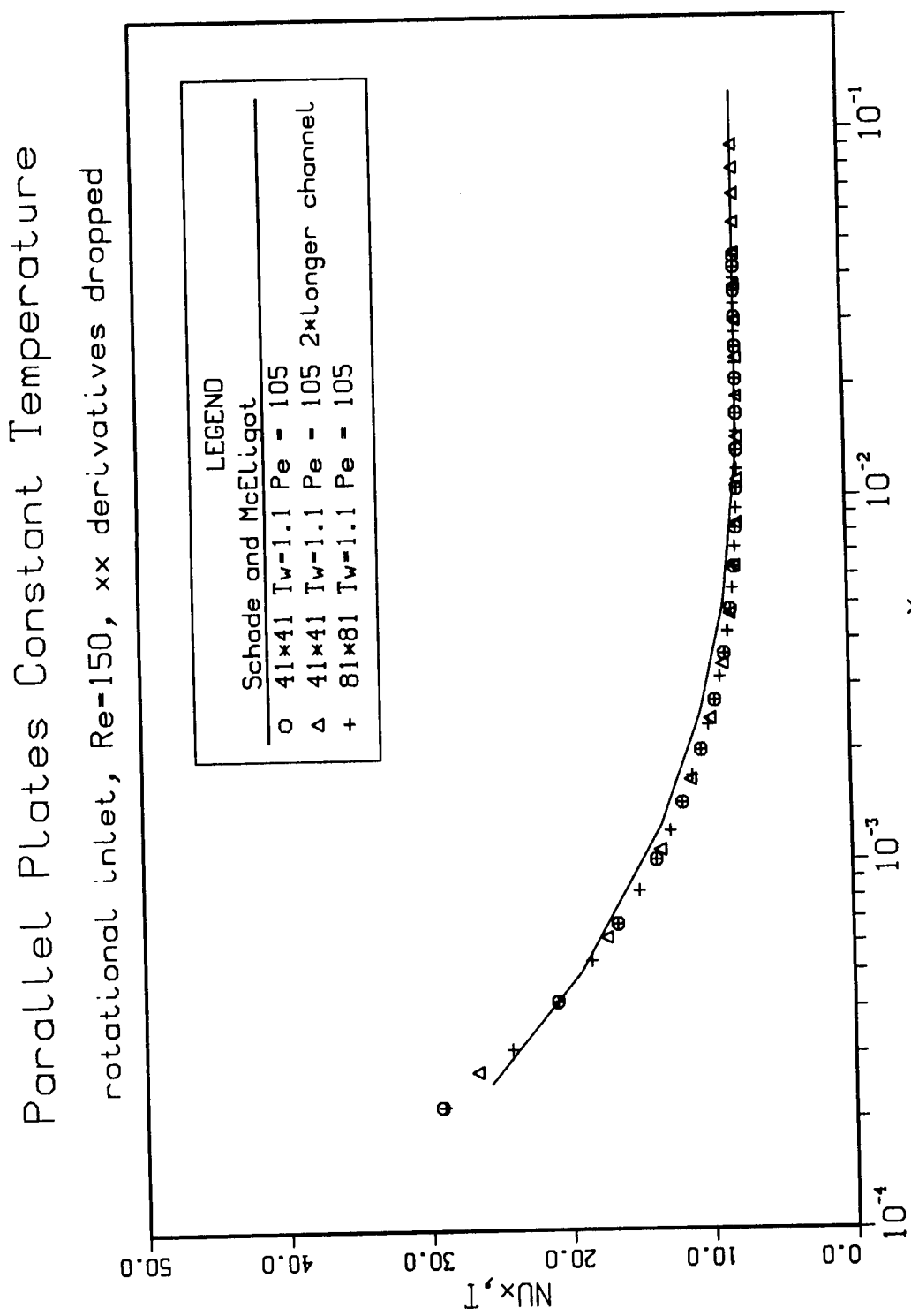

Figure 4.10: Local Nusselt number for flow between parallel plates at constant temperature. Dual potential code with boundary-layer assumptions

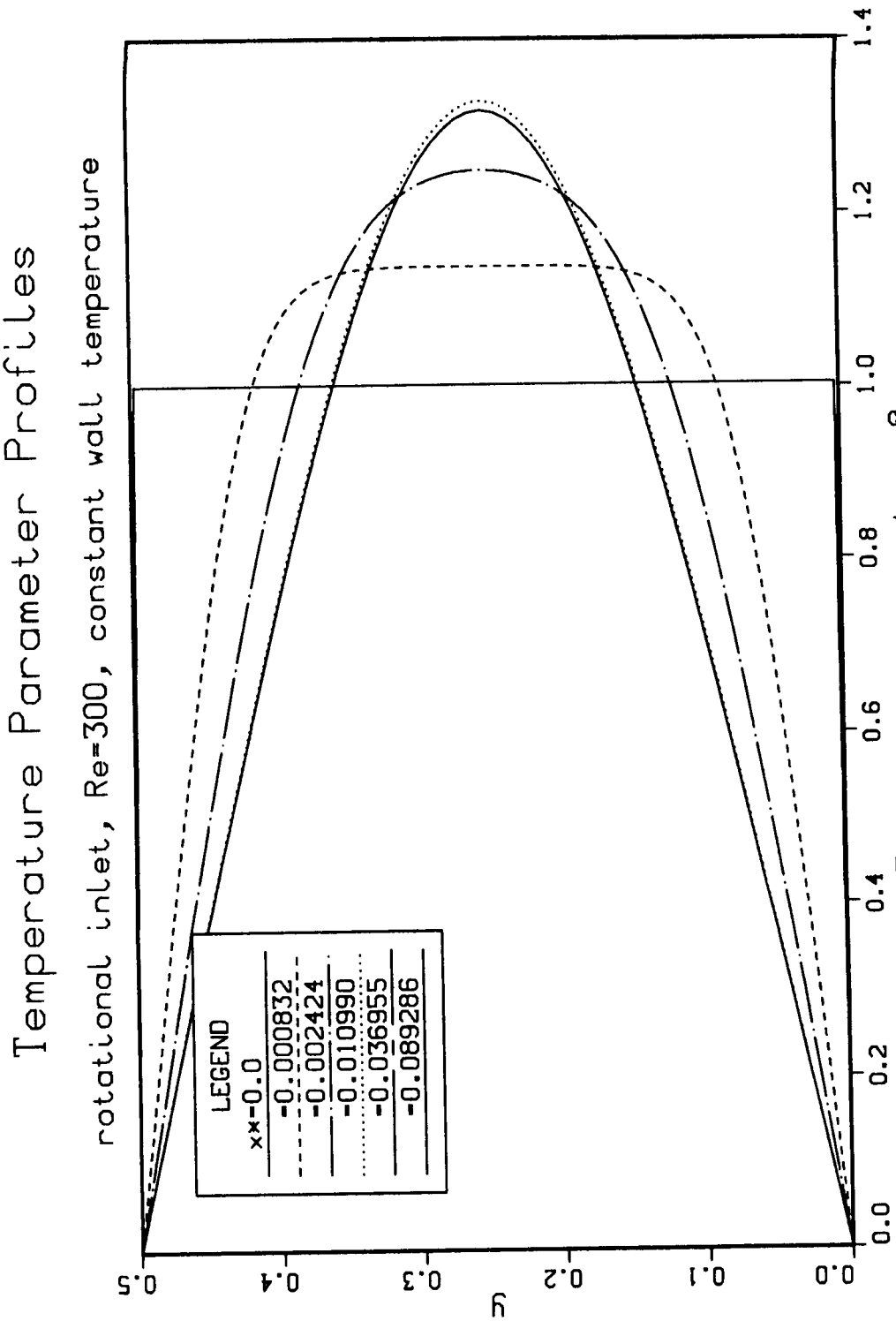

Figure 4.11: Profiles of the temperature parameter at various x^* for the constant wall temperature case

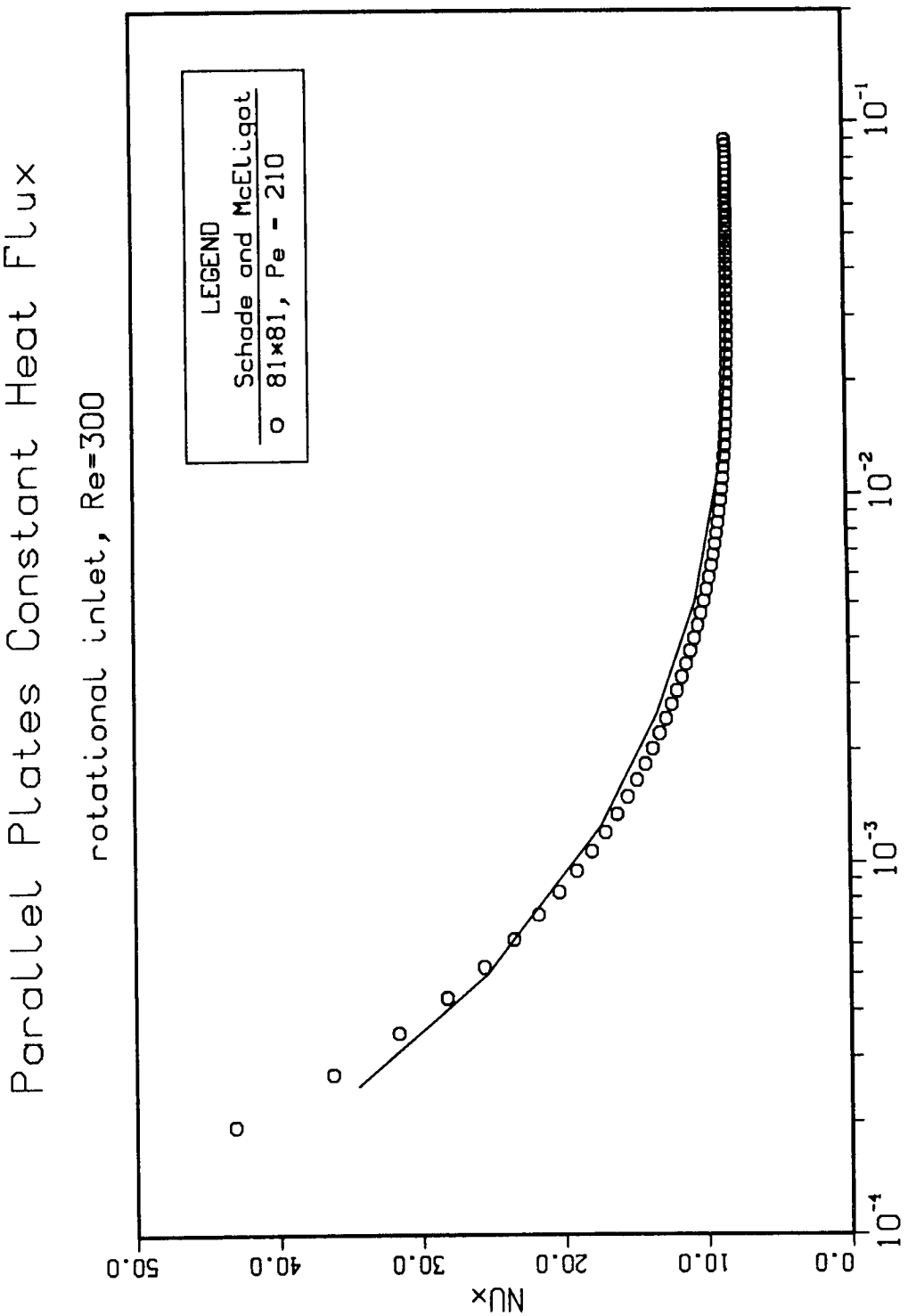

Figure 4.12: Local Nusselt number for flow between parallel plates with constant wall heat flux. Pe=210. Asymptotic Nu=8.235

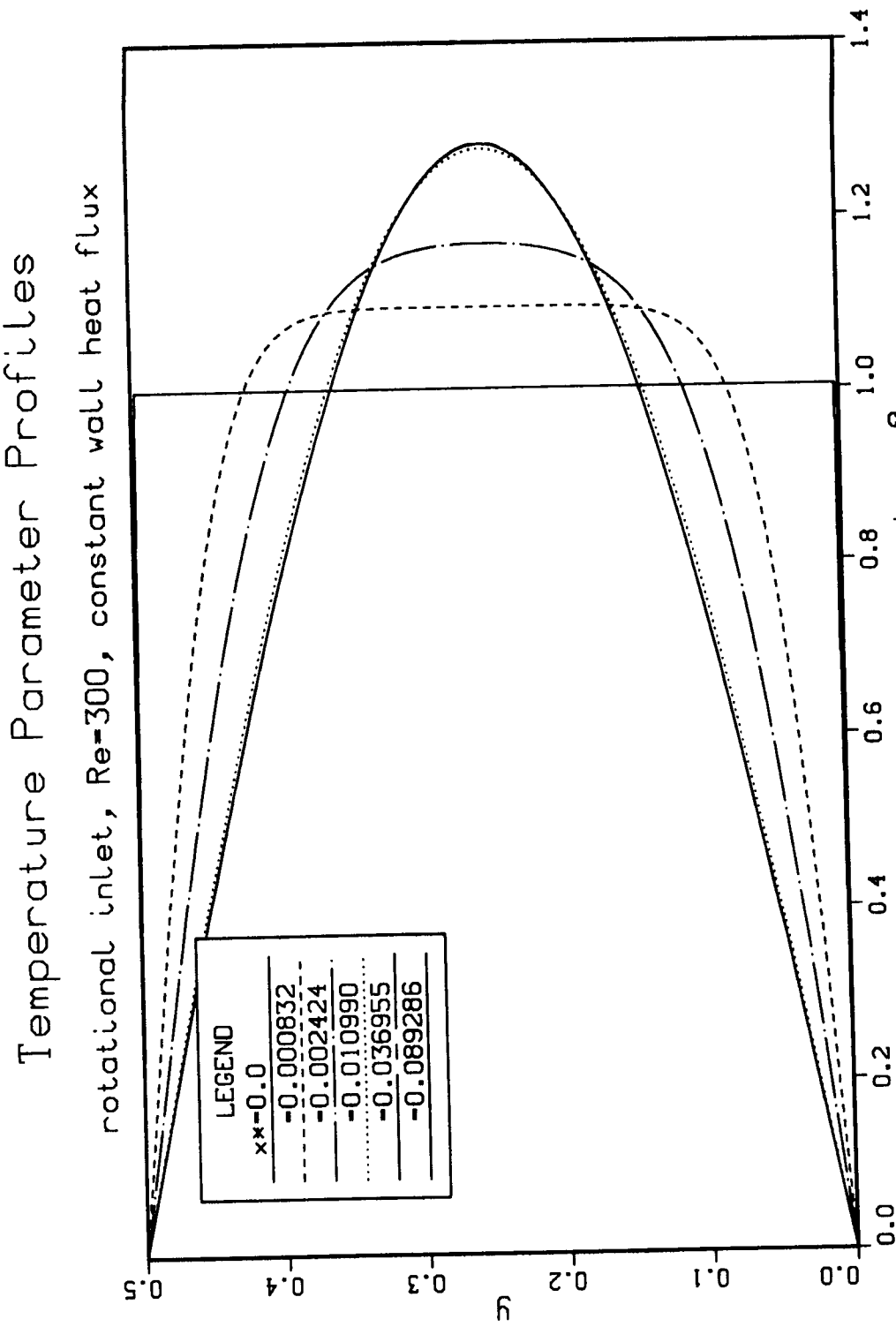

Figure 4.13: Profiles of the temperature parameter at various x^* for the constant wall heat flux case

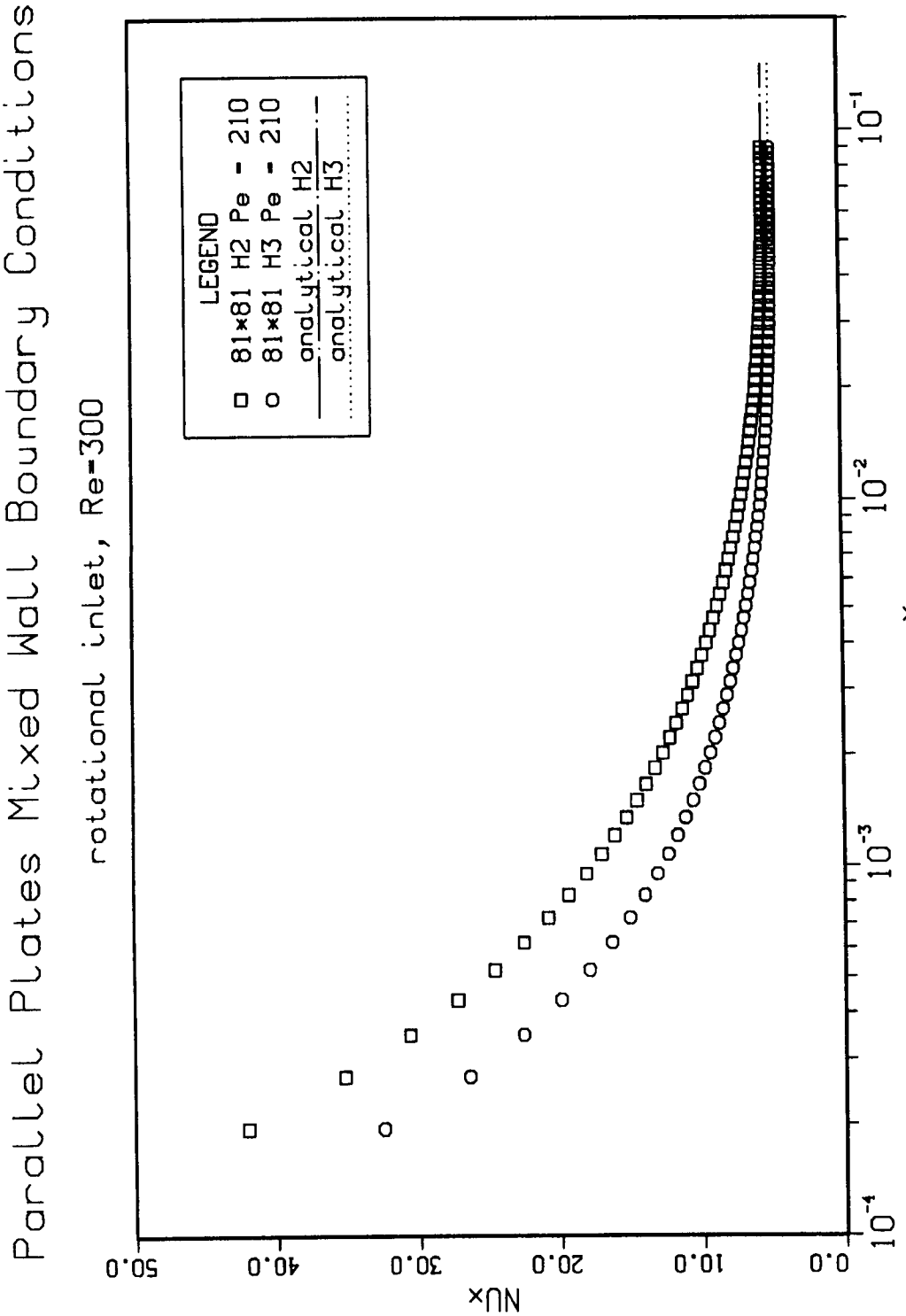

Figure 4.14: Local Nusselt number for flow between parallel plates with mixed wall conditions. Pe=210.
Asymptotic Nu=5.385 for one wall insulated and the other at constant heat flux.
Asymptotic Nu=4.861 for one wall insulated and the other at constant temperature

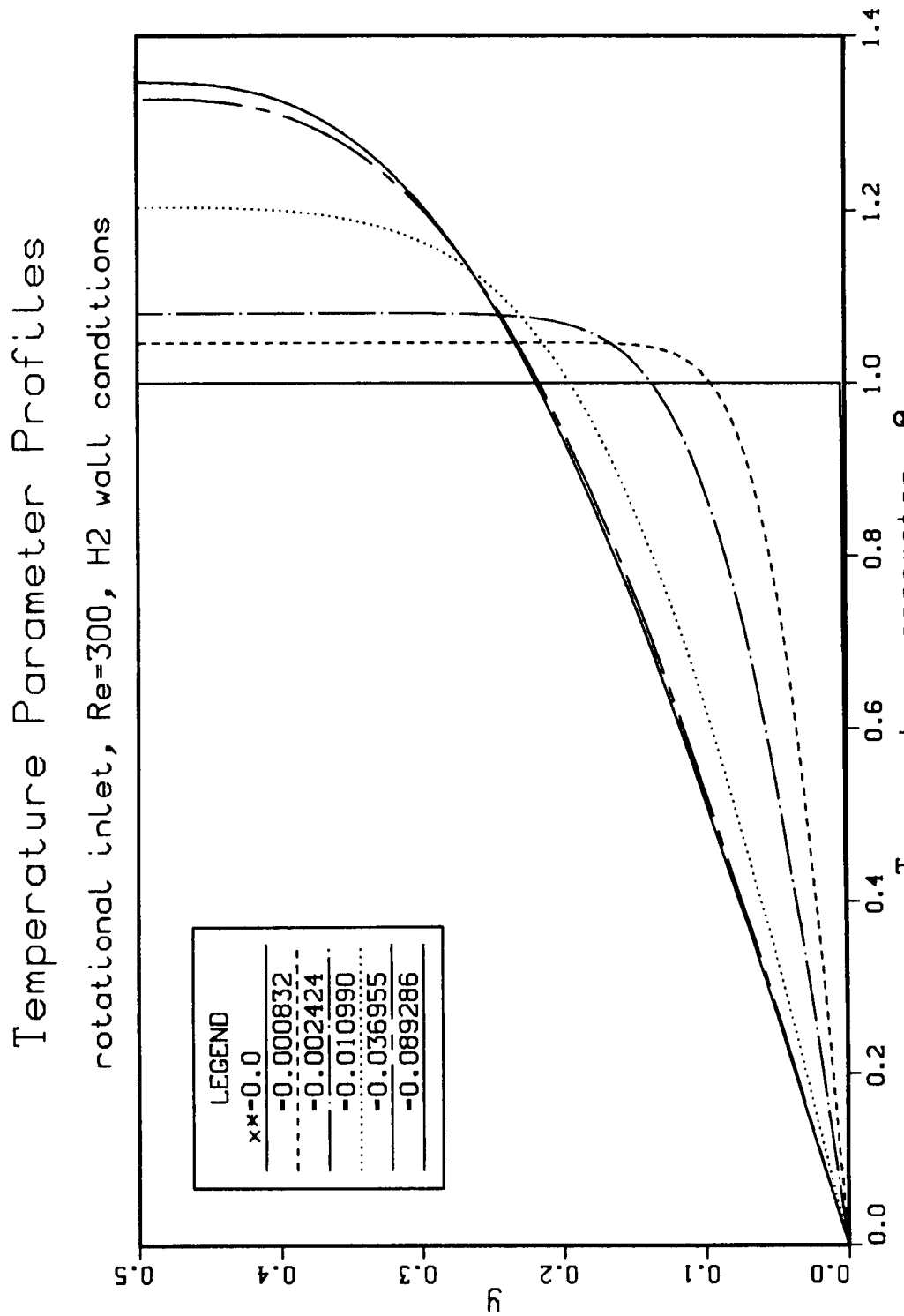

Figure 4.15: Profiles of the temperature parameter at various x^* for the case of one wall insulated and the other at constant heat flux

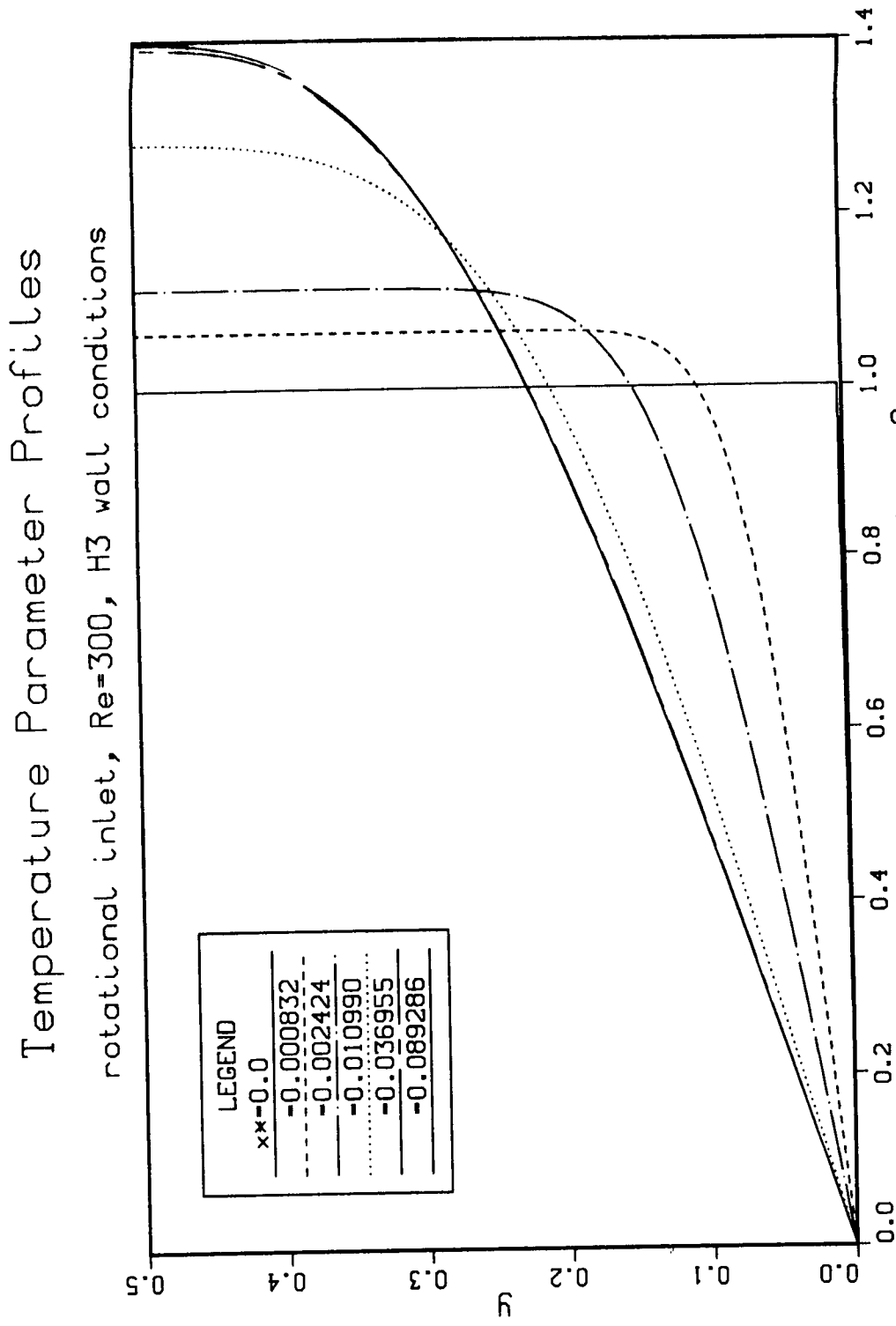

Figure 4.16: Profiles of the temperature parameter at various x^* for the case of one wall insulated and the other at constant temperature

of one wall insulated and the other at constant temperature is computed analytically to be Nu = 4.861. This case will be designated by H3 in the results. The computed Nusselt number development for these two cases and the analytical asymptotic Nusselt number are shown in Figure 4.14. Temperature parameter profiles for these two cases are plotted in Figures 4.16 and 4.15.

Boundary layer This case is considered to provide yet another check on the accuracy of the dual potential scheme since the laminar boundary-layer solution is well known. Despite the simplicity of this flow, it is not always easy to obtain good comparisons with numerical solutions to the full Navier-Stokes equations.

The boundary conditions for the laminar incompressible flow over a flat plate are shown in Figure 4.17. Since this is an incompressible constant property flow, B, T and ρ need not be computed.

Concerning the vorticity boundary conditions, an irrotational or rotational inlet flow may be specified. The best comparison with Blasius results was obtained for a zero inlet plane vorticity (irrotational condition). This gives a non-zero v velocity at the inlet. Both u and v are fixed to be zero at the stagnation point. The wall vorticity is computed as in all viscous wall cases. The freestream is assumed to be irrotational. The exit condition is based on the usual fully-developed assumption that second order streamwise derivatives are zero.

The vector potential inlet and viscous wall conditions are the usual $A = 0$. In this case the vector potential is used to account for the throughflow velocity (i.e., leakage velocity) at the top boundary. It was stated in the boundary condition section that only the scalar potential would be used to give throughflow velocities. This is the only

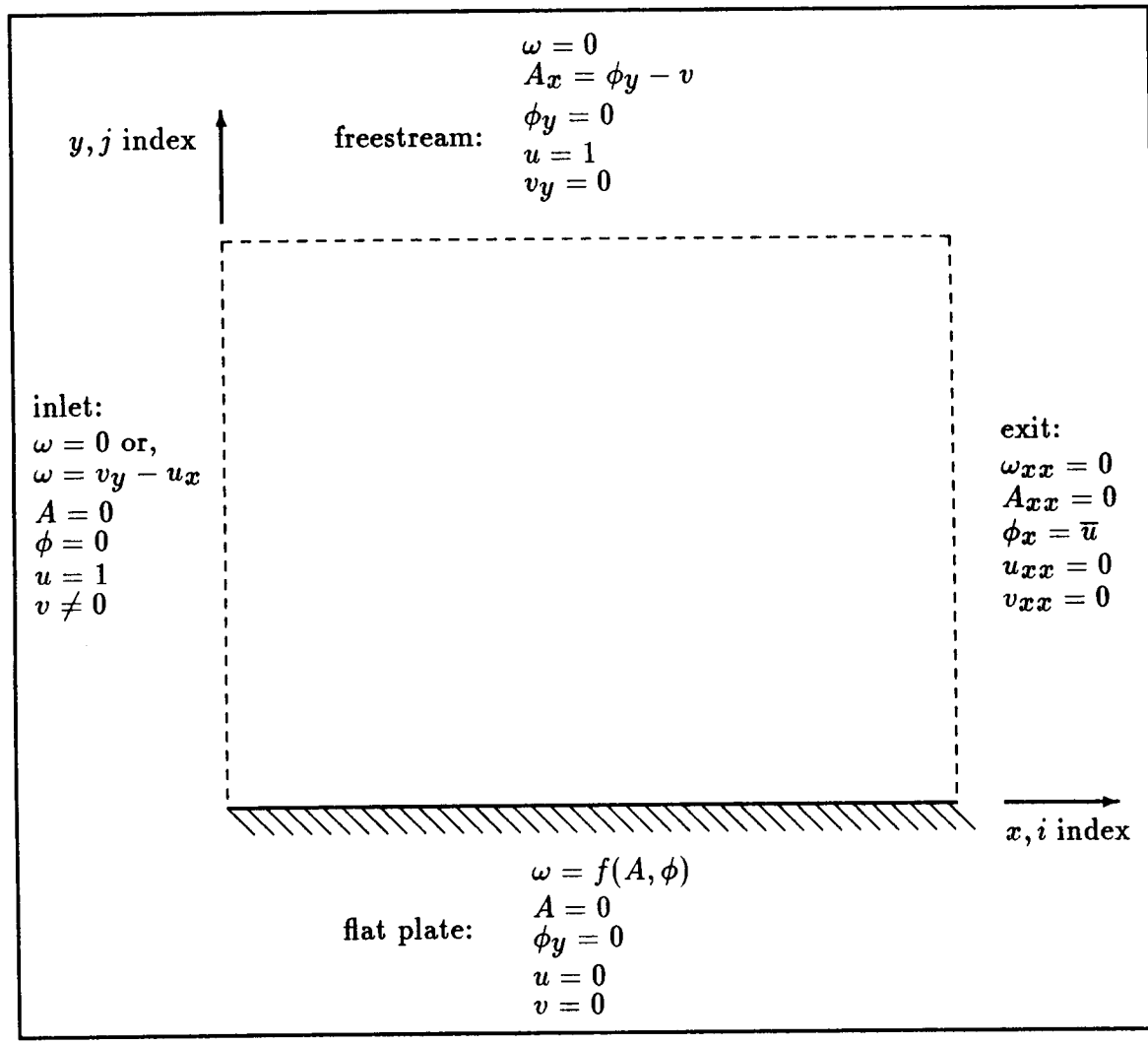

Figure 4.17: Boundary conditions for laminar incompressible flow over a flat plate

exception. The v velocity is given at the top boundary by assigning the same velocity at the boundary as at the point just inside. This implies that $\frac{\partial v}{\partial y} = 0$. Hence, A_x along the top boundary is computed from the assumed v leakage velocity using the velocity decomposition for v, $v = \phi_y - A_x$. More elaborate calculations can be used to compute the v leakage velocity from the displacement thickness. For example, the leakage can be accurately written as

$$\frac{d\delta^*}{dx} = \frac{v}{U_\infty}$$

Thus the leakage can be controlled based on a known or computed displacement thickness, δ^*. These ideas worked no better than simply assigning $v(i, nj) = v(i, nj - 1)$ at the freestream boundary. At the exit $u_x = 0$ was acceptable, but $u_{xx} = 0$ gave a slightly better boundary-layer profile as compared to the Blasius (1908) solution. Note that the exit condition on the vector potential, $A_{xx} = 0$, is equivalent to an extrapolation technique. The vector potential at a point just outside the exit plane boundary is computed by $A_{xx} = 0$ for use in the Poisson equation for A. The Poisson equation is solved at the exit plane. This assumes that the flow is fully developed and removes the need to specify the velocity at the exit. The scalar potential boundary conditions are the same as for the incompressible channel case. Therefore, the solution of the scalar potential Poisson equation is known a priori and $\phi = x$ is simply assigned and not re-computed. The same boundary conditions as the channel case were used to avoid a solution for the scalar potential in this case. The only difficulty was a need to change the top boundary condition on the vector potential to account for a leakage flow. This leakage flow is small and could be neglected with the boundary far enough away. If it is neglected and the top boundary is too close, the

boundary-layer profile tends to overshoot the freestream value by several percentage points. Allowing leakage at the top wall permits the solution to be obtained on a smaller grid.

The laminar boundary-layer computation agrees well with the Blasius solution. A boundary-layer profile comparison is shown in Figure 4.18. An 81×81 grid was used with stretching in the y direction. This puts about 22 points in the boundary layer at $\mathrm{Re}_x = 312,500$. The solution is attained in 54.5 seconds at 85 MFLOPS overall on a single processor of the Cray X-MP. The data marked with triangles were computed by limiting the solution domain of the vorticity transport equation to 31 transverse points. This example was specifically used to demonstrate the ability to reduce the computational effort by dropping the calculation of vorticity where it is negligible and still obtaining a full field solution for the problem. Even faster solutions are possible using this method. Normally the Poisson equations dominate the solution time. That does occur in this problem also, but iterations on the vector potential calculation were limited with no deleterious effect on the final solution. With the vector potential limited, the vorticity transport equation becomes the dominant time consuming computation for this problem. It is this condition that was used to demonstrate the ability to reduce computation time for the vorticity. This speed-up affect is shown in Table 4.1.

For problems that one knows have vorticity approaching zero at a boundary, the point-wise convergence check used in the code can be helpful in deciding where and how much to limit the solution domain for vorticity. For example, if vorticity goes to zero at the freestream boundary as in this problem, one will note that for the

Table 4.1: Speed-up affect of limiting the vorticity solution domain

81×81 grid. $Re_L = 312,500$		
Transverse pts for vorticity solution	CPU time (s)	MFLOP
81	54.5	85
41	40.2	77
31	36.9	73

convergence checking used here (which is point by point and normalized on the largest value in a plane), the biggest error will be in the region where vorticity is important. If the point of maximum error is far away from the known $\omega = 0$ boundary, then limiting of the solution domain is indicated.

The MFLOP rate in Table 4.1 drops as the solution domain for vorticity is limited because the vorticity transport subroutine had a high MFLOP rate. The solution was speeded up by limiting the vorticity solution domain and thereby reducing the CPU time spent in computing the vorticity in regions where it is nearly zero anyway. The vorticity transport subroutine is a 107+ MFLOP code. Reducing the computation time on vorticity reduced its high MFLOP rate in the weighted average to compute the overall MFLOP rate for the code.

Solutions were obtained for Re_x up to 2,000,000 using both rotational and irrotational inlet conditions. The rotational inlet condition gave a higher skin friction and a slight velocity overshoot. The computed skin friction along the flat plate for the two inlet conditions is shown in Figure 4.19. The rotational inlet condition produces a higher C_f than the irrotational inlet by the conservation of vorticity. Since the inlet vorticity is non-zero in the rotational case, there is an additional amount of vorticity in the rotational as opposed to the irrotational inlet case. The boundary-layer

calculation for the rotational inlet ($\omega \neq 0$) has vorticity in excess of that assumed in the Blasius solution. The extra vorticity is the inlet amount. The Blasius solution is obviously for an irrotational inlet. The results presented here were obtained using first order upwinding of the streamwise convective term. Weighting toward central differencing works but requires more CPU time to converge. The equations used here do not use the boundary-layer assumptions and so can accurately model the near leading edge flow. The skin friction is computed as:

$$C_f\sqrt{\mathrm{Re}_x} = \frac{\mu_{\mathrm{wall}}\left.\frac{\partial u}{\partial y}\right|_{\mathrm{wall}}}{\frac{1}{2}\rho_\infty V_\infty^2}\sqrt{\frac{\rho_\infty V_\infty x}{\mu_\infty}} \tag{4.29}$$

The velocity derivative is computed using a second order polynomial fit to the u velocity component. The computed asymptotic value for the skin friction is $C_f\sqrt{\mathrm{Re}_x} = 0.664$ for the irrotational inlet case and $C_f\sqrt{\mathrm{Re}_x} = 0.704$ for the rotational inlet.

The x and y distances in Figures 4.19–4.21 are non-dimensionalized by the length of plate required to give $\mathrm{Re}_L = 312,500$. Velocity vectors for this boundary-layer flow are plotted in Figures 4.20 and 4.21. The most easily observed difference in these two figures is the flow at the inlet plane. The irrotational inlet flow condition produces a v velocity component at the inlet plane.

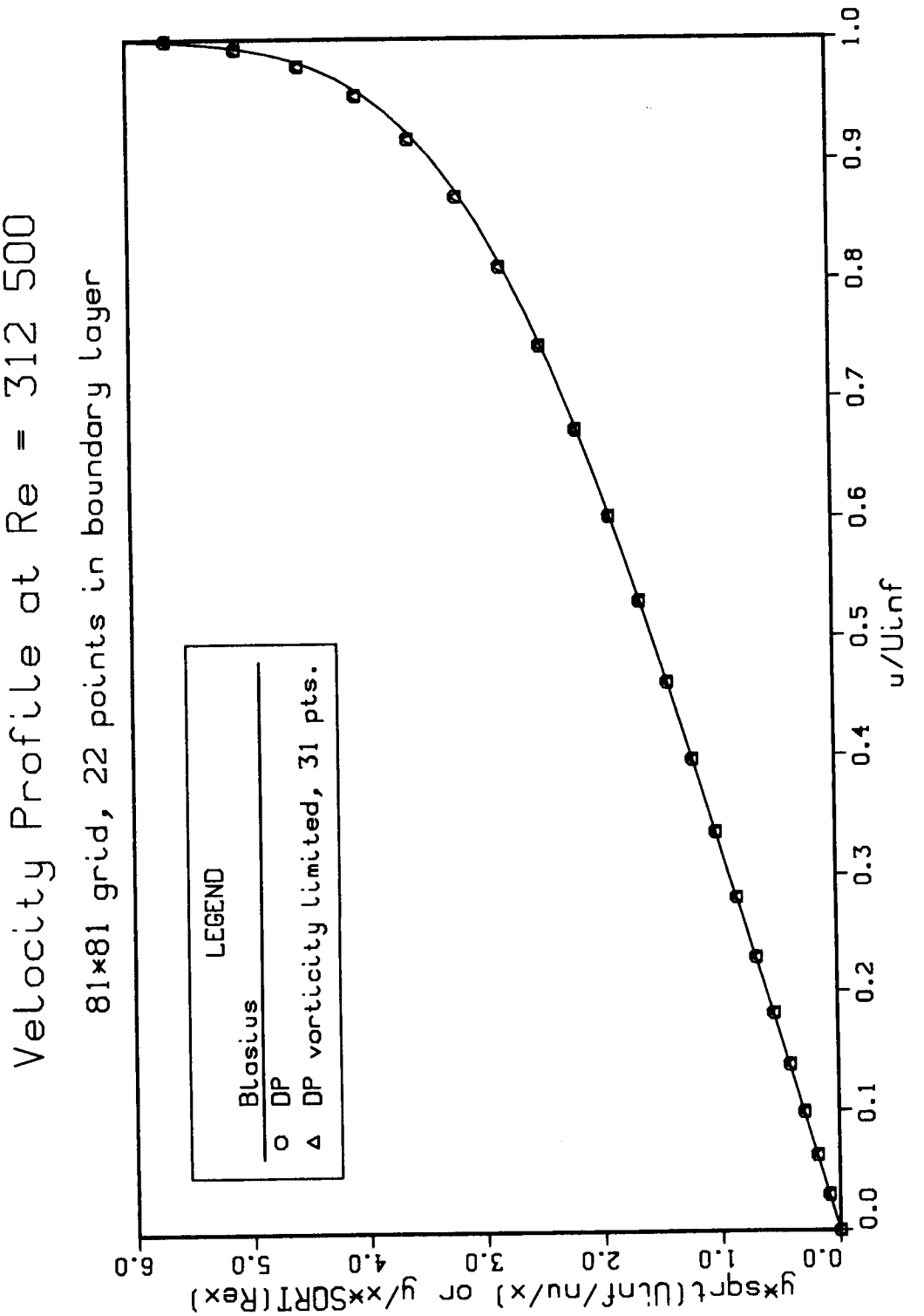

Figure 4.18: Laminar incompressible boundary-layer velocity profile at $Re_x = 312{,}500$

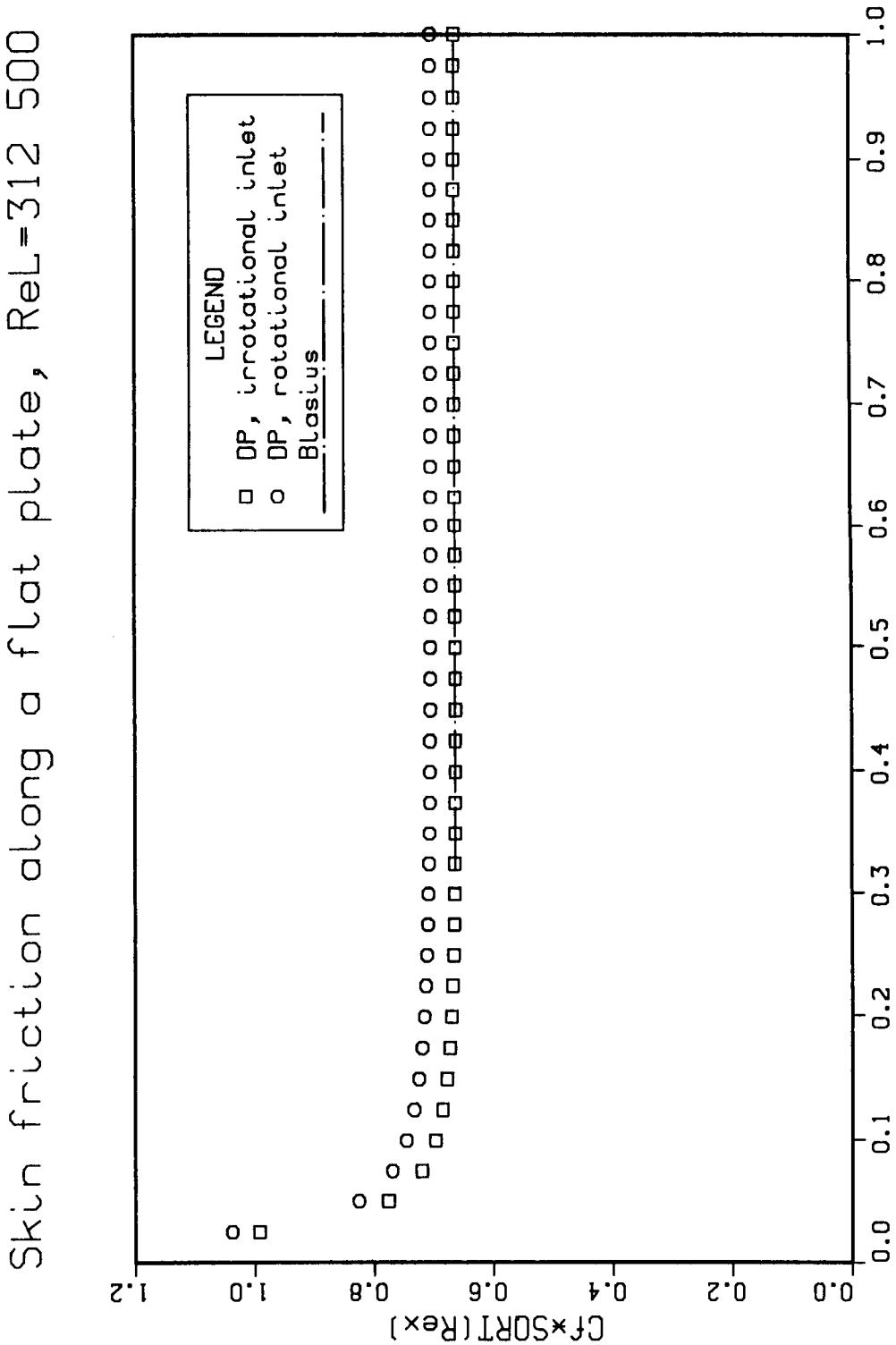

Figure 4.19: Skin friction along a flat plate

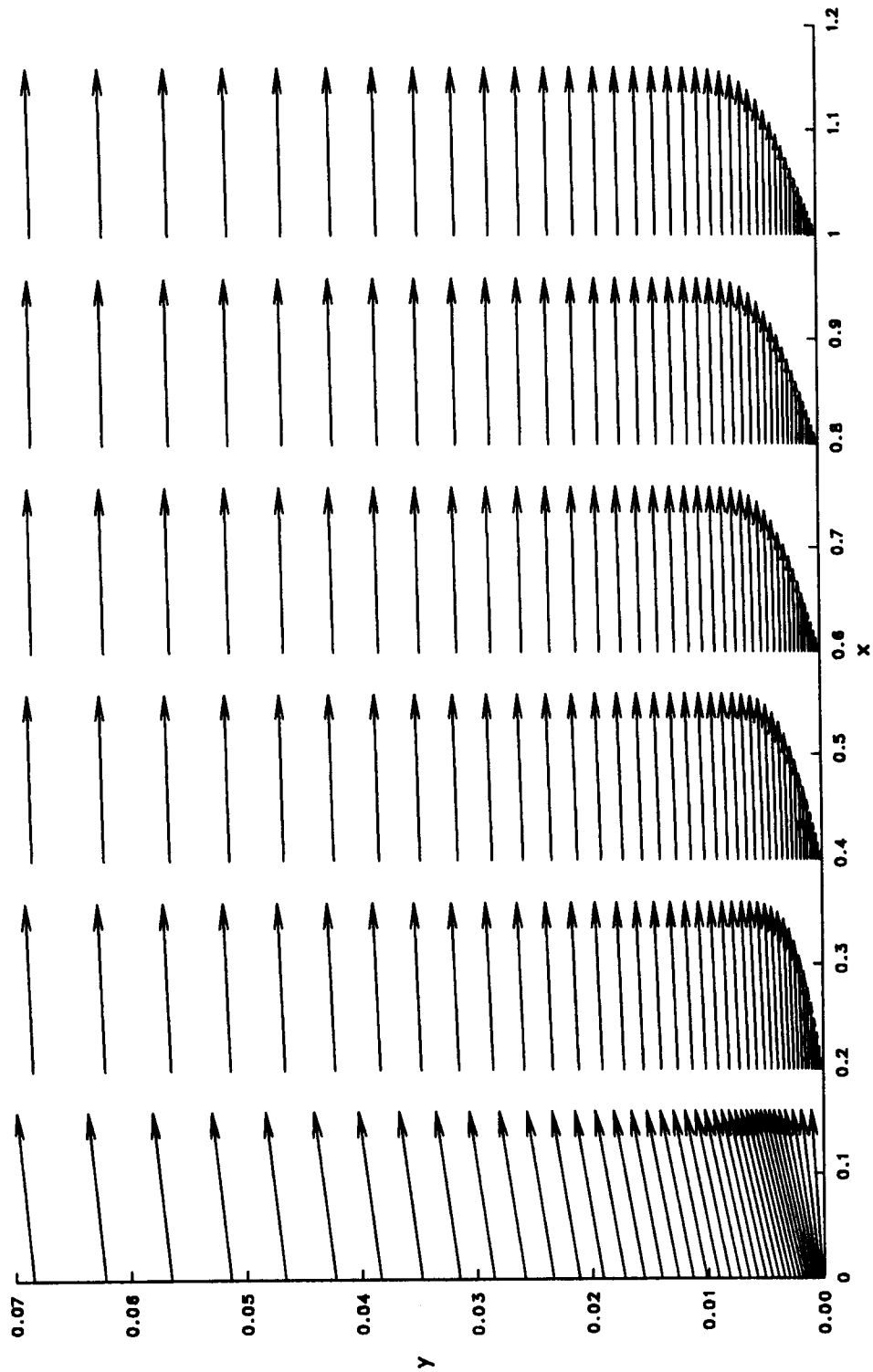

Figure 4.20: Velocity vectors for laminar flow over a flat plate with an irrotational inlet condition

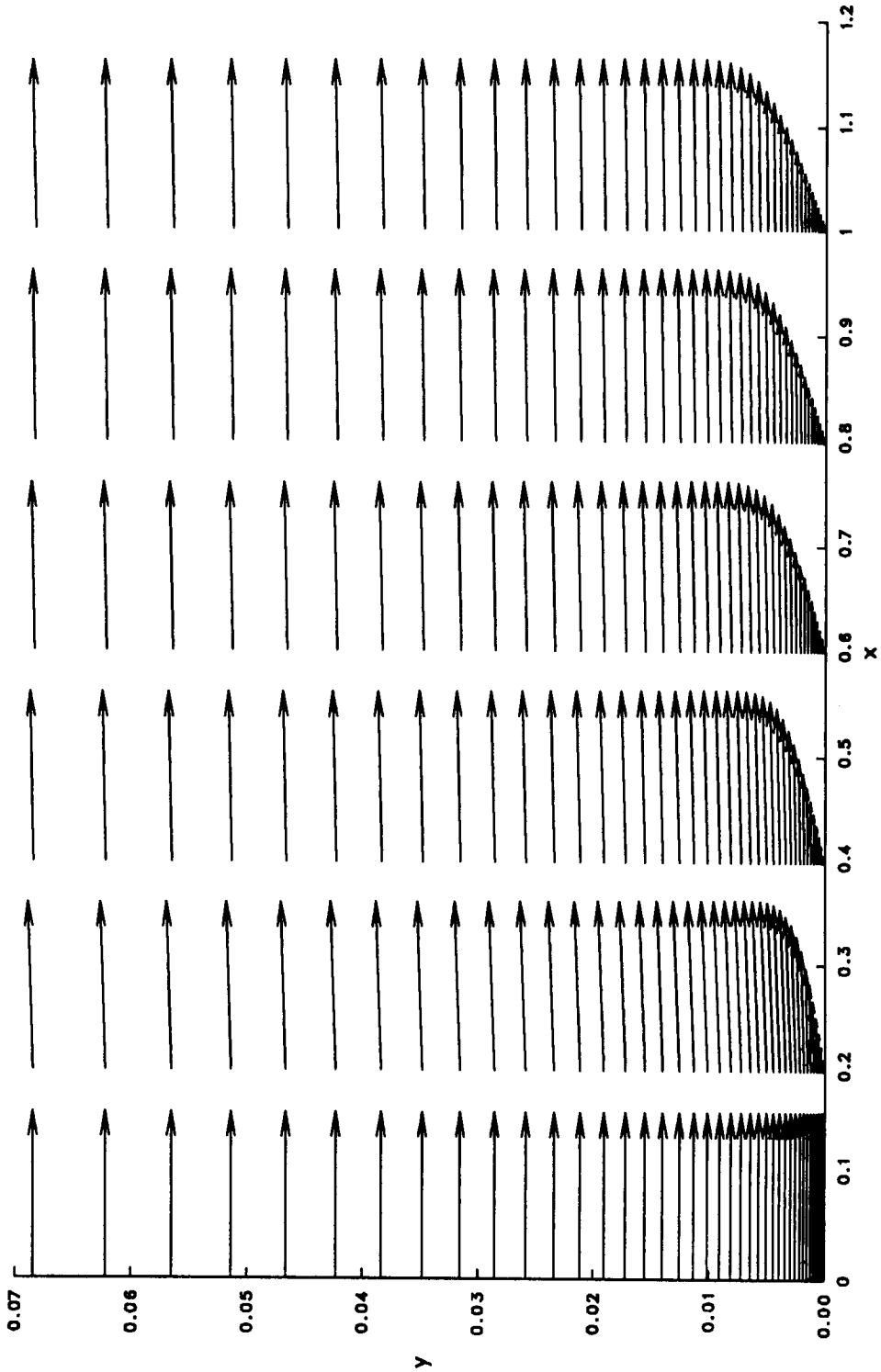

Figure 4.21: Velocity vectors for laminar flow over a flat plate with a rotational inlet condition

4.3.2 Compressible flow

4.3.2.1 Steady irrotational inviscid flow

Bump cases The flow assumptions for this problem are the same as in the previous bump test case:

1. inviscid
2. irrotational
3. isentropic
4. no body forces

The flow can be incompressible or compressible and steady or unsteady. The boundary conditions for this case are shown in Figure 4.22. The same boundary conditions apply for the unsteady problem which is discussed in the next section. The assumptions for this test case are the same as in the bump cases previously discussed on pages 83–92 except that the compressible solution is computed directly rather than scaled from an incompressible result.

There are many possible well-tested solution methods for this irrotational problem. The dual potential method is easily adapted to solve the flow using any of the following combinations of governing equations. Either potential may be used. The scalar potential may be used as the traditional velocity potential for a full potential solution. The vector potential may assume the role of the stream function for a compressible stream function solution. In addition, an Euler mode of solution is available

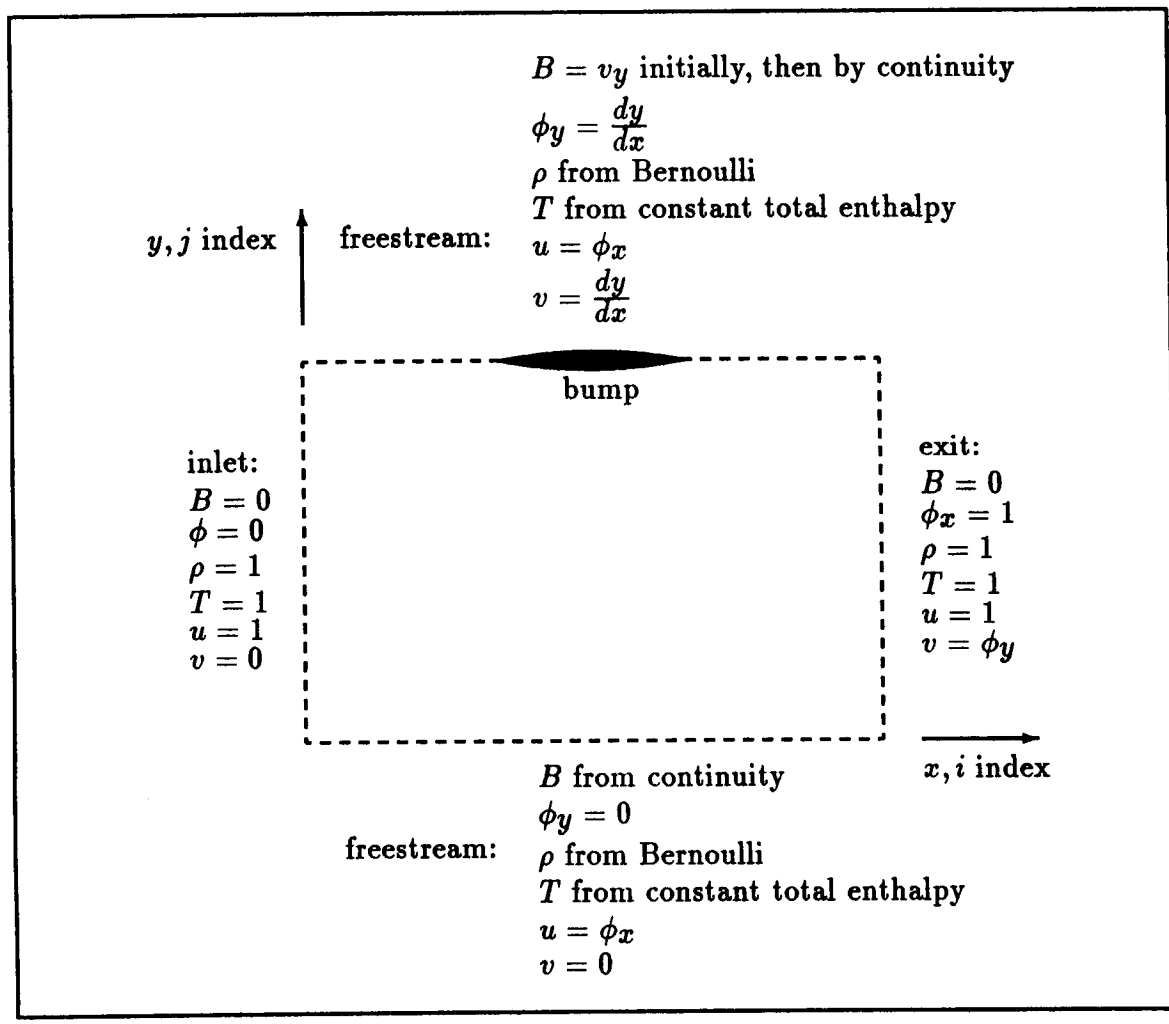

Figure 4.22: Boundary conditions for laminar compressible irrotational flow over a bump

using the dual potential method with viscous terms and thermal conductivity set to zero.

The traditional potential methods simply require the velocity potential or stream function with a version of the Bernoulli equation. These two methods will be presented in a form only applicable to steady flows. The full potential equation written in conservation law form is

$$\frac{\partial}{\partial x}(\rho\phi_x) + \frac{\partial}{\partial y}\left(\rho\phi_y\right) = 0 \tag{4.30}$$

This may be solved by the scalar potential solver in the dual potential code with a redefinition of the scalar potential derivatives to be the parenthesized quantities in the equation above. This requires a modification of the boundary conditions also. Since the flows to be computed here are subsonic, it is permissible to write the full potential equation in non-conservative form:

$$\nabla^2\phi = -\frac{\rho_x\phi_x + \rho_y\phi_y}{\rho} \tag{4.31}$$

This is easily solved by the scalar potential solver with no modification to the boundary conditions. The steady compressible Bernoulli equation is then solved for density,

$$\rho = \left\{1 + \frac{\gamma-1}{2}\mathrm{M}_\infty^2\left(1 - \phi_x^2 - \phi_y^2\right)\right\}^{\frac{1}{\gamma-1}} \tag{4.32}$$

Using the stream function, only the velocity decomposition and Bernoulli equation are required. For the stream function approach, solve the following:

$$\begin{aligned}
\vec{V} &= \frac{1}{\rho}\vec{\nabla} \times \psi \\
\rho &= \left\{1 + \frac{\gamma-1}{2}M_\infty^2\left(1 - \frac{1}{\rho^2}\left(\psi_y^2 + \psi_x^2\right)\right)\right\}^{\frac{1}{\gamma-1}}
\end{aligned}$$

$$T = T_t - \frac{u^2 + v^2}{2c_p}$$

The stream function, ψ, above is defined to satisfy continuity automatically by:

$$u = \frac{\psi_y}{\rho}$$
$$v = -\frac{\psi_x}{\rho}$$

The above would require some code modification to define the vector potential, A, as the stream function, ψ. An alternate approach is to define

$$A_x = \frac{\psi_x}{\rho}$$
$$A_y = \frac{\psi_y}{\rho}$$

then the vector potential solver remains unchanged for a stream function solution and only the boundary conditions must be modified by ρ. This also permits easy use of the non-linear form of Bernoulli's equation which becomes

$$\rho = \left\{1 + \frac{\gamma - 1}{2} M_\infty^2 \left(1 - A_y^2 - A_x^2\right)\right\}^{\frac{1}{\gamma - 1}} \tag{4.33}$$

The energy equation is not specifically needed if the Bernoulli equation is solved since it is a statement of conservation of momentum and energy.

The dual potential formulation may be easily converted to an Euler solver by dropping the viscous terms and thermal conductivity. All that is required is to set $\mu = k = 0$. For the bump problems, the flow is irrotational so that the vorticity transport equation is also dropped. The DP code in the Euler mode solves the governing equations in the following order:

1. $\nabla^2 \phi = B$

2. $\vec{V} = \vec{\nabla}\,\phi$

3. the energy equation for T

4. an equation for B

5. an equation for ρ

6. the equation of state, $p = \rho RT$

The assumptions for this problem allow the energy equation to simplify to a statement of constant total enthalpy. There are several equations to choose from to compute density and dilatation. Using the DP code in Euler mode, three possible equation sets are given below. These are listed in order of increasing complexity, or, in other words, from fastest to slowest.

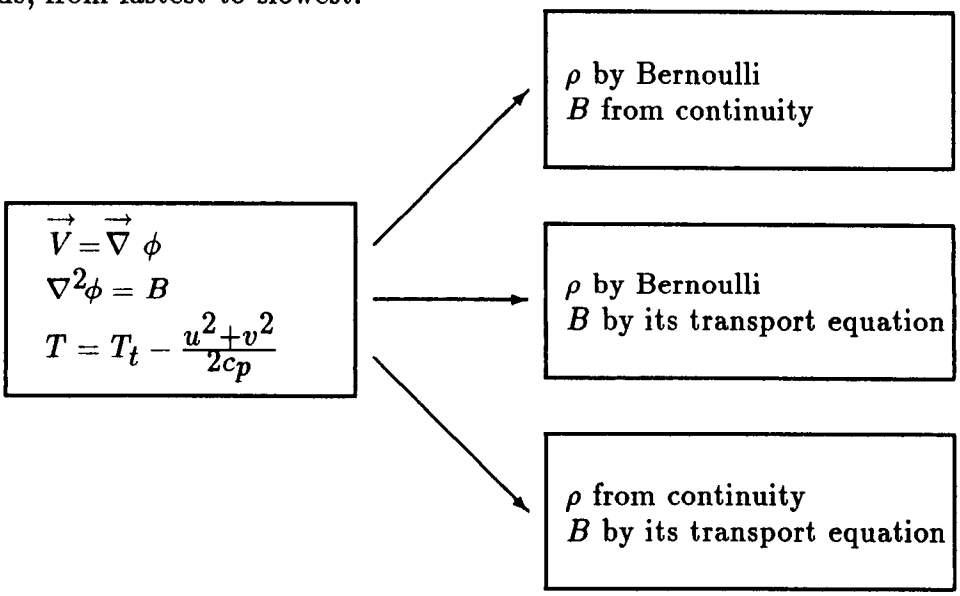

All these equation sets give the same results. Obtaining ρ from the Bernoulli equation and B from continuity is as fast as the compressible stream function ap-

proach. Using the continuity equation to obtain ρ and the dilatation transport equation for B takes about 10 times more CPU time than the fastest methods. Only the last equation set will be applicable to an unsteady flow, provided the energy equation is also time accurate.

For the compressible flow over a bump, the dual potential code uses the following initial conditions:

1. $u = 1$, $v = 0$ except at the bump where $v = \frac{dy}{dx}$ (the slope of the boundary)
2. $B = 0$ everywhere except at the bump, where $B = v_y$ (Euler version only)
3. $\rho = 1$ everywhere
4. $\phi = 0$ everywhere (Euler and full potential versions only)
5. $A = 0$ everywhere (Stream function version only)
6. $T = 1$ everywhere
7. $\mu = k = 0$ everywhere for all time.

There were initial difficulties solving the bump test cases due to abrupt function changes at the boundaries. It was necessary to smooth the variables (T, ρ, B) into the boundaries either by extrapolation or by solving for the variable at the boundary using available information and a governing equation—usually a simplified equation such as the Bernoulli equation. The far- and near-field boundaries then have values that are near the expected steady condition but differ slightly to provide smooth derivatives into the boundary. For example, the density is not exactly 1.0 at the far-field boundary when it is computed by the Bernoulli equation at that boundary,

but the derivatives of density which occur in the dilatation transport equation and elsewhere are much smoother using this approach. The y=constant boundaries were the most critical.

The pressure coefficient can be computed from the definition

$$C_p = \frac{p - p_\infty}{\frac{1}{2}\rho_\infty V_\infty^2}$$

or, if the scalar potential is used,

$$C_p = -2\phi_t - 2\phi_x - \phi_y^2$$

where $V_\infty^2 = u_\infty^2 + v_\infty^2$.

The flow over a 4% thick sine wave arc airfoil and a 6% thick parabolic arc airfoil was computed for a freestream Mach number of $M_\infty = 0.6$. The dual potential code was used in a compressible stream function mode and in an Euler mode. Results for the sine wave arc are shown in Figures 4.23–4.28 and results for the parabolic arc in Figures 4.29–4.34. The DP code is solved on a uniform 61×41 grid. The computational domain is 3 chords in the streamwise direction and extends 2 chords away from the airfoil. The airfoil is centered in x. The sine wave arc was the first successful compressible calculation. There are no stagnation points to contend with on the sine wave arc. Note the fair agreement between the stream function and Euler solution for this case shown in Figure 4.23. A grid refinement study shows that the 61×41 grid gives an Euler solution independent of further refinement. The solutions have not been obtained on a larger domain to examine whether the solution is grid independent in that respect. The discrepancy between the stream function result and the Euler solution is caused in part by the inconsistency of the small perturbation

boundary condition with the stream function and Euler solvers. The intent here is to show the capability of the solver, not ultimate solutions. The Euler solution requires about 3–10 times more CPU time than the potential solution using the same DP code—depending on which equations are used to solve for the density and dilatation. In the Euler code the convective terms are weighted toward central differencing by 0.9. The Euler solution is not exactly symmetric as can be seen in the contour plots of dilatation (Figures 4.24 and 4.30). This has been observed by others for inviscid solutions.

4.3.2.2 Unsteady irrotational inviscid flow

Bump cases The flow assumptions for this problem are the same as in the previous bump test case, except that the flow will be unsteady. The dual potential code will be used in an Euler mode. Constant total enthalpy has been assumed for the energy equation. Formally this requires a steady flow, but it will be applied here at each time step for the unsteady problem. The particular unsteady problems to be computed here have primarily low frequency disturbances (Ballhaus and Steger 1975; Beam and Ballhaus 1975). The validity of using the energy equation in a quasi-steady fashion was evaluated by computing the unsteady flow with the complete energy equation. The pressure coefficient results were within 4%. This problem was studied mainly to test the dilatation transport equations and the density determination from the continuity equation. The constant total enthalpy (or constant total temperature since c_p is constant) is written

$$T_t = T + \frac{u^2 + v^2}{2c_p} \tag{4.34}$$

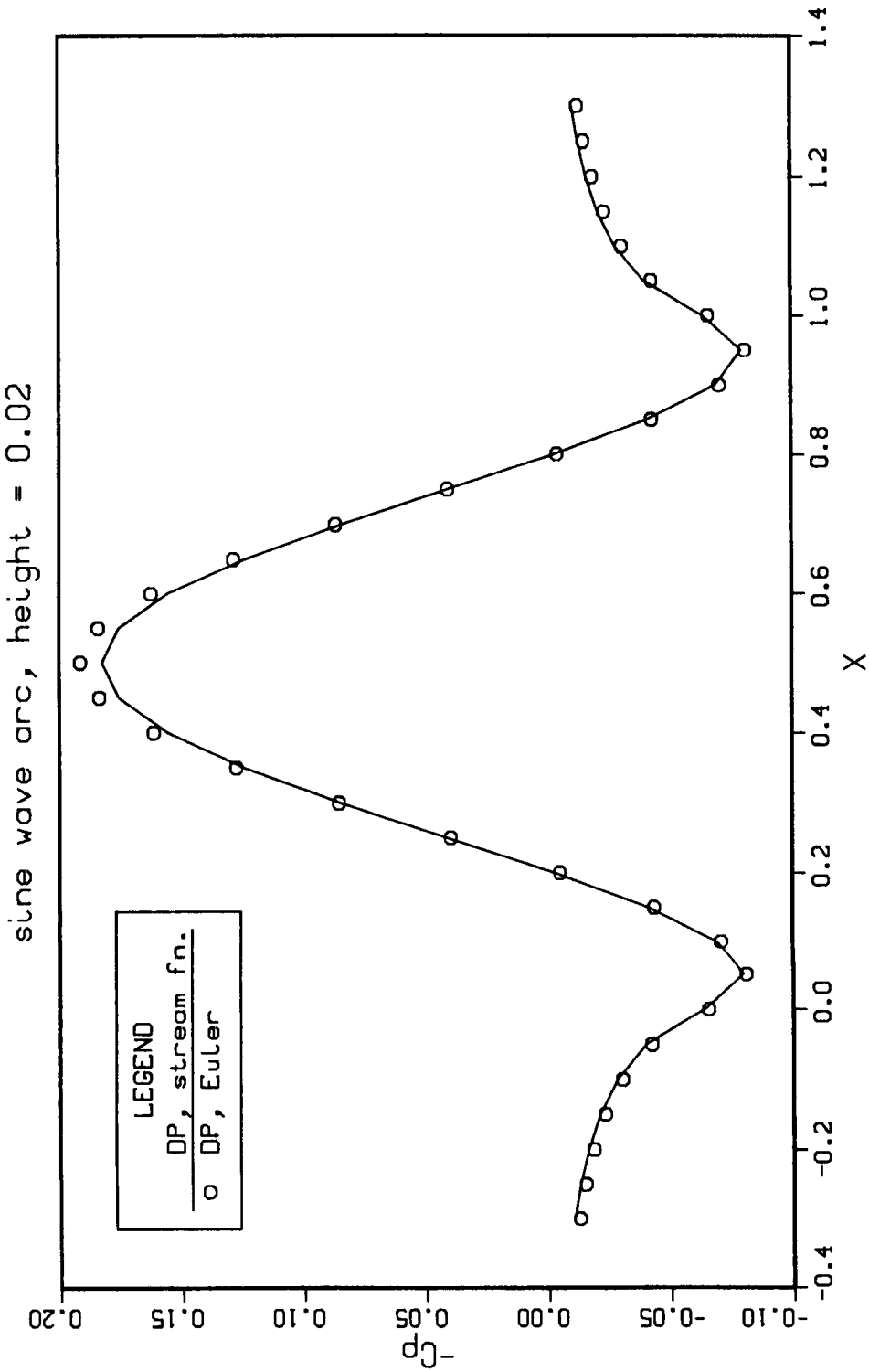

Figure 4.23: Pressure coefficient for $M_\infty = 0.6$ flow over a sine wave arc airfoil with maximum thickness = 4% of chord

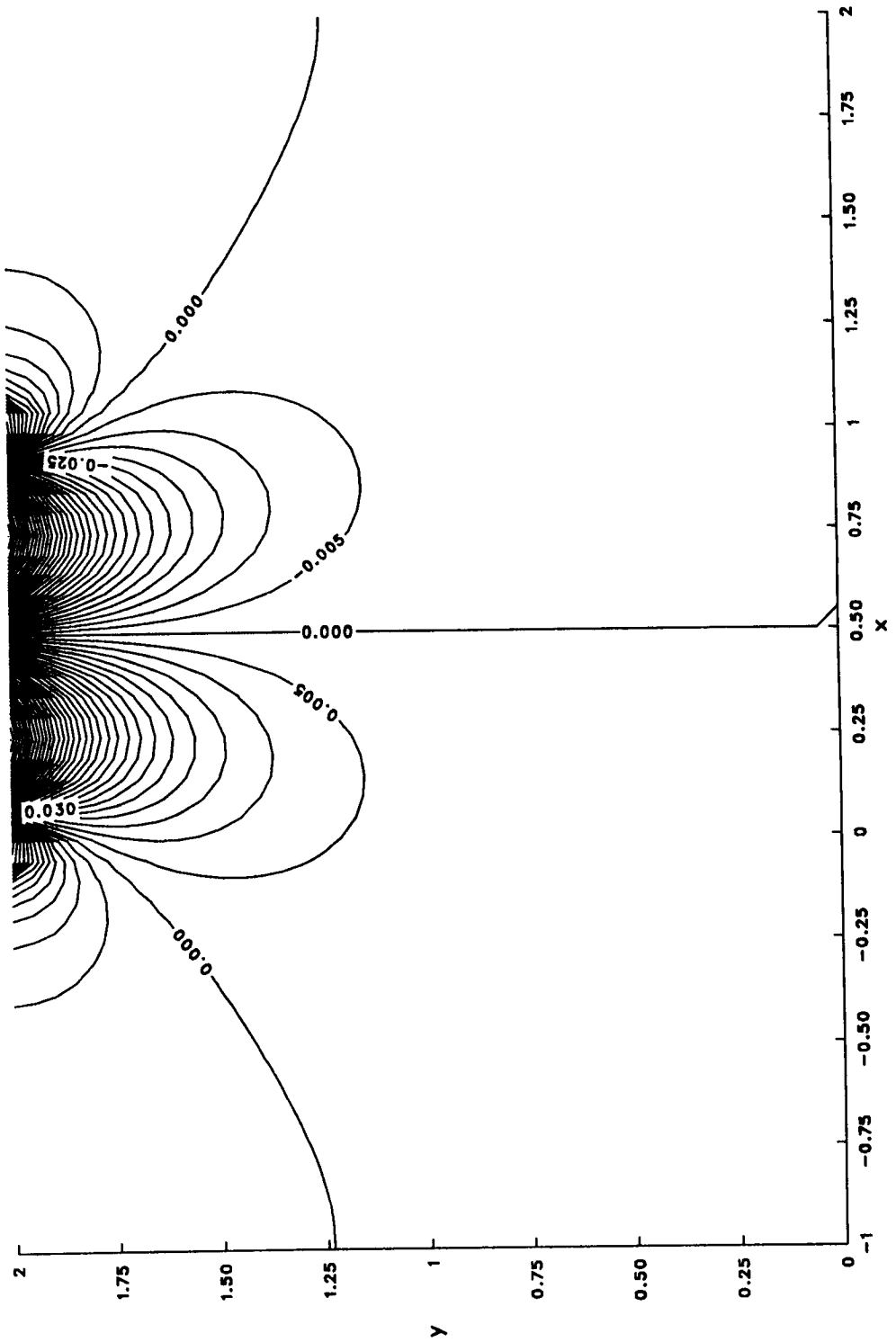

Figure 4.24: Dilatation contours for $M_\infty = 0.6$ flow over a sine wave arc airfoil

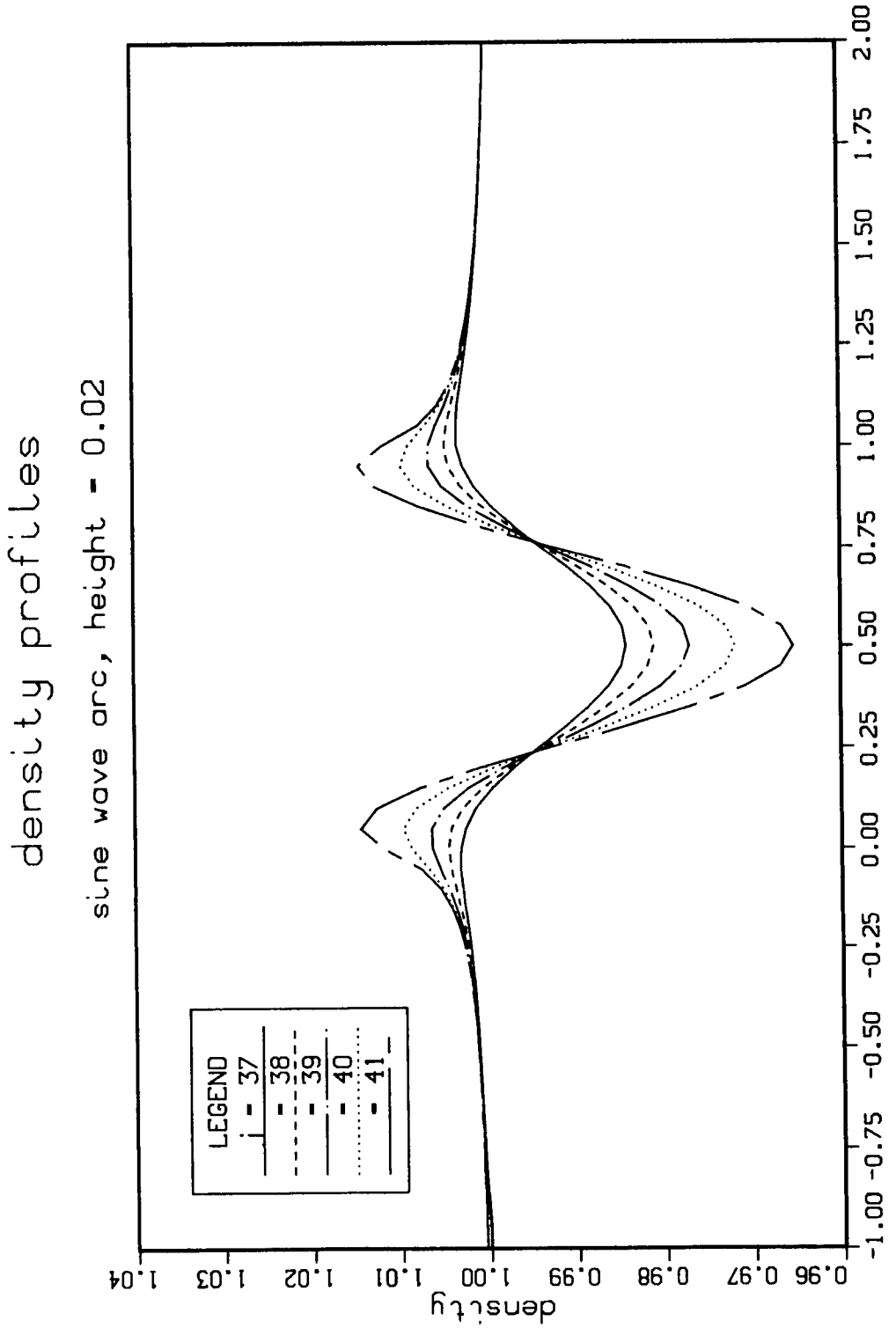

Figure 4.25: Density profiles from inlet to exit for the sine wave arc airfoil

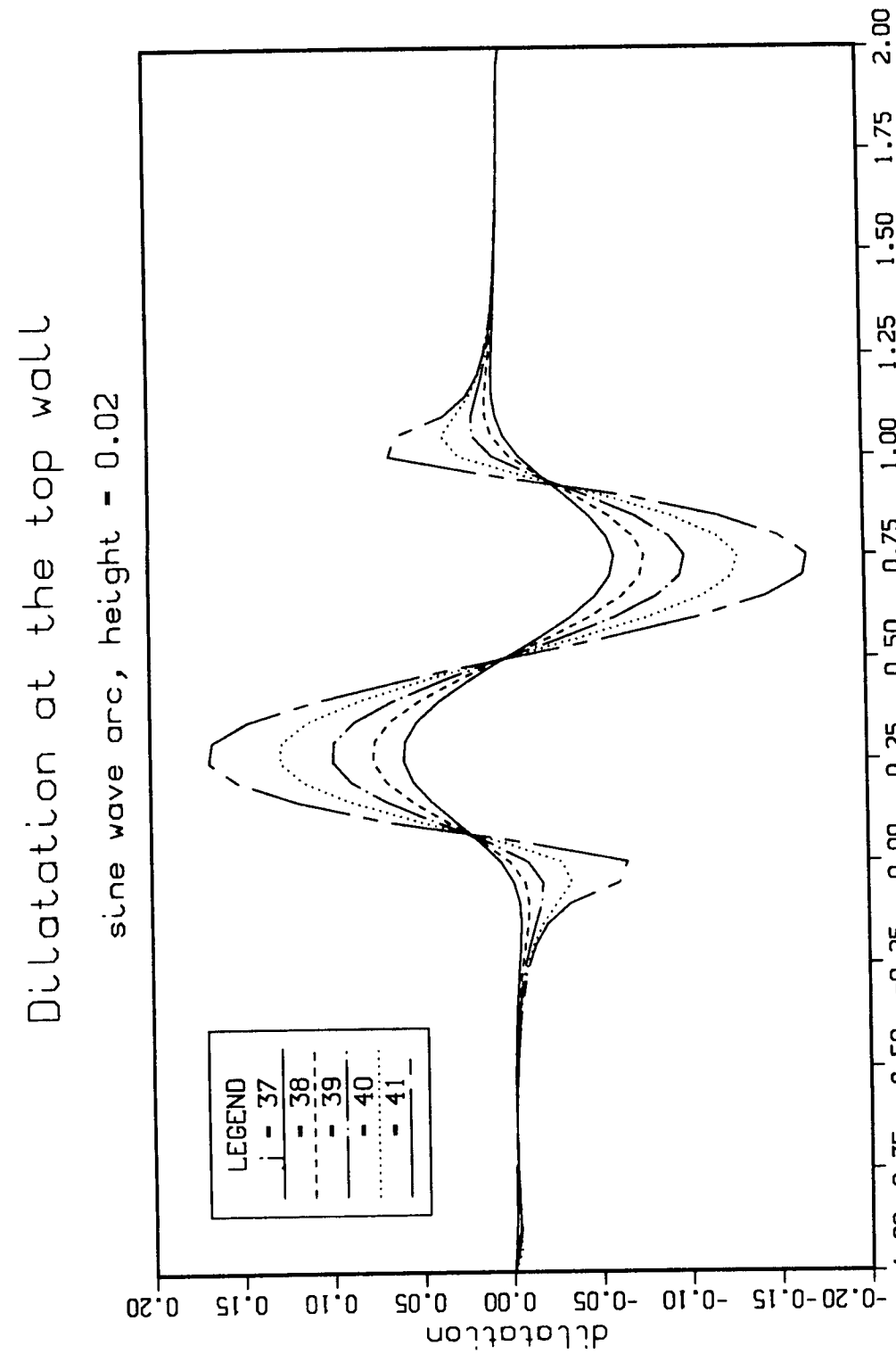

Figure 4.26: Dilatation profiles from inlet to exit for the sine wave arc airfoil

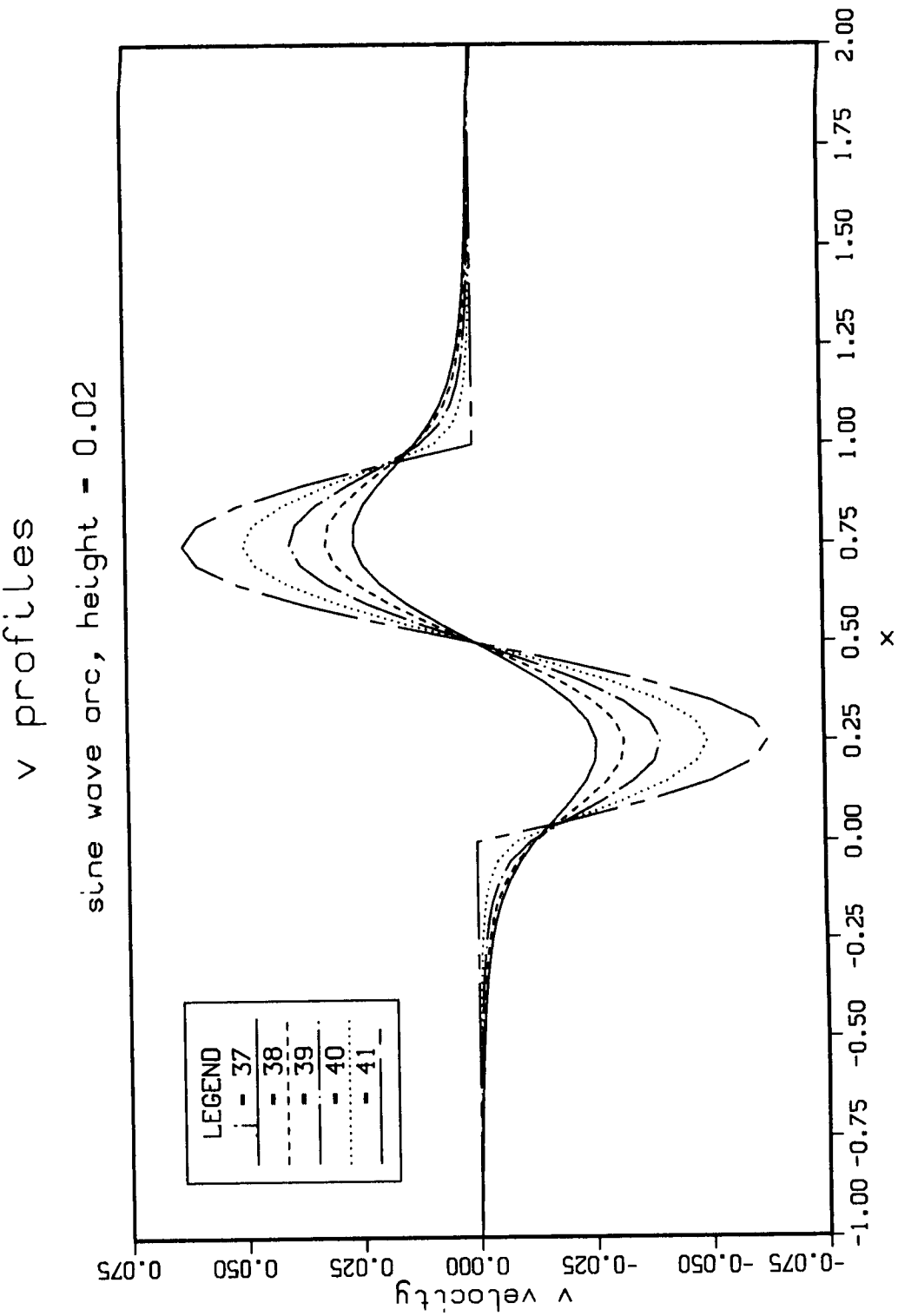

Figure 4.27: V velocity profiles from inlet to exit for the sine wave arc airfoil

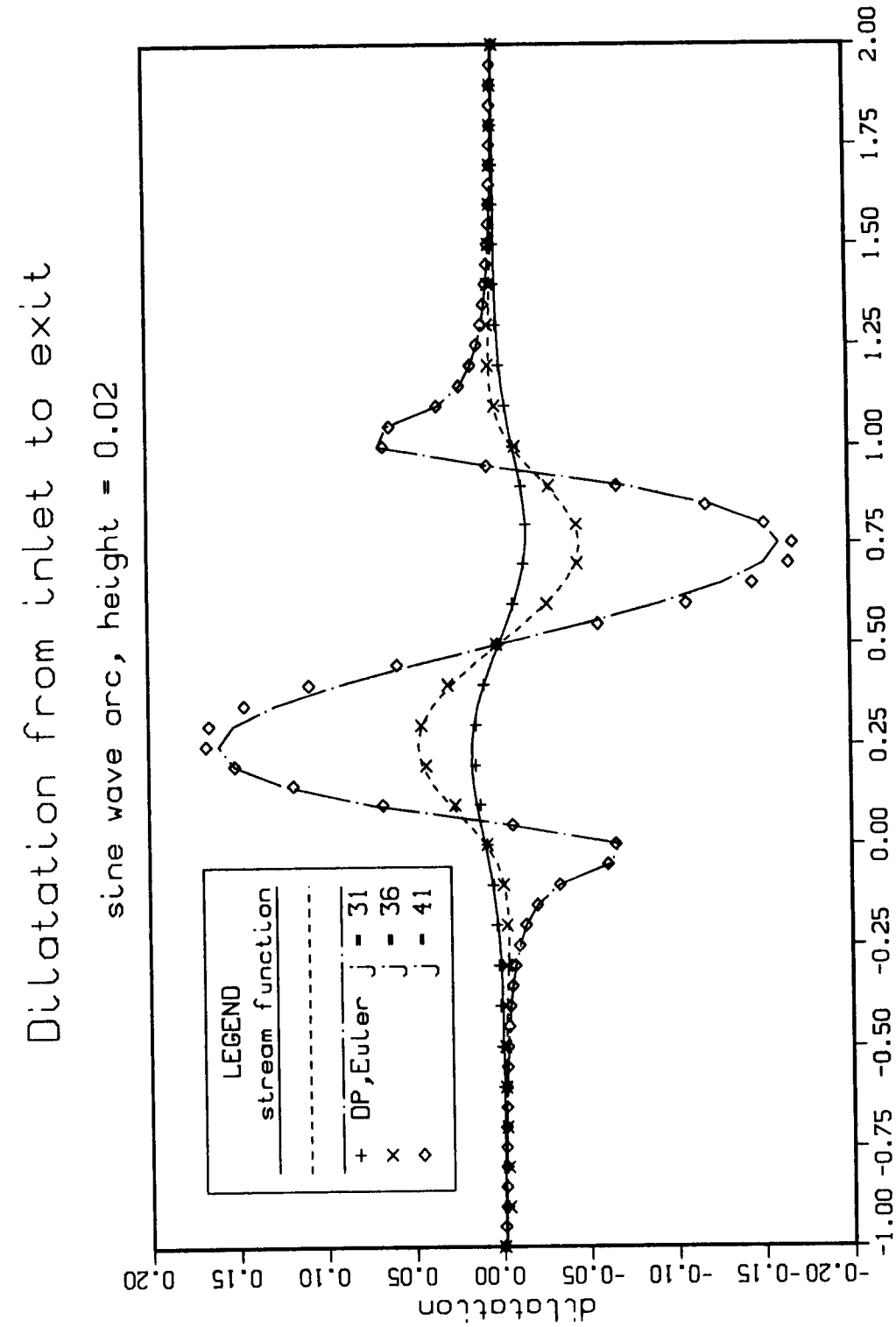

Figure 4.28: Comparison of the dilatation profiles for the stream function and Euler mode of computation by the DP code. Sine wave arc airfoil

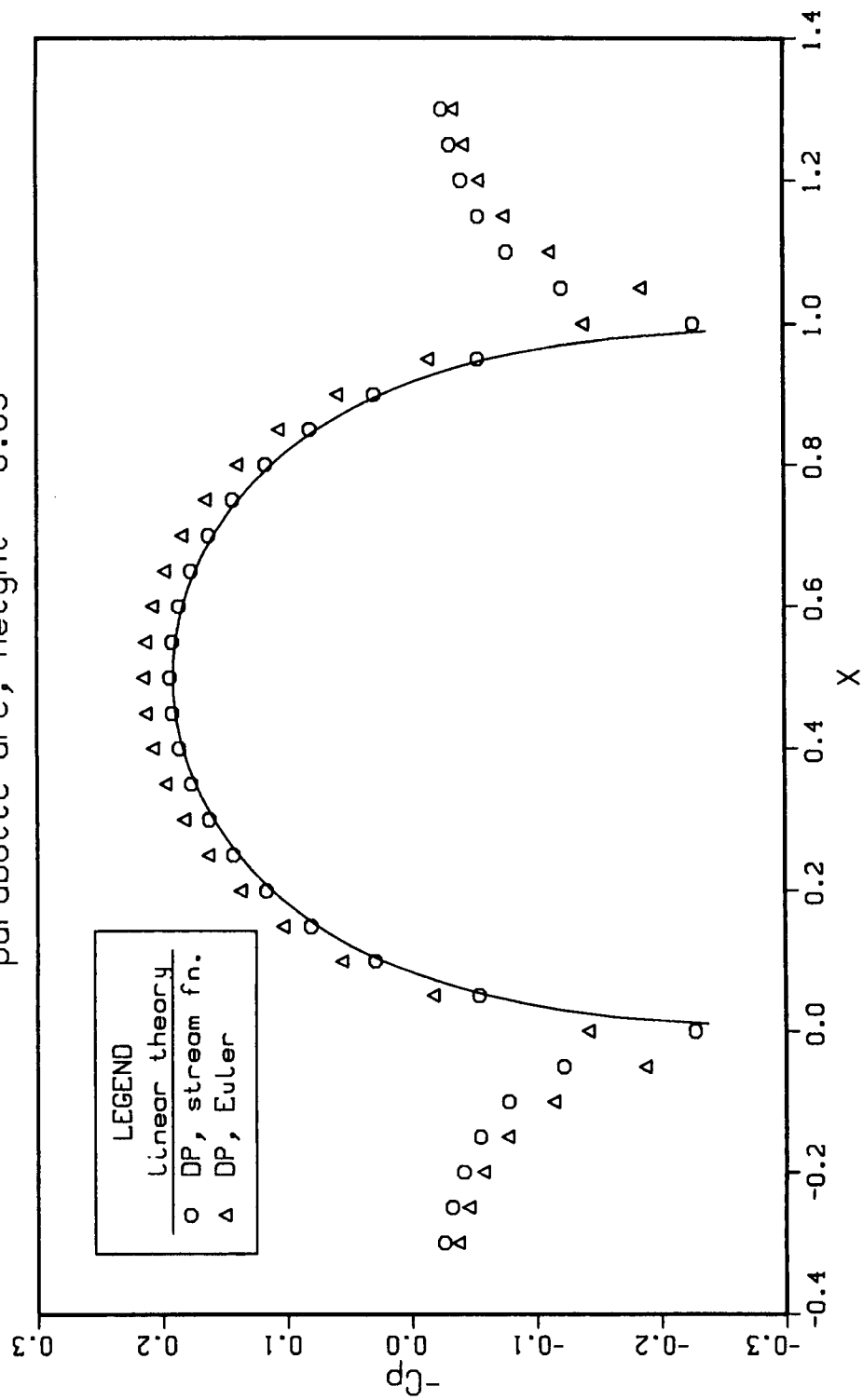

Figure 4.29: Pressure coefficient for $M_\infty = 0.6$ flow over a parabolic arc airfoil with maximum thickness = 6% of chord

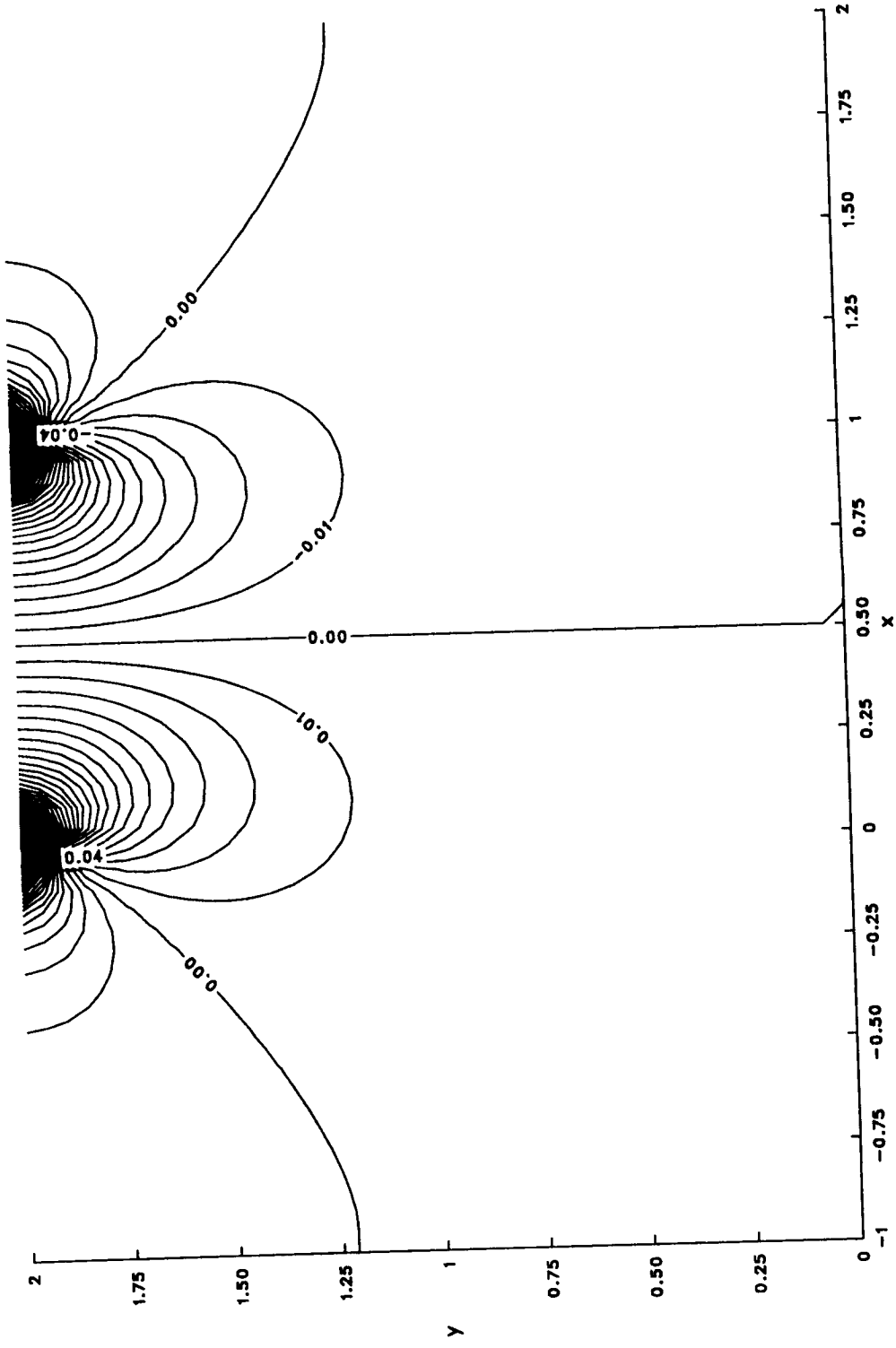

Figure 4.30: Dilatation contours for $M_\infty = 0.6$ flow over a parabolic arc airfoil

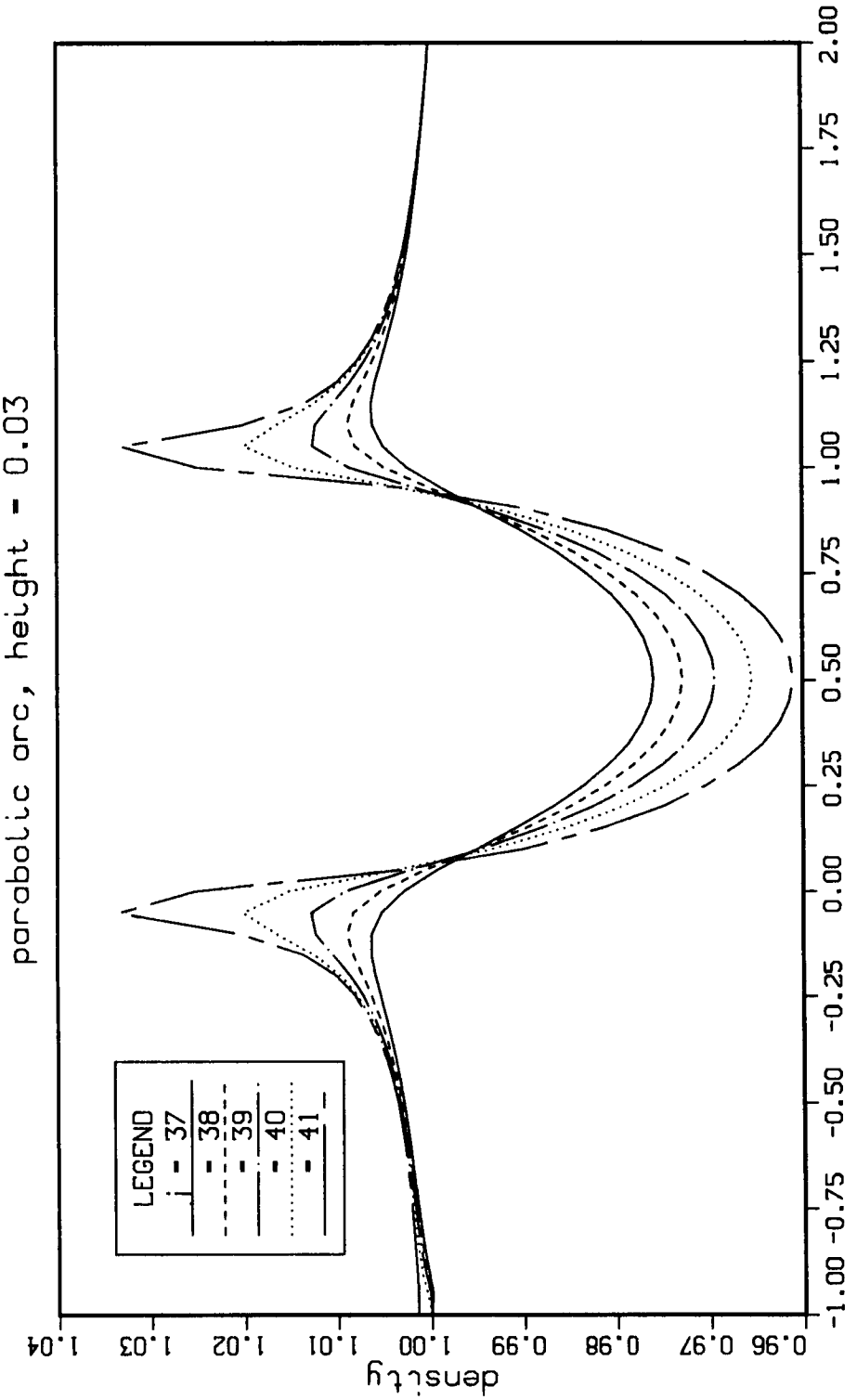

Figure 4.31: Density profiles from inlet to exit for the parabolic arc airfoil

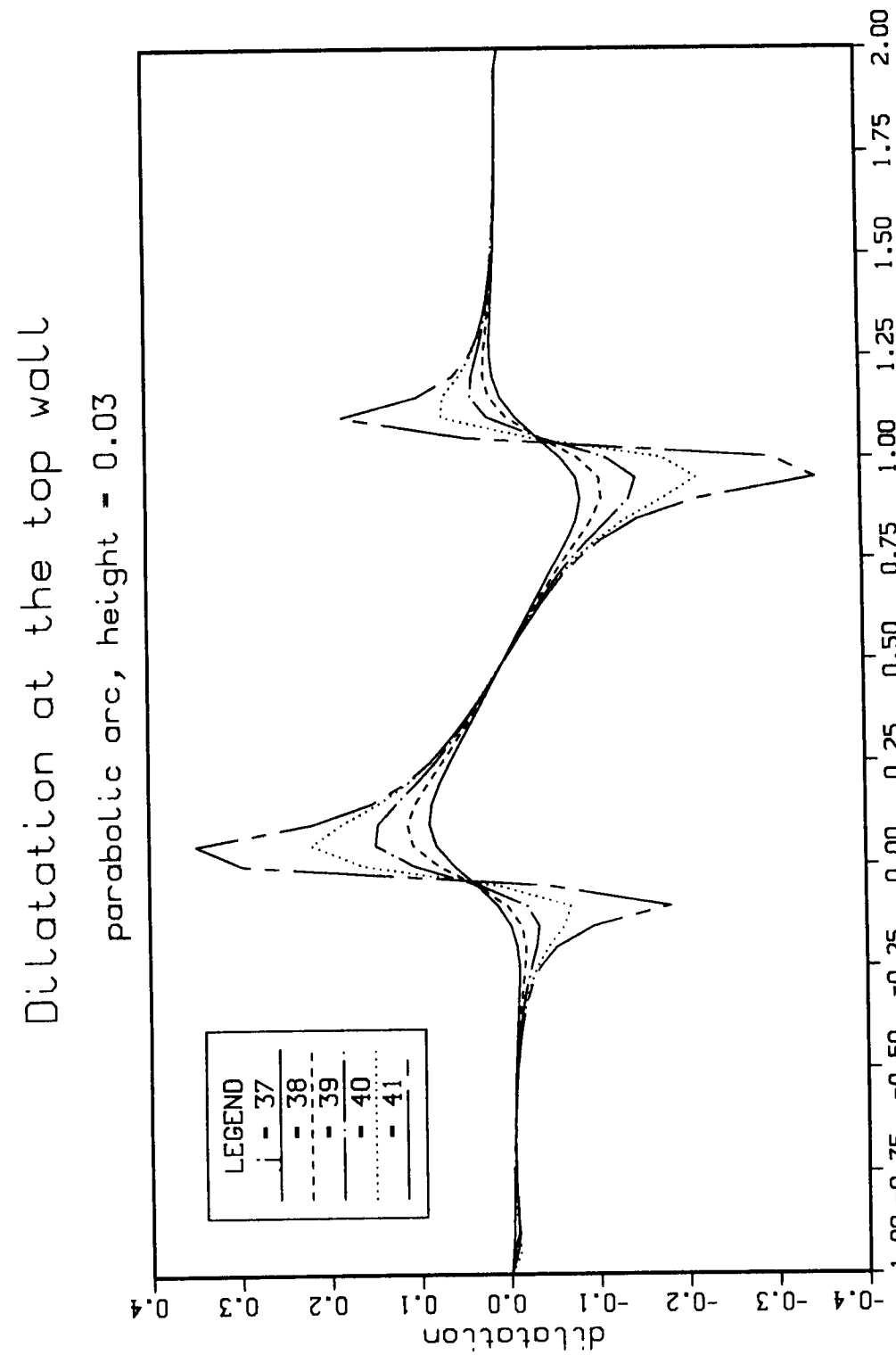

Figure 4.32: Dilatation profiles from inlet to exit for the parabolic arc airfoil

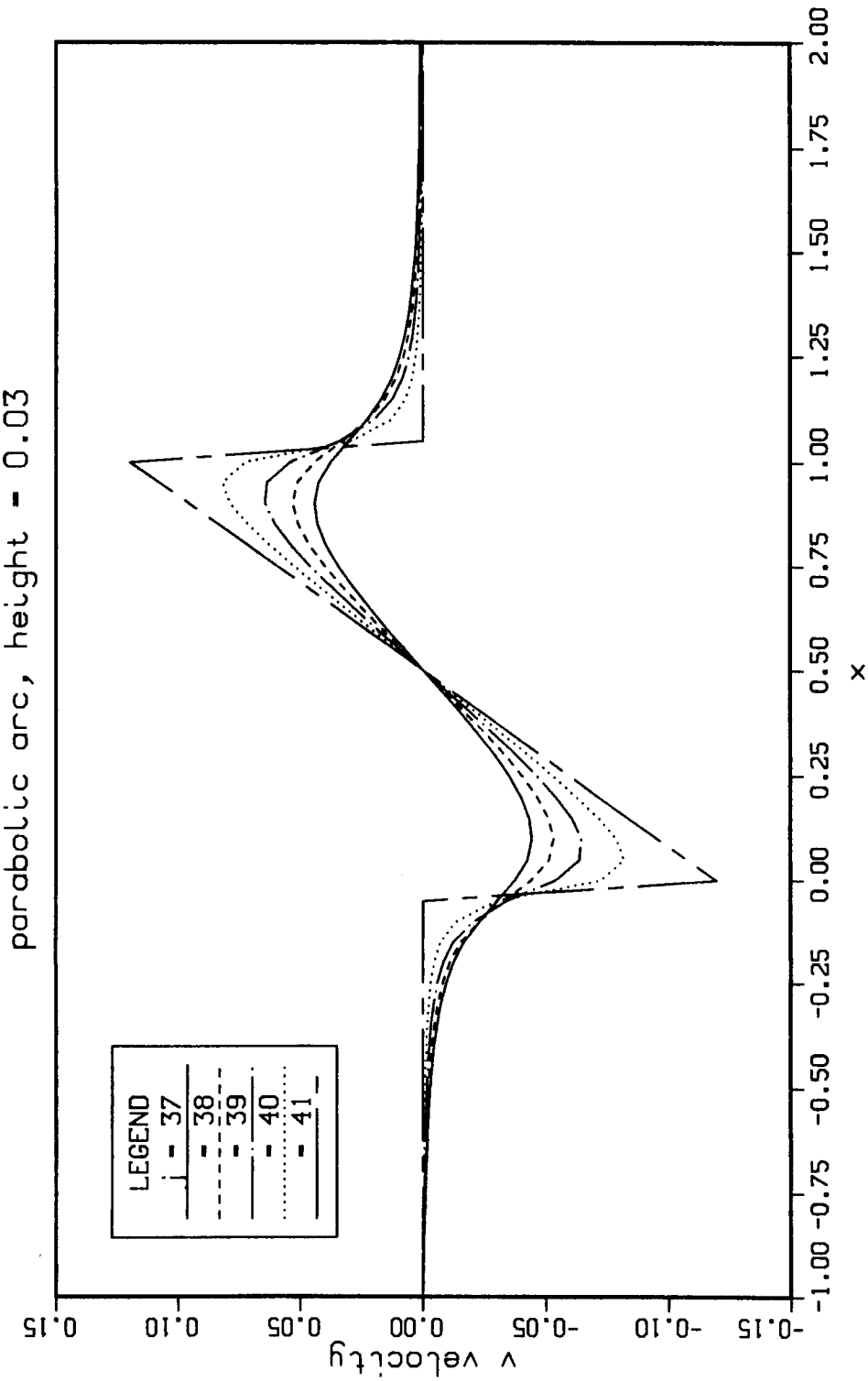

Figure 4.33: V velocity profiles from inlet to exit for the parabolic arc airfoil

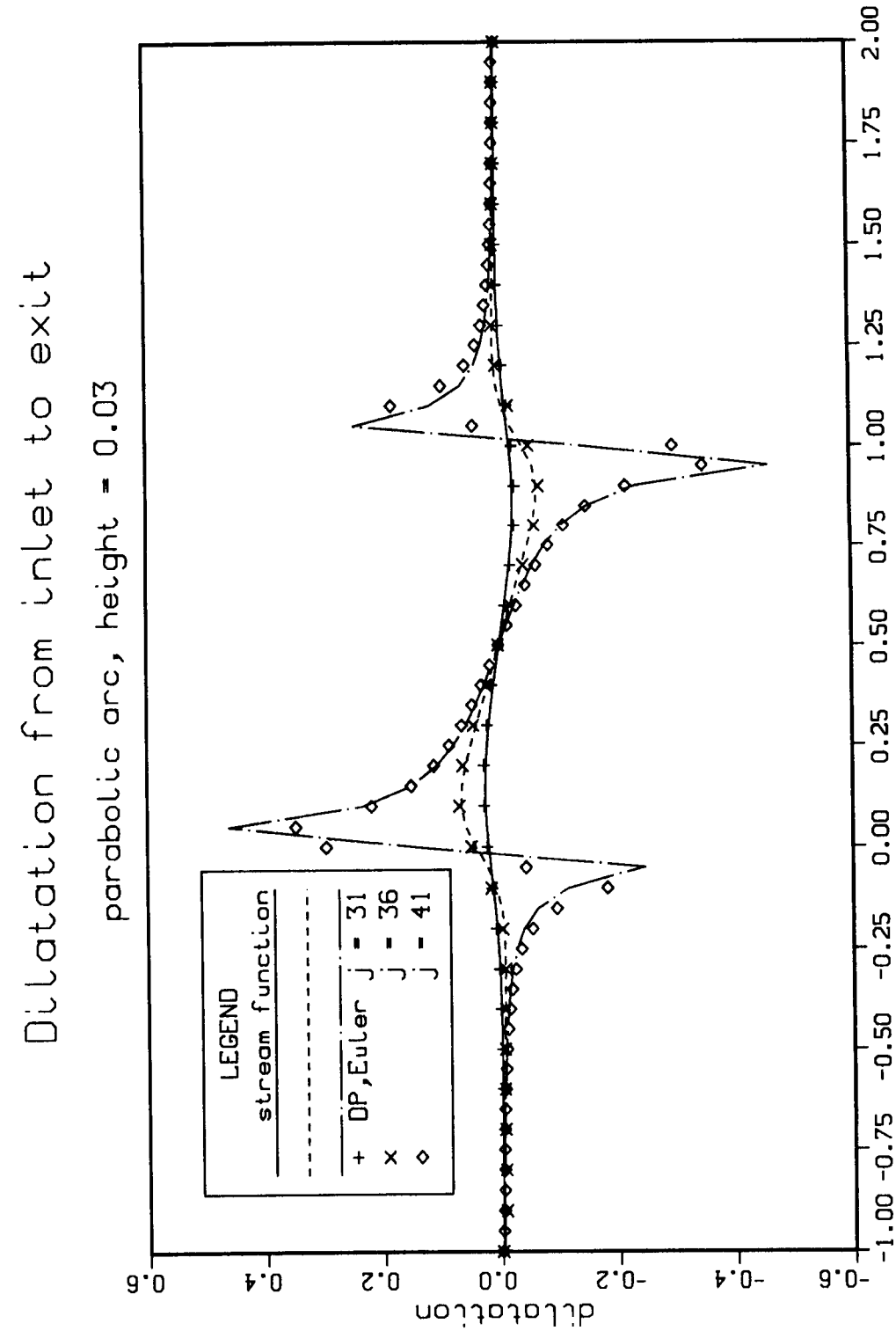

Figure 4.34: Comparison of the dilatation profiles for the stream function and Euler mode of computation by the DP code. Parabolic arc airfoil

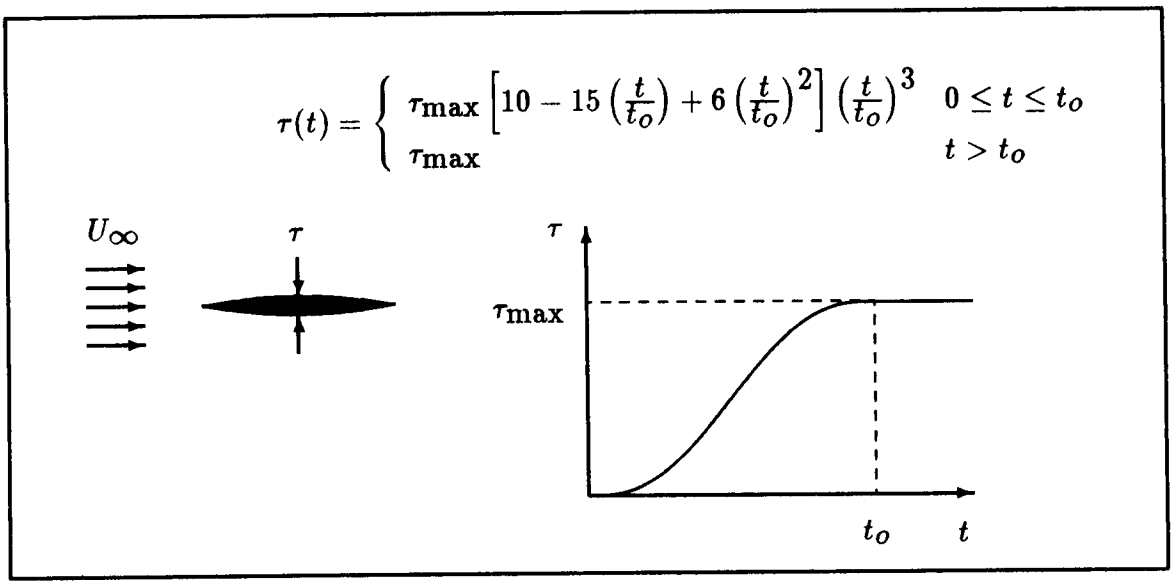

Figure 4.35: Thickening airfoil

The unsteady case computed here is that of an airfoil thickening from zero thickness to 10% of chord. The airfoil grows in 20 chord lengths of time measured with respect to the freestream velocity. The airfoil growth is given in Figure 4.35. For this problem $\tau_{max} = 0.1$ and $t_o = 20$. This test case may be used as a model for the flow about the advancing rotor of a helicopter. The dual potential results are compared to an Euler solution and transonic small disturbance equation solution of Beam and Ballhaus (1975) in Figure 4.36. The pressure coefficient as a function of time is plotted at the position $x/c = 0.525$ measured from the leading edge of the airfoil. The dual potential code in Euler mode computes the unsteady solution for the thickening parabolic arc airfoil in best agreement with the small disturbance computation. All results in the figure are for a domain that is three chord lengths long and extending two chord lengths out from the bump. The grids are nearly alike. The DP code had

61 streamwise by 41 transverse points all uniformly spaced. With a 121×81 grid on this domain the DP solution is only slightly lower (no more than 1.3%) with a more pronounced overshoot. Beam and Ballhaus used 25 points on the airfoil. No claim is made that this solution is grid independent. In fact, further calculations using the DP method on refined grids and on a domain that is five chords in the streamwise and four chords to the far field have given pressure coefficient results that asymptote about 8.5% below the results in Figure 4.36. Though the DP Euler solution is short of the overshoot of Beam and Ballhaus, it is close to the transonic small disturbance (TSD) equation result for this case.

The solution for this unsteady problem converges slowly at first as the scalar potential is computed from an initial field of $\phi = 0$. Later, during periods of slow change, the solution is obtained rapidly. When the bump grows the fastest the solution speed is slowest.

Another result is shown in Figure 4.37. For this test the parabolic arc airfoil grows to 10% thickness in $t = 15$ chord lengths. The dual potential solution is compared to a solution of the linearized transonic small disturbance equation. The pressure coefficient is plotted for $x/c = 0.525$ as measured from the leading edge of the airfoil. Early unsteady calculations made it to steady state by reducing the tolerance on the dilatation, B. The boundary conditions for the unsteady problem are actually fixed for all time except at the bump. Thus, unsteady terms are not required in most boundary conditions at the far- and near-field. A tight tolerance on the scalar potential is important here.

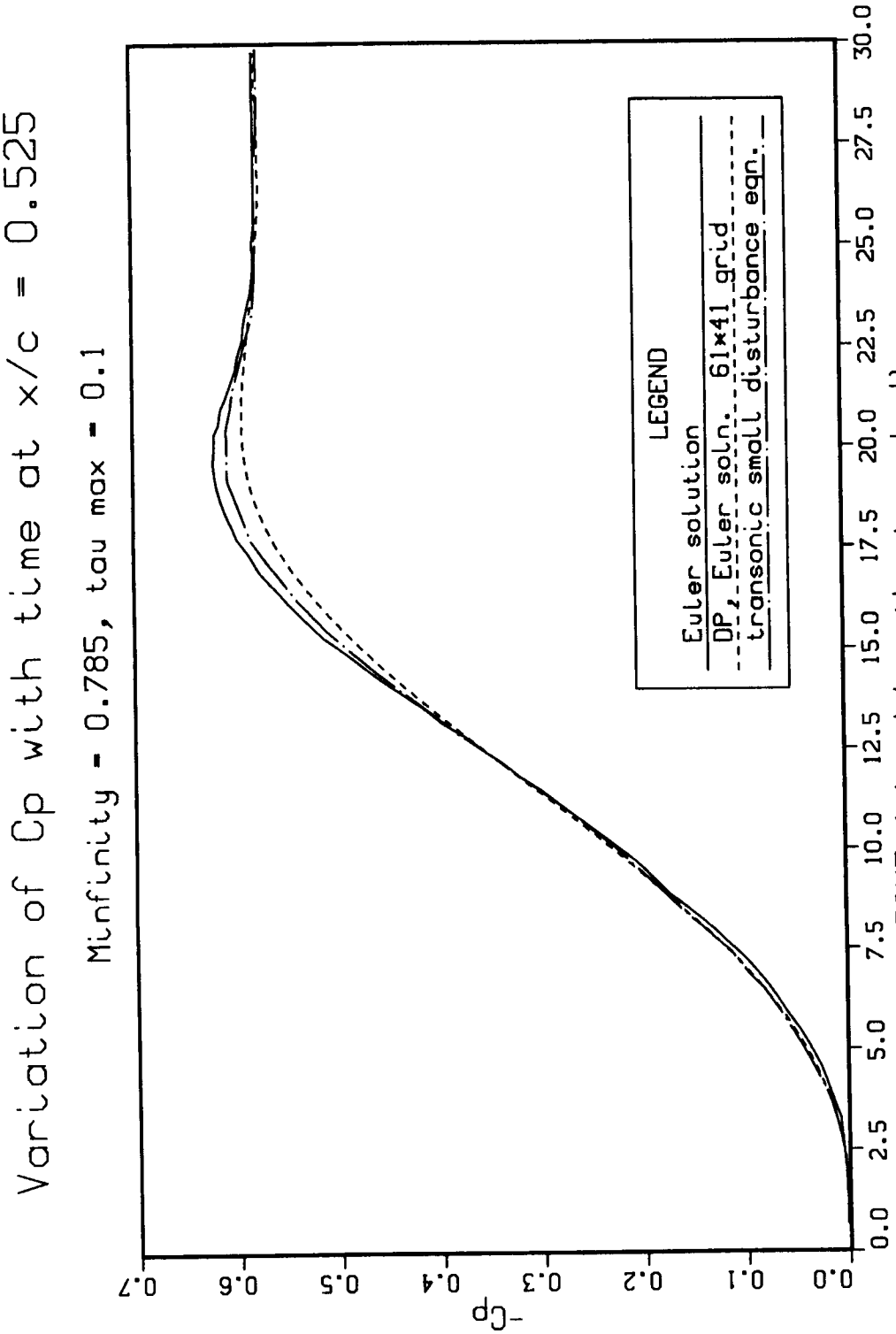

Figure 4.36: Variation of the pressure coefficient with time at $x/c = 0.525$ for a thickening parabolic arc airfoil. $M_\infty = 0.785$, maximum thickness = 0.1 in $t = 20$ chord lengths

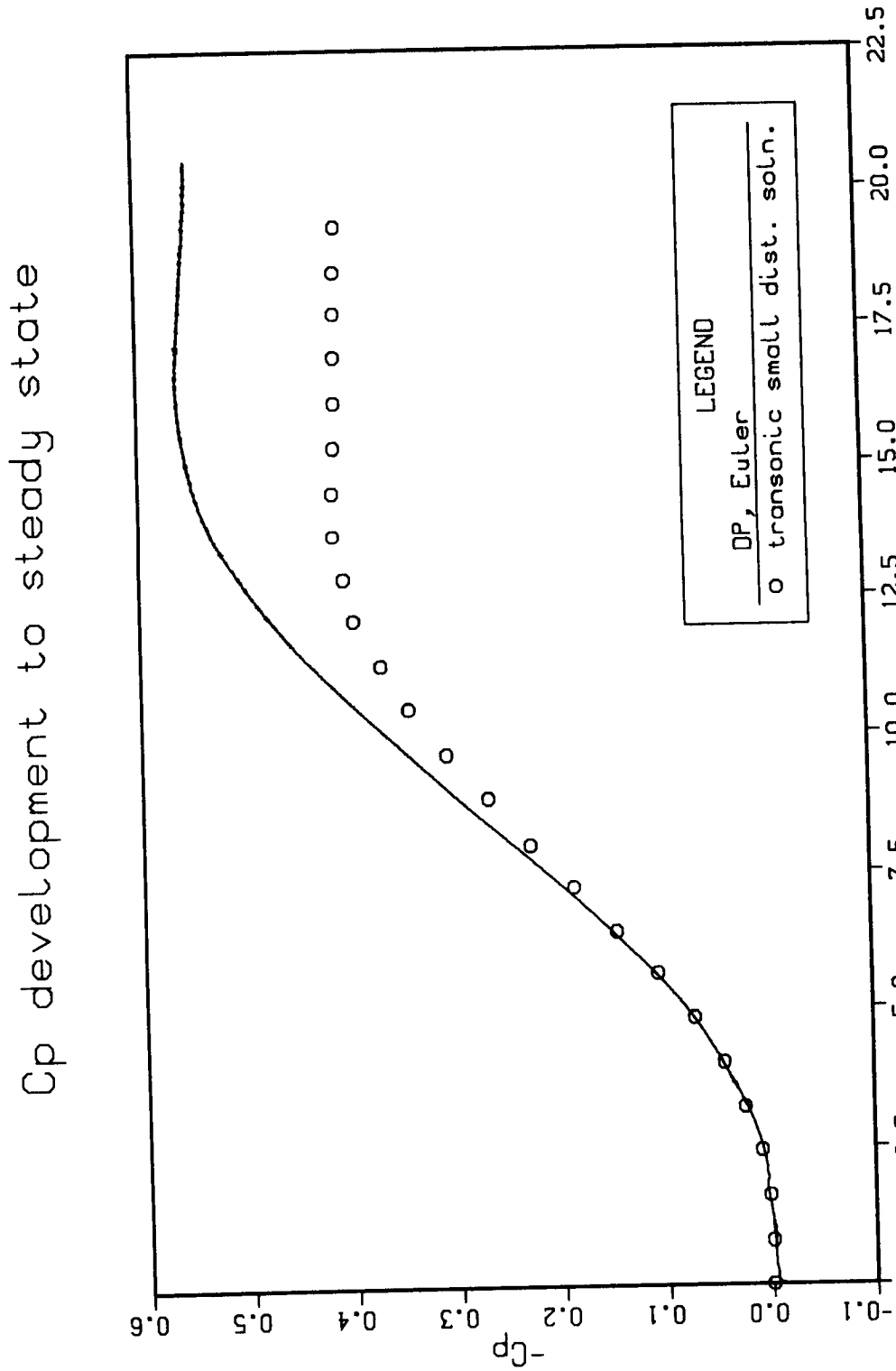

Figure 4.37: Pressure coefficient for a thickening parabolic arc airfoil. $M_\infty = 0.785$, maximum thickness = 0.1 in $t = 15$ chord lengths

4.3.2.3 Steady viscous flow

Variable property channel flows Only a few results will be shown to demonstrate the capability of the dual potential code. Clearly, an infinite number of different wall boundary conditions exist. The full Navier-Stokes solution for variable property flow in a two-dimensional channel could be computed for any wall conditions of interest. The computation of variable property channel flows has not been wholly successful. High wall temperatures and high wall heat fluxes lead to a computed flow separation near the inlet and subsequent reattachment and flow development. The addition of energy to the flow gives a lower "fully-developed" Nusselt number than the constant property cases. Also, the Nusselt number does not asymptote as it does in the constant property case. Rather, the Nusselt number continues to drop for wall heating.

Results for Re = 40 and Re = 150 will be presented for the constant wall temperature case with $\frac{T_{\text{wall}}}{T_{\text{inlet}}} = 1.1$. The higher Reynolds number is more difficult to compute. Contours of temperature, u velocity and dilatation are shown in Figures 4.39, 4.40 and 4.41 for the Re = 40 case. Similar plots for Re = 150 are shown in Figures 4.42, 4.43 and 4.44. The Nusselt number development for these cases is plotted in Figure 4.45 along with results from Schade and McEligot (1971) and a solution from the code of Nelson and Pletcher (1974). Both of these references used the boundary-layer equations.

For a wall temperature of $\frac{T_{\text{wall}}}{T_{\text{inlet}}} = 2.0$ the flow separates near the inlet and redevelops. The separation is evident in the contour plot of u velocity in Figure 4.46. This case does not converge. A high wall heat flux will also not yield a converged

solution. A non-dimensional heat flux, Q, is defined as

$$Q = \frac{q_o'' D_{\text{hyd}}}{k_o T_o} \tag{4.35}$$

A near inlet separation develops as shown in Figure 4.47 for $Q = 25.0$. Lower wall heat fluxes do yield converged solutions. A non-dimensional wall heat flux of $Q = 0.5$ was computed for Re = 150 and M = 0.1. Contours of the temperature, u velocity and dilatation are shown in Figures 4.48, 4.49 and 4.50 respectively. The Nusselt number was again below constant property predictions and does not asymptote but continues to fall. This behavior is expected for solutions which include viscous dissipation (Shah and London 1978).

The difficulties in solving this problem have been isolated to the density and dilatation determination. Let us consider the density first. Density is computed from the continuity equation. Since that equation has first order time, x and y derivatives, only one condition on time, x and y are needed. In Figure 3.3 for the boundary conditions of this problem, however, note that density is constrained by an inlet and two wall conditions. An initial condition is also assumed. This is one condition too many. The specification of the wall density at both walls seems to be the problem. Though many methods of determining the wall density are possible, none seemed to be completely satisfactory. The wall density has been determined alternatively from

1. the x momentum equation solved along the wall,
2. continuity solved at the line of points just above the wall followed by a statement that $p_y = 0$, or
3. density equals a constant, $\rho = \frac{1}{T}$.

Of these, number two gives a constant pressure on a transverse plane, but a realistic looking negative streamwise pressure gradient has not been obtained. Mass is conserved for all of these approaches. All approaches give the same Nusselt number for the conditions computed. So, at least for these low Mach number, and "low" Reynolds number flows, the density doesn't seem to interfere much with the temperature field determination.

Next, consider the dilatation variable, B. The dilatation transport equation evidenced early on that it would be difficult to solve. Many approaches were tried:

1. Divergence theorem constraint on the B field
2. Under-relaxation
3. Weighting the B field using the transport equation solution and the definition, $B = u_x + v_y$ from the velocities.
4. Smaller time steps.

A useful check is to make sure that the solution for the dilatation satisfies the divergence theorem (also called Green's theorem or Green's identity). Only two-dimensional compressible problems in Cartesian grids were studied so the following derivation will be useful for all the compressible test cases.

From the Poisson equation for the scalar potential, Equation 2.13:

$$\nabla^2 \phi = B \tag{4.36}$$

Thus;

$$\iint_D \nabla^2 \phi \, dA = \iint_D B \, dA \tag{4.37}$$

Applying the divergence theorem yields:

$$\iint_D \nabla^2\phi \, dA = \oint_{\partial D} \vec{\nabla}\phi \cdot \vec{n} \, ds = \oint_{\partial D} \frac{\partial \phi}{\partial n} \, ds \tag{4.38}$$

$$\iint_D B \, dA = \iint_D \left(u_x + v_y\right) \, dA = \oint_{\partial D} \left(un_x + vn_y\right) \, ds \tag{4.39}$$

where D is the domain, ∂D is the boundary of the domain and n is the outward unit normal. The implication of the above is that the scalar potential should be used to handle the throughflow velocities at domain boundaries. This is exactly how the scalar potential boundaries are imposed (except for the boundary-layer calculations where the vector potential is used for the throughflow velocity). A representative two-dimensional geometry is shown in Figure 4.38. The outward normal derivative is indicated on the figure. Proceeding counterclockwise around the domain and applying the divergence theorem, the area integral of B must satisfy:

$$\begin{aligned} \iint_D B \, dA \;\; = \;\; & -\int_0^{x_1} v \, dx + \int_0^{y_1} u \, dy \\ & + \int_{x_1}^{0} -v \, dx + \int_{y_1}^{0} u \, dx \end{aligned} \tag{4.40}$$

Writing the above integrals in the positive coordinate directions gives:

$$\begin{aligned} \iint_D B \, dA \;\; = \;\; & -\int_0^{x_1} v \, dx + \int_0^{y_1} u \, dy \\ & + \int_0^{x_1} v \, dx - \int_0^{y_1} u \, dx \end{aligned} \tag{4.41}$$

The area integral of dilatation and the boundary integrals of the throughflow velocities are easily computed to provide a check on the dilatation field.

This constraint was observed to be satisfied automatically to acceptable tolerance for all the compressible problems except the viscous variable property channel flows.

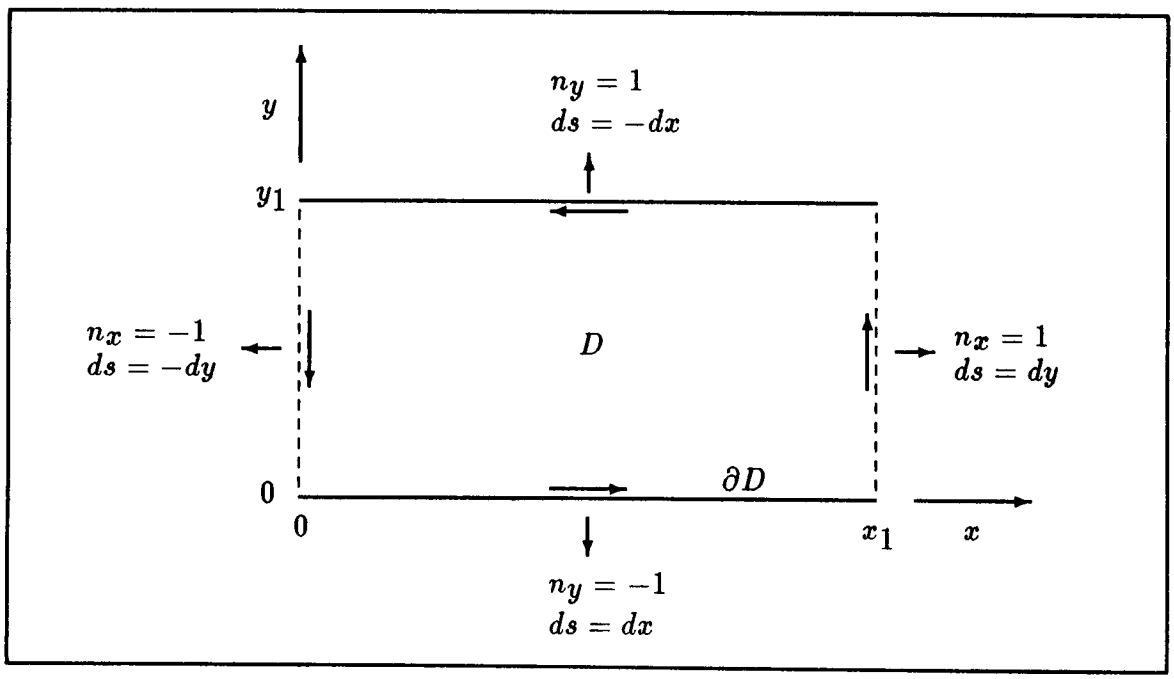

Figure 4.38: 2-D solution domain for divergence theorem application

In that case, converged solutions can best be obtained by enforcing the divergence theorem constraint on the computed B field.

In spite of these problems, solutions were obtained without applying any simplifying assumptions (i.e., no terms were dropped in the governing equations). The results here were obtained by method 2 for the density boundary condition and the divergence theorem constraint applied to the solution for B.

Some trends that were observed will be reported next. For variable property flow, the Nusselt number does not asymptote but continues to fall for wall heating. This is in agreement with the findings of others. Shah and London (1978) indicate that the limiting Nusselt number is zero for variable property flow with wall heating. This is reason for confidence in the trends computed by the dual potential method. Dilatation has no choice but to conform to the numerical satisfaction of Green's theorem. This constraint must be used throughout the calculation. The correction becomes smaller and smaller as the steady state is approached, but without the correction the convergence is slowed and seemingly halted. At this point the only remaining problem appears to be getting a believable negative streamwise pressure gradient. The finest grid solution presented here is for 41×41 points. For this coarse grid the skin friction asymptotes to $C_f \mathrm{Re} = 23.6$. The fully-developed skin friction for an incompressible channel case would be $C_f \mathrm{Re} = 24.0$.

The code runs at 83 MFLOP for full Navier-Stokes calculations. The low wall heating cases converge at $\sim \frac{32\,\mu\mathrm{s}}{\text{global iteration} \times \text{grid point}}$.

Constant wall temperature Converged solutions were obtained for $\frac{T_{\text{wall}}}{T_{\text{inlet}}} = 1.1$. Results for Re = 40 and Re = 150 will be presented. The flow Mach number is M = 0.1. Contours of temperature, u velocity and dilatation are shown in Figures 4.39, 4.40 and 4.41 for the Re = 40 case. Similar plots for Re = 150 are shown in Figures 4.42, 4.43 and 4.44. Recall that the physical distances, x and y, for the two-dimensional channel cases are non-dimensionalized by the hydraulic diameter. The non-dimensional wall separation distance is then $y_{\max} = \frac{1}{2}$ so that y is in the range $0 \leq y \leq \frac{1}{2}$ for the results plotted here from wall to wall. The u velocity contours in Figures 4.40 and 4.43 are similar to results for an incompressible channel case. Notice that the core velocity attains $u = 1.5$ which is the exact value for the incompressible case. The temperature contours in Figures 4.39 and 4.42 are realistic considering that the wall temperature is a constant $\frac{T_{\text{wall}}}{T_{\text{inlet}}} = 1.1$. The dilatation contours indicate that most of the compressible effects for this flow are concentrated near the inlet. The Nusselt number development for these cases is plotted in Figure 4.45 along with results from Schade and McEligot (1971) and a solution from the code of Nelson and Pletcher (1974). Schade and McEligot used the boundary-layer assumptions and neglect viscous dissipation in the energy equation. They compute an increase in Nusselt number for heating when properties are variable. The computations of Pletcher are also based on the boundary-layer equations but include the dissipation terms in the energy equation. His results confirm the behavior predicted by the dual potential solution of the Navier-Stokes equations. Shah and London (1978) also confirm that the Nusselt number does not asymptote for variable property conditions with heating.

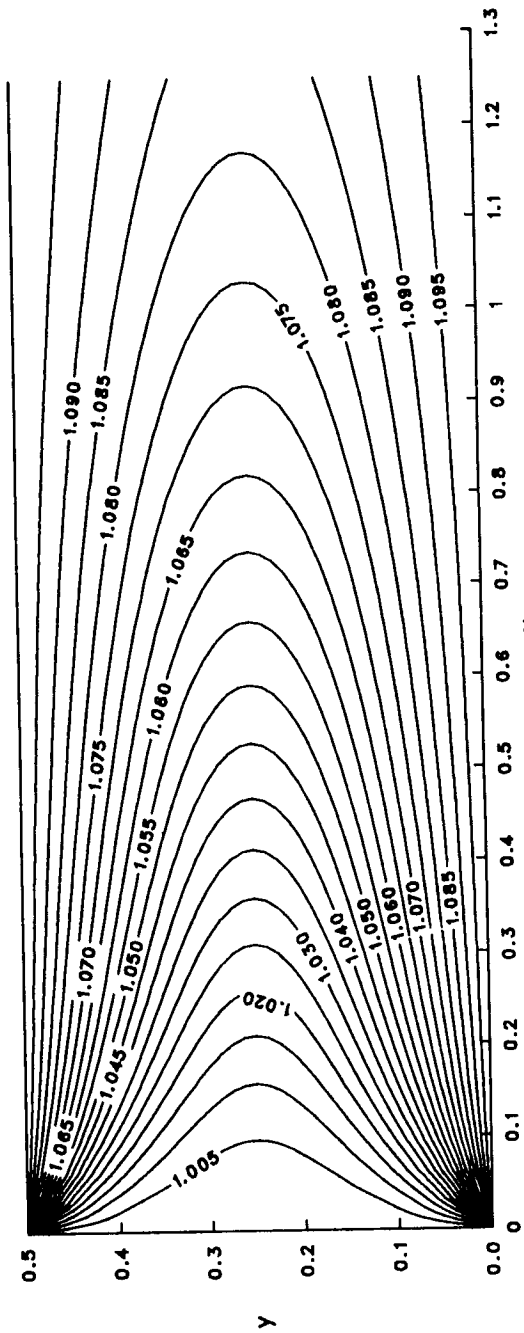

Figure 4.39: Temperature contours for a variable property flow with constant wall temperature. $T_{\text{wall}} = 1.1$, $\text{Re} = 40$ and $\text{M} = 0.1$

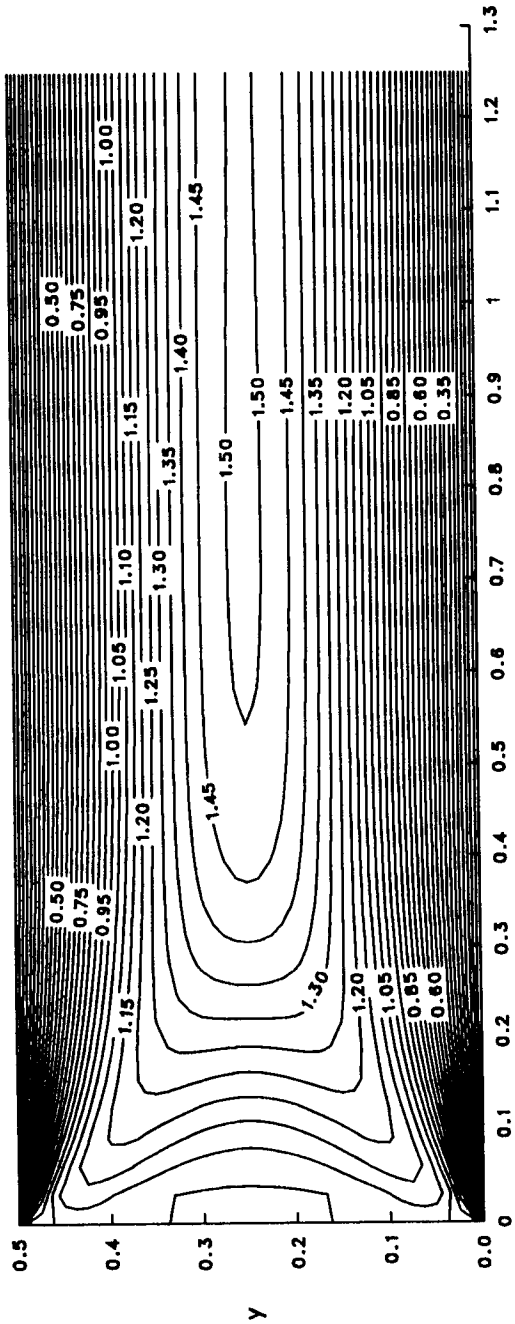

Figure 4.40: U velocity contours for a variable property flow with constant wall temperature. $T_{\text{wall}} = 1.1$, $\text{Re} = 40$ and $\text{M} = 0.1$

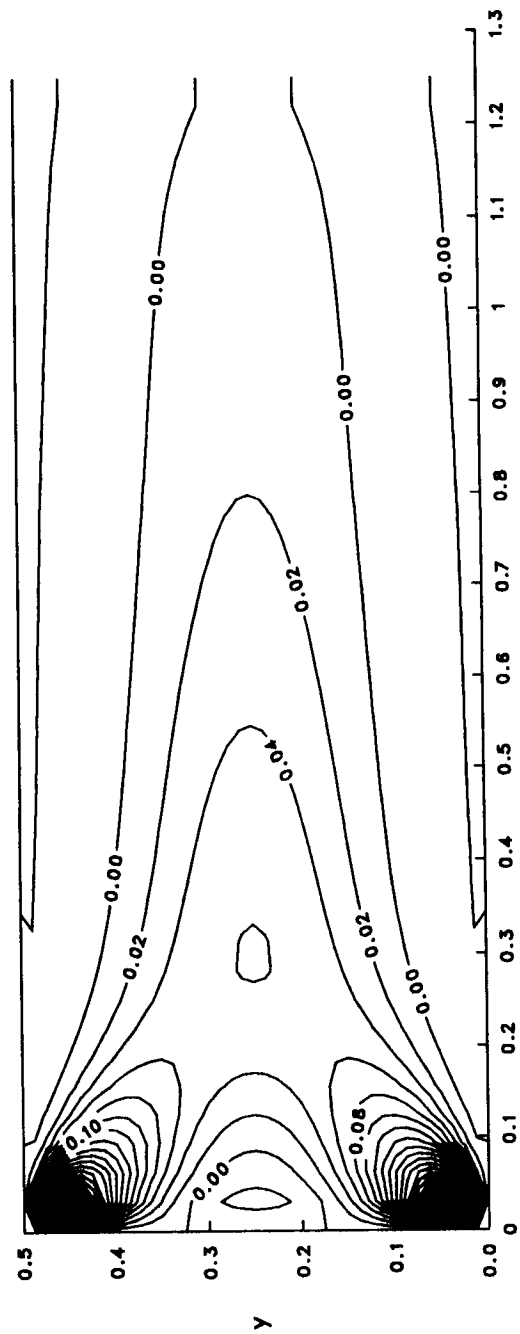

Figure 4.41: Dilatation contours for a variable property flow with constant wall temperature. $T_{\text{wall}} = 1.1$, $\text{Re} = 40$ and $\text{M} = 0.1$

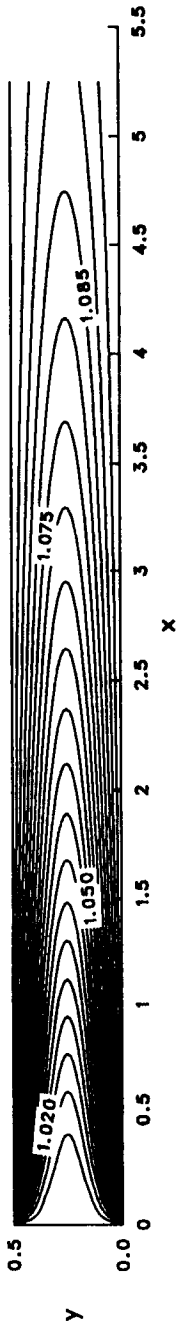

Figure 4.42: Temperature contours for a variable property flow with constant wall temperature. $T_{\text{wall}} = 1.1$, Re = 150 and M = 0.1

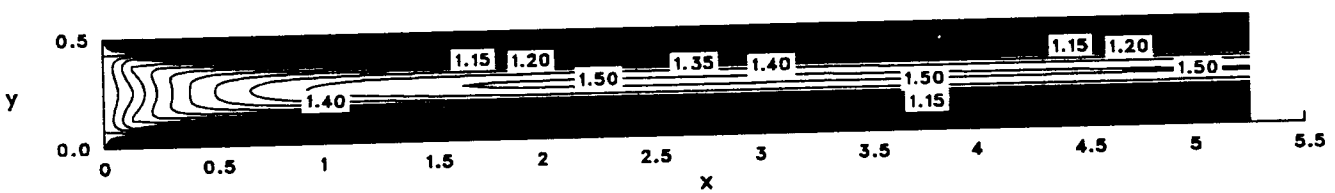

Figure 4.43: U velocity contours for a variable property flow with constant wall temperature. $T_{\text{wall}} = 1.1$, Re $= 150$ and M $= 0.1$

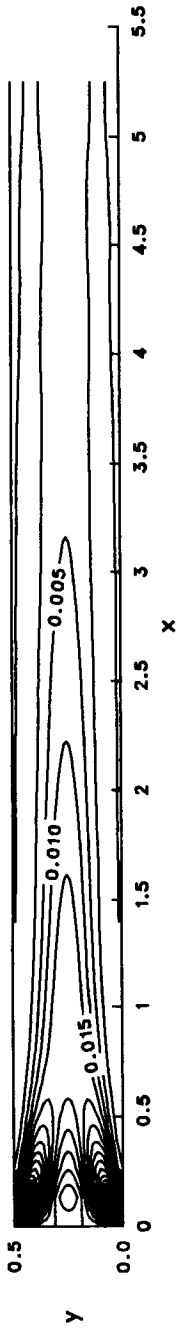

Figure 4.44: Dilatation contours for a variable property flow with constant wall temperature. $T_{\text{wall}} = 1.1$, Re = 150 and M = 0.1

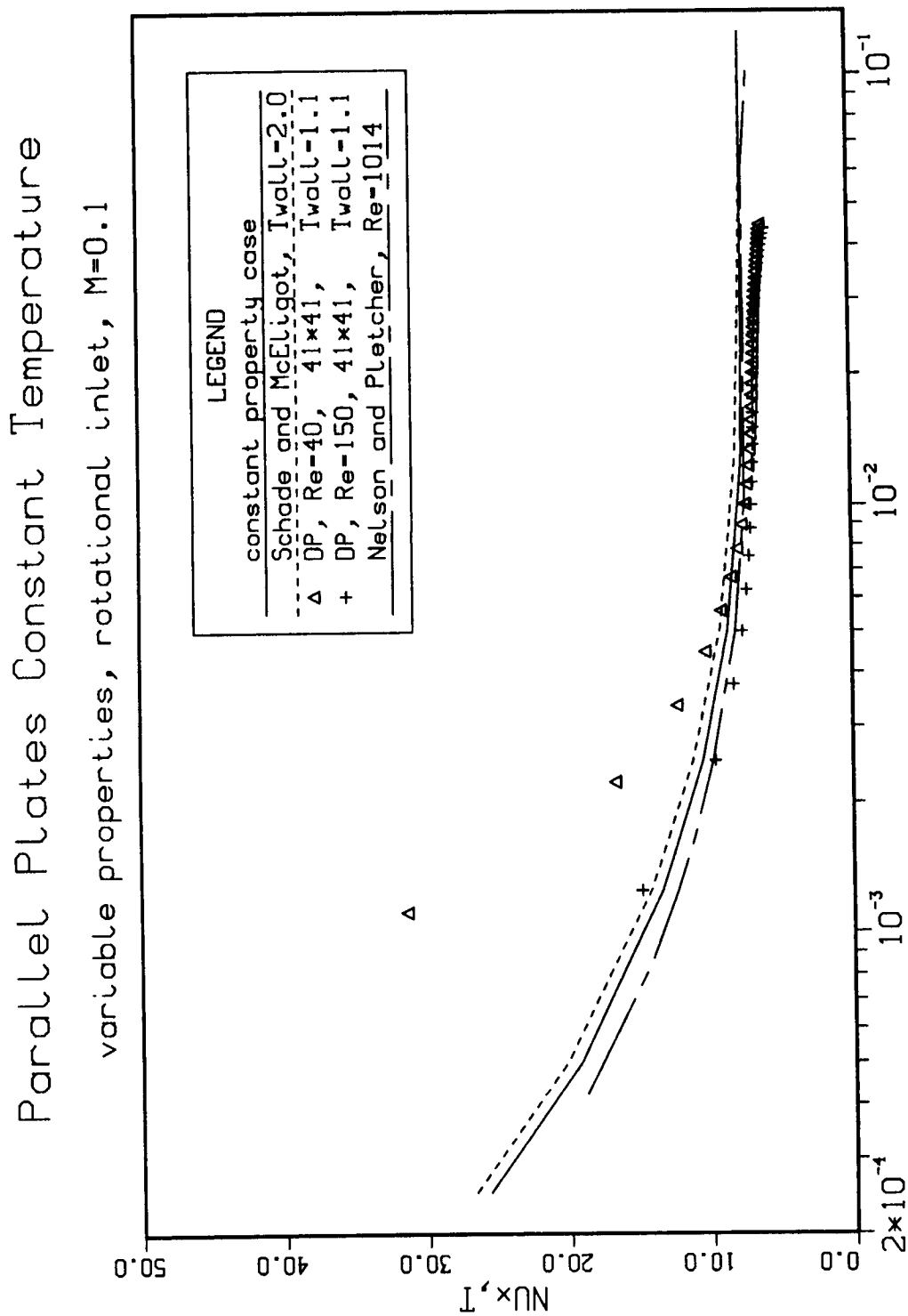

Figure 4.45: Nusselt number comparison for constant wall temperature and variable properties

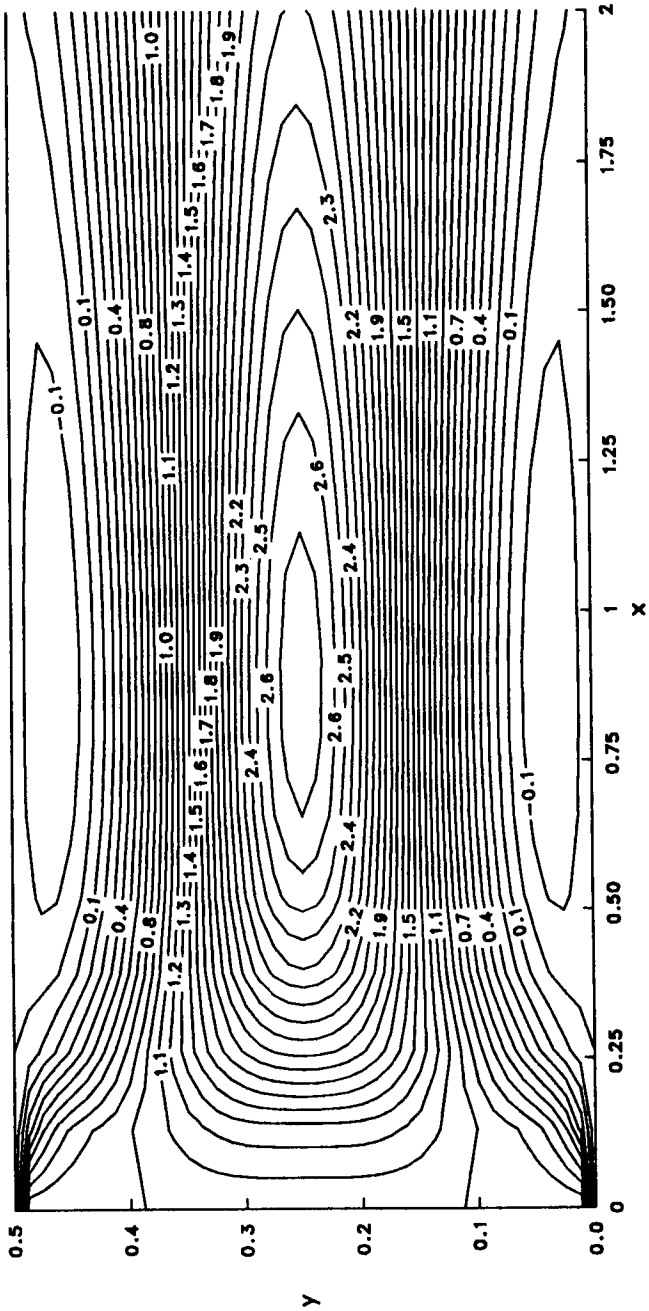

Figure 4.46: U velocity contours near the inlet for a variable property flow with constant wall temperature. $T_{\text{wall}} = 2.0$, Re = 150 and M = 0.1

Figure 4.46 is from the results of the case with $\frac{T_{\text{wall}}}{T_{\text{inlet}}} = 2.0$. This case does not converge. These results are shown mainly to show the separation that is computed by the DP code. For convenience, the constant wall temperature is given as T_{wall} in the figures. It is to be understood that it is actually the ratio of $\frac{T_{\text{wall}}}{T_{\text{inlet}}}$.

Constant wall heat flux Figure 4.47 is for the case with $Q = 25.0$. This case also does not converge. These results are shown mainly to show the separation that is computed by the DP code. The high heat flux and high wall temperature cases exhibit this same feature.

A converged solution is obtained for lower heat fluxes. Results are plotted in Figures 4.48–4.50 for $Q = 0.5$, Re = 150 and M = 0.1. The non-dimensional wall separation distance is $y_{\text{max}} = \frac{1}{2}$ since y is non-dimensionalized on the hydraulic diameter which is simply twice the wall spacing.

Compressible boundary layer

Subsonic freestream The compressible subsonic flow over a flat plate was computed to test the code on an external, viscous, compressible flow case. The conditions at the plate are adiabatic. The normal pressure gradient at the plate, p_y, is assumed to be zero. This is consistent with a boundary-layer assumption. The boundary conditions for this case are shown in Figure 4.51.

The full dual potential method and a variation were used to compute the solution. The variation on the dual potential method was used as a self check on this problem. It uses dilatation computed from the continuity equation and density computed from

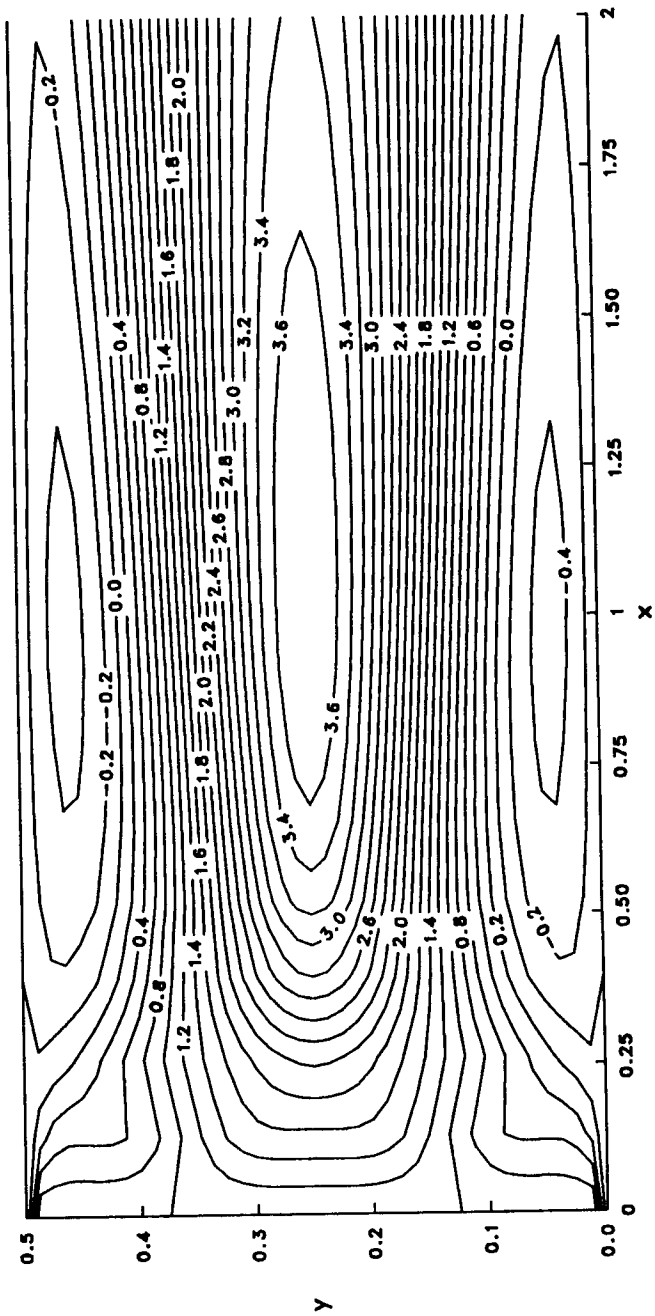

Figure 4.47: U velocity contours near the inlet for a variable property flow with constant wall heat flux. $Q = 25.0$, $\mathrm{Re} = 150$ and $\mathrm{M} = 0.1$

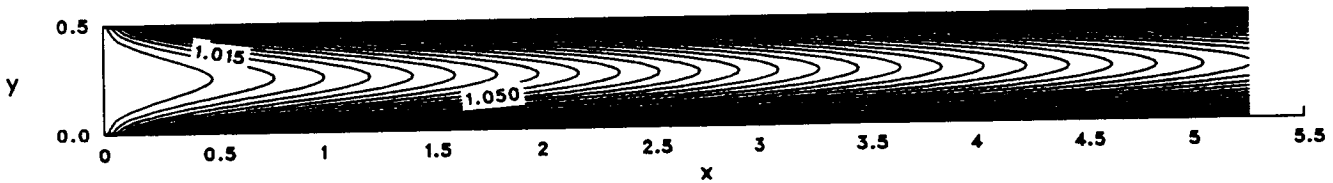

Figure 4.48: Temperature contours for a variable property flow with constant wall heat flux. $Q = 0.5$, Re $= 150$ and M $= 0.1$

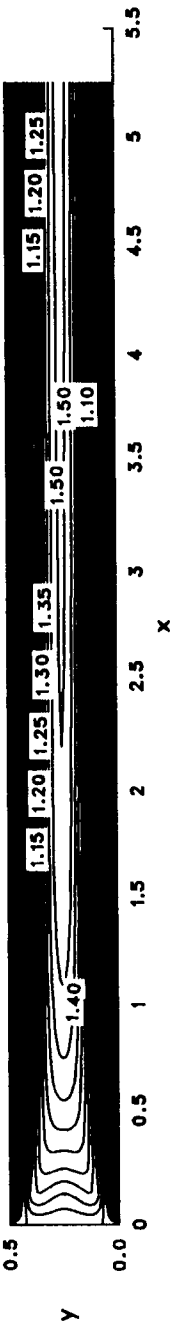

Figure 4.49: U velocity contours for a variable property flow with constant wall heat flux. $Q = 0.5$, $\mathrm{Re} = 150$ and $\mathrm{M} = 0.1$

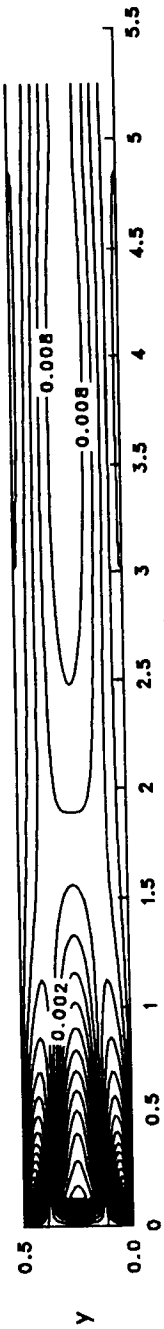

Figure 4.50: Dilatation contours for a variable property flow with constant wall heat flux. $Q = 0.5$, $\mathrm{Re} = 150$ and $\mathrm{M} = 0.1$

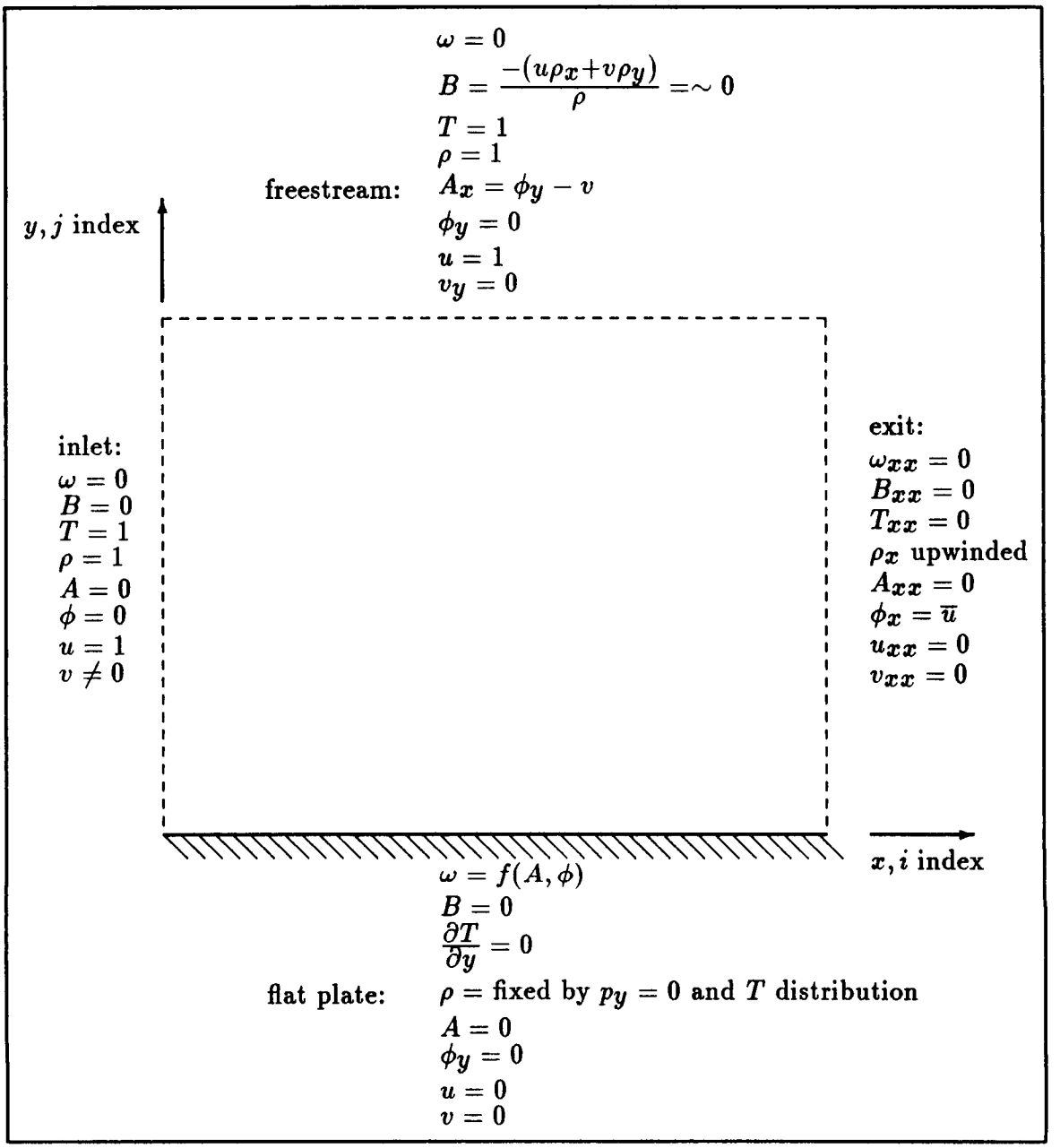

Figure 4.51: Boundary conditions for laminar compressible flow over a flat plate

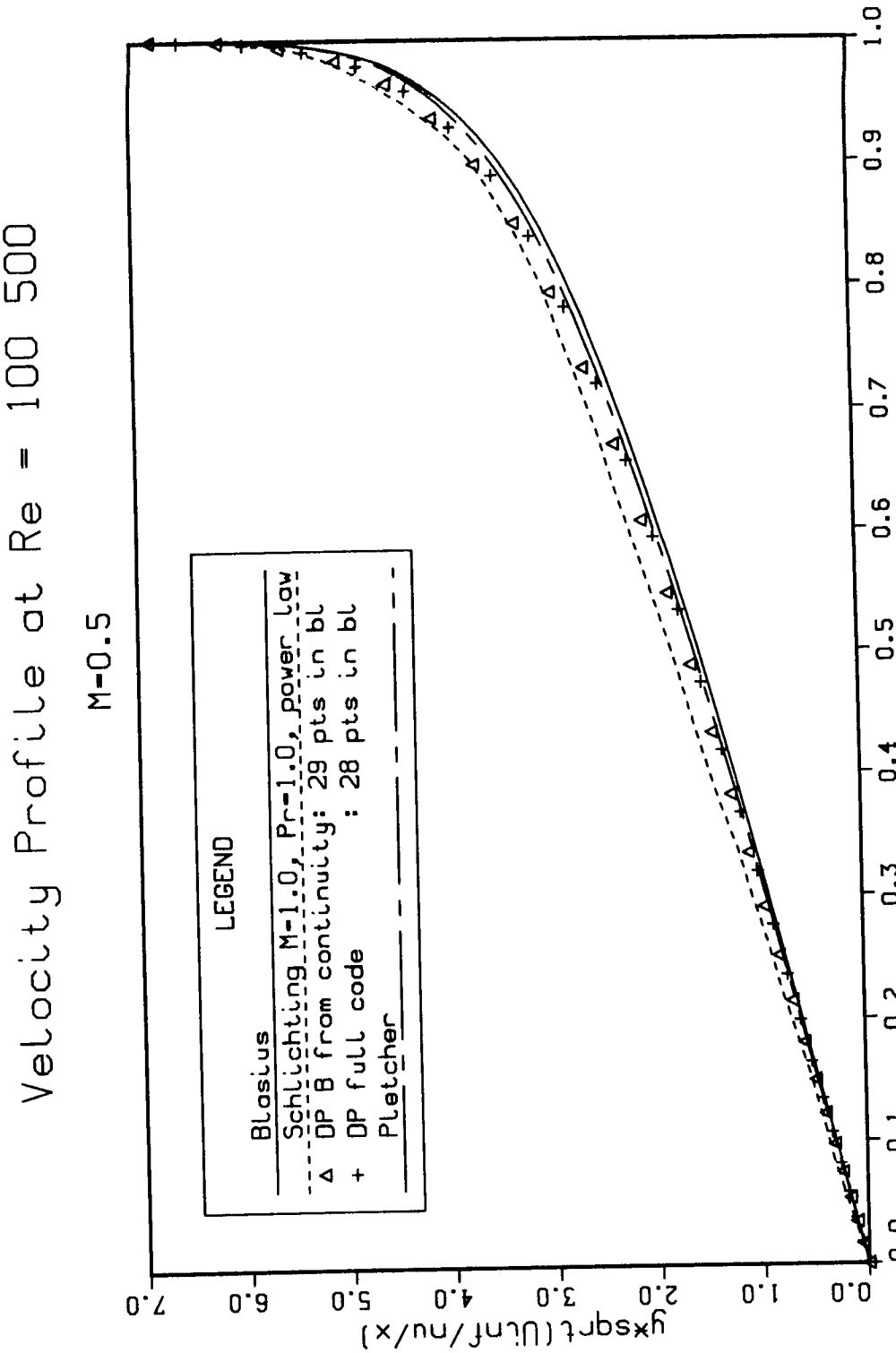

Figure 4.52: Boundary layer profile at $\mathrm{Re}_x = 100,500$ and $\mathrm{M}_\infty = 0.5$

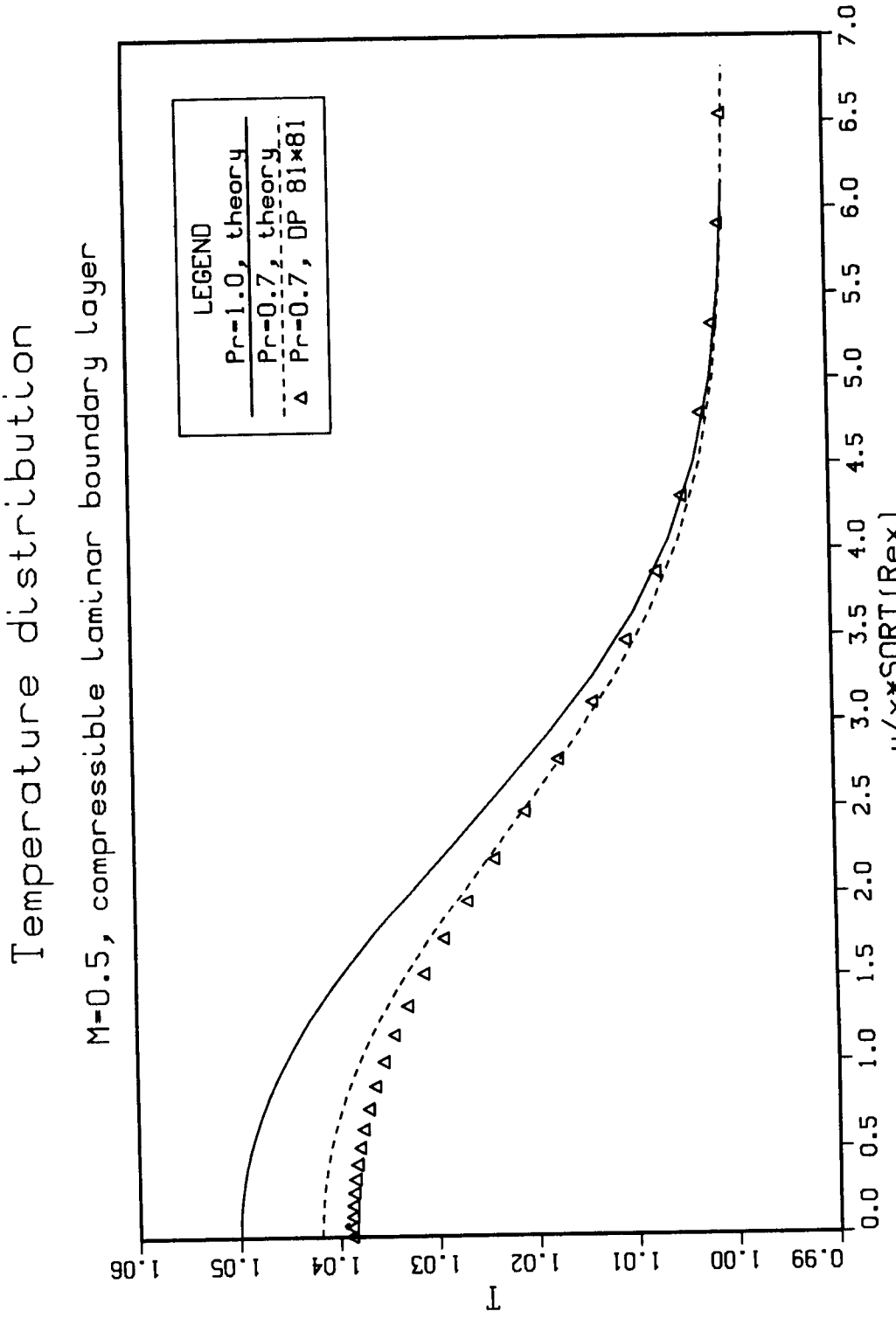

Figure 4.53: Temperature distribution for adiabatic flow over a flat plate at $M_\infty = 0.5$

the ideal gas law as follows. From continuity, and assuming steady state conditions,

$$B = \frac{-\left(u\rho_x + v\rho_y\right)}{\rho}$$

It is possible to assume that the pressure is constant and uniform for this case, so that density can be computed from the ideal gas law by

$$\rho = \frac{p}{RT} = \frac{1}{T} \quad \text{where } \frac{p}{R} = 1$$

This variant is possible because of the simplifying assumptions of this problem. This gives a much faster solution than the transport equations. When the transport equations are solved for dilatation and density, the boundary conditions shown in Figure 4.51 are used. The wall density can actually be obtained by other methods as mentioned in the variable property channel flow discussion on page 146. A comparison of the two solution methods and results from a boundary-layer finite-difference scheme (Christoph and Pletcher 1983) are shown in Figure 4.52 for a M = 0.5 flow. Pletcher's data were computed using the above mentioned finite-difference boundary-layer scheme with approximately 50 points in the boundary layer. For reference, the Blasius profile and a solution at M = 1.0 from Schlichting (1979) are included in Figure 4.52. It can be seen that the compressible boundary layer thickens as the Mach number increases.

The temperature profile for this case is shown in Figure 4.53. The results from the boundary-layer finite-difference scheme are not plotted but coincide with the Pr = 0.7 theoretical curve. More grid points in the dual potential solution could be required for better agreement. However, the results are within 1% of theory. In the present calculations, the wall temperature is computed by using the zero wall

derivative condition for temperature as a boundary condition on the energy equation. Pletcher reported setting the adiabatic wall temperature in his calculations. The wall temperature is 1.042 by theory and 1.039 as computed using the dual potential method.

This was the first compressible viscous case to be computed successfully. There was initially a problem computing this flow using the full dual potential equation set. The dilatation transport equation could only be converged by dropping the terms which originated from the pressure terms in the primitive variable momentum equations. (Dropping those terms is equivalent to assuming that the pressure is everywhere constant.) This led to the determination that those terms (second order derivatives in the B equation source term) must be differenced conservatively. This is necessary because the pressure gradient is zero, yet numerically it is non-zero for $p = \rho RT$ substituted into the pressure derivative terms.

These cases were computed by the full dual potential method without using boundary-layer assumptions other than $p_y = 0$ at the plate. The full energy equation was used. Streamwise convective terms were upwinded. The time step limitation is controlled by the dilatation variable. The skin-friction development is nearly indistinguishable from the incompressible boundary layer solution for an irrotational inlet. The skin friction asymptotes to a value slightly lower than for incompressible flow with the difference in the fourth place behind the decimal point (*cf.* Van Driest 1952). The asymptotic value computed here was $C_f\sqrt{\mathrm{Re}} = 0.6646$ at $\mathrm{Re}_x = 100,500$. At the same Reynolds number the incompressible solution computed $C_f\sqrt{\mathrm{Re}} = 0.6647$.

With 81 transverse points it is observed that the vorticity magnitude is less than

10^{-5} from $j = 35$–81 and the dilatation magnitude is less than 10^{-5} from $j = 54$–81. The solvers for vorticity and dilatation can be shut off beyond these points with no adverse affect on the solution and a speed up of approximately 14%.

Supersonic freestream A supersonic flow over a flat plate was also computed. The conditions at the plate are adiabatic. The result in Figure 4.54 was obtained by computing the dilatation from the continuity equation. A zero streamwise pressure gradient was assumed. Then, by the boundary-layer assumption, a zero normal pressure gradient is also assumed so that pressure is constant for this problem. The dilatation may then be computed from the continuity equation

$$B = \frac{-\left(u\rho_x + v\rho_y\right)}{\rho} \tag{4.42}$$

and density can be computed from the ideal gas law and the constant pressure assumption

$$\rho = \frac{p}{RT} = \frac{1}{T} \text{ for a unit pressure field.} \tag{4.43}$$

It was not possible to compute this flow using the transport equation for B.

The abscissa in Figure 4.54 is $\frac{y}{\delta_2}$ where δ_2 is the momentum thickness defined by

$$\delta_2 = \int_{y=0}^{\infty} \frac{\rho u}{\rho_\infty U_\infty}\left(1 - \frac{u}{U_\infty}\right) dy$$

Experimental results for this case were obtained by O'Donnell (1954). The theoretical calculation is by Chapman and Rubesin (1949). The achievement of good results here may be due in part to the use of the fixed pressure assumption.

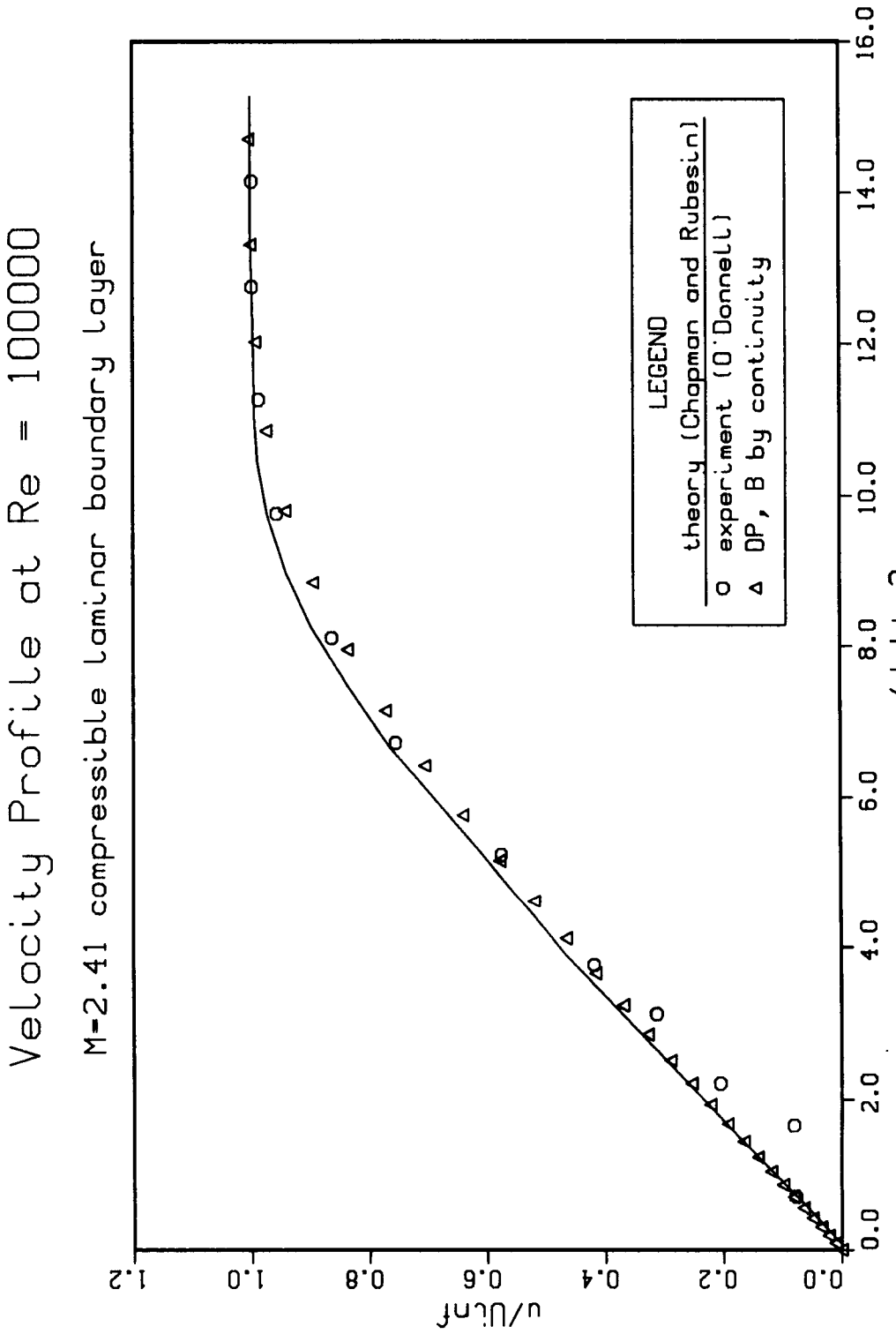

Figure 4.54: Velocity profile in an adiabatic laminar boundary layer in supersonic flow

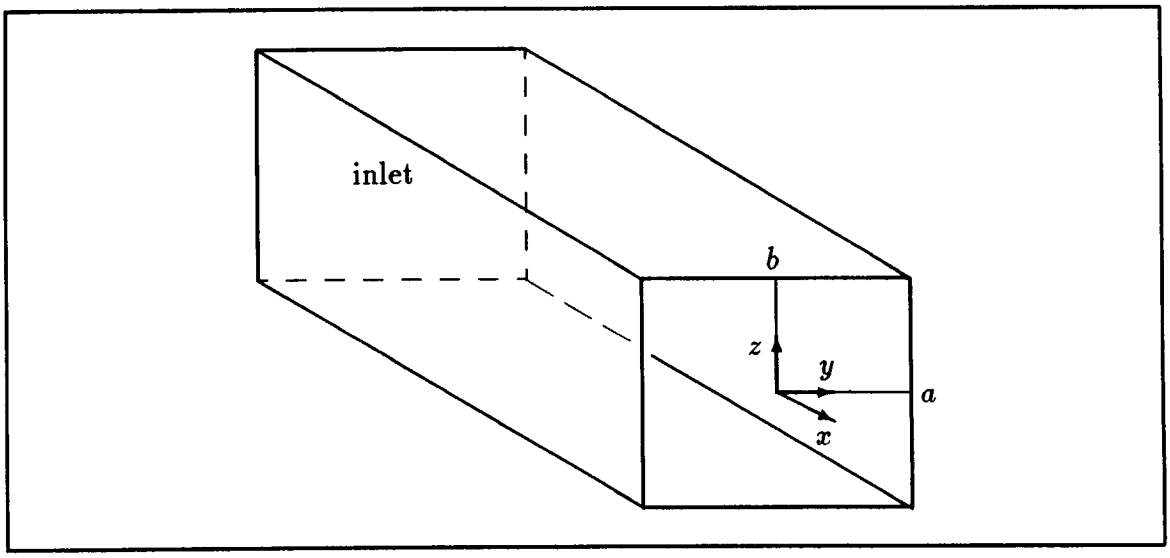

Figure 4.55: 3-D duct geometry

4.4 Three-dimensional Cases

Only a first step to three-dimensional calculations using the dual potential method has been taken here. For incompressible flow, solutions were computed for the developing flow in rectangular ducts of constant cross section. This may be considered as a stepping stone to more complex geometries. Compressible flow solutions in three-dimensions have not been obtained. Time did not permit further development of the dual potential method, but the capability of this method has been demonstrated for three-dimensional incompressible flow calculations in a simple geometry.

4.4.1 Incompressible flow

4.4.1.1 Incompressible channel inlet A three-dimensional, laminar, incompressible flow code has been programmed using the dual potential method. The

formulation (Wong and Reizes 1984) is applicable to ducts of arbitrary but constant cross section. The code has been used to calculate the developing flow in rectangular ducts of various aspect ratios for Reynolds numbers of 10 and 50. The duct geometry is shown in Figure 4.55. Uniform Cartesian grids were used to compute the solutions to be presented.

For the three-dimensional duct geometry shown in Figure 4.55, the aspect ratio is b/a. White (1974) and Shah and London (1978) give a formula to compute the fully-developed velocity profile for constant property incompressible flow in a rectangular duct of constant cross-section.

For the streamwise direction x and a rectangular section with $-a \leq y \leq a$ and $-b \leq z \leq b$:

$$u(y,z) = \frac{16a^2}{\mu\pi^3}\left(-\frac{dp}{dx}\right)\sum_{n=1,3,5,\ldots}^{\infty}\frac{1}{n^3}(-1)^{(n-1)/2}\left[1-\frac{\cosh(n\pi z/2a)}{\cosh(n\pi b/2a)}\right]\cos\left(\frac{n\pi y}{2a}\right)$$

$$Q = \frac{4}{3}\frac{ba^3}{\mu}\left(-\frac{dp}{dx}\right)\left[1-\frac{192}{\pi^5}\left(\frac{a}{b}\right)\sum_{n=1,3,5,\ldots}^{\infty}\frac{1}{n^5}\tanh\left(\frac{n\pi b}{2a}\right)\right]$$

Where Q is the volume flow rate, $Q = u_{\mathrm{m}}A$ and $A = 2a \times 2b$.

Note that the viscosity μ does not matter for the fully-developed velocity profile of $\frac{u}{u_{\mathrm{m}}}$. The pressure gradient may be eliminated in the equation for u so that $\frac{u}{u_{\mathrm{m}}}$ may be determined readily from the above equations.

The computed flow development and fully-developed profiles agree well with the known results. Better agreement could be obtained using stretched grids. The centerline velocity development for a square duct is shown in Figure 4.56. Computed results using the dual potential method are indicated by symbols. The centerline velocity development as computed on stretched grids by Wong and Reizes (1984)

Table 4.2: Fully-developed centerline velocity and skin friction

			u_{max}/u_m		C_fRe	
Aspect ratio	Re	dual pot. grid	ref.	dual pot.	ref.	dual pot.
1.00	10	$15 \times 15 \times 45$	2.096	2.065	14.22708	14.07
1.00	50	$29 \times 29 \times 60$	2.096	2.084	14.22708	14.23
0.75	50	$21 \times 15 \times 30$	2.077	2.051	14.47570	14.38
0.50	50	$31 \times 15 \times 30$	1.992	1.968	15.54806	15.40
0.25	50	$61 \times 15 \times 30$	1.774	1.752	18.23278	17.90

is shown as the Re = 10, 50 and 200 results. Experimental results of Goldstein and Kreid (1967) would be very near the Re = 200 results. The fully-developed velocity profile for Re = 50 is compared to the analytical solution in Figure 4.57. The transverse velocity vectors near the exit of a square duct are shown in Figure 4.58 and near the exit of an aspect ratio = 0.50 rectangular duct in Figure 4.59. The velocity vectors are magnified 100 times to show the persistent vortical flow in the corners even at the fully-developed condition. A similar symmetric pattern is exhibited in all the rectangular ducts. The transverse flow is toward the corner along the walls and away from the corners along the corner bisector. Note that this flow pattern happens to be the opposite of the Reynolds stress driven secondary flow for a fully-developed turbulent flow in a rectangular duct (Demuren and Rodi 1987; Speziale 1987a). The flow patterns here probably result from initial disturbances that have not yet decayed. Stretched grids are needed for more efficient calculation of this flow.

A summary of the fully-developed centerline velocity and wall skin friction coefficient for various aspect ratio ducts is given in Table 4.2. The tolerance used in computing the dual potential results was 0.0001. These results were computed on a uniform Cartesian grid. For the square cross-section duct, the skin friction coefficient

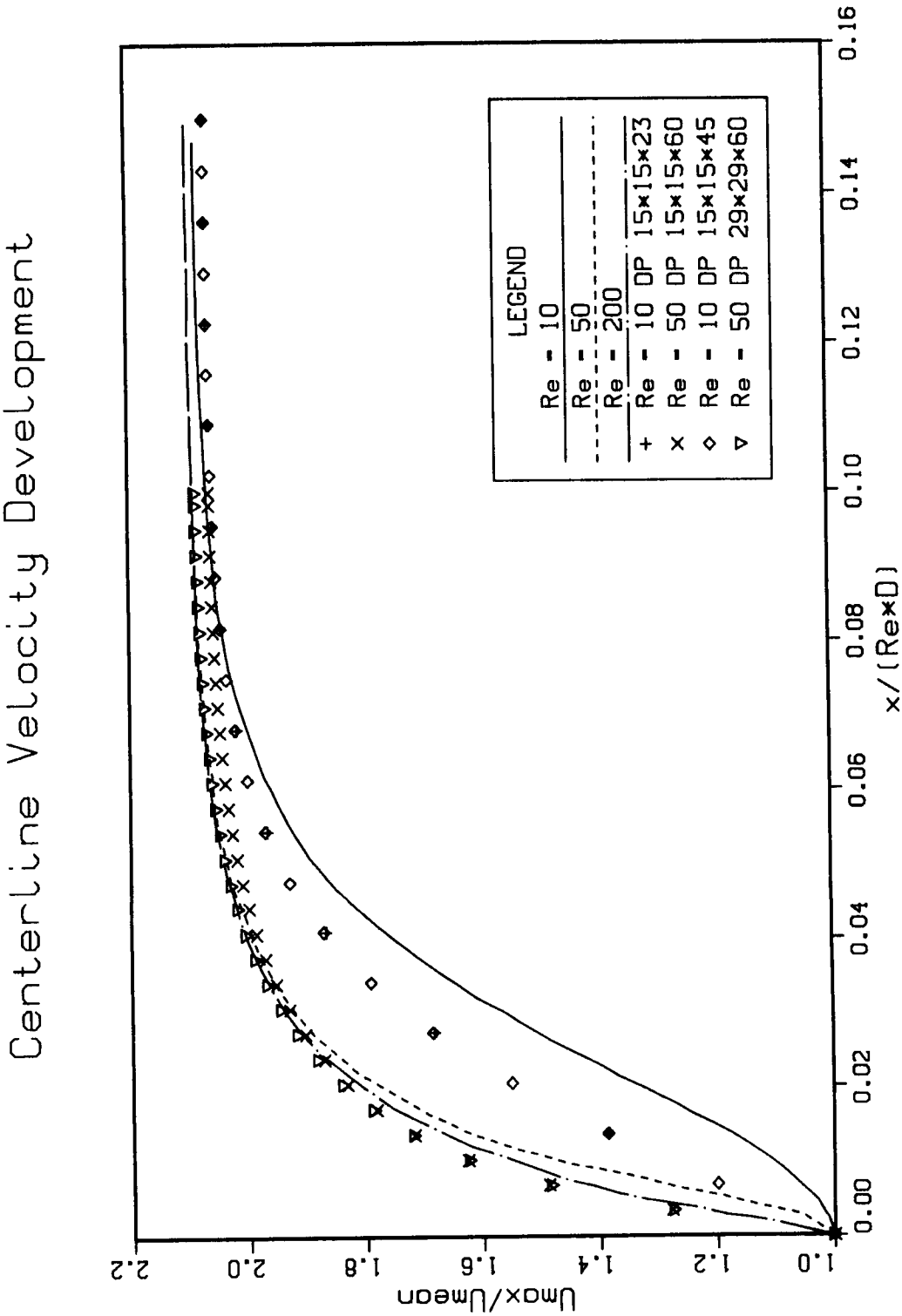

Figure 4.56: Centerline velocity development for a 3-D square duct

C-3

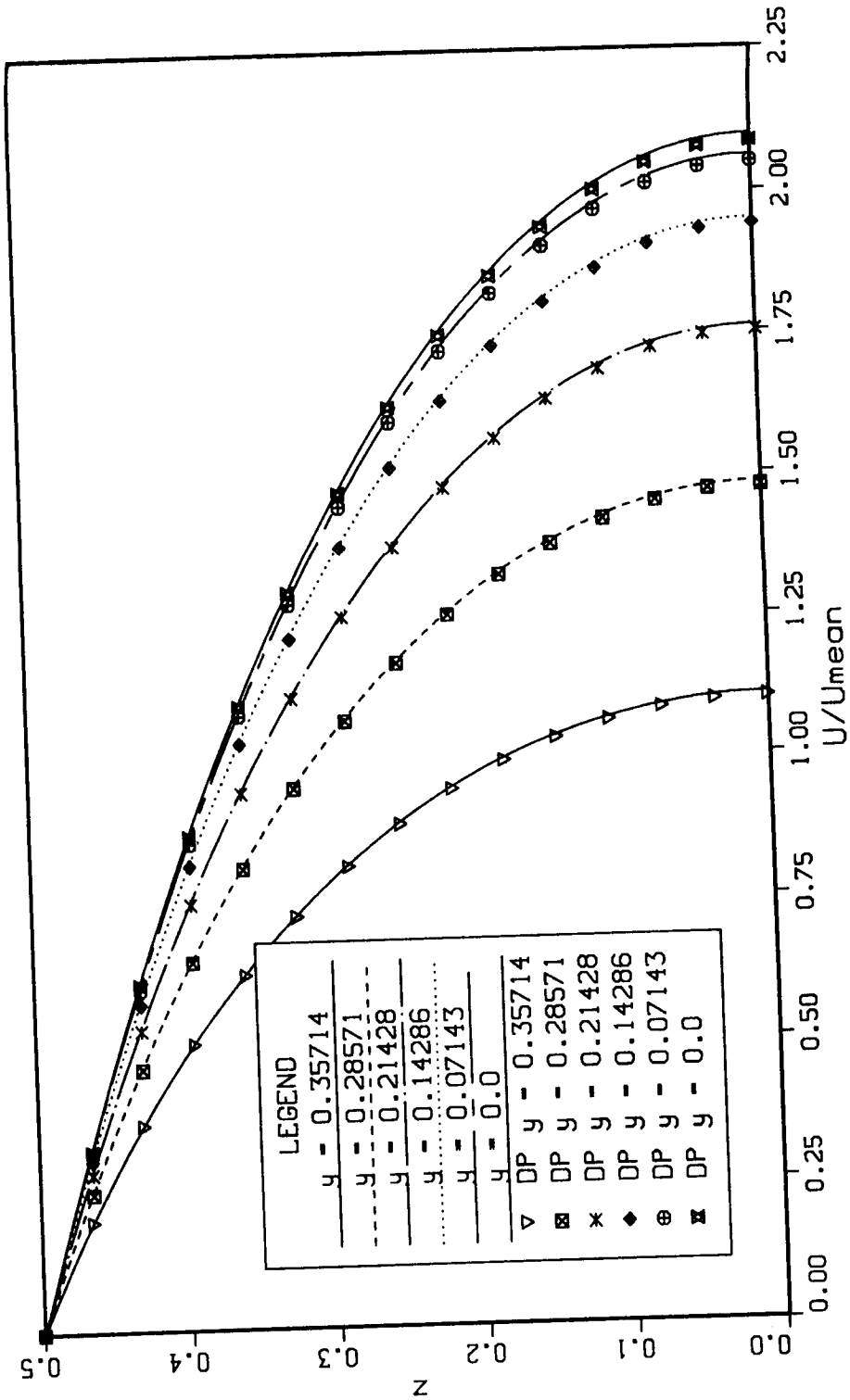

Figure 4.57: Fully-developed velocity profile comparison for a square duct at Re = 50. The Dual Potential (DP) code used a $29 \times 29 \times 60$ uniform grid

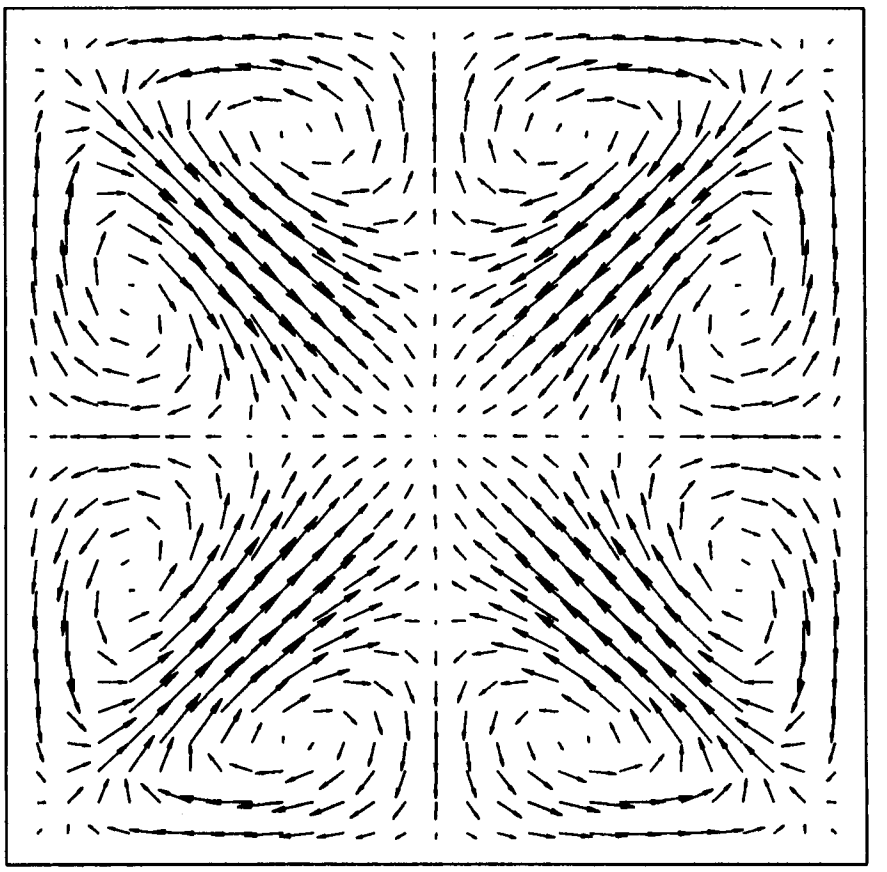

Figure 4.58: Transverse velocity vectors at a plane near the exit of a square duct with Re = 50

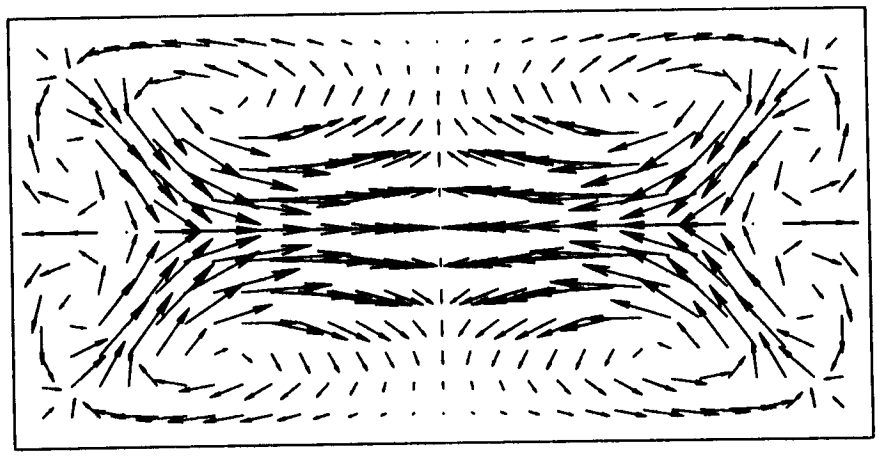

Figure 4.59: Transverse velocity vectors at a plane near the exit of a 0.50 aspect ratio duct with Re = 50

asymptotic value is computed to be $C_f\mathrm{Re} = 14.23$ on a $29 \times 29 \times 60$ grid. This is the exact answer to two places behind the decimal point.

The shear force was computed by integrating the product of the first order velocity derivative and the local wall area over the entire wall surface. A second order polynomial fit of the u velocity component is used to compute the velocity derivative in the shear stress equation. The local wall shear stress is computed from:

$$\begin{aligned} \tau_{xy} &= \mu\left(\frac{\partial u}{\partial y} + \frac{\partial v}{\partial x}\right) \\ \tau_{xz} &= \mu\left(\frac{\partial w}{\partial x} + \frac{\partial u}{\partial z}\right) \\ \tau_{yz} &= \mu\left(\frac{\partial v}{\partial z} + \frac{\partial w}{\partial y}\right) \end{aligned}$$

The shear stresses τ_{xy} and τ_{xz} are used in this computation. The integrated wall shear force is then used to compute $C_f\mathrm{Re}$.

The three-dimensional code has not been vectorized and uses point Gauss-Seidel with SOR for the vector potential Poisson equation. That particular scheme becomes

more and more inefficient as the number of grid points increases. The computation time can be reduced somewhat for steady state calculations by tightening the tolerance gradually as iterations increase. For a uniform Cartesian grid, $15 \times 15 \times 30$ points is a good compromise of accuracy and solution speed. It has been observed that a solution tolerance of 0.001–0.0001 is adequate. For more accurate results on a uniform Cartesian grid at the Reynolds numbers reported here, the spacing as in the square duct case with $29 \times 29 \times 60$ points should be used. This gives fully-developed flow solutions within 1% of the exact. Note that for incompressible flow the scalar potential can be solved once and for all for a given fixed geometry. This feature is used in the solution presented here. For the rectangular duct geometry, $\phi = x$ is the analytical solution to the Laplace equation $\nabla^2\phi = 0$ with the boundary conditions discussed in Section 3.2.1.

The computation rate for this unvectorized code is $\sim \frac{74\,\mu s}{\text{global iteration} \times \text{grid point}}$ on a single processor of the Cray X-MP. The complete flow field is solved by the current code. The symmetry of this problem was not used to speed the solution. This would immediately reduce the computation time by about a factor of four. The MFLOP rate is 12 MFLOP overall, without any enhancements.

The three-dimensional incompressible code should be extended by adding the energy equation, generalized coordinates (so a curved duct case can be computed) and a rotating coordinate capability for centrifugal compressor modeling. A more efficient Poisson solver is needed and other enhancements to improve the computation speed.

4.4.2 Compressible flow

The transport equations for $\vec{\omega}$ and B in the three-dimensional compressible formulation are given in Appendix A. No solutions were attempted.

5. DISCUSSION AND CONCLUSIONS

A dual potential procedure has been developed and evaluated for flow calculations ranging from potential flow to full Navier-Stokes solutions in two dimensions. A three-dimensional incompressible formulation has also been presented.

Compressibility has been handled by the dilatation variable. A dilatation transport equation is obtained from the momentum equations. Workable dilatation boundary conditions have been presented.

From this study the following conclusions can be made:

1. The dual potential formulation of the Navier-Stokes equations is very flexible in that it is easy to compute subset equations (potential, Euler).

2. The dual potential method can simulate irrotational and rotational inflow easily. In fact, it is interesting to note that the test cases for which experimental results are available agreed best with the computed results for an irrotational inflow condition—boundary layer and three-dimensional duct inlet flow. Yet many of the computations had to be compared with the rotational inlet condition as this is what other computational investigators have used, namely in the channel heat transfer cases. Van Dyke (1970) reports that the irrotational inlet condition may be more realistic for experimental models with a rounded entrance. The

above statement and the small sampling of experimental results suggests that the irrotational inlet condition is an important feature to be able to simulate. The dual potential method handles either condition easily.

3. Computational effort can be reduced in irrotational regions ($\vec{\omega} = 0$) and in incompressible regions ($B = 0$).

4. The method appears to be very accurate for incompressible calculations.

5. It appears possible to extend the dual potential method to compressible flow, but the dilatation transport equation may need more work. It seems that some problem still persists here—perhaps self consistency of the inflow B boundary condition—that is most noticeable for viscous compressible problems. Also, the dilatation can undergo much variation in certain regions of the flow field making it difficult to resolve. For example, in stagnation regions B changes sign as shown in Figure 4.32 for the flow over a parabolic arc bump. This behavior of the dilatation variable may be undesirable in practical use of this method.

6. The scalar potential requires a tight convergence tolerance as used in the test cases here. This may be explained by the fact that the scalar potential is the largest component in the velocity decomposition for the streamwise velocity. The convergence tolerance on the vector potential can be 1–2 orders of magnitude less restrictive than for the scalar potential. This observation may be problem specific since the streamwise velocity component was the dominant component for the test cases studied in this work.

7. For incompressible flows, the dual potential approach can be very competitive

with primitive variable methods. As an example, the original INS3D code (Kwak et al. 1986) performs at $\sim \frac{100\,\mu s}{\text{global iteration} \times \text{grid point}}$ on the Cray X-MP. The non-optimized version of the three-dimensional incompressible dual potential code runs at $\sim \frac{74\,\mu s}{\text{global iteration} \times \text{grid point}}$ on the X-MP. The only significant point to make about this comparison is that the dual potential code is written for uniform Cartesian grids while the INS3D code can handle generalized three-dimensional coordinates.

8. It is possible to solve the dual potential equation set in an iterative, uncoupled way.

A number of capabilities of this formulation have been demonstrated, some for the first time. The success seems to be limited for compressible viscous flows with a pressure gradient. Determination of the wall density is awkward for these cases and perhaps causes some problems for the dilatation transport equation. The dilatation transport equation seems to work fine for a known density and temperature field as was the case for the boundary-layer solutions. More remains to be done before a trouble free compressible formulation is available.

6. RECOMMENDATIONS FOR FUTURE WORK

The key advantages and disadvantages of the dual potential method have been stated in Section 1.3.2.2. Speziale (1987b) describes further advantages of non-primitive variable methods using vorticity. He shows that these methods have simpler boundary conditions than primitive variable formulations for problems in a rotating reference frame. A review of the literature (Ozoe et al. 1985) suggests that a dual potential formulation is the method of choice for confined flows. The solution speed of the dual potential type methods for incompressible flows is well documented (Aziz and Hellums 1967). However, the disadvantages have precluded solutions in complex geometries.

It seems best then to concentrate research efforts on the known advantages of this method and solve problems of practical interest. A few problems will be suggested that exploit the advantages of the dual potential method. Global weather forecasting is one such interesting practical problem. The geometry is simple, the flow is confined and density variations can be obtained from simple correlations. Incompressible flows inside curved, twisted ducts have been solved using the dual potential method (Yang and Camarero 1986). It should be possible to build on these solutions by allowing the duct to rotate. Many practical fluid flow problems could then be modeled such as the flow through an automotive water pump, a centrifugal compressor, a flow

PRECEDING PAGE BLANK NOT FILMED

meter, etc. Further interesting practical solutions could be obtained for problems that resemble the bump cases studied here. The "walls" in that two-dimensional problem can be allowed to move and the bump can have a time-dependent growth. Also, the flow can be treated as viscous. Since solutions have been obtained for subsonic compressible flows, the dual potential method may be well suited for computing flows with embedded compressible regions. Examples of practical flows with these features are the flow under an automobile and flow through a carburetor. Heat transfer effects can be included in all of these simulations.

In other research areas the dual potential method may also be of importance. Direct simulations of channel flow and a flat plate boundary layer have been obtained by Rai and Moin (private communication, NASA/Ames Research Center). They used a non-conservative primitive variable method on a staggered grid to simulate incompressible turbulent flow. The dual potential method could be used to compute direct simulations of these flows with little modification. If the speed advantage of the dual potential method for incompressible flow calculations extends to direct simulations, then interest in the formulation will surely increase.

It is always wise to seek out similarities in the other disciplines. The Helmholtz decomposition theorem was developed and used extensively by scientists working in electrodynamics. There may be some analogous physical problem in physics, mathematics or other field that could help in the understanding and use of the dual potential method. A search of the literature quickly turned up the paper by Müller (1987) on the topic of vector splitting applied to a physics problem.

Since the dependent variables in the dual potential formulation are vorticity and

dilatation, one should use these variables to his advantage not only in computing a flow, but in the understanding of the physics. For example, vorticity is generated by such natural phenomenon as walls and shocks. A code which solves for vorticity directly, such as the dual potential method, may be useful in problems in which one wishes to track the vorticity. The dilatation variable can also be useful in understanding some flow situations. The dilatation changes sign in the vicinity of stagnation points and shocks. This physical behavior can help give insight into the problem being studied (and cause problems numerically!).

Finally, it is important to have a code that is a good Navier-Stokes solver, but also is easily and efficiently used in other modes. It has been demonstrated that the dual potential method can be used in a potential, Euler and Navier-Stokes mode. Further work can improve the performance even more and address the issues of shock capturing, turbulence modeling, direct simulations, etc. If this method is ever to prove useful in applications, it must be able to run in all these modes efficiently and reliably. In addition it must be faster than existing methods. Unfortunately, the ideas behind the dual potential method are not as familiar as the primitive variable approaches. This unfamiliarity is a handicap since the details of application codes should be easily understood. To increase the familiarity of this method it must be tested on some problems of practical interest.

The two- and three-dimensional dual potential codes written as a part of this research are still under development. A copy of a version of the codes may be obtained from the first author or through the Department of Mechanical Engineering, Iowa State University, Ames, Iowa 50010 (Attn: Professor R. H. Pletcher).

7. REFERENCES

Ames, William F. (1977). *Numerical methods for partial differential equations.* 2d ed. Orlando: Academic Press.

Anderson, D. A., Tannehill, J. C. and Pletcher, R. H. (1984). *Computational fluid mechanics and heat transfer.* New York: McGraw-Hill.

Aregbesola, Y. A. S. and Burley, D. M. (1977). "The vector and scalar potential for the numerical solution of two- and three-dimensional Navier-Stokes equations." *J. Computational Physics,* **24**, 398–415.

Ashley, Holt and Landahl, Marten (1965). *Aerodynamics of wings and bodies.* Reading, Massachusetts: Addison-Wesley.

Aziz, K. and Hellums, J. D. (1967). "Numerical solution of the three-dimensional equations of motion for laminar natural convection." *Phys. Fluids,* **10**, 314–325.

Ballhaus, W. F. and Steger, J. L. (1975). "Implicit approximate-factorization schemes for the low-frequency transonic equation." NASA TM X-73,082.

Beam, R. M. and Ballhaus, W. F. (1975). "Numerical integration of the small-disturbance potential and Euler equations for unsteady transonic flow." NASA SP-347, **2**, 789–809.

Beam, R. M. and Warming, R. F. (1978). "An implicit factored scheme for the compressible Navier-Stokes equations." *AIAA J.,* **16**, 393–401.

Blasius, H. (1908). "Grenzschichten in Flüssigkeiten mit kleiner Reibung." *Z. Math. Phys.,* **56**, 1–37. English translation in NACA TM 1256.

Briley, W. R. and McDonald, H. (1977). "Solution of the multidimensional compressible Navier-Stokes equations by a generalized implicit method." *J.*

Computational Physics, **24**, 372–397.

Chaderjian, N. M. and Steger, J. L. (1985). "The numerical simulation of steady transonic rotational flow using a dual potential formulation." AIAA Paper 85-0368, Reno, Nevada.

Chapman, Dean R. and Rubesin, Morris W. (1949). "Temperature and velocity profiles in the compressible laminar boundary layer with arbitrary distribution of surface temperature." *J. of the Aeronautical Sciences,* **16**, 547–565.

Chorin, A. J. (1967). "A numerical method for solving incompressible viscous flow problems." *J. Computational Physics,* **2**, 12–26.

Christoph, G. H. and Pletcher, R. H. (1983). "Prediction of rough-wall skin friction and heat transfer." *AIAA J.,* **21**, 509–515.

Currie, I. G. (1974). *Fundamental mechanics of fluids.* New York: McGraw-Hill.

Davis, R. L., Carter, J. E. and Hafez, M. (1986). "Three-dimensional viscous flow solutions with a vorticity-stream function formulation." AFOSR-TR-86 (see also AIAA Paper 87-0601, Reno, Nevada).

Davis, R. L., Carter, J. E. and Hafez, M. (1989). "Three-dimensional viscous flow solutions with a vorticity-stream function formulation." *AIAA J.,* **27**, 892–900.

Dennis, S. C. R., Ingham, D. B. and Cook, R. N. (1979). "Finite-difference methods for calculating steady incompressible flows in three dimensions." *J. Computational Physics,* **33**, 325–339.

Douglas, J., Jr. (1962). "Alternating directions method for three space variables." *Numerische Mathematik,* **4**, 41–63.

D'Yakonov, Ye. G. (1963). "On the application of disintegrating difference operators." *Zh. vȳchisl. Mat. Mat. Fiz.,* **3**, 385–388.

El-Refaee, M. M. (1981). "A numerical study of laminar unsteady compressible flow over airfoils." Ph.D. dissertation, Georgia Institute of Technology, Atlanta, Georgia.

El-Refaee, M. M., Wu, J. C. and Lekoudis, S. G. (1981). "Solutions of the compressible Navier-Stokes equations using the integral method." *AIAA J.,* **20**,

356–362.

Farouk, B. and Fusegi, T. (1985). "A coupled solution of the vorticity-velocity formulation of the incompressible Navier-Stokes equations." *Int. J. for Numer. Meth. in Fluids,* **5**, 1017–1034.

Fasel, H. (1976). "Investigation of the stability of boundary layers by a finite-difference model of the Navier-Stokes equations." *J. Fluid Mechanics,* **78**, 355–383.

Fasel, H. and Booz, O. (1984). "Numerical investigation of supercritical Taylor-vortex flow for a wide gap." *J. Fluid Mechanics,* **138**, 21–52.

Gatski, T. B., Grosch, C. E. and Rose, M. E. (1982). "A numerical study of the two-dimensional Navier-Stokes equations in vorticity-velocity variables." *J. Computational Physics,* **48**, 1–22.

Gentzsch, W. and Neves, K. J. (1987). "Computational fluid dynamics: Algorithms and supercomputers." In *AGARDograph No. 311,* ed. H. Yoshihara.

Giannakoglou, K., Chaviaropoulos, P. and Papailiou, K. D. (1988). "Computation of rotational transonic flows using a decomposition method." *AIAA J.,* **26**, 1175–1180.

Goldstein, R. J. and Kreid, D. K. (1967). "Measurement of laminar flow development in a square duct using a laser-doppler flowmeter." *Trans. ASME Ser. E, J. Appl. Mech.,* **34**, 813–818.

Guj, G. and Stella, F. (1988). "Numerical solutions of high-Re recirculating flows in vorticity-velocity form." *Int. J. for Numer. Meth. in Fluids,* **8**, 405–416.

Hafez, M. M., Habashi, W. G., Przybytkowski, J. L. and Peeters, M. F. (1987). "Compressible viscous internal flow calculations by a finite element method." AIAA Paper 87-0644, Reno, Nevada.

Hirasaki, G. J. and Hellums, J. D. (1970). "Boundary conditions on the vector and scalar potentials in viscous three-dimensional hydrodynamics." *Q. Appl. Math.,* **28**, 293–296.

Holst, T. L. (1987). "Numerical solution of the Navier-Stokes equations about three-dimensional configurations—A survey." *Supercomputing in Aerospace.*

NASA CP 2454, 281–298.

Hwang, Ching-Lai and Fan, Liang-Tseng (1964). "Finite difference analysis of forced-convection heat transfer in entrance region of a flat rectangular duct." *Appl. Sci. Res., Sect. A,* **13**, 401–422.

Kays, W. M. and Crawford, M. E. (1980). *Convective heat and mass transfer.* 2d ed. New York: McGraw-Hill.

Kwak, D., Chang, J. L. C., Shanks, S. P. and Chakravarthy, S. (1986). "A three-dimensional incompressible Navier-Stokes flow solver using primitive variables." *AIAA J.,* **24**, 390–396.

MacCormack, R. W. (1981). "A numerical method for solving the equations of compressible viscous flow." AIAA Paper 81-0110, St. Louis, Missouri.

Mallinson, G. D. and De Vahl Davis, G. (1973). "The method of the false transient for the solution of coupled elliptic equations." *J. Computational Physics,* **12**, 435–461.

McDonald, J. W., Denny, V. E. and Mills, A. F. (1972). "Numerical solutions of the Navier-Stokes equations in inlet regions." *Trans. ASME Ser. E, J. Appl. Mech.,* **39**, 873–878.

Mitchell, A. R. and Griffiths, D. F. (1980). *The finite difference method in partial differential equations.* New York: John Wiley & Sons.

Morino, L. (1985). "Scalar/vector potential formulation for compressible viscous unsteady flows." NASA CR 3921.

Morino, L. (1986). "Helmholtz decomposition revisited: Vorticity generation and trailing edge condition." *Computational Mechanics,* **1**, 65–90.

Müller, E. E. (1987). "Scalar potentials for vector fields in quantum electrodynamics." *J. Math Phys.,* **28**, 2786–2790.

Nelson, R. M. and Pletcher, R. H. (1974). "An explicit scheme for the calculation of confined turbulent flows with heat transfer." Proceedings of the 1974 Heat Transfer and Fluid Mechanics Institute. Stanford University Press. 154–170.

O'Donnell, Robert M. (1954). "Experimental investigation at a Mach number of

2.41 of average skin-friction coefficients and velocity profiles for laminar and turbulent boundary layers and an assessment of probe effects." NACA TN 3122.

Orlandi, P. (1987). "Vorticity-velocity formulation for high Re flows." *Computers & Fluids,* **15**, 137–149.

Osswald, G. A., Ghia, K. N. and Ghia, U. (1987). "A direct algorithm for solution of incompressible three-dimensional unsteady Navier-Stokes equations." AIAA Paper 87-1139.

Ozoe, H., Yamamoto, K., Churchill, S. W. and Sayama, H. (1976). "Three-dimensional, numerical analysis of laminar natural convection in a confined fluid heated from below." *J. Heat Transfer,* Transactions of the ASME, **98**, 202–207.

Ozoe, H., Yamamoto, K., Sayama, H. and Churchill, S. (1977). "Natural convection patterns in a long inclined rectangular box heated from below. Part II. Three-dimensional numerical results." *Int. J. Heat Mass Transfer,* **20**, 131–139.

Ozoe, H., Yamamoto, K. and Churchill, S. W. (1979). "Three-dimensional numerical analysis of natural convection in an inclined channel with a square cross section." *AIChE J.,* **25**, 709–716.

Ozoe, H., Mouri, A., Ohmuro, M., Churchill, S. and Lior, N. (1985). "Numerical calculations of laminar and turbulent natural convection in water in rectangular channels heated and cooled isothermally on the opposing vertical walls." *Int. J. Heat Mass Transfer,* **28**, 125–138.

Patankar, S. V. (1975). "Numerical prediction of three-dimensional flows." In *Studies in convection: theory, measurement, and applications,* ed. B. E. Launder, **1**, 1–78. New York: Academic Press.

Patankar, S. V. (1981). "A calculation procedure for two-dimensional elliptic situations." *Numer. Heat Transfer,* **4**, 409–425.

Peaceman, D. W. and Rachford, H. H. (1955). "The numerical solution of parabolic and elliptic differential equations." *J. Soc. Indust. App. Math.,* **3**, 28–41.

Rao, K. V. (1987). "A three-dimensional dual potential procedure with applications to wind tunnel inlets and interacting boundary layers." Ph.D. dissertation, Iowa State University, Ames, Iowa.

Rao, K. V., Steger, J. L. and Pletcher, R. H. (1989). "Three-dimensional dual potential procedure for inlets and indraft wind tunnels." *AIAA J.*, **27**, 876–884.

Richardson, S. M. and Cornish, A. R. H. (1977). "Solution of three-dimensional incompressible flow problems." *J. Fluid Mechanics,* **82**, 309–319.

Roache, P. J. (1972). *Computational fluid dynamics.* New Mexico: Hermosa Publishers.

Roberts, G. O. (1971). "Computational meshes for boundary layer problems." *Proc. Second Int. Conf. Num. Methods Fluid Dyn., Lecture Notes in Physics,* **8**, 171–177, New York: Springer-Verlag.

Rogers, S. E. and Kwak, D. (1988). "An upwind differencing scheme for the time-accurate incompressible Navier-Stokes equations." AIAA Paper 88-2583, Williamsburg, Virginia.

Rogers, S. E., Kwak, D. and Chang, J. L. C. (1987). "INS3D—An incompressible Navier-Stokes code in generalized three-dimensional coordinates." NASA Technical Memorandum 100012.

Schade, K. W. and McEligot, D. M. (1971). "Cartesian Graetz problems with air property variation." *Int. J. Heat Mass Transfer,* **14**, 653–666.

Schlichting, H. (1979). *Boundary-layer theory.* 7th ed. Translated by J. Kestin. New York: McGraw-Hill.

Shah, R. K. and London, A. L. (1978). "Laminar flow forced convection in ducts: A source book for compact heat exchanger analytical data." In *Advances in Heat Transfer,* ed. Thomas F. Irvine, Jr. and James P. Hartnett. New York: Academic Press.

Speziale, Charles G. (1987a). "On nonlinear K-l and K-ϵ models of turbulence." *J. Fluid Mechanics,* **178**, 459–475.

Speziale, Charles G. (1987b). "On the advantages of the vorticity-velocity formulation of the equations of fluid dynamics." *J. Computational Physics,* **73**, 476–480.

Steger, J. L., Ying, S. X. and Schiff, L. B. (1986). "A partially flux-split algorithm for numerical simulation of compressible inviscid and viscous flow." Proceedings

of the Workshop on Computational Fluid Dynamics. Institute of Nonlinear Sciences. University of California, Davis, CA.

Tenpas, P. W. and Pletcher, R. H. (1987). "Solution of the Navier-Stokes equations for subsonic flows using a coupled space-marching method." AIAA Paper 87-1173.

Van Driest, E. R. (1952). "Investigation of laminar boundary layer in compressible fluids using the Crocco method." NACA TN 2597.

Van Dyke, M. (1970). "Entry flow in a channel." *J. Fluid Mechanics,* **44**, 813–823.

Wang, Y. L. and Longwell, P. A. (1964). "Laminar flow in the inlet section of parallel plates." *AIChE J.,* **10**, 323–329.

White, F. M. (1974). *Viscous fluid flow.* New York: McGraw-Hill.

Wong, A. K. and Reizes, J. A. (1984). "An effective vorticity-vector potential formulation for the numerical solution of three-dimensional duct flow problems." *J. Computational Physics,* **55**, 98–114.

Wong, A. K. and Reizes, J. A. (1986). "The vector potential in the numerical solution of three-dimensional fluid dynamics problems in multiply connected regions." *J. Computational Physics,* **62**, 124–142.

Yang, H. and Camarero, R. (1986). "An improved vorticity-potential method for three-dimensional duct flow problems." *Int. J. for Numer. Meth. in Fluids,* **6**, 35–45.

8. APPENDIX A: THREE-DIMENSIONAL VORTICITY AND DILATATION TRANSPORT EQUATIONS

The momentum equations for a three-dimensional flow of a Newtonian Stokesian fluid will be presented here. They will be written in terms of vorticity (actually $\frac{\omega}{\rho}$) and dilatation as the dependent variables. First a point will be made about the number of transport equations which must be solved for the vorticity in three dimensions.

In three dimensions it is only necessary to solve two of the three component vorticity transport equations because the third vorticity can always be obtained by a linear combination of derivatives of the other two. To see this, consider the vorticity definition,

$$\vec{\omega} = \vec{\nabla} \times \vec{V}$$

where,

$$\begin{aligned} \omega_1 &= w_y - v_z \\ \omega_2 &= u_z - w_x \\ \omega_3 &= v_x - u_y \end{aligned}$$

therefore,

$$\omega_{3z} = -\omega_{1x} - \omega_{2y}$$

Hence, the third vorticity component can always be obtained from the other two components. In the above, the numbers 1,2,3 represent directions and the letters x, y, z are derivatives.

The vorticity transport and the dilatation transport equations follow. They represent the momentum equations for a three-dimensional flow. To compute a flow field using the dual potential method, additional equations are required to satisfy mass and energy conservation. Also, the Poisson equations for the potentials must be solved (Equations 2.13 and 2.14):

$$\nabla^2 \phi = B$$
$$\nabla^2 \vec{A} = -\vec{\omega}$$

Equations 8.1–8.3 display the vorticity transport equations in the dependent variable, $\left(\frac{\omega}{\rho}\right)$. The three-dimensional dilatation transport equation is presented in Equation 8.4. The ideal gas law ($p = \rho RT$) has been used to replace the pressure gradient term in the momentum equations. Body forces are neglected. The following equations have not been coded. Their numerical behavior is unknown.

Vorticity transport: x–component

$$
\begin{aligned}
&\left(\frac{\omega_1}{\rho}\right)_t + u\left(\frac{\omega_1}{\rho}\right)_x + v\left(\frac{\omega_1}{\rho}\right)_y + w\left(\frac{\omega_1}{\rho}\right)_z = \\
&\quad \left[u_x + \frac{1}{\rho^2}\frac{1}{\mathrm{Re}}\left\{\mu\nabla^2\rho + \mu_x\rho_x + \mu_y\rho_y + \mu_z\rho_z\right\}\right]\left(\frac{\omega_1}{\rho}\right) \\
&\qquad + \frac{1}{\rho}\frac{1}{\mathrm{Re}}\left[\mu_x\left(\frac{\omega_1}{\rho}\right)_x + \mu_y\left(\frac{\omega_1}{\rho}\right)_y + \mu_z\left(\frac{\omega_1}{\rho}\right)_z\right] \\
&\qquad + \frac{1}{\rho}\frac{1}{\mathrm{Re}}\mu\nabla^2\left(\frac{\omega_1}{\rho}\right) \\
&\qquad + u_y\left(\frac{\omega_2}{\rho}\right) + u_z\left(\frac{\omega_3}{\rho}\right) \\
&\qquad + \frac{R}{\rho^2}\left[T_z\rho_y - T_y\rho_z\right] \\
&\qquad + \frac{1}{\rho}\frac{1}{\mathrm{Re}}\Bigg[\quad \left(\frac{\mu}{\rho}\right)_y\left(\nabla^2 w + \frac{1}{3}\frac{\partial}{\partial z}\vec{\nabla}\cdot\vec{V}\right) \\
&\qquad\qquad - \left(\frac{\mu}{\rho}\right)_z\left(\nabla^2 v + \frac{1}{3}\frac{\partial}{\partial y}\vec{\nabla}\cdot\vec{V}\right) \\
&\qquad\qquad + \left(\frac{\mu_y}{\rho}\right)\frac{2}{3}\frac{\partial}{\partial z}\vec{\nabla}\cdot\vec{V} - \left(\frac{\mu_z}{\rho}\right)\frac{2}{3}\frac{\partial}{\partial y}\vec{\nabla}\cdot\vec{V} \\
&\qquad\qquad + \left(\frac{\mu_x}{\rho}\right)_y\left(w_x + u_z\right) \\
&\qquad\qquad + \left(\frac{\mu_y}{\rho}\right)_y\left(v_z + w_y\right) \\
&\qquad\qquad + \left(\frac{\mu_z}{\rho}\right)_y\left(2w_z - \frac{2}{3}\vec{\nabla}\cdot\vec{V}\right) \\
&\qquad\qquad - \left(\frac{\mu_x}{\rho}\right)_z\left(u_y + v_x\right) \\
&\qquad\qquad - \left(\frac{\mu_y}{\rho}\right)_z\left(2v_y - \frac{2}{3}\vec{\nabla}\cdot\vec{V}\right) \\
&\qquad\qquad - \left(\frac{\mu_z}{\rho}\right)_z\left(v_z + w_y\right)\Bigg]
\end{aligned}
\tag{8.1}
$$

Vorticity transport: y–component

$$
\begin{aligned}
&\left(\frac{\omega_2}{\rho}\right)_t + u\left(\frac{\omega_2}{\rho}\right)_x + v\left(\frac{\omega_2}{\rho}\right)_y + w\left(\frac{\omega_2}{\rho}\right)_z = \\
&\quad \left[v_y + \frac{1}{\rho^2}\frac{1}{\mathrm{Re}}\left\{\mu\nabla^2\rho + \mu_x\rho_x + \mu_y\rho_y + \mu_z\rho_z\right\}\right]\left(\frac{\omega_2}{\rho}\right) \\
&\qquad + \frac{1}{\rho}\frac{1}{\mathrm{Re}}\left[\mu_x\left(\frac{\omega_2}{\rho}\right)_x + \mu_y\left(\frac{\omega_2}{\rho}\right)_y + \mu_z\left(\frac{\omega_2}{\rho}\right)_z\right] \\
&\qquad + \frac{1}{\rho}\frac{1}{\mathrm{Re}}\mu\nabla^2\left(\frac{\omega_2}{\rho}\right) \\
&\qquad + v_x\left(\frac{\omega_1}{\rho}\right) + v_z\left(\frac{\omega_3}{\rho}\right) \\
&\qquad + \frac{R}{\rho^2}\left[T_x\rho_z - T_z\rho_x\right] \\
&\qquad + \frac{1}{\rho}\frac{1}{\mathrm{Re}}\Bigg[\quad \left(\frac{\mu}{\rho}\right)_z\left(\nabla^2 u + \frac{1}{3}\frac{\partial}{\partial x}\vec{\nabla}\cdot\vec{V}\right) \\
&\qquad\qquad - \left(\frac{\mu}{\rho}\right)_x\left(\nabla^2 w + \frac{1}{3}\frac{\partial}{\partial z}\vec{\nabla}\cdot\vec{V}\right) \\
&\qquad\qquad + \left(\frac{\mu_z}{\rho}\right)\frac{2}{3}\frac{\partial}{\partial x}\vec{\nabla}\cdot\vec{V} - \left(\frac{\mu_x}{\rho}\right)\frac{2}{3}\frac{\partial}{\partial z}\vec{\nabla}\cdot\vec{V} \\
&\qquad\qquad + \left(\frac{\mu_x}{\rho}\right)_z\left(2u_x - \frac{2}{3}\vec{\nabla}\cdot\vec{V}\right) \\
&\qquad\qquad + \left(\frac{\mu_y}{\rho}\right)_z\left(u_y + v_x\right) \\
&\qquad\qquad + \left(\frac{\mu_z}{\rho}\right)_z\left(w_x + u_z\right) \\
&\qquad\qquad - \left(\frac{\mu_x}{\rho}\right)_x\left(w_x + u_z\right) \\
&\qquad\qquad - \left(\frac{\mu_y}{\rho}\right)_x\left(v_z + w_y\right) \\
&\qquad\qquad - \left(\frac{\mu_z}{\rho}\right)_x\left(2w_z - \frac{2}{3}\vec{\nabla}\cdot\vec{V}\right)\Bigg]
\end{aligned}
\tag{8.2}
$$

Vorticity transport: z–component

$$
\begin{aligned}
&\left(\frac{\omega_3}{\rho}\right)_t + u\left(\frac{\omega_3}{\rho}\right)_x + v\left(\frac{\omega_3}{\rho}\right)_y + w\left(\frac{\omega_3}{\rho}\right)_z = \\
&\quad \left[w_z + \frac{1}{\rho^2}\frac{1}{\mathrm{Re}}\left\{\mu\nabla^2\rho + \mu_x\rho_x + \mu_y\rho_y + \mu_z\rho_z\right\}\right]\left(\frac{\omega_3}{\rho}\right) \\
&\qquad + \frac{1}{\rho}\frac{1}{\mathrm{Re}}\left[\mu_x\left(\frac{\omega_3}{\rho}\right)_x + \mu_y\left(\frac{\omega_3}{\rho}\right)_y + \mu_z\left(\frac{\omega_3}{\rho}\right)_z\right] \\
&\qquad + \frac{1}{\rho}\frac{1}{\mathrm{Re}}\mu\nabla^2\left(\frac{\omega_3}{\rho}\right) \\
&\qquad + w_x\left(\frac{\omega_1}{\rho}\right) + w_y\left(\frac{\omega_2}{\rho}\right) \\
&\qquad + \frac{R}{\rho^2}\left[T_y\rho_x - T_x\rho_y\right] \\
&\qquad + \frac{1}{\rho}\frac{1}{\mathrm{Re}}\Bigg[\quad \left(\frac{\mu}{\rho}\right)_x\left(\nabla^2 v + \frac{1}{3}\frac{\partial}{\partial y}\vec{\nabla}\cdot\vec{V}\right) \\
&\qquad\qquad - \left(\frac{\mu}{\rho}\right)_y\left(\nabla^2 u + \frac{1}{3}\frac{\partial}{\partial x}\vec{\nabla}\cdot\vec{V}\right) \\
&\qquad\qquad + \left(\frac{\mu_x}{\rho}\right)\frac{2}{3}\frac{\partial}{\partial y}\vec{\nabla}\cdot\vec{V} - \left(\frac{\mu_y}{\rho}\right)\frac{2}{3}\frac{\partial}{\partial x}\vec{\nabla}\cdot\vec{V} \\
&\qquad\qquad + \left(\frac{\mu_x}{\rho}\right)_x\left(u_y + v_x\right) \\
&\qquad\qquad + \left(\frac{\mu_y}{\rho}\right)_x\left(2v_y - \frac{2}{3}\vec{\nabla}\cdot\vec{V}\right) \\
&\qquad\qquad + \left(\frac{\mu_z}{\rho}\right)_x\left(v_z + w_y\right) \\
&\qquad\qquad - \left(\frac{\mu_x}{\rho}\right)_y\left(2u_x - \frac{2}{3}\vec{\nabla}\cdot\vec{V}\right) \\
&\qquad\qquad - \left(\frac{\mu_y}{\rho}\right)_y\left(u_y + v_x\right) \\
&\qquad\qquad - \left(\frac{\mu_z}{\rho}\right)_y\left(w_x + u_z\right)\Bigg]
\end{aligned}
\tag{8.3}
$$

Dilatation transport:

$$
\begin{aligned}
&B_t + uB_x + vB_y + wB_z - \left(\frac{4}{3}\frac{\mu}{\rho \mathrm{Re}}\right)\nabla^2 B = \\
&\quad -\left(u_x^2 + v_y^2 + w_z^2 + 2u_y v_x + 2u_z w_x + 2v_z w_y\right) \\
&\quad -\frac{\mu}{\rho^2 \mathrm{Re}}\Big[\rho_x\left(\omega_{2z} - \omega_{3y} + \frac{4}{3}B_x\right) + \rho_y\left(\omega_{3x} - \omega_{1z} + \frac{4}{3}B_y\right) \\
&\qquad\quad +\rho_z\left(\omega_{1y} - \omega_{2x} + \frac{4}{3}B_z\right)\Big] \\
&\quad -R\nabla^2 T - \frac{RT}{\rho}\nabla^2\rho - \frac{R}{\rho}(T_x\rho_x + T_y\rho_y + T_z\rho_z) + \frac{RT}{\rho^2}(\rho_x^2 + \rho_y^2 + \rho_z^2) \\
&\quad +\frac{\mu_x}{\rho \mathrm{Re}}\left[2\omega_{2z} - 2\omega_{3y} + \frac{8}{3}B_x - \frac{\rho_x}{\rho}\left(2u_x - \frac{2}{3}B\right) - \frac{\rho_y}{\rho}\left(u_y + v_x\right) - \frac{\rho_z}{\rho}\left(w_x + u_z\right)\right] \\
&\quad +\frac{\mu_y}{\rho \mathrm{Re}}\left[2\omega_{3x} - 2\omega_{1z} + \frac{8}{3}B_y - \frac{\rho_x}{\rho}\left(u_y + v_x\right) - \frac{\rho_y}{\rho}\left(2v_y - \frac{2}{3}B\right) - \frac{\rho_z}{\rho}\left(v_z + w_y\right)\right] \\
&\quad +\frac{\mu_z}{\rho \mathrm{Re}}\left[2\omega_{1y} - 2\omega_{2x} + \frac{8}{3}B_z - \frac{\rho_x}{\rho}\left(w_x + u_z\right) - \frac{\rho_y}{\rho}\left(v_z + w_y\right) - \frac{\rho_z}{\rho}\left(2w_z - \frac{2}{3}B\right)\right] \\
&\quad +\frac{2}{\rho \mathrm{Re}}\left[\mu_{xy}\left(u_y + v_x\right) + \mu_{xz}\left(w_x + u_z\right) + \mu_{zy}\left(v_z + w_y\right)\right] \\
&\quad +\frac{2}{\rho \mathrm{Re}}\left(\mu_{xx}u_x + \mu_{yy}v_y + \mu_{zz}w_z\right) - \frac{2}{3}\frac{B}{\rho \mathrm{Re}}\nabla^2\mu
\end{aligned}
\tag{8.4}
$$

9. APPENDIX B: ALTERNATE NON-PRIMITIVE VARIABLE EQUATIONS

An approach different from that presented in the main body of this report is to form a different combination with the x, y momentum equations.

In two dimensions the governing equations are:

1. continuity
2. x momentum
3. y momentum
4. energy

The cross product applied to the momentum equations yields the vorticity transport equation. This leaves one with still another usage of the momentum equations. In the main body of this report the dilatation variable, $B = u_x + v_y$, was selected as the final usage. Another possible operation on the momentum equations is to compute $\frac{\partial}{\partial y}$ (x momentum) + $\frac{\partial}{\partial x}$ (y momentum). Then, choosing the dependent variable to be $(u_y + v_x)$, an equation for the rate of shear deformation is derived. Let $\Gamma = u_y + v_x$.

The two-dimensional equation for Γ is

$$\rho\left[\Gamma_t + u\Gamma_x + v\Gamma_y + \Gamma B\right] = -2p_{xy} + \frac{\mu}{\mathrm{Re}}\nabla^2\Gamma + \frac{2}{\mathrm{Re}}\nabla\Gamma\cdot\nabla\mu + \frac{\Gamma}{\mathrm{Re}}\nabla^2\mu + \frac{1}{\mathrm{Re}}\frac{\partial^2}{\partial x\partial y}\mu B - \rho_y\frac{\mathrm{D}u}{\mathrm{D}t} - \rho_x\frac{\mathrm{D}v}{\mathrm{D}t} \tag{9.1}$$

Then, the momentum equations provide the solution for ω and Γ. Recalling the definitions,

$$\omega = v_x - u_y \tag{9.2}$$

$$\Gamma = v_x + u_y \tag{9.3}$$

one obtains the following compact formulas for some velocity derivatives:

$$v_x = \frac{\omega + \Gamma}{2} \tag{9.4}$$

$$u_y = \frac{\Gamma - \omega}{2} \tag{9.5}$$

This adaptation to the dual potential method could be used as an inverse solution procedure since the wall shear stress is simply $\mu\Gamma$.

NOTICE: At a no-slip impermeable boundary, $v_x = 0$. There is no trouble getting the vorticity at the wall. Therefore, Γ should be simple to obtain once the vorticity is computed! At the wall $\Gamma = -\omega$. Also, the potentials are not needed for this use of the momentum equations.